Development of a pH-sensitive Nanoformulation for Combined Chemo-Immunotherapy of Breast Cancer

THESIS

Submitted in partial fulfillment
of the requirements for the degree of

DOCTOR OF PHILOSOPHY

by

MARAVAJJALA KAVYA SREE

ID. No. 2019PHXF0053P

Under the Supervision of

Dr. ANIRUDDHA ROY

Under the Co-supervision of

Dr. GAUTAM SINGHVI

BITS Pilani
Pilani | Dubai | Goa | Hyderabad | Mumbai

BIRLA INSTITUTE OF TECHNOLOGY & SCIENCE, PILANI

2024

DECLARATION

I hereby declare that the work carried out in this thesis entitled "**Development of a pH-sensitive Nanoformulation for Combined Chemo-Immunotherapy of Breast Cancer**" is an original piece of research work carried out by me under the guidance of Dr. Aniruddha Roy (supervisor) and Dr. Gautam Singhvi (co-supervisor) at BITS-Pilani, Pilani campus, Rajasthan, India. I have not submitted this thesis for the award of any other degree from any other university/institute.

Kavya Sree Maravajjala

Date:

Place: Pilani, Rajasthan, India

BIRLA INSTITUTE OF TECHNOLOGY AND SCIENCE, PILANI

CERTIFICATE

This is to certify that the thesis titled **Development of a pH-sensitive Nanoformulation for Combined Chemo-Immunotherapy of Breast Cancer** submitted by **Maravajjala Kavya Sree** ID No **2019PHXF0053P** for award of Ph.D. of the Institute embodies original work done by him/her under my supervision.

Signature of the Supervisor:
Name in capital letters: ANIRUDDHA ROY
Designation: Associate Professor

Signature of the Co-Supervisor:
Name in capital letters: GAUTAM SINGHVI
Designation: Associate Professor

Date:

TABLE OF CONTENTS

Acknowledgment

I want to express my gratitude and heartfelt appreciation to my Ph.D. supervisor, **Prof. Aniruddha Roy**, Associate Professor at BITS-Pilani, Pilani Campus, for his unwavering support and encouragement throughout my research journey. I am deeply indebted to him for taking me under his wing and instilling in me the values of independent thinking and the pursuit of excellence in research. His dedication to advancing the frontiers of knowledge and his remarkable ability to manage multiple tasks have always served as a great source of inspiration to me. I would also like to thank my co-supervisor, **Prof. Gautam Singhvi**, for his invaluable support, guidance, and motivation. I am thankful to him for imparting essential lessons about the intricacies of professional life in various ways, enriching my academic and personal growth.

I wish to thank **Prof. Swati Biswas** and **Mr. Milan Paul** from the BITS-Pilani Hyderabad campus for their generous support and invaluable assistance in conducting animal studies.

I am thankful to **Prof. V. Ramgopal Rao**, Vice-Chancellor, BITS-Pilani, **Prof. Sudhir Kumar Barai,** Director, BITS-Pilani, Pilani Campus, **Col Soumyabrata Chakraborty**, Registrar, BITS-Pilani, Pilani Campus, **Prof. Shamik Chakraborty**, Associate Dean, AGSRD, BITS-Pilani, Pilani Campus, for providing work facilities and an absorbing research environment. I sincerely thank **Prof. Anil Gaikwad**, Head of the Department of Pharmacy, **Prof. Hemant Jadhav,** and **Prof. Atish Paul**, former Head, for their constant support in providing the resources required during my research work.

I want to express my profound gratitude to the members of my Doctoral Advisory Committee (DAC), **Prof. Anil Jindal** and **Prof. Anupama Mittal**, for their thorough review of my thesis and their valuable contributions through constructive criticism, who served as the Convener of the Departmental Research Committee, for her invaluable guidance in the process of compiling this thesis.

I want to express my gratitude to the dedicated faculty members of the Department of Pharmacy, including **Prof. R.N. Saha** (Retired Professor), **Prof. R. Mahesh, Prof. S. Murugesan, Prof. Rajeev Taliyan, Prof. Deepak Chitkara, Prof. M.M. Pandey, Prof. Sandeep Sundriyal, Dr. Richa Srivastava, Dr. Pragyanshu Khare,** and **Dr. Sunil Kumar Dubey** (former Assistant Professor), for their invaluable teachings and guidance. Additionally, I extend my thanks to **Dr. Sushil Kumar Yadav** for his support in conducting animal studies.

Your collective contributions have greatly enriched my academic journey, and I appreciate the knowledge and assistance you have provided.

I would also like to express my heartfelt appreciation to my senior colleagues, **Dr. Karanam Laxmi Swetha and Dr. Swati Sharma,** as well as my fellow lab mates, **Mr. Shrikant Kirawale, Ms. Ruchika Rajani, Mr. Vagesh Verma and Ms. Ritika**. I am deeply grateful for their unwavering support, willingness to dedicate valuable time, patience in always listening to me, and motivating presence throughout my journey.

All my seniors and colleagues Dr. Kowthavarapu Venkata Krishna, Dr. Saurabh Sharma, Dr. Kishan Italiya, Dr. Dhanashree Surve, Dr. Vajir Malek, Dr. Nisha Sharma, Dr. Ginson George, Dr. Pracheta Sengupta, Dr. Sudeep Pukale, Dr. Vamshi Krishna Rapalli, Dr. Sarathlal K.C., Dr. Samrat Mazumdar, Dr. Geethika, Dr. Paramita, Dr. Violina, Dr. Karan Kumar, Dr. Himanshu, Dr. Tejashree Waghule, Dr. Kedar Prayag, Dr. Srividya Gorantla, Dr. Deepak Kumar Sahel, Mr. Rupesh Jain, Mr. Rajesh Pradhan, Mr. Amritansh Bhanot, Mr. Arihant Kumar Singh, Mr. Prabhjeet Singh, Ms. Moumita Basak, Ms. Nikita Hinge, Mr. Mahipal Donthi, Ms. Manisha Choudhari, Mr. Ajinath Kale, Mr. Atharva Bhide, Mr. Prashant Auti, Mr. N. Saibhargav, Ms. Reena, Ms. Karnam Serravalle, Ms. Nisha, Mr. Mukesh, Ms. Shreya Das, Ms. Sharyu Kesharwani, Mr. Amit Sharma, Mr. Mukesh, Mr. Vishwadeep, Mr. Sai Pradyuth, Mr. Shivanshu, Ms. Sakshi, Ms. Ila, Ms. Yashika, Mr. Shivanshu, Ms. Shobha, Mr. Shubham, Ms. Sonia, Mr. Abhay, Ms. Shikha, Ms. Neha, Mr. Giriprasad, Mr. Chandu Ala, Mr. Jayant, Md Muzaffar Rehaman, Ms. Lavanya, Mr. Utkarsh, Mr. Yash Patidar, Ms. Shivangi, Ms. Vaibhavi, Ms. Shivani, Ms. Priyanka, Ms. Jyothika, Ms. Aarthi, Mr. Jagdish, Mr. Bhupendra, Mr. Animesh, Ms. Pranali, Mr.Prathik, Mr. Sanat, Ms. Ila deserve Special appreciation is due to them for fostering a delightful working atmosphere in the laboratory and for infusing it with fun and enjoyment.

I want to thank graduates and postgraduates with whom I worked closely for exploring things. I thank Mr.Thanmai, Ms. Daksha, Mr. Kinshuk, Mr. Swapnil, Mr. Ashish, Mr. Mehul, Ms. Dhanashree, Ms. Kaushitha, Mr. Abhijeet, Ms. Akanksha, Ms. Sharvani and Ms. Ruchitha. Ms. Vruthi, Mr. Ameya Deshpande, Mr. Ameya Kothekar.

I would also like to thank **Mrs. Propanna, Mr. Yash** and all the scholars from the **Department of Biological Sciences** and **Ms. Prachi sharma, Ms. Aishwarya, Sumit** and other scholars

from the **Department of Chemistry** for their exceptional support and kindness during my Ph.D. journey.

I would also like to convey my heartfelt thanks to all the non-teaching staff in the Department of Pharmacy. **Mr. Puran, Mr. Lakshman, Mr. Tarachand, Mr. Naveen, Mr. Abhishek, Mr. Sandeep, Mr. Ram Suthar, Mr. Vikas, Mr. Surender, Mr. Vishal, Mr. Mukesh, Mr. Shyam Sunder,** and **Mr. Shiv Kumar** for their kind support during this work.

With profound affection and gratitude, I dedicate all my efforts to **my grandmother, father, and mother, who have inspired me to pursue** this career. **My father's unwavering support and motivation have been constant pillars in my life**. I am also deeply indebted to **my brother, sister, and entire family**, as their encouragement and blessings have been instrumental in every achievement I have attained. **To them and the divine, I owe my deepest appreciation.**

Maravajjala Kavya Sree

List of Abbreviations

ACN	Acetonitrile
AUC	Area Under the Curve
ATCC	American Type Culture Collection
APC	Antigen Presenting Cells
BC	Breast Cancer
BD	Biodistribution
BrdU	Bromodeoxyuridine
CD44	Cluster of Differentiation 44
CDR	Cumulative drug release
CHEMS	Cholesteryl hemisuccinate
Cl	Clearance
CQ	Chloroquine diphosphate
CSCs	Cancer stem cells
CSF1	Colony-stimulating factor-1
CAFs	Cancer-associated fibroblasts
DC	Dendritic cells
DCF	2',7'-dichloro- fluorescin
DCFDA	2',7'-dichlorofluorescein diacetate
DiI	3,3′-dioctadecyloxacarbocyanine perchlorate
DiO	1,1'-dioctadecyl-3,3,3',3'-tetramethylindocarbocyanine Perchlorate
DLS	Dynamic light scattering
DMAP	4-(dimethyl amino)pyridine
DMEM	Dulbecco's Modified Eagle medium
DMF	Dimethylformamide
DMSO	Dimethyl sulfoxide
DNA	Deoxyribo nucleic acid
DOPC	Dioleoyl phosphatidylcholine
DOPE	Dioleoyl phosphatidyl-ethanolamine
EDC	N-(3-Dimethylaminopropyl)-N′-ethyl carbodiimide hydrochloride
EDTA	Ethylenediaminetetraacetic acid
EE	Entrapment efficiency
EPR	Enhanced permeation and retention

ER	Estrogen receptor
FACS	Fluorescence-activated single-cell sorting
FBS	Fetal Bovine Serum
FESEM	Field emission scanning electron microscopy
FITC	Fluorescein isothiocyanate
GEM	Gemcitabine
GSH	Glutathione
H&E	Hematoxylin and Eosin
HER2	Human epidermal growth factor receptor 2
HIF-1	Hypoxia-inducible factor-1
IARC	International Agency for Research on Cancer
ICD	Immunogenic cell death
IMQ	Imiquimod
IMPDH	Inosine 5′-monophosphate dehydrogenase
IS	Internal standard
IVIS	*In-vivo* imaging system
LOD	Limit of Detection
LOQ	Limit of Quantification
l-PLGA	Linear PLGA
LQC	Low Quality control
M1	Immune stimulatory macrophages
M2	Immune Inhibitory macrophages
MDC	Monodansylcadaverine
MDR	Multi-drug resistance
MMP-2	Metalloproteinases-2
MTT	(3-(4,5-Dimethyl-2-thiazolyl)-2,5-diphenyl-2H-tetrazolium bromide)
NAC	N-acetyl cysteine
NCCS	National Centre for Cell Science
NF-kB	Nuclear factor kappa-light-chain-enhancer of activated B cells
NK	Natural Killer cells
NP	Nanoparticle
p62	Sequestosome-1
PAEMA	poly(2-azepane ethyl methacrylate)

PBS	Phosphate buffer saline
PDGFB	Pericyte growth factor
PDI	Polydispersity index
P-gp	Permeability glycoprotein
PI	Propidium Iodide
PTM	Pidotimod
PK	Pharmacokinetics
PLGA	Poly D, L- Lactic-Co- Glycolic Acid
P-LPS	Polymeric immunomodulator
PR	Progesterone receptor
PTX	Paclitaxel
PVA	Poly (vinyl alcohol)
RES	Reticuloendothelial system
RNA	Ribo Nucleic acid
ROS	Reactive Oxygen Species
RSQ	Resiquimod
RT	Room temperature
Rt	Retention time
SEM	Scanning Electron Microscopy
SP	Soluplus
sPLGA	Five-arm star poly(lactic-co-glycolic acid)
TAMs	Tumor-associated macrophages
TME	Tumor microenvironment
TECs	Tumor endothelial cells
TFA	Trifluoroacetic acid
TLR	Toll-like receptors
TNBC	Triple Negative Breast Cancer
TPGS	Tocopherol polyethylene glycol succinate
VEGF	Vascular endothelial growth factor
Vd	Volume of Distribution

LIST OF TABLES

LIST OF FIGURES

Abstract

Abstract

Recent advanced studies have highlighted cancer's multidimensional nature. However, most cancer therapies remain one-dimensional, targeting only a single facet of the intricate tumor ecosystem. Unfortunately, such singular approaches often prompt the tumor microenvironment (TME) to adopt a more aggressive nature, fueling resistance. The implementation of a multidimensional strategy becomes imperative to enhance therapeutic outcomes. One such emerging approach is the concept of combined chemo-immunotherapy. Chemotherapy could kill the tumor cells, reduce tumor-cell-mediated immune suppression, and generate tumor antigens for T-cell activation. However, many chemotherapeutic agents exhibit inherent immunosuppressive traits, rendering them unsuitable for this approach. Exceptions like paclitaxel (PTX) stand out, displaying immune-stimulating properties at therapeutic levels with improved cross-priming of antitumor CD8+ T cells and enhanced immune cell infiltration. However, effective T-cell activation hinges on antigen presentation. Tumor-associated macrophages (TAMs), the primary antigen-presenting cells in TME, often exist in an immune-suppressed state and are the most abundant immune cells in the TME in almost all types of solid tumors. They play a vital role in regulating tumor growth. TAM-targeted therapies are primarily designed for TAM depletion; however, it was found that TAM depletion did not show required anti-cancer activity. An alternative therapeutic approach is re-educating TAMs, which can actively promote antitumor immune responses and could be more efficacious. Several approaches have been proposed for re-educating the TAMs, among which the use of TLR agonists is highly effective, exhibiting potent immunogenic properties by triggering macrophage activation. Thus, we propose therapy with PTX combined with TLR agonist for effectively converting tumor immune suppressive microenvironment to immune-stimulatory microenvironment by M1 macrophage polarization and potential combined chemo-immunotherapeutic activity.

Various TLR agonists were initially screened to find the most potent one. Among them, the TLR7/8 agonist RSQ exhibited the highest potency. Numerous studies have attested to the effectiveness of RSQ in cancer immunotherapy, indicating its ability to enhance immunity. However, no previous study evaluated the efficacy of PTX and RSQ combination. In our current study, we observed a remarkable enhancement in the chemo-immunotherapeutic effectiveness of the PTX+RSQ combination.

Abstract

Extensive research has been conducted to pursue tumor-targeted drug delivery, resulting in the approval of a few formulations for clinical application. Nevertheless, many of these formulations adhere to intricate design parameters that hinder the scalability of production. Traditionally, nanoformulations have primarily been synthesized using batch processes such as ultrasonication, microemulsion, nanoprecipitation, and thin film methods. Unfortunately, these processes often lead to significant batch-to-batch variations. To successfully transition nanocarriers from the laboratory to clinical practice, precise control over particle size distribution, uniformity, colloidal stability, reproducibility between batches, and scalability is essential. To accomplish this, we have established a continuous flow microfluidics system-based nanoprecipitation method. The effectiveness and reproducibility of this method were initially established to prepare PTX-encapsulated NPs, allowing for the modulation of NP size by adjusting the PTX: polymer ratio. NPs prepared by this method were found to be more uniform in size and demonstrated increased cytotoxicity against both 2D and 3D *in-vitro* models, along with improved internalization into tumor cells and penetration into 3D spheroids. In summary, this continuous flow microfluidics-based nanoprecipitation method holds great promise for developing an economical and effective NP delivery system. With this approach, we can readily produce various types of polymeric NPs with consistent results and the potential for scalability.

Designing nano-formulations for multi-drug delivery, where each drug targets different cells, presents a significantly greater challenge than single drug-loaded NPs. Various nanocarriers, including liposomes, polymeric NPs, micelles, and drug conjugates, can be internalized by cells, with the encapsulated drug(s) exhibiting effectiveness against the specific cell type they enter. Therefore, in the context of a multi-drug-loaded nanocarrier targeting diverse cell types, it becomes essential for these drugs to be efficiently released within the TME to allow the drug combination to act on their respective target cells.

This study synthesized a pH-responsive polymer to enable precise drug release within the TME. The TME exhibits an acidic extracellular pH (ranging from pH 6.5 to 6.9) compared to the normal physiological pH (typically between pH 7.2 to 7.5) due to elevated glycolysis and the accumulation of lactic acid in the TME. This lower pH in the TME was leveraged to achieve the TME-specific release of PTX and RSQ. Histidine, a key component in this pH-responsive system, contains an imidazole ring with a lone pair of electrons on an unsaturated nitrogen atom. This imidazole ring can undergo pH-dependent protonation-deprotonation and polarity changes. At physiological pH, histidine predominantly remains in the non-protonated form,

facilitating interactions with other hydrophobic groups. However, when the pH drops below its pKa, the imidazole ring becomes protonated, resulting in a solubility transition that functions as an efficient pH-sensitive moiety. Furthermore, histidine's high pH buffering capacity, commonly referred to as the "proton sponge effect," has been observed to play a crucial role in facilitating the endosomal escape of the NPs.

In this study, pH-sensitive polymers were synthesized by conjugating a poly-histidine moiety with two different types of poly(lactic-co-glycolic acid) (PLGA) polymers: a five-armed PLGA (spH) and a linear PLGA (lpH). These polymers were compared for their effectiveness in co-delivering PTX and RSQ. The NPs were prepared using an optimized microfluidic-based nanoprecipitation method, allowing for the incorporation of variable polymers. Notably, the spH NPs exhibited increased loading of both PTX and RSQ compared to the lpH NPs.

Previous studies have established the influence of polymer shape on drug loading and release. Multi-armed polymers, such as spH, have been shown to accommodate more drug loading than their linear counterparts. In the drug release experiments, lpH and spH NPs displayed enhanced drug release at lower pH levels than neutral pH. However, in the case of spH NPs, the drug release ratio between PTX and RSQ was nearly 1:1, a feature not observed in lpH NPs. Maintaining this specific drug ratio could be advantageous for synergistic activity. The hypothesis is that in lpH NPs, only one end of the polymer underwent ionization while the rest remained stable, potentially leading to differential drug release. In contrast, with spH NPs, histidine modification at the end of each arm of its multi-arm structure resulted in ionization across all arms, leading to uniform charge repulsion and complete opening of the NPs, releasing the encapsulated drugs fully. This hypothesis supported the variation in NP size observed at different pH levels.

The pH-sensitive delivery of this drug combination was found to impact its bioactivity significantly. When tested against cancer cells in isolation, both the free drug combination and the NP-encapsulated drug combination exhibited similar cytotoxicity. However, when tested against a more complex spheroid model comprised of cancer and macrophage cells, mimicking actual tumor conditions, treatment with PTX and RSQ alone resulted in marginal cancer cell death, with cell viability rates of 76±2.3% and 81±3.8% for PTX and RSQ, respectively. In contrast, the drug combination group exhibited a significantly increased level of cancer cell death, with cell viability of 51±2.6% when treated with the PTX+RSQ combination. These results strongly indicated the potential for synergistic efficacy when using the drug

combination. Interestingly, encapsulation of PTX+RSQ in the pH-sensitive NPs exhibited a differential effect. With the sp NPs, the cancer cell viability was 58±5.5%, whereas, with spH NPs, the cancer cell viability was 29±3.6%. The significantly higher cell death with the spH NPs could be due to the more uniform (maintaining 1:1 ratio of PTX and RSQ, as shown in release data) drug release observed in the spH NPs. This could also be due to improved spheroid core delivery of the encapsulated drugs by the spH NPs. This was confirmed using a spheroid penetration study, where a significant difference in fluorescence distribution and penetration of DiI fluorescence was observed between the pH-sensitive and non-pH-sensitive NPs. With both lp and sp NPs, DiI fluorescence was mainly localized in the periphery of the cancer spheroid. However, with lpH and spH NPs, significantly increased spheroid core penetration was observed. Among all the groups, spH NPs exhibited the highest spheroid core penetration, significantly more than lpH NPs.

After that, to confirm that the pH-sensitive release of the NPs at the TME is the reason for the enhanced penetration, we analyzed the colocalization of the NPs loaded with DiI and DiO in tumor complex spheroids. After 24h of treatment of the DiO+DiI loaded NPs, we have found increased colocalization of non-pH sensitive NPs, i.e., 0.84 with lp NPs and 0.75 with sp NPs, compared to 0.6 with lpH NPs and 0.5 with spH NPs. The least colocalization index of spH NPs shows the release of payload, i.e., DiI +DiO at the acidic pH of the TME, when compared to other groups, were found to be stable with the dyes encapsulated inside, showing increased colocalization.

Treatment with spH NPs also exhibited reversal of the M2-phenotype of cancer, which was confirmed by increased M1 macrophage polarization marker expression, i.e., TNF-α expression with almost 100-fold in 2D, 390-fold increase in conditioned media and 410-fold increase in 3D complex spheroids when compared to control indicating M1 macrophage polarization. With spH NPs, there was a significant increase in TNF-α expression, i.e., 200-fold in 2D, 420-fold increase in conditioned media, and 820-fold increase in 3D complex, which has more effective macrophage activation with immune activation when compared to the free drug combination. Similarly, IL-10 expression (M2 marker) decreases with PTX+RSQ combination, i.e., 50-fold in 2D, 100-fold decrease in conditioned media, and 120-fold decrease in 3D complex spheroids. Regarding spH NPs, there are 20 folds in 2D, 60 fold decrease in conditioned media, and 70 fold decrease in 3D complex spheroids, proving that M2 macrophage expression was about to basal level, leading to decreased immunosuppressive nature of the TME. We have also observed improved tumor-specific cell death with spH NPs

compared to other groups using live dead staining and luciferin-tagged tumor cells. After that, it was also confirmed that improved combined chemoimmunotherapeutic activity has involved ROS induction in both macrophage polarization and cancer cell death.

After successful demonstration of in-vitro combined chemo-immunotherapeutic acidity of spH NPs loaded with PTX+RSQ, *ex-vivo* splenocyte + 4T1 complex spheroids were used to check antigen presentation capability, wherein we observed ~ 2-fold increased MHC-I and MHC-II expression with the spH NPs compared to the PTX+RSQ combination, proving an improved immunogenic potential, in turn leading to M1 polarization. This might be because MHC-II expression can help in activating CD4+T cells, which in turn helps in the immunogenic potential of other immune cells, which is merely because MHC-II can typically expressed by immune cells but not cancer cells to help in effective immune response to cancer cells was also found to be increased showing successful combined chemo-immunotherapeutic activity of spH NPs.

After successful confirmation of in-vitro and ex-vivo chemo-immunotherapeutic activity of spH NPs, we then moved into *in-vivo* studies, where, in the initial toxicity studies, we didn't find any signs of toxicity and no change in the body weight of the animals throughout the study with all the treatment groups at the given doses. After that, improved PK parameters were observed with PTX and RSQ when given in spH NPs form. The plasma half-life ($t_{1/2}$) of PTX and RSQ were improved with ~2 folds when administered in combination with PTX+RSQ. Similarly, when administered as SpH NPs, there was a ~ 7-fold increase in the AUC, ~11-fold reduction in the clearance (cl), and ~150-fold increase in the $t_{1/2}$, with PTX whereas, with RSQ, there was a ~ 68-fold increase in the AUC (0-∞), ~ 16-fold reduction in cl, and a ~130- fold increase in the $t_{1/2}$. In the *in-vivo* biodistribution study, mice treated with spH NPs displayed consistently superior fluorescence intensity at all time points compared to those treated with sp NPs. Both sp and spH NPs demonstrated increased accumulation in the tumor compared to other organs; however, the fluorescence signal from sp NPs decreased significantly within 1440 minutes due to their interaction with plasma proteins and subsequent clearance by the liver. In continuation, *in-vivo* efficacy study after 21 days of treatment, the mean tumor volumes were as follows: 624 ± 23 mm^3 for the PTX group, 510 ± 28 mm^3 for the RSQ group, 310 ± 87 mm^3 for the PTX+RSQ group, and 167 ± 23 mm^3 for the spH NPs group. Tumor weight displayed a similar trend, with average tumor weights of 3.82 ± 0.20 g for the control group, 2.62 ± 0.12 g for the PTX group, 1.67 ± 0.70 g for the RSQ group, 1.20 ± 0.45 g for the PTX+RSQ group, and 0.32 ± 0.12 g for the SpH NPs group. This decreased tumor weight and volume with spH

NPs might be because of the pH-sensitive tumor-targeted drug delivery of spH NPs. It was also found that decreased tumor growth involves ROS induction as well. spH NPs were also found to show decreased proliferation rate (Ki67), improved apoptosis rate, decreased metastasis rate, and number of lung nodules with spH NPs treatment. Altogether, we can conclude that spH NPs loaded with PTX and RSQ have improved *in-vivo* efficacy in a breast cancer model.

Chapter 1:
Introduction

1.0. Breast Cancer:

Breast cancer (BC) has become one of the most prevalent life-threatening diseases among women worldwide, with a high prevalence (2.3 million new cases reported in 2020 and over 685,000 deaths). In 2020, it surpassed lung cancer as the leading cause of cancer incidence universally, with an expected 2.3 million new cases, with 11.7% of all cancer cases [1]. Epidemiological analysis expects that the global burden of BC will reach approximately 2 million cases by the year 2030 [2].

In India, the occurrence of BC has increased dramatically, almost by 50%, between 1965 and 1985 [3]. In 2016, it was estimated that there were 118,000 new cases of BC in India [4]. Over the past 25 years, the incidence rate of BC in Indian women increased by 39.1% and was observed in every state of the country [4]. According to Globocan data for 2020, breast cancer accounted for 13.5% of all cancer cases and 10.6% of all cancer-related deaths in India [5]. In the 1990s, cervical cancer was the leading among the Indians, while BC had a lower incidence. However, by the early 2000s, breast cancer had surpassed cervical cancer as the leading cancer site in India, indicating a notable shift in the disease landscape [6]. Current research suggests that most of the BC cases in India occur in younger women compared to Western countries.

Significant variability in the survival rate was observed in the BC patients based on the disease status. The 5-year overall survival rate was found to be highest among the stage I BC patients (95%), followed by stage II (92%), stage III (70%), and stage IV (21%) [7]. Unfortunately, the survival rate for BC patients in India is lower compared to Western countries due to an earlier age at onset, late-stage diagnosis, delayed treatment initiation, and fragmented or inadequate treatment [5]. According to the World Cancer Report 2020, early detection and prompt treatment are the most effective interventions for controlling BC [8]. A 2018 review of 20 studies also revealed that treatment costs for breast cancer increased with the stage of cancer at diagnosis, underscoring the importance of early detection in reducing treatment costs [9].

Despite significant improvements in screening techniques and systemic treatments, a complex interplay of genetic and non-genetic factors made BC therapy challenging. Current treatment for BC primarily includes surgery, radiation therapy with adjuvant chemotherapy, followed by hormonal therapy. BC is a heterogeneous form of cancer composed of a collection of diverse biological entities with distinct pathology, genomic alterations, gene expression patterns, and the tumor microenvironment (TME). BC is grouped into three categories based on histological [10], molecular [11], and clinical subtypes of breast cancer (**Figure 1.1**).

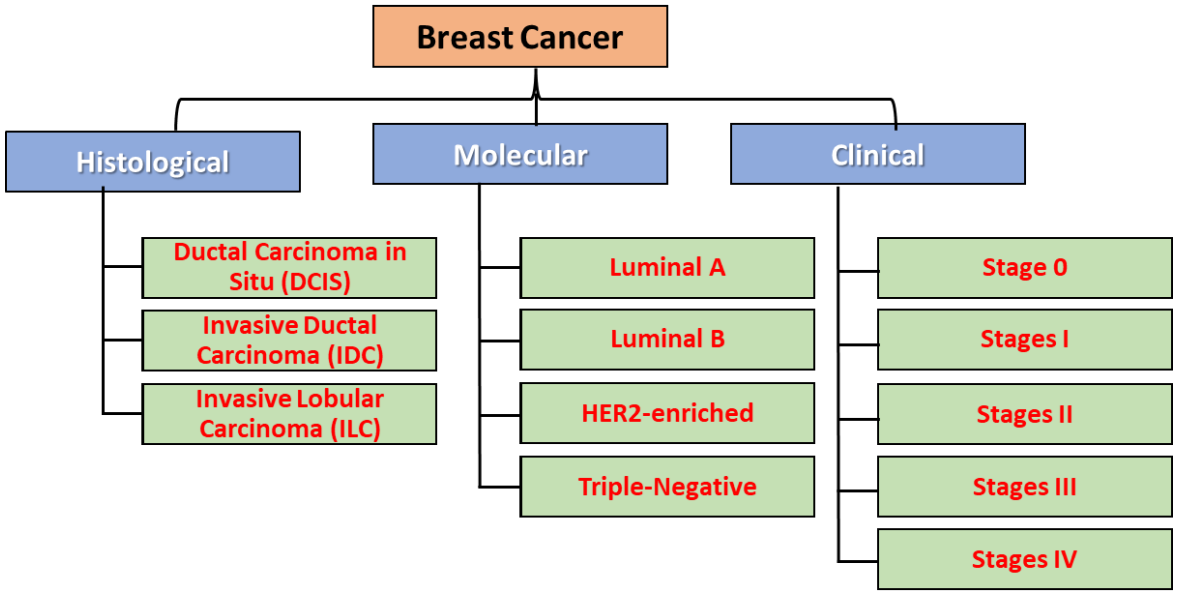

Figure 1.1. Classification of breast cancer.

Limitations of Traditional chemotherapeutics:

Most of the traditional chemotherapeutics currently used in the clinic target cancer cells alone. However, such monodimensional therapies commonly lead to therapeutic failure. Some standard recommendations for initial chemotherapy in the treatment of metastatic breast cancer typically involve anthracycline-based regimens and the use of taxanes such as paclitaxel and docetaxel. These are majorly associated with response rates ranging from 30% to 70% [5]. However, these responses are often of short duration, with a median time to disease progression of 6 to 10 months [12]. For patients with disease progression and resistance development to these drugs, alternative strategies include capecitabine, gemcitabine, vinorelbine, albumin-bound paclitaxel, or ixabepilone. Unfortunately, response rates with these drugs are also relatively low, typically within the range of 20% to 30% [13]. The duration of responses is generally less than 6 months, and these results do not always lead to improved long-term survival [14]. Therefore, a proper understanding of tumor and TME is essential for effectively targeting BC for an improved treatment outcome [15, 16]. Some examples of chemotherapeutic combinations and their response rates are mentioned in **Table 1.1**.

Table 1.1: Current treatment approaches against breast cancer.

DRUG	OVERALL SURVIVAL	Progression Free survival	REFERENCE
Docetaxel + Gemcitabine	22.99 months	9.01 months	[17]
Capecitabine	94.0% (3 years), 89.2% (5 years)	82.8% (3 years), 74.1% (5 years)	[18]
Cyclophosphamide, Methotrexate, and 5-Fluorouracil	9.4 months	3.1 months	[19]
Eribulin Mesylate	9.0 months	2.6 months	[20]
Gemcitabine	7.8 months	4 months	[21]
ixabepilone	11.3 months	3.6 months	[22]
Thiotepa (Intrathecal)	4.5 months	3.3 months	[23]
Mitomycin C, vinblastine and cisplatin	8 months	4 months	[24]
5-fluorouracil+vinorelbine	15 months	Information not available	[24]
Docetaxel	16 months	6.5 months	[25]
Nab-Pacliatxel	20.9 months	5.3 months	[26]
Cyclophosphamide + Doxorubicin +Paclitaxel		68.75% (5 years)	[27]
Cyclophosphamide, Ixabepilone	53.57% (36 months)	Information not available	[28]
Pemetrexed + Cyclophosphamide	12 months	6.26 months	[29]
Eribulin Mesylate	12.9 months	3.6 months	[30]
Exemestane	92%	4.1%	[31]
Fulvestrant	22.8 months	Information not available	[32]
Ixabepilone +carboplatin	12.5 months	7.6 months	[33]
Vinflunine plus Capecitabine	13.9 months	5.6 months	[34]

The existing chemotherapeutics failed because, for decades, neoplastic diseases were considered autonomous disorders involving only the cancer cells, and the pathophysiology and disease prognosis were linked to the phenotypic and genotypic changes in the cancer cells only. Though the importance of the tumor microenvironment (TME) was proposed more than a century ago by Stephen Paget [35], the role of non-cancerous cells present in the TME has been ignored for a long time. Recent advanced studies have established that cancer is a multicellular disorder, and the proliferation and metastasis of the neoplastic cells are supported by a complex interaction with the non-neoplastic cells in the TME [36-38]. Apart from the tumor cells, TME contains cancer-associated fibroblasts (CAFs), tumor endothelial cells (TECs), tumor-associated macrophages (TAMs), cancer stem cells (CSCs), and extracellular matrix, all of which play critical roles in tumor development and progression [39]. However, the interplay between the tumoral and non-tumoral cells contributes to the niche formation, resistance to conventional treatment approaches, and cancer metastasis. Most of the current therapeutic strategies against cancer are still one-dimensional, i.e., they are directed against only one component (cancer cells) of this complex, multi-integrant tumor ecosystem. This one-

dimensional treatment strategy is ineffective, as the other supporting cells can help the tumor cell to survive and/or prevent the activity of the anticancer drugs [40]. For example, it has been demonstrated that CAFs promote resistance to common anticancer drugs in tumor cells [41]. Similarly, TECs make the tumor cells less responsive to anticancer drugs by expressing multi-drug resistance proteins, like P-glycoprotein [42]. These findings suggest that drug resistance is not an intrinsic property of the cancer cells but also depends on the parallelly evolving TME.

1.2. Cellular components of the tumor microenvironment (TME):

A large variety of cells contribute to the formation of the TME. Apart from a heterogeneous population of cancer cells, it also contains various resident and infiltrating non-malignant cells such as CAFs, TAMs, and TECs. As described in **Figure 1.2**, these components of the TME have a profound effect on tumor progression [43]. The TME niche involving tumoral and non-tumoral components plays an intertwining dynamic role reflecting the pathological state of TME. Functional modulation of these non-neoplastic components of the TME holds significant potential as a possible therapeutic strategy. Additionally, unlike cancer cells, the supporting cells in the TME are genetically stable, making them a good target [38].

The following sections summarize the role of different cellular components in the TME, how they influence tumor development and progression, and combination therapeutics strategies targeting them.

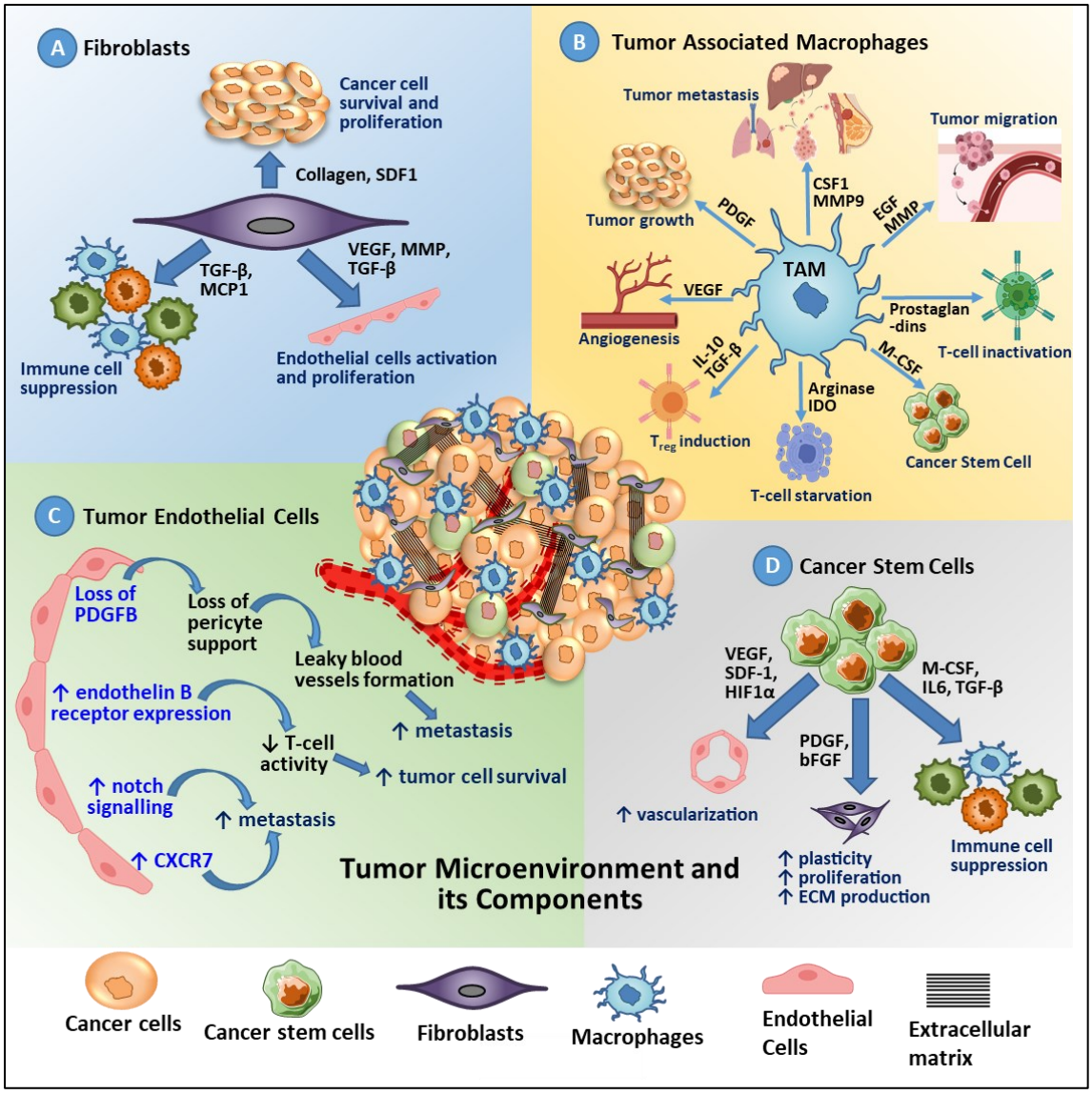

Figure 1.2: Components of the tumor microenvironment and its impact on the survival and growth of the tumor. (Source: Swetha *et al*., Drug Deliv. and Transl. Res. 2022).

Cancer-Associated Fibroblasts (CAF):

Fibroblasts are present in all epithelial tissues, where they maintain the tissue architecture by producing the extracellular matrix (ECM), such as collagens and fibronectin. Fibroblasts can also secrete various proteases to remodel the overall tissue architecture [44]. In the TME, fibroblasts are activated by factors released by the tumor cells, like FGF, PDGF, and TGF-β, and become cancer-associated fibroblasts (CAFs) [45]. CAFs are the primary stromal cells present in the TME, producing tumor ECM. They also potentiate tumor angiogenesis by secreting VEGF and PDGF, promoting tumor growth and invasion [46]. CAFs also modulate antitumor immunity by secreting CCL2, CCL5, and TGF-β, attracting regulatory T cells (Treg) and myeloid-derived suppressor cells [45, 47]. It is also found that CAFs promote physical resistance to chemotherapy by building ECM that compresses the blood and lymphatic vessels,

leading to reduced perfusion, elevated interstitial fluid pressure, and poor drug penetration [48, 49].

Tumor-Associated Endothelial Cells (TECs):

Tumor-associated endothelial cells (TECs) play a vital role in the development of the TME. Likewise, tumors need a high rate of angiogenesis to get the oxygen and nutrients required for their growth [50]. To aid the angiogenesis, a large number of endothelial cells are recruited to the TME, rendering the tumor blood vessels different from the normal blood vessels in many aspects, including morphology and gene expression [51]. The genotypic and phenotypic abnormality of the TECs results in the aberrant expression of endothelial markers like CD31, CD105 [68], and VEGFR, which leads to defective endothelial monolayer formation [52]. Normal blood capillaries are surrounded by pericytes, improving blood vessel stability. However, the loss of pericyte growth factor (PDGFB) and its receptor in the tumor vasculature leads to the loss of pericyte support, resulting in unstable and leaky blood vessel formation, promoting tumor metastasis [53, 54]. Increased expression of CXCR7 in the TECs promotes tumor cell proliferation, invasion, and trans-endothelial migration [55]. TECs are responsible for hypoxia-inducible factor-1 (HIF-1) dependent augmentation of VEGF expression, which further induces angiogenesis [56].

Cancer Stem Cells (CSCs):

Cancer stem cells (CSCs) have heterogeneous phenotypes and can self-renew and differentiate, which helps form tumorigenic and non-tumoral cells, including CAF, TEC, and TAM [57]. It is well reported that the presence of CSC markers in a tumor leads to poor disease prognosis [58]. CSCs are not a single type of cells; they are of multiple heterogeneous phenotypes [59]. Different CSC markers have been identified, and many of which are associated with poor disease prognosis. For example, CSC marker CD133 has been associated with drug resistance and reduced survival in many cancers [60]. CD44, a transmembrane receptor for many ECM components and co-receptor for growth factors and cytokines, is associated with increased tumor progression [61]. Many other CSC markers, like aldehyde dehydrogenase (ALDH), CD166, CD9, CD24, and CD49f, have been shown to play an important role in developing resistance to therapeutics [62-64]. CSCs are resistant to radiation therapy and chemotherapy and can enter a dormant stage, resulting in recurrence and metastasis [60, 65].

Tumor-Associated Macrophages (TAM):

Macrophages are one of the most prominent components present in the TME among all the other cells in various cancers, and breast cancer (BC) is one among them. In most cases, macrophages constitute 50% of cell populations, and when coming to BC, multiple clinical studies have proved a strong correlation between the TAM population and the survival of patients [66]. A meta-analysis report stated that an increased macrophage population correlated with a poor prognosis in over 80% of breast cancer patients [67].

Macrophages are commonly known as the "Swiss army knife" of the immune system because of their wide range of functions [68]. When activated appropriately, they have specific and dedicated roles. Multiple factors influence macrophage function and behavior, including hypoxia, lipids, and cytokines like CCL2, CCL3, CSF-1, TNF-α, INF-γ, and MIF. Specific chemoattractants regulate the migration ability of macrophages into tissues. One among them is CCL2 (monocyte chemoattractant protein-1, MCP-1), which has been connected to the recruitment of TAMs to the stromal tissue of BC and plays a vital role in BC relapse [69]. Another major chemoattractant, macrophage migration inhibitory factor (MIF), also plays a crucial role in tumor progression [70]. MIF interacts with CXCR2 and CXCR4 to recruit leukocytes and activate cellular responses. Increased MIF levels were primarily observed in prostate and breast cancer [71]. MIF remains upregulated in breast cancer cells and macrophage co-cultured experiments [72]. MIF from tumor cells increases the production of macrophage MMPs and facilitates tumor cell invasion [73].

As the significant immune-inhibitory cells found in the TME, TAMs significantly promote tumorigenesis and metastasis through non-immune and immune mechanisms, negatively affecting clinical outcomes in various cancer types [74, 75]. TAMs augment tumor proliferation by releasing growth factors (e.g., EGF, PDGF, TGF-β) and cytokines, impacting cancer initiation [76]. They support cancer stem cells, enhancing tumor progression and therapy resistance via TNF-α, IL-6, and Akt/mTOR pathway [77]. TAMs also sustain the CSC niche through juxtacrine communications [78] and promote CSC survival during chemotherapy [79]. Inhibiting CSF1R or CCR2 on TAMs improves chemotherapeutic responses [80].

TAMs play a crucial role in angiogenesis by secreting pro-angiogenic factors (e.g., VEGF, PDGF, bFGF) and promoting tumor neovascularization, supporting cancer growth [81]. Hypoxia and CSF-1 upregulate Tie2 expression on TAMs, activating the angiogenic switch [82]. TAMs, through HIF-1α, contribute to pro-angiogenic functions [83]. Moreover, TAMs'

signaling cascades can enhance metastasis by promoting tumor cell invasiveness with MMPs, serine proteases, and cathepsins [84]. Various molecules from TAMs induce cancer cell invasion and migration, including cathepsin B, macrophage inflammatory protein 1-β, and TGF-β [85]. TAMs support intravasation and metastasis through CCL18 and other factors [86]. Additionally, TAMs enhance epithelial-mesenchymal transition (EMT) in tumor cells [87] and create a pre-metastatic niche [88].

TAMs suppress adaptive immune responses through various mechanisms, decreasing antitumoral immune cells while increasing immunosuppressive cell types. They impede CD8+ T cell activation by affecting T cell trafficking, depleting essential metabolites, and secreting anti-inflammatory cytokines [89]. Metabolism of L-arginine and L-tryptophan by TAMs inhibits T cell receptor (TCR) complex re-expression [89]. Hypoxia and tissue hypoxia also contribute to T cell suppression [90]. TAMs produce anti-inflammatory cytokines, including IL-10, TGF-β, and PGE2, which hinder T cell functions [91]. They express PD-L1 and other inhibitory ligands, affecting T-cell activation and proliferation [92]. TAMs attract immunosuppressive cells like Treg cells, further hampering immune responses [93]. Moreover, TAMs can induce Treg cells in the tumor microenvironment [94]. Overall, TAMs play a substantial role in immune evasion in the tumor microenvironment, making them potential targets for cancer treatment to boost immune responses [95].

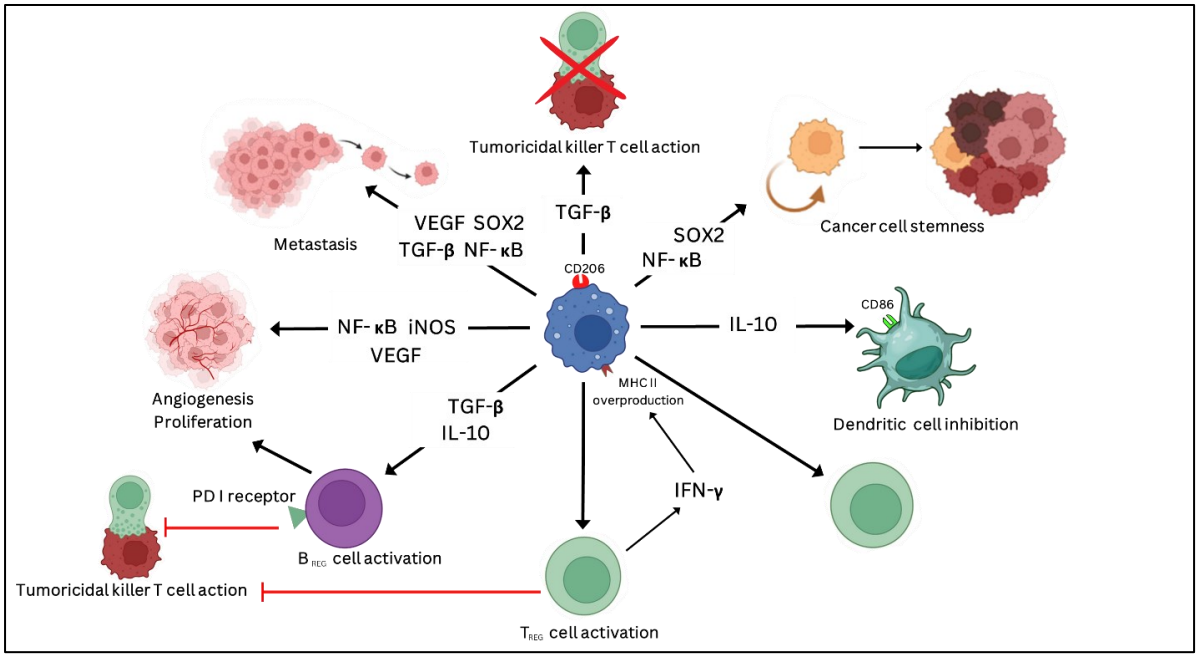

Figure 1.3. Role of tumor-associated macrophages (TAM) in immunosuppressive tumor microenvironment.

1.3. Drugs targeting TAMs:

Different drugs have been developed to modulate the TAMs for cancer therapy (**Fig. 1.4**). These drugs can be divided into three main categories: i) drugs that deplete TAMs, ii) drugs that stimulate and polarize TAMs into the immunostimulatory M1 phenotype, and iii) drugs that inhibit the production of immunoregulatory factors by the TAMs. Many of these drugs have shown promising efficacy in preclinical or clinical studies [96]. Apart from these, metronomic chemotherapy has been demonstrated to polarize TAMs through the induction of immunogenic cancer cell death (ICD) [97].

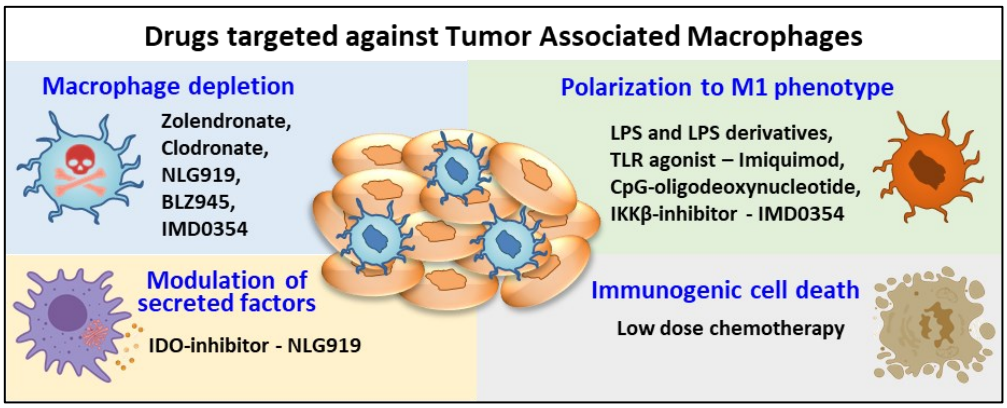

Figure 1.4. Drugs targeted against tumor-associated macrophages for cancer therapy. (Source: Swetha *et al*., Drug Deliv. and Transl. Res. 2022).

1.4. Immunotherapy alone targeting macrophages:

To overcome the limitations of the established traditional chemotherapy and other cancer treatments, immunotherapy has now become an important and promising candidate for cancer therapy. Various immunotherapeutic strategies have emerged recently, including adoptive cellular immunotherapy, vaccines, antibodies, small molecule inhibitors, immune checkpoint inhibitors, and many more. All these strategies target macrophages directly or indirectly, significantly affecting the TME.

Among all the categories of drugs that target macrophages, the class of drugs that limits the recruitment of monocytes has gained significant interest because the migration of monocytes from bone marrow to tumor depends on the CCL2-CCR2 signaling. Elevated CCL2 levels in human neoplasia are linked to increased metastasis and decreased survival. Blocking CCL2-CCR2 signaling reduced tumor growth and metastasis in mouse models [98]. PF-04136309 was found to act by CCR2 activation and has an excellent treatment response in pancreatic cancer patients [99]. CCX872, a CCR2 antagonist, has also shown a great response in pancreatic cancer treatment [100]. Carlumab (CNTO88), a CCL2 antibody, has limited clinical efficacy [101]. Dual blockade of CXCL12/CXCR4 and PD-1-PD-L1 signaling has shown

reduced tumor burden[101]. Integrin αMβ2 (CD11b/CD18) on myeloid cells also had a major role in their migration. Antibodies against CD11b have shown reduced myeloid cell recruitment, while ADH-503 prevented tissue infiltration, with a significant reduction in TAMs in multiple solid tumors [102]. From this, it was found that limiting TAM infiltration was an effective strategy for overcoming the immunosuppressive nature of solid tumors. Other examples are listed in **Table 1.2**.

TAM depletion in another category of drugs targeting macrophages. CSF-1 plays a major role in TAM differentiation and survival, and blocking CSF1-CSF1R signaling might reduce TAM viability and survival [103]. Recent preclinical studies have shown that inhibiting the CSF signaling pathway has decreased primary tumor growth, metastasis, and enhanced survival rate in mice [104]. Other molecules like BLZ945, PLX3397, and antibodies against CSF1R have shown promising results in TAM depletion, with improved activation of immune cells and therapeutic activity in various cancer models [105].

Reprogramming TAMs is another promising technique used in macrophage-targeted immunotherapy. TLR activation and CD40 agonists are most likely to activate pro-inflammatory TAMs from anti-inflammatory TAMs [106]. TLR agonists like 3M-052 were found to be effective in many preclinical models with enhanced antitumor activity and enhanced activity of checkpoint inhibitors when given in combination [107]. TLR7 agonists, when administered topically, have been found to show promising results in breast cancer patients with skin metastasis [108]. Motolimod, a TLR8 agonist, has now been in clinical trials with HPV-positive squamous cell carcinoma [109]. CD40 agonists were also found to activate TAMs, enhance the release of pro-inflammatory cytokines and T-cell activation, and reduce tumor growth. Combining CD40 activation with CSF-1R inhibitors effectively suppressed tumor cytokine production in TAMs [110].

Multiple advancements have been made that are helpful in selectively repolarizing TAMs into a pro-inflammatory M1 phenotype. Some of the approaches include using NPs to deliver M1 polarizing agents, synthetic molecules like RP-182, inhibition of RIP1, suppression of PI3Kγ signaling, and hedgehog signaling modulation [111]. Reprogrammed TAMs were also found to serve as "Trojan Horses" to deliver drugs directly at the tumor site, inducing complex modifications in the TME and avoiding systemic toxicity [106]. These developments offer promising avenues for TAM targeting by enhancing tumoricidal effects and minimizing the immunosuppressive activity of TME.

Table 1.2. Various immunotherapeutics targeting TAMs in tumor microenvironment

Treatment Strategy	Molecule	Mechanism	Phase	Clinical Trial Number
Limiting monocyte recruitments	PF-04136309	CCR2 antagonist	1b	NCT01413022
	CCX872	CCR2 antagonist	1b	NCT02345408
	Carlumab	CCL2 antibody	Ib	NCT01204996
			I	NCT00537368
			II	NCT00992186
	LY2510924	CXCR4 antibody	I	NCT02737072
	Motixafortide	CXCR4 antagonist	IIb	NCT02907099
Depleting TAMs	PLX3397	CSF-1R antibody	III	NCT02371369
			Ib	NCT01525602
	RG7155	CSF-1R antibody	I	NCT01494688
	AMG 820	CSF-1R antibody	I	NCT01444404
	IMC-CS4	CSF-1R antibody	I	NCT01346358
	MCS110	CSF-1 antibody	Ib/II	NCT02807844
Reprogramming TAMs	Imiquimod	TLR7 agonist	II	NCT00899574
	Motolimod	TLR8 agonist	II	NCT01836029
	APX005M	CD40 agonist	I/II	NCT03214250
	RO7009789	CD40 agonist	I	NCT02665416
	SEA-CD40	CD40 agonist	I	NCT02376699
	CP-870893	CD40 agonist	I	NCT01103635
	IPI-549	PI3Kγ inhibitor	Ib	NCT02637531
			II	NCT03961698
Targeting inhibitory molecules on TAMs	Hu5F9-G4	CD47 antibody	I	NCT02216409
			I/II	NCT02953509
			I	NCT03558139
			I/II	NCT02953782
	CC90002	CD47 antibody	I	NCT02367196
	TTI-621	SIRP antibody	I	NCT02663518
			I/II	NCT04996004
	CC-95251	SIRP antibody	I	NCT03783403

1.5. Limitations of macrophage targeting monotherapy and the need for combination therapy:

Immunotherapy alone targeting macrophages might not be highly effective in the treatment of cancer which is due to several reasons, such as:

1) The primary reason behind this is that macrophages in TME are polarized into TAMs, which often exists in M2 immune inhibitory macrophages, i.e., anti-inflammatory phenotype. M2 macrophages can promote tumor growth and progression by suppressing anti-tumor immune responses, in turn supporting angiogenesis and helping in tumor evasion immune surveillance. In this case, individual targeting of macrophages might not help in converting immune inhibitory macrophages (M2) to immune-stimulatory macrophages (M1); for successful conversion of pro-tumor to antitumor response anti-cancer agents, a combination is also necessary [106].

2) TAMs are heterogeneous in nature, play multiple roles in TME, and have both pro-tumorigenic and anti-tumorigenic properties. Targeting all TAMs without distinguishing the role of macrophage present could also disrupt the macrophages with anti-tumor properties. Thus, to avoid this, targeting agents are deployed in combination for effective cancer treatment [112].
3) It is well-reported that tumors can easily develop resistance to therapies, including immunotherapy. The therapeutic resistance can lead to multiple complex mechanisms that enhance tumor growth, proliferation, and invasion, which cannot be addressed just by targeting macrophages alone. Thus, combination therapy is needed [113].
4) Reports also suggest that tumors create an immunosuppressive microenvironment, which might be because of multiple immune cell inactivation, such as T cells and dendritic cells, which are responsible for improved antigen presentation and anti-tumor response. Though macrophages also play a major role in immune suppressive TME, macrophage targeting alone cannot solve this problem [114].
5) Some of the successful immunotherapies available in the market, including checkpoint inhibitors, were given in combination with other immunotherapies for effective cancer treatment, which makes our view clear that combination of multi-targeted immunotherapies or immunotherapy in combination with other strategies will be helpful for effective cancer treatment [115].

1.6. Rationale behind the combination of chemotherapy with immunotherapy:

Conventional treatment with cytotoxic drugs used for cancer target and destroy tumor cells through various mechanisms, including DNA damage, inhibition of DNA replication, and mitosis prevention. While chemotherapeutic drugs have limited efficacy in solitary treatment, combination chemotherapy offers a more promising approach. Combination chemotherapy aims to maximize eradication while maintaining tolerable toxicity, targeting a broader array of tumor cells with varying genetic and epigenetic abnormalities. It also serves as a deterrent against drug resistance. Conventional chemotherapy has cytotoxic and cytostatic effects on healthy, rapidly proliferating cells, leading to myelosuppression [116].

This raises concerns about a potential antagonistic relationship between chemotherapy and immunotherapy. However, evidence suggests that activating the host's immune system contributes significantly to the effectiveness of specific cytotoxic drugs. Under specific conditions, these drugs may exhibit an immune-stimulatory effect, creating opportunities for their combination with immunotherapy. Immunotherapy excels at eliminating disseminated

and metastatic cancer but faces challenges when eradicating solid tumor masses. Chemotherapy complements immunotherapy by reducing the primary tumor mass and decreasing the number of cells that need to be eliminated by immune cells [113]. Chemotherapy can also mitigate the production of immunosuppressive factors by cancer cells. Some chemotherapeutic agents can directly stimulate antitumor immunity, particularly in cases involving cold tumors with low effector T cell infiltration. The synergy between chemotherapy and immunotherapy offers a promising avenue for enhancing the overall efficacy of cancer treatment [117, 118].

1.7. Combined chemo-immunotherapy targeting macrophages:

Significant research has been done to evaluate the efficacy of combined anti-TAM treatment with chemotherapy for synergistic effects. For example, in a phase I clinical trial, zoledronate was evaluated along with carboplatin plus paclitaxel, which exhibited superior efficacy [119]. Sui et al. have developed a sialic acid-modified liposome to deliver epirubicin and zoledronate [120]. They have observed a differential therapeutic effect depending on the administration methods: delivery of epirubicin and zoledronate together (either in separate liposomes or in the same liposome) did not exhibit better efficacy; however, sequential administration of epirubicin liposome followed by (after 24 h) zoledronate liposome resulted in increased efficacy. The initial tumor cell death caused by epirubicin might reduce the tumor cell-mediated TAM sustenance in the TME, enhancing the activity of zoledronate. An IDO-inhibitor NLG919 was co-encapsulated with paclitaxel in a charge-convertible micelles to induce immunogenic cell death and inactivation of IDO, resulting in effective antitumor activity [121].

Reprogramming the TAM phenotype from anti-inflammatory M2 to pro-inflammatory M1 can mount an antitumor response [122]. As potent toll-like receptor (TLR) agonists, bacterial cell walls have been used to polarize TAMs. Bacterial cell wall components have been incorporated into liposomal membranes to make immunostimulatory liposomes. Such liposomes, when loaded with anticancer drugs, showed combined chemo-immunotherapeutic activity. For example, Ektate et al. developed a temperature-sensitive liposome laden with Salmonella cell wall components (thermobots), which delivered doxorubicin [123]. Similarly, liposomes decorated with *the outer membrane of Klebsiella pneumonia*e (OMV) were synthesized to deliver doxorubicin [124]. In both cases, the cell wall lipopolysaccharide (LPS) present on the liposomal membrane contributed to the TAM's polarization to the M1 phenotype. However, as LPS is toxic and can lead to systemic inflammation, Roy et al. developed a non-toxic derivative of LPS (SP-LPS) to circumvent the issue. NP-mediated codelivery of paclitaxel and SP-LPS

led to heightened antitumor activity, which could be attributed to a significantly higher percentage of M1 macrophages (CD14+/ CD40+) in the TME [125, 126]. Apart from using LPS as a TLR agonist, other researchers have used different synthetic TLR agonists. Imiquimod was the first FDA-approved small molecule TLR7 agonist for treating basal cell carcinoma [127]. Different groups have evaluated imiquimod for combined chemo-immunotherapy. A combination of fluorouracil and imiquimod is in phase III clinical trial as a topical or ablative treatment to prevent anal cancer in patients with anal high-grade squamous intraepithelial lesions (NCT02135419). Nanogel prepared by electrostatic interactions between negatively charged lipid vesicles (containing gemcitabine and imiquimod) and positively charged liposomes (containing clodronate) exhibited a robust antitumor response [128]. Multi-walled carbon nanotubes, co-delivering doxorubicin and CpG-oligodeoxynucleotide (TLR 9 agonist), were shown to promote polarization of TAMs from M2 to M1 type macrophages and decreased Treg cells in a melanoma model [129]. Polymeric NP-mediated co-delivery of zymosan (polysaccharide, TLR 2 agonist) and doxorubicin resulted in improved anticancer effect with decreased CD206+ cells, indicating modulation of TAM differentiation into the M1 phenotype and synergistic effect with chemotherapy [130]. Effective TAM polarization to the M1 phenotype was also achieved by IKKβ-siRNA co-encapsulated with doxorubicin in a layered NP prepared with polyethyleneimine and carboxymethyl-chitosan [131]. As discussed above, NP-mediated delivery of TAM-targeted drugs and cytotoxic agents was highly effective. More such examples are listed in **Table 1.3**.

Table 1.3. Multidimensional nanocarriers targeting macrophages against cancer.

Carrier system	Molecule and mechanism of action	Combination therapy	Outcome	Reference
Liposomal epirubicin (SEL) and Liposomal zoldronate (SZL)	Zoledronate – inhibits TAM infiltration	Epirubicin	Sequential administration of SZL 24hr after SEL led to no tumor growth and 100% survival of treated murine sarcoma mice model.	[120]
Charge convertible polymeric micelles	NLG919 – IDO inhibitor and TAM eliminator	Paclitaxel (PTX)	Combination of PTX and NLG919 induced inactivation of IDO, elimination of TAM, and ICD of tumor cells, resulting in effective antitumor immunogenicity.	[121]
NLG919 conjugated poly(oligo(ethylene glycol) methacrylate)	NLG919 – IDO inhibitor and TAM eliminator	Doxorubicin	Better efficacy than Doxil in 4T1 tumor bearing mice with increased CD4 and	[132]

(POEG) NPs loaded with doxorubicin			CD8 T cell infiltration in the TME.	
Salmonella-laden temperature-sensitive liposomes (thermobots)	Lipopolysaccharide from *Salmonella* – TLR agonist and immune stimulator	Doxorubicin	Thermobots treatment increased both M1 macrophage and Th1 cells in the TME, enhancing therapeutic outcome in mice model of colon cancer.	[123]
Bacterial outer membrane vesicular (OMV) Liposomes	OMVs from attenuated *Klebsiella pneumonia* – TLR agonist and immune stimulator	Doxorubicin	Treatment with OMVs elicited enhanced immune responses and increased antitumor effects.	[124]
Polymeric nanoparticle	SP-LPS – TLR4 agonist, acts as immunostimulant	Paclitaxel	Synergistic antitumor activity, significantly increased percentage of M1 macrophages (CD14+/ CD40+) and CD4 and CD8 T-cells in the TME.	[125, 126]
Multidomain Nanogel + Clodronate liposome	Clodronate + Imiquimod – deplete TAM	Gemcitabine	Combination treatment showed strong anti-tumor effects due to ICD and generation of memory T-cell response in mice breast tumor model.	[128]
Multiwalled carbon nanotubes	CpG –TLR 9 agonist	Doxorubicin + photothermal (NIR)	Promoted TAM polarization from M2 to M1 with a decreased Treg cells in the TME, contributed to the enhanced anti-tumor efficacy.	[129]
Polymeric nanoparticle	Zymosan (an immunotherapeutic polysaccharide) –TAM differentiation	Doxorubicin	TAMs differentiation with decreased CD206 population and improved anti-angiogenic effect.	[130]
Layer peeling NPs	IKKβ-siRNA – TAM polarization	Doxorubicin	Effective TAM polarization with improved anti-tumor efficacy due to synergistic effect of combination therapy.	[131]
Sensitive cluster NPs (SCNs) (pH-sensitive NPs)	BLZ-945 – Colony-stimulating factor 1 receptor (CSF-1R) inhibitor - depletes TAM from tumor tissue	Platinum prodrug	Cancer cells and TAM were killed, modulating TME to augment the anti-tumor effect mediated by CD8+ T cells.	[133]
Synthetic high-density lipoprotein nanoparticles (sHDL)	CpG oligodeoxynucleotides– TLR9 agonist	Docetaxel	Improved survival compared to chemotherapy alone in mice model of colon adenocarcinoma.	[134]

Polymer-drug conjugate	P-LPS (LPS derivative) – TLR-4 agonist	Paclitaxel	Combined chemo-immunotherapeutic activity, TAM activation into M1 phenotype, increased T cell infiltration in the TME.	[135]
Self-assembly of iRGD peptide derivatives, paclitaxel, and imiquimod	Imiquimod (R837) –TLR-7 agonist	Paclitaxel	ICD and enhanced tumor-specific immune response, including CD4 and CD8 T cell infiltration.	[136]
Twin like core-shell pH-responsive NPs	IMD-0354 – IKKβ inhibitor, TAM polarization	Sorafenib	Combination therapy exhibited enhanced antitumor efficacy.	[137]
PEG-PLGA NPs	Gd-metallofullerenol – TAM polarization	Doxorubicin	Showed strong immune-stimulating effect through TAM polarization and induced Th1 immune response suppressing the tumor growth.	[138]
Separate PLGA NPs loaded with doxorubicin and resiquimod, complexed with glycol chitosan and nonpathogenic bacterium E. coli MG1655	Resiquimod – TLR-7 agonist and nonpathogenic E. coli	Doxorubicin	TAM polarization, improved infiltration of T lymphocytes, enhanced antitumor activity.	[139]

1.8.Nanoparticles in cancer treatment:

Nanoparticles (NPs): the term indicates that they are fine-tuned and designed with a nm size range (10^{-9} m). Typically, it ranges from a few nm to several hundred nm, based on their application. NPs in cancer treatment help them navigate through the gaps present in the leaky vasculature of the endothelial cells due to the deficiency of the tumor lymphatic drainage system, which helps them reach the tumor site easily. This phenomenon is known as the Enhanced Permeability and Retention (EPR) effect [140]. Besides the use of NPs, their size plays an important role where they can be easily taken up and eliminated by the reticuloendothelial system (RES), which primarily includes highly perfused organs such as the liver, lungs, spleen, and bone marrow. This phenomenon is commonly known as RES uptake, and this can be avoided by surface modification of the NPs like PEGylation, which helps give a "stealth effect", where it prevents macrophage uptake of NPs and evades RES recognition as well [141]. Surface modification of NPs, which can help them to be more hydrophilic, can also help reduce the opsonization effect, which reduces macrophage clearance. This is known as the "cloud effect" [142].

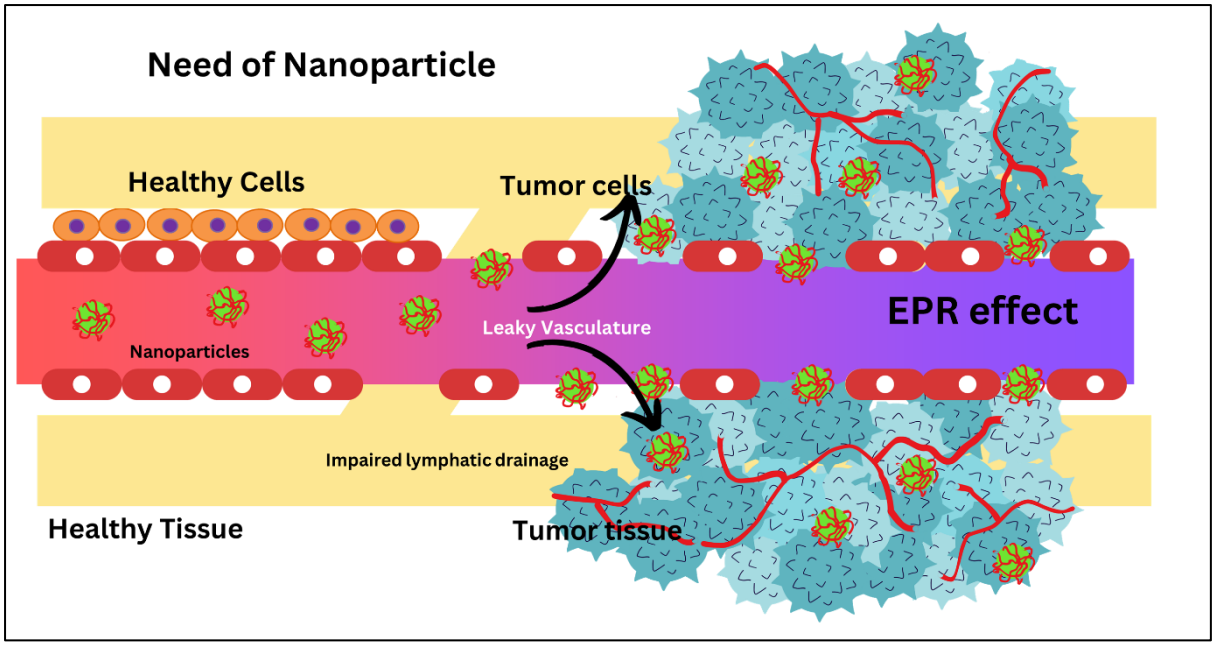

Figure 1.5. Role and need of nanoparticles for the delivery of payload for the treatment of cancer.

1.9. NP design strategies for multidimensional combination therapy:

NP formulations offer advantages over free drugs for tumor-targeted multi-drug delivery. Almost all types of combination therapeutics work best at a particular dose ratio [143]. NPs deliver encapsulated drugs to tumors in a fixed-dose ratio, which is highly challenging to achieve with conventional formulations. NPs shield drugs from normal metabolism and deliver them in a pre-decided encapsulation ratio.

Designing NPs for multi-drug delivery is significantly more challenging compared to a single drug. Different drugs have different physicochemical properties (like molecular weight, log P, and pKa), so their NP encapsulation efficiencies could be different. Polymeric or micellar NPs are often used if both drugs are hydrophobic, as these NPs contain a hydrophobic core for the drug loading. This strategy could co-deliver different hydrophobic drug combinations [144-147]. On the other hand, encapsulating drugs with different physicochemical properties in the same nanocarrier becomes challenging. However, liposome-based formulations were more successful for this purpose, as they have both hydrophobic (lipid bilayer) and hydrophilic (aqueous core) compartments. Few such formulations are being evaluated clinically as well, including cytarabine + daunorubicin (CPX-351) [148] and irinotecan + floxuridine (CPX-1) [149]. However, incorporating any hydrophobic drug in a liposomal formulation has dose limitations, as the lipid bilayer exhibited a relatively low loading capacity. Also, incorporating drugs inside the liposomal membrane can make the liposome unstable, leading to quick drug

release. To improve drug delivery, Park et al. developed a method to incorporate hydrophobic drugs into the core of a liposome. They made a water-soluble complex of a hydrophobic drug with cyclodextrin, mixed it with a hydrophilic protein interleukin-2, and encapsulated this mixture in the core of a liposomal formulation [150]. The solvent-assisted active loading technology (SALT) approach was developed by Tang et al. to encapsulate hydrophobic drugs into the liposomal core [151]. They showed that a limited amount of organic solvent can dissolve poorly soluble drugs in the aqueous loading mixture and permeabilize the liposomal membrane, enabling efficient drug penetration into the liposomal core for loading [151-153].

Like liposomal formulations, polymeric NPs prepared by the double-emulsion method can also encapsulate hydrophilic and lipophilic drugs. Roy et al. reported the development of such an NP using PLGA. The double-emulsion-based NP's hydrophilic core was loaded with an immunomodulator, SP-LPS, and the hydrophobic shell had the chemotherapeutic drug paclitaxel [125]. This combined chemo-immunotherapeutic NP exhibited enhanced efficacy in both in-vitro and in-vivo studies [125, 126].

Another potential approach to encapsulate a hydrophobic-hydrophilic drug combination is the conjugation of the hydrophilic drug with a polymer and then using the drug-conjugated polymer to encapsulate the hydrophobic drug. Kolishetti et al. used this strategy for codelivery of docetaxel and platinum complex [Pt(IV)] [154]. The Pt(IV) complex was chemically conjugated with a PEG-PLA copolymer, which was then used to encapsulate the docetaxel to make a micellar NP. Roy et al. used a hydrophilic, polymeric immunomodulator (P-LPS) to conjugate with the chemotherapeutic drug paclitaxel [135]. This drug conjugate exhibited combined chemo-immunotherapeutic activity and converted the immunosuppressive TME into an immune active state with macrophage activation into M1 phenotype and increased T cell infiltration.

Most of the combination drug delivery strategies discussed above did not consider targeting two different cells. Nano-carriers, like liposomes, polymeric NPs, micelles, drug-conjugates, etc., can be taken up by cells [155], and the drug/s encapsulated in that nano-carrier would be effective against that cell only. Hence, a multi drug-loaded nano-carrier targeting different types of cells should release the drugs efficiently upon reaching the TME to act on their specific target cells. For this purpose, different types of stimuli-responsive NPs have been developed.

TME-specific stimuli-responsive NPs:

Compared to active targeting that depends on some tumor-specific proteins, stimuli release NPs, which depend on tumor microenvironmental conditions like pH, temperature, and redox conditions, appear to be more effective because of variability in expression of tumor-specific proteins [156]. Various strategies exist for TME-responsive delivery systems. NPs commonly use the enlarged fenestrae present in the tumor vasculature for selective accumulation. Other physiological abnormalities in TME, like decreased pH and hypoxia, can be exploited to release drugs from the NPs.

Redox sensitive NPs:

In the tumor microenvironment, the higher concentration of glutathione (GSH) leads to multi-drug resistance in cancer. Redox-sensitive nanoparticles (NPs) are developed due to the variation in GSH levels [157]. Most redox-responsive NPs have disulfide bonds (S-S) in their backbone, linkers, side chains, or surface [158-163]. Some other linkers include diselenide (Se-Se), succinimide-thioether and trimethyl-locked benzoquinone as redox-sensitive moieties [157, 164, 165]. Though most of these formulations are used to deliver a single drug [166-168], a few multi-drug-loaded nano-carriers have been prepared. A redox-responsive immunostimulatory polymeric prodrug carrier (PSSN10) was developed to deliver doxorubicin for combined chemo-immunotherapy [132]. The PSSN10 system consists of a POEG hydrophilic block and a PNLG hydrophobic block with several motifs attached via redox-sensitive S-S linkages. This polymer-drug conjugate was used for loading doxorubicin for combined chemo-immunotherapy.

Hypoxia-sensitive NPs:

Insufficient amount of oxygen, because of impaired vascularization and commonly termed hypoxia, also plays a major role in the TME [169]. Multiple NPs have been explored for tumor-specific drug release using hypoxia with various groups like quinone, nitroaromatic, and azobenzene as hypoxia-sensitive compounds. [170]. In hypoxic cancers, these compounds are reduced to amino-aromatics; in normoxic cells, they remain oxidized. In the majority of the reported studies, only a single drug was incorporated. For example, Thavasyappan et al. developed a hypoxia-sensitive NP by conjugating hydrophobically modified 2-nitroimidazole with carboxymethyl dextran for the delivery of doxorubicin [171]. Under hypoxic conditions, the 2-nitroimidazole groups were converted to hydrophilic 2-aminoimidazoles via a series of selective bio reductions, resulting in NP destabilization and release of the payload.

Enzyme responsive NPs:

Another important strategy explored for tumor-targeted drug delivery is enzyme-responsive NPs using specific TME enzymes, like proteases, phosphatases, and glycosidases. Multiple enzymes, such as plasmin, cathepsin B, MMP-2, hyaluronidase, etc., are overexpressed in tumor cells [172]. For example, Zhang and co-workers developed a multi-responsive, peptide-based prodrug platform using a peptide (2-Nap)- FFKGGGPLGVRG [173]. This peptide was used for simultaneous delivery of cisplatin (Pt, chemotherapeutic), adjudin (ADD, anticancer agent), and WKYMVm (formyl peptide receptor 1 agonist, an immune adjuvant) for combined chemo-immunotherapy. Pt and ADD were conjugated to the peptide through the amino group of lysine (K) via a pH-sensitive 4-carboxybenzaldehyde (CBA) linker, while WKYMVm was conjugated with the terminal glycine (G). This drug-conjugated peptide was self-assembled into spherical NPs (~50 nm). After the accumulation in the tumor, WKYMVm was released from the NPs by MMP-2 cleavage. In the presence of GSH and the weakly acidic conditions in the TME, both Pt and ADD were released due to the dissociation of the CBA linkers. This drug cocktail of Pt, ADD, and WKYMVm exhibited synergistic efficacy against a mouse s.c. tumor model.

pH-responsive NPs:

pH-responsive nanoparticles are a prominent class of nanomaterials that respond to the acidic conditions in the tumor microenvironment (TME) for controlled drug release. The TME has a lower pH (~6.5 to 6.9) due to increased lactic acid accumulation from cancer cell glycolysis, making it an ideal target for drug delivery [135]. Several approaches have been explored to develop pH-sensitive nanoparticles, including those with acid-sensitive linkers or ionizable moieties, to exploit the acidic TME for drug release.

One approach involves the incorporation of nitrogen-containing ring systems into polymer structures. These ring systems exhibit pH-dependent ionization, capturing H+ ions at low pH. For instance, poly(2-azepane ethyl methacrylate) (PAEMA) modified poly(amidoamine) dendrimers were developed for pH-sensitive drug delivery, destabilizing in the TME to release a platinum prodrug and a small molecule inhibitor [58]. Similarly, a piperazine ring-containing diacrylate-based polymer was used to create pH-sensitive nanoparticles for the co-delivery of doxorubicin and curcumin [136]. The protonation of the piperazine ring at acidic pH led to rapid drug release. Other strategies involved attaching histidine to a polymer to develop pH-sensitive nanoparticles for synergistic drug delivery [137]. These nanoparticles, ionized at

acidic pH, released anticancer and cancer stem cell inhibitory agents. Imidazole-based pH-responsive polymers were employed to create magnetic nanoparticles that could release therapeutic cargo upon protonation in the TME [138].

Another strategy is to employ pH-sensitive linkers to conjugate drugs with nanoparticles. These linkers are hydrolyzed at the acidic pH of the TME, facilitating drug release. For instance, single-walled carbon nanotubes were conjugated with salinomycin and paclitaxel using a pH-sensitive hydrazone linker [117]. Lipid-based nanoparticles with pH-sensitive Schiff's base linkers were developed for the delivery of doxorubicin and curcumin [139]. Inorganic nanoparticles, such as pH-responsive silica nanoparticles, were designed using pH-sensitive boronic ester linkages, leading to tumor-targeted drug release [140]. pH-sensitive crosslinked protein-based nanoparticles loaded with doxorubicin were created by using an ortho ester-based crosslinking agent, enhancing drug penetration into the tumor [141]. Additionally, certain inorganic nanoparticles, like PEG-modified CaCO3 nanoparticles, exhibit intrinsic pH-dependent drug release capabilities, degrading under acidic TME conditions to release encapsulated drugs [142].

Liposomes are another versatile platform for pH-sensitive drug delivery, often composed of dioleoyl phosphatidyl-ethanolamine (DOPE), dioleoyl phosphatidylcholine (DOPC), and weakly acidic amphiphiles like cholesteryl hemisuccinate (CHEMS). These lipids can be protonated at low pH, leading to membrane destabilization and drug release [143]. Some liposomes incorporate pH-sensitive polymers to enhance drug release characteristics [144]. To maximize the internalization of PEGylated liposomes, some formulations utilize detachable pH-sensitive PEG in their design [146, 147].

Among all the stimuli-responsive NPs, pH-sensitive NPs are particularly relevant and beneficial in BC treatment as they offer several advantages like:

a) Selective drug release: pH-sensitive destabilization to release drugs in the acidic pH of the tumor microenvironment (TME). This enhances tumor accumulation, reduces off-target effects, and improves therapeutic activity.
b) As pH-sensitive NPs have the capability to enhance the solubility and BA of the drugs, it can lead to improved drug delivery to the tumor site.
c) pH-sensitive NPs are also highly useful when we need to target different types of cells with multidimensional therapeutics.

d) It can also help in the controlled and prolonged release of the payload, improving the drug's pharmacokinetic profile.
e) These can also help overcome therapeutic resistance by bypassing drug efflux pumps and other resistance mechanisms, allowing the payload to reach tumor cells directly.

Thus, we have opted for pH-sensitive NPs in our study as they offer a promising strategy for improving the targeted delivery and efficacy of anti-cancer drugs and combinational therapeutics in BC treatment.

1.10. Background of the Proposed Research

Among different non-neoplastic cells present in the tumor stroma, tumor-associated immune cells play one of the most critical roles by promoting angiogenesis, modifying other stromal cells, and maintaining an immune inhibitory milieu [174]. If adequately activated, these immune cells can become tumoricidal, as has been shown by multiple studies [175]. Understanding the importance of immune cell reactivation in the tumor microenvironment, different immunotherapeutic strategies have been designed for cancer therapy [175]. However, as tumor cells are responsible for nurturing the immunosuppressive tumor microenvironment, activation of the antitumor immune response is highly challenging without tumor depletion. Due to that, the combination of chemotherapy with immunotherapy can have significant advantages as chemotherapy can alter the immune tolerance and regulation induced by tumor cells to generate a more potent immune activation [176]. Also, chemotherapy-induced cancer cell death will produce cancer-specific antigens for enhanced cross-priming of T cells [177, 178]. Expression of MHC molecules on the tumor cells also increases with chemotherapeutic treatment, making them an easier target for cytotoxic T cells [179]. Unfortunately, most of the chemotherapeutic drugs are immunosuppressive, hence not useful for this purpose. One significant exception is Paclitaxel (PTX), which has shown immune stimulatory activity, including increased accumulation and activation of effector T cells, dendritic cells (DCs), natural killer (NK) cells, and macrophages [180]. Another exception is gemcitabine (GEM), which has shown immune stimulatory activity at the therapeutic dose. It was shown to enhance the cross-priming of antitumor CD8+ T cells as well as immune cell infiltration [181]. However, antigen presentation is essential for effective activation of the T cells. The primary antigen-presenting cells (APCs) present in the tumor are the tumor-associated macrophages (TAMs) [74], which exhibit immune suppression by the production of a host of immune

inhibitory cytokines, including IL-10, TGF-β, CCL2 etc. and helps to maintain the immunosuppressive tumor microenvironment [182]. Re-educating these TAMs from their immunosuppressive state to the immune stimulatory phenotype can be a potential strategy for a successful antitumor response [183]. Toll-like receptor (TLR) agonists are one of the most potent ligands for activation of macrophages. Breast cancer is the most common cancer among women, and it is the second leading cause of deaths in women. Treatment options are limited for metastatic breast cancer, and the failure rate is high. However, complete response rate is rare. Many subtypes of breast cancer have been identified, triple-negative breast cancer (TNBC), characterized by the absence of estrogen and progesterone receptor as well as HER2, is one of them. TNBC is a poor prognostic factor as no effective targeted therapy is available for TNBC [184]**.** Recently it has been observed that lymphocytic infiltration is significantly higher in TNBC, making them highly suitable for immunotherapy.

Our main goal is to come up with a strategy for combined chemo-immunotherapy for TNBC. To achieve this, we propose to create pH-sensitive nanoparticles that can deliver both chemotherapy and immunomodulator drugs to the tumor. Since we want to target two types of cells, it is crucial that the drugs are available to interact with their specific target cells in the tumor microenvironment. At the same time, we need to protect the drugs from elimination by the body and nonspecific accumulation. To do this, we need a delivery system to protect the drugs during systemic circulation and release them when they reach their target tissue. pH-sensitive nanoparticles are currently the most advanced trigger-sensitive formulation for clinical application. These nanoparticles are designed to release the drugs at the tumor site, taking advantage of the different pH levels in tumor tissue compared to normal tissue [185]. By using two strategies - passive accumulation at the tumor site through the EPR effect and active drug release at the tumor site upon external acidic pH stimulus - these triggered release nanoparticles can deliver cytotoxic drugs to the tumor site.

1.11. Gap in Existing Research

As a strategy, combined chemo-immunotherapy has gained significant interest in the last few years. Currently, mostly checkpoint inhibitors (CTLA-4, PD-1, or PD-L1 inhibitors) are used for immunotherapy along with different chemotherapeutic drugs [186]. Checkpoint inhibitors prevent tumor-mediated CTL deactivation through cell-cell interaction. It is an ingenious therapeutic strategy; however, to function, they need a high amount of CTL in the tumor microenvironment. Other prognostic markers for the success of checkpoint inhibitor therapy include the presence of a high amount of neoantigen, a high Teff to Treg ratio, low MDSC

levels, and increased secretion of IFN-γ and other immune stimulatory cytokines [187]. The presence of a high level of immunosuppressive cells, such as Tregs and myeloid-derived suppressor cells (MDSCs), and very low levels of activated T cells is a negative prognostic indicator [187]. In most of the solid tumors, the tumor microenvironment is maintained in a highly immunosuppressive milieu, which prevents the activation and function of effector T cells, which can potentially prevent the activity of checkpoint inhibitors [188].

Among different cellular components of the tumor, macrophages have the most significant contribution in maintaining the immunosuppressive tumor microenvironment. Tumor-associated macrophages (TAM) are of M2 phenotype, which secrete a host of immune inhibitory cytokines, thereby preventing other immune cells, including CTL activation. Interestingly, these M2 macrophages exhibit functional plasticity, i.e., they can be activated to the M1 phenotype if a proper activation signal is present [189, 190]. Activation of M1 macrophages can lead to the secretion of immunostimulatory cytokines and the conversion of the immunosuppressive tumor microenvironment into an activated one. There are several benefits of targeting the TAMs: they are the most abundant immune cells present in the tumor, they are the major mediator for tumor immunosuppression, and they show functional plasticity, hence can be converted to the stimulatory phenotype, strengthening the hypothesis of macrophage stimulation for cancer therapy.

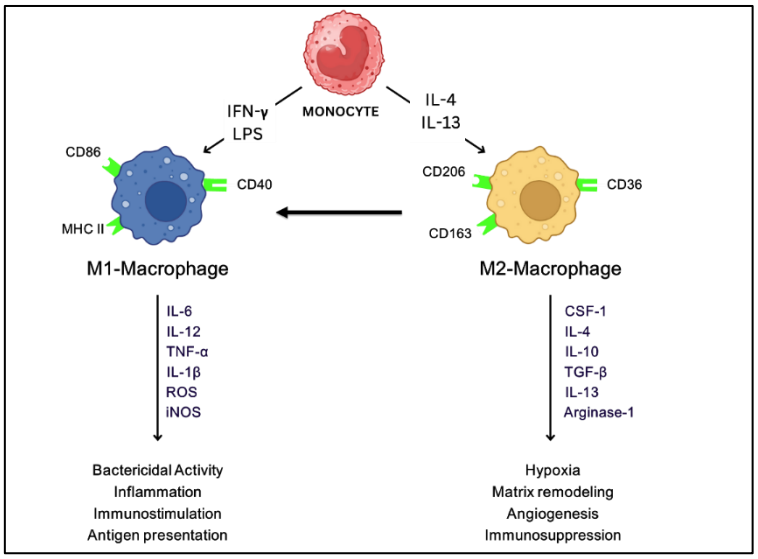

Figure 1.6. Types of macrophages and their roles after stimulating with chemokines.

There are several ligands that can stimulate macrophage conversion. Among them, TLR agonists are the most potent [191]. Research indicated that the administration of a combination of TLR agonist with a chemotherapeutic drug can have synergistic anticancer efficacy. However, developing a specifically designed delivery system for such multidimensional

therapy is still in its infancy. Most of the advanced studies on combined chemo-immunotherapy have been done using two separate formulations delivering two drugs separately. However, as both drugs are supposed to function in the tumor microenvironment, their co-delivery using the same vector would be beneficial to enhance their tumor bioavailability and efficacy. Different nano-delivery systems have been developed for tumor-targeted delivery of different chemotherapeutic drugs; however, almost all of them are for single-drug delivery. The delivery of a multidimensional drug combination is more complicated than a single drug. As different drugs target different types of cells, their bioavailability in the tumor microenvironment is critical. Different targeting strategies have been evaluated for tumor delivery of NPs. One of the most researched areas is active targeting, i.e., targeting the tumor cells using tumor-specific ligands. However, although active targeting has demonstrated better efficacy than non-targeted NPs, these NPs exhibited a unique intra-tumoral distribution pattern. Upon entering the tumor, the targeted NPs encounter the peripheral tumor cells and are immobilized there, after binding with the respective receptor [192]. Due to this, most of the actively targeted NPs are concentrated in the peripheral region of the tumor, and tumor core penetration is very low. The tumor core harbors most of the tumor-supporting cells, and tumor core penetration has been shown to be one of the most important factors for efficacy [193]. Burst release of the encapsulated drugs in the tumor microenvironment would facilitate drug penetration by diffusion as well as free availability to their target cells. We would like to exploit the acidic pH of the tumor interstitial fluid to develop a smart release delivery system for a multidimensional drug combination.

1.12. Hypothesis:

Cancer therapy has traditionally focused on targeting cancer cells alone. However, recent research has shown that cancer is a multi-cellular disorder that involves a variety of supporting cells. As a result, therapies targeting these supporting cells have been developed and are proving to be highly effective in combination with other treatment modalities. Tumor-associated macrophages (TAMs) are one of the most important supporting cells for tumor growth. They promote angiogenesis, modify stromal cells for the benefit of cancer cells, and contribute to maintaining an immune inhibitory environment at the tumor microenvironment. However, with proper stimulation, TAMs can be transformed into an immune-stimulatory phenotype, which can help T cell activation. Transforming the immunosuppressive tumor microenvironment into an immune-stimulatory state is challenging without neutralizing the cancer cells. Chemotherapy can induce immune tolerance, so combining a chemotherapeutic

drug with an immune stimulant can be advantageous. Additionally, chemotherapy-mediated cancer cell death provides cancer antigens to the effector T cells for better T cell activation. Although there has been extensive research on developing NP formulation of anticancer drugs, research on immunotherapeutic NPs is scarce. The development of an advanced tumor-targeted pH-responsive nanoformulation for combined chemo-immunotherapy can be highly advantageous. Based on that, we propose developing a smart nanocarrier (NP) system encapsulating a chemotherapeutic drug and an immunomodulator in a pH-responsive NP system.

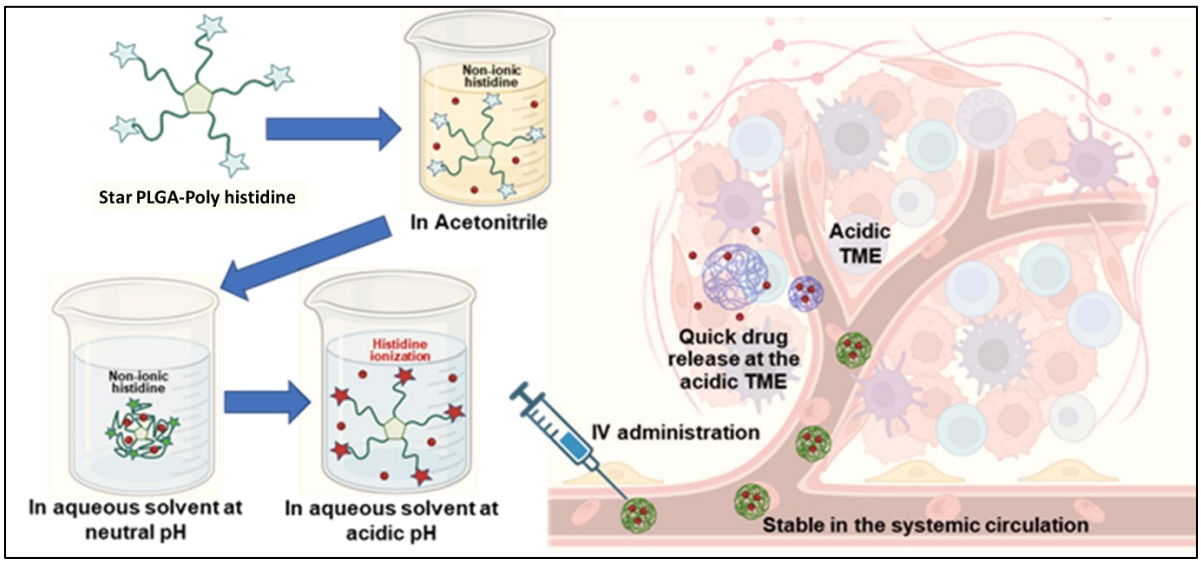

Figure 1.7. Fabrication of pH-sensitive nanocarrier targeting tumor microenvironment.

1.13. Objective of the Proposed Research:

Based on the current literature and observed gaps in the existing research, we have made a hypothesis of combining a chemotherapeutic agent and an immunomodulator (TLR agonist) for macrophage targeting combined chemo-immunotherapy against breast cancer and develop a novel pH-triggered nanoformulation for dual drug delivery of chemotherapeutic and TLR agonist to target macrophages. Accordingly, we have designed our objectives as follows:

Objective 1:

Screening of anticancer drugs and immunomodulators for synergistic anticancer efficacy.

Objective 2:

Formulation optimization and Preparation of a pH-sensitive nanoparticle encapsulating the selected chemotherapeutic agent and immunomodulator. Physicochemical characterization of the nanoparticles in terms of size, polydispersity, encapsulation efficiency, stability, and drug release profile.

Objective 3:

Determination of the pharmacological activity of the combination therapy in the in-vitro model using both 2D and 3D co-culture systems. Analysis of the synergy and the molecular mechanism responsible.

Objective 4:

In-vivo pharmacokinetic and bio-distribution analysis. Efficacy study in mouse model of tumor.

References:

1. Sung, H., et al., *Global Cancer Statistics 2020: GLOBOCAN Estimates of Incidence and Mortality Worldwide for 36 Cancers in 185 Countries.* CA Cancer J Clin, 2021. **71**(3): p. 209-249.
2. DeSantis, C., et al., *Breast cancer statistics, 2011.* CA Cancer J Clin, 2011. **61**(6): p. 409-18.
3. Saxena, S., et al., *BRCA1 and BRCA2 in Indian breast cancer patients.* Hum Mutat, 2002. **20**(6): p. 473-4.
4. *The burden of cancers and their variations across the states of India: the Global Burden of Disease Study 1990-2016.* Lancet Oncol, 2018. **19**(10): p. 1289-1306.
5. Mehrotra, R. and K. Yadav, *Breast cancer in India: Present scenario and the challenges ahead.* World J Clin Oncol, 2022. **13**(3): p. 209-218.
6. Takiar, R. and A. Srivastav, *Time trend in breast and cervix cancer of women in India - (1990-2003).* Asian Pac J Cancer Prev, 2008. **9**(4): p. 777-80.
7. Babu, G.R., S.B. Lakshmi, and J.A. Thiyagarajan, *Epidemiological correlates of breast cancer in South India.* Asian Pac J Cancer Prev, 2013. **14**(9): p. 5077-83.
8. Armuss, A., *[Breast cancer update].* Versicherungsmedizin, 2014. **66**(2): p. 68-71.
9. Sun, L., et al., *Global treatment costs of breast cancer by stage: A systematic review.* PLoS One, 2018. **13**(11): p. e0207993.
10. Makki, J., *Diversity of Breast Carcinoma: Histological Subtypes and Clinical Relevance.* Clin Med Insights Pathol, 2015. **8**: p. 23-31.
11. Zhang, X., *Molecular Classification of Breast Cancer: Relevance and Challenges.* Arch Pathol Lab Med, 2023. **147**(1): p. 46-51.
12. Andreopoulou, E. and J.A. Sparano, *Chemotherapy in Patients with Anthracycline- and Taxane-Pretreated Metastatic Breast Cancer: An Overview.* Curr Breast Cancer Rep, 2013. **5**(1): p. 42-50.
13. Gradishar, W.J., *Taxanes for the treatment of metastatic breast cancer.* Breast Cancer (Auckl), 2012. **6**: p. 159-71.
14. Rivera, E. and H. Gomez, *Chemotherapy resistance in metastatic breast cancer: the evolving role of ixabepilone.* Breast Cancer Res, 2010. **12 Suppl 2**(Suppl 2): p. S2.
15. Hashim, D., et al., *The global decrease in cancer mortality: trends and disparities.* Ann Oncol, 2016. **27**(5): p. 926-33.
16. Danaei, G., et al., *Causes of cancer in the world: comparative risk assessment of nine behavioural and environmental risk factors.* Lancet, 2005. **366**(9499): p. 1784-93.
17. Hoon, S.N., et al., *Capecitabine for hormone receptor-positive versus hormone receptor-negative breast cancer.* Cochrane Database Syst Rev, 2021. **5**(5): p. Cd011220.
18. Masuda, N., et al., *Adjuvant Capecitabine for Breast Cancer after Preoperative Chemotherapy.* N Engl J Med, 2017. **376**(22): p. 2147-2159.
19. Park, J.H., et al., *Cyclophosphamide, Methotrexate, and 5-Fluorouracil as Palliative Treatment for Heavily Pretreated Patients with Metastatic Breast Cancer: A Multicenter Retrospective Analysis.* J Breast Cancer, 2017. **20**(4): p. 347-355.
20. Vahdat, L.T., et al., *Phase II study of eribulin mesylate, a halichondrin B analog, in patients with metastatic breast cancer previously treated with an anthracycline and a taxane.* J Clin Oncol, 2009. **27**(18): p. 2954-61.
21. Smorenburg, C.H., et al., *Phase II study of weekly gemcitabine in patients with metastatic breast cancer relapsing or failing both an anthracycline and a taxane.* Breast Cancer Res Treat, 2001. **66**(1): p. 83-7.
22. Thomas, E., et al., *Phase II clinical trial of ixabepilone (BMS-247550), an epothilone B analog, in patients with taxane-resistant metastatic breast cancer.* J Clin Oncol, 2007. **25**(23): p. 3399-406.
23. Comte, A., et al., *Survival of breast cancer patients with meningeal carcinomatosis treated by intrathecal thiotepa.* J Neurooncol, 2013. **115**(3): p. 445-52.

24. Urruticoechea, A., et al., *Mitomycin C, vinblastine and cisplatin (MVP): an active and well-tolerated salvage regimen for advanced breast cancer.* Br J Cancer, 2005. **92**(3): p. 475-9.
25. Marty, M., et al., *Prospects with docetaxel in the treatment of patients with breast cancer.* Eur J Cancer, 1997. **33 Suppl 7**: p. S26-9.
26. Vishnu, P. and V. Roy, *Safety and Efficacy of nab-Paclitaxel in the Treatment of Patients with Breast Cancer.* Breast Cancer (Auckl), 2011. **5**: p. 53-65.
27. Verma, S. and M. Ewer, *Is cardiotoxicity being adequately assessed in current trials of cytotoxic and targeted agents in breast cancer?* Annals of oncology, 2011. **22**(5): p. 1011-1018.
28. Yardley, D.A., et al., *A phase II trial of ixabepilone and cyclophosphamide as neoadjuvant therapy for patients with HER2-negative breast cancer: correlation of pathologic complete response with the 21-gene recurrence score.* Breast cancer research and treatment, 2015. **154**: p. 299-308.
29. Dittrich, C., et al., *A phase II multicenter study of two different dosages of pemetrexed given in combination with cyclophosphamide as first-line treatment in patients with locally advanced or metastatic breast cancer.* Cancer Investigation, 2012. **30**(4): p. 309-316.
30. John Smith, I., et al., *Phase 2 study evaluating the efficacy and safety of eribulin mesylate administered biweekly for patients with human epidermal growth factor receptor 2-negative metastatic breast cancer.* 2018.
31. Goss, P.E., et al., *Exemestane versus anastrozole in postmenopausal women with early breast cancer: NCIC CTG MA.27--a randomized controlled phase III trial.* J Clin Oncol, 2013. **31**(11): p. 1398-404.
32. Al-Mubarak, M., et al., *Fulvestrant for advanced breast cancer: a meta-analysis.* Cancer treatment reviews, 2013. **39**(7): p. 753-758.
33. Di Leo, A., et al., *First-line vs second-line fulvestrant for hormone receptor-positive advanced breast cancer: A post-hoc analysis of the CONFIRM study.* Breast, 2018. **38**: p. 144-149.
34. Aapro, M.S., et al., *Vinflunine plus capecitabine for advanced breast cancer previously treated with or resistant to anthracycline and resistant to taxane: A phase III study versus capecitabine*. 2014, American Society of Clinical Oncology.
35. Fidler, I.J., *The pathogenesis of cancer metastasis: the 'seed and soil' hypothesis revisited.* Nat Rev Cancer, 2003. **3**(6): p. 453-8.
36. Roy, A. and S.D. Li, *Modifying the tumor microenvironment using nanoparticle therapeutics.* Wiley Interdiscip Rev Nanomed Nanobiotechnol, 2016. **8**(6): p. 891-908.
37. Jain, R.K., *Normalizing tumor microenvironment to treat cancer: bench to bedside to biomarkers.* J Clin Oncol, 2013. **31**(17): p. 2205-18.
38. Quail, D.F. and J.A. Joyce, *Microenvironmental regulation of tumor progression and metastasis.* Nat Med, 2013. **19**(11): p. 1423-37.
39. Wang, M., et al., *Role of tumor microenvironment in tumorigenesis.* J Cancer, 2017. **8**(5): p. 761-773.
40. Son, B., et al., *The role of tumor microenvironment in therapeutic resistance.* Oncotarget, 2017. **8**(3): p. 3933-3945.
41. Li, X.Y., S.Q. Hu, and L. Xiao, *The cancer-associated fibroblasts and drug resistance.* Eur Rev Med Pharmacol Sci, 2015. **19**(11): p. 2112-9.
42. Hida, K., et al., *Tumour endothelial cells acquire drug resistance in a tumour microenvironment.* J Biochem, 2013. **153**(3): p. 243-9.
43. Ribeiro Franco, P.I., et al., *Tumor microenvironment components: Allies of cancer progression.* Pathol Res Pract, 2020. **216**(1): p. 152729.
44. Driskell, R.R., et al., *Distinct fibroblast lineages determine dermal architecture in skin development and repair.* Nature, 2013. **504**(7479): p. 277-81.
45. Dumont, N., et al., *Breast fibroblasts modulate early dissemination, tumorigenesis, and metastasis through alteration of extracellular matrix characteristics.* Neoplasia, 2013. **15**(3): p. 249-62.

46. Wang, F.T., et al., *Cancer-associated fibroblast regulation of tumor neo-angiogenesis as a therapeutic target in cancer.* Oncol Lett, 2019. **17**(3): p. 3055-3065.
47. Gascard, P. and T.D. Tlsty, *Carcinoma-associated fibroblasts: orchestrating the composition of malignancy.* Genes Dev, 2016. **30**(9): p. 1002-19.
48. Martin, J.D., G. Seano, and R.K. Jain, *Normalizing Function of Tumor Vessels: Progress, Opportunities, and Challenges.* Annu Rev Physiol, 2019. **81**: p. 505-534.
49. Provenzano, P.P., et al., *Enzymatic targeting of the stroma ablates physical barriers to treatment of pancreatic ductal adenocarcinoma.* Cancer Cell, 2012. **21**(3): p. 418-29.
50. Nishida, N., et al., *Angiogenesis in cancer.* Vasc Health Risk Manag, 2006. **2**(3): p. 213-9.
51. Lugano, R., M. Ramachandran, and A. Dimberg, *Tumor angiogenesis: causes, consequences, challenges and opportunities.* Cell Mol Life Sci, 2020. **77**(9): p. 1745-1770.
52. Lee, E., N.B. Pandey, and A.S. Popel, *Lymphatic endothelial cells support tumor growth in breast cancer.* Sci Rep, 2014. **4**: p. 5853.
53. Barlow, K.D., et al., *Pericytes on the tumor vasculature: jekyll or hyde?* Cancer Microenviron, 2013. **6**(1): p. 1-17.
54. Bergers, G. and S. Song, *The role of pericytes in blood-vessel formation and maintenance.* Neuro Oncol, 2005. **7**(4): p. 452-64.
55. Santagata, S., et al., *CXCR4 and CXCR7 Signaling Pathways: A Focus on the Cross-Talk Between Cancer Cells and Tumor Microenvironment.* Front Oncol, 2021. **11**: p. 591386.
56. Zimna, A. and M. Kurpisz, *Hypoxia-Inducible Factor-1 in Physiological and Pathophysiological Angiogenesis: Applications and Therapies.* Biomed Res Int, 2015. **2015**: p. 549412.
57. Yu, Z., et al., *Cancer stem cells.* Int J Biochem Cell Biol, 2012. **44**(12): p. 2144-51.
58. Bao, B., et al., *Overview of cancer stem cells (CSCs) and mechanisms of their regulation: implications for cancer therapy.* Curr Protoc Pharmacol, 2013. **Chapter 14**: p. Unit 14.25.
59. Rich, J.N., *Cancer stem cells: understanding tumor hierarchy and heterogeneity.* Medicine (Baltimore), 2016. **95**(1 Suppl 1): p. S2-s7.
60. Phi, L.T.H., et al., *Cancer Stem Cells (CSCs) in Drug Resistance and their Therapeutic Implications in Cancer Treatment.* Stem Cells Int, 2018. **2018**: p. 5416923.
61. Senbanjo, L.T. and M.A. Chellaiah, *CD44: A Multifunctional Cell Surface Adhesion Receptor Is a Regulator of Progression and Metastasis of Cancer Cells.* Front Cell Dev Biol, 2017. **5**: p. 18.
62. Clark, D.W. and K. Palle, *Aldehyde dehydrogenases in cancer stem cells: potential as therapeutic targets.* Ann Transl Med, 2016. **4**(24): p. 518.
63. Li, Y., et al., *Drug resistance and Cancer stem cells.* Cell Commun Signal, 2021. **19**(1): p. 19.
64. Yang, L., et al., *Targeting cancer stem cell pathways for cancer therapy.* Signal Transduct Target Ther, 2020. **5**(1): p. 8.
65. Ayob, A.Z. and T.S. Ramasamy, *Cancer stem cells as key drivers of tumour progression.* J Biomed Sci, 2018. **25**(1): p. 20.
66. Lewis, C.E., et al., *Cytokine regulation of angiogenesis in breast cancer: the role of tumor-associated macrophages.* J Leukoc Biol, 1995. **57**(5): p. 747-51.
67. Bingle, L., N.J. Brown, and C.E. Lewis, *The role of tumour-associated macrophages in tumour progression: implications for new anticancer therapies.* J Pathol, 2002. **196**(3): p. 254-65.
68. Winston, B.W., et al., *Cytokine-induced macrophage differentiation: a tale of 2 genes.* Clin Invest Med, 1999. **22**(6): p. 236-55.
69. Fujimoto, H., et al., *Stromal MCP-1 in mammary tumors induces tumor-associated macrophage infiltration and contributes to tumor progression.* Int J Cancer, 2009. **125**(6): p. 1276-84.
70. Bernhagen, J., et al., *MIF is a noncognate ligand of CXC chemokine receptors in inflammatory and atherogenic cell recruitment.* Nat Med, 2007. **13**(5): p. 587-96.
71. Lourenco, S., et al., *Macrophage migration inhibitory factor-CXCR4 is the dominant chemotactic axis in human mesenchymal stem cell recruitment to tumors.* J Immunol, 2015. **194**(7): p. 3463-74.

72. Bando, H., et al., *Expression of macrophage migration inhibitory factor in human breast cancer: association with nodal spread.* Jpn J Cancer Res, 2002. **93**(4): p. 389-96.
73. Hagemann, T., et al., *Macrophages induce invasiveness of epithelial cancer cells via NF-kappa B and JNK.* J Immunol, 2005. **175**(2): p. 1197-205.
74. Petty, A.J. and Y. Yang, *Tumor-associated macrophages: implications in cancer immunotherapy.* Immunotherapy, 2017. **9**(3): p. 289-302.
75. Petty, A.J. and Y. Yang, *Tumor-Associated Macrophages in Hematologic Malignancies: New Insights and Targeted Therapies.* Cells, 2019. **8**(12).
76. Pan, Y., et al., *Tumor-Associated Macrophages in Tumor Immunity.* Front Immunol, 2020. **11**: p. 583084.
77. Kreso, A. and J.E. Dick, *Evolution of the cancer stem cell model.* Cell Stem Cell, 2014. **14**(3): p. 275-91.
78. Lu, H., et al., *A breast cancer stem cell niche supported by juxtacrine signalling from monocytes and macrophages.* Nat Cell Biol, 2014. **16**(11): p. 1105-17.
79. Jinushi, M., et al., *Tumor-associated macrophages regulate tumorigenicity and anticancer drug responses of cancer stem/initiating cells.* Proc Natl Acad Sci U S A, 2011. **108**(30): p. 12425-30.
80. Mitchem, J.B., et al., *Targeting tumor-infiltrating macrophages decreases tumor-initiating cells, relieves immunosuppression, and improves chemotherapeutic responses.* Cancer Res, 2013. **73**(3): p. 1128-41.
81. Kessenbrock, K., V. Plaks, and Z. Werb, *Matrix metalloproteinases: regulators of the tumor microenvironment.* Cell, 2010. **141**(1): p. 52-67.
82. Lin, E.Y. and J.W. Pollard, *Tumor-associated macrophages press the angiogenic switch in breast cancer.* Cancer Res, 2007. **67**(11): p. 5064-6.
83. Palazon, A., et al., *An HIF-1α/VEGF-A Axis in Cytotoxic T Cells Regulates Tumor Progression.* Cancer Cell, 2017. **32**(5): p. 669-683.e5.
84. Chanmee, T., et al., *Tumor-associated macrophages as major players in the tumor microenvironment.* Cancers (Basel), 2014. **6**(3): p. 1670-90.
85. Vasiljeva, O., et al., *Tumor cell-derived and macrophage-derived cathepsin B promotes progression and lung metastasis of mammary cancer.* Cancer Res, 2006. **66**(10): p. 5242-50.
86. Chen, J., et al., *CCL18 from tumor-associated macrophages promotes breast cancer metastasis via PITPNM3.* Cancer Cell, 2011. **19**(4): p. 541-55.
87. Fan, Q.M., et al., *Tumor-associated macrophages promote cancer stem cell-like properties via transforming growth factor-beta1-induced epithelial-mesenchymal transition in hepatocellular carcinoma.* Cancer Lett, 2014. **352**(2): p. 160-8.
88. Qian, B., et al., *A distinct macrophage population mediates metastatic breast cancer cell extravasation, establishment and growth.* PLoS One, 2009. **4**(8): p. e6562.
89. Peranzoni, E., et al., *Macrophages impede CD8 T cells from reaching tumor cells and limit the efficacy of anti-PD-1 treatment.* Proc Natl Acad Sci U S A, 2018. **115**(17): p. E4041-e4050.
90. Munn, D.H., et al., *GCN2 kinase in T cells mediates proliferative arrest and anergy induction in response to indoleamine 2,3-dioxygenase.* Immunity, 2005. **22**(5): p. 633-42.
91. Noman, M.Z., et al., *Hypoxia-induced autophagy: a new player in cancer immunotherapy?* Autophagy, 2012. **8**(4): p. 704-6.
92. Kuang, D.M., et al., *Activated monocytes in peritumoral stroma of hepatocellular carcinoma foster immune privilege and disease progression through PD-L1.* J Exp Med, 2009. **206**(6): p. 1327-37.
93. Liu, J., et al., *Tumor-associated macrophages recruit CCR6+ regulatory T cells and promote the development of colorectal cancer via enhancing CCL20 production in mice.* PLoS One, 2011. **6**(4): p. e19495.

94. Denning, T.L., et al., *Lamina propria macrophages and dendritic cells differentially induce regulatory and interleukin 17-producing T cell responses.* Nat Immunol, 2007. **8**(10): p. 1086-94.
95. Koh, J., et al., *Regulatory (FoxP3(+)) T cells and TGF-β predict the response to anti-PD-1 immunotherapy in patients with non-small cell lung cancer.* Sci Rep, 2020. **10**(1): p. 18994.
96. Pathria, P., T.L. Louis, and J.A. Varner, *Targeting Tumor-Associated Macrophages in Cancer.* Trends Immunol, 2019. **40**(4): p. 310-327.
97. Larionova, I., et al., *Interaction of tumor-associated macrophages and cancer chemotherapy.* Oncoimmunology, 2019. **8**(7): p. 1596004.
98. Roblek, M., et al., *CCL2 Is a Vascular Permeability Factor Inducing CCR2-Dependent Endothelial Retraction during Lung Metastasis.* Mol Cancer Res, 2019. **17**(3): p. 783-793.
99. Nywening, T.M., et al., *Targeting tumour-associated macrophages with CCR2 inhibition in combination with FOLFIRINOX in patients with borderline resectable and locally advanced pancreatic cancer: a single-centre, open-label, dose-finding, non-randomised, phase 1b trial.* Lancet Oncol, 2016. **17**(5): p. 651-62.
100. Noel, M.S., et al., *Orally administered CCR2 selective inhibitor CCX872-b clinical trial in pancreatic cancer.* Journal of Clinical Oncology, 2017. **35**(4_suppl): p. 276-276.
101. Brana, I., et al., *Carlumab, an anti-C-C chemokine ligand 2 monoclonal antibody, in combination with four chemotherapy regimens for the treatment of patients with solid tumors: an open-label, multicenter phase 1b study.* Target Oncol, 2015. **10**(1): p. 111-23.
102. Panni, R.Z., et al., *Agonism of CD11b reprograms innate immunity to sensitize pancreatic cancer to immunotherapies.* Sci Transl Med, 2019. **11**(499).
103. Holmgaard, R.B., et al., *Timing of CSF-1/CSF-1R signaling blockade is critical to improving responses to CTLA-4 based immunotherapy.* Oncoimmunology, 2016. **5**(7): p. e1151595.
104. Lin, Y., J. Xu, and H. Lan, *Tumor-associated macrophages in tumor metastasis: biological roles and clinical therapeutic applications.* J Hematol Oncol, 2019. **12**(1): p. 76.
105. Tap, W.D., et al., *Pexidartinib versus placebo for advanced tenosynovial giant cell tumour (ENLIVEN): a randomised phase 3 trial.* Lancet, 2019. **394**(10197): p. 478-487.
106. Petty, A.J., et al., *Targeting Tumor-Associated Macrophages in Cancer Immunotherapy.* Cancers (Basel), 2021. **13**(21).
107. Zanker, D.J., et al., *Intratumoral administration of the Toll-like receptor 7/8 agonist 3M-052 enhances interferon-driven tumor immunogenicity and suppresses metastatic spread in preclinical triple-negative breast cancer.* Clin Transl Immunology, 2020. **9**(9): p. e1177.
108. Adams, S., et al., *Topical TLR7 agonist imiquimod can induce immune-mediated rejection of skin metastases in patients with breast cancer.* Clin Cancer Res, 2012. **18**(24): p. 6748-57.
109. Chow, L.Q.M., et al., *Phase Ib Trial of the Toll-like Receptor 8 Agonist, Motolimod (VTX-2337), Combined with Cetuximab in Patients with Recurrent or Metastatic SCCHN.* Clin Cancer Res, 2017. **23**(10): p. 2442-2450.
110. Wiehagen, K.R., et al., *Combination of CD40 Agonism and CSF-1R Blockade Reconditions Tumor-Associated Macrophages and Drives Potent Antitumor Immunity.* Cancer Immunol Res, 2017. **5**(12): p. 1109-1121.
111. De Henau, O., et al., *Overcoming resistance to checkpoint blockade therapy by targeting PI3Kγ in myeloid cells.* Nature, 2016. **539**(7629): p. 443-447.
112. Boutilier, A.J. and S.F. Elsawa, *Macrophage Polarization States in the Tumor Microenvironment.* Int J Mol Sci, 2021. **22**(13).
113. Zhu, S., et al., *Combination strategies to maximize the benefits of cancer immunotherapy.* J Hematol Oncol, 2021. **14**(1): p. 156.
114. Drake, C.G., *Combination immunotherapy approaches.* Ann Oncol, 2012. **23 Suppl 8**(Suppl 8): p. viii41-6.
115. Vafaei, S., et al., *Combination therapy with immune checkpoint inhibitors (ICIs); a new frontier.* Cancer Cell Int, 2022. **22**(1): p. 2.

116. Pol, J., et al., *Trial Watch: Immunogenic cell death inducers for anticancer chemotherapy.* Oncoimmunology, 2015. **4**(4): p. e1008866.
117. Liu, P., et al., *PD-1 blockade synergizes with oxaliplatin-based, but not cisplatin-based, chemotherapy of gastric cancer.* Oncoimmunology, 2022. **11**(1): p. 2093518.
118. Kroemer, G., et al., *Immunogenic cell stress and death.* Nat Immunol, 2022. **23**(4): p. 487-500.
119. Ishiwata, T., et al., *A feasibility study of zoledronic acid combined with carboplatin/nedaplatin plus paclitaxel in patients with non-small cell lung cancer with bone metastases.* Tumori, 2011. **97**(5): p. 568-72.
120. Sui, D., et al., *Sequential administration of sialic acid-modified liposomes as carriers for epirubicin and zoledronate elicit stronger antitumor effects with reduced toxicity.* Int J Pharm, 2021. **602**: p. 120552.
121. Luo, K.P., et al., *Charge convertible biomimetic micellar nanoparticles for enhanced melanoma-targeted therapy through tumor cells and tumor-associated macrophages dual chemotherapy with IDO immunotherapy.* Chemical Engineering Journal, 2021. **412**.
122. Genard, G., S. Lucas, and C. Michiels, *Reprogramming of Tumor-Associated Macrophages with Anticancer Therapies: Radiotherapy versus Chemo- and Immunotherapies.* Front Immunol, 2017. **8**: p. 828.
123. Ektate, K., et al., *Chemo-immunotherapy of colon cancer with focused ultrasound and Salmonella-laden temperature sensitive liposomes (thermobots).* Sci Rep, 2018. **8**(1): p. 13062.
124. Kuerban, K., et al., *Doxorubicin-loaded bacterial outer-membrane vesicles exert enhanced anti-tumor efficacy in non-small-cell lung cancer.* Acta Pharm Sin B, 2020. **10**(8): p. 1534-1548.
125. Roy, A., et al., *Combined chemo-immunotherapy as a prospective strategy to combat cancer: a nanoparticle based approach.* Mol Pharm, 2010. **7**(5): p. 1778-88.
126. Roy, A., et al., *Nanoparticle mediated co-delivery of paclitaxel and a TLR-4 agonist results in tumor regression and enhanced immune response in the tumor microenvironment of a mouse model.* Int J Pharm, 2013. **445**(1-2): p. 171-80.
127. van der Zanden, S.Y., et al., *Opportunities for Small Molecules in Cancer Immunotherapy.* Trends Immunol, 2020. **41**(6): p. 493-511.
128. Song, C., et al., *Syringeable immunotherapeutic nanogel reshapes tumor microenvironment and prevents tumor metastasis and recurrence.* Nat Commun, 2019. **10**(1): p. 3745.
129. Wang, X., et al., *MWCNT-mediated combinatorial photothermal ablation and chemo-immunotherapy strategy for the treatment of melanoma.* J Mater Chem B, 2020. **8**(19): p. 4245-4258.
130. Pawar, V.K., et al., *Doxorubicin Hydrochloride Loaded Zymosan-Polyethylenimine Biopolymeric Nanoparticles for Dual 'Chemoimmunotherapeutic' Intervention in Breast Cancer.* Pharm Res, 2017. **34**(9): p. 1857-1871.
131. Wang, T., et al., *"Layer peeling" co-delivery system for enhanced RNA interference-based tumor associated macrophages-specific chemoimmunotherapy.* Nanoscale, 2020. **12**(32): p. 16851-16863.
132. Sun, J.J., et al., *Programmable co-delivery of the immune checkpoint inhibitor NLG919 and chemotherapeutic doxorubicin via a redox-responsive immunostimulatory polymeric prodrug carrier.* Acta Pharmacol Sin, 2017. **38**(6): p. 823-834.
133. Shen, S., et al., *Spatial Targeting of Tumor-Associated Macrophages and Tumor Cells with a pH-Sensitive Cluster Nanocarrier for Cancer Chemoimmunotherapy.* Nano Lett, 2017. **17**(6): p. 3822-3829.
134. Scheetz, L.M., et al., *Synthetic HDL Nanoparticles Delivering Docetaxel and CpG for Chemoimmunotherapy of Colon Adenocarcinoma.* Int J Mol Sci, 2020. **21**(5).
135. Roy, A., et al., *Anticancer and immunostimulatory activity by conjugate of paclitaxel and non-toxic derivative of LPS for combined chemo-immunotherapy.* Pharm Res, 2012. **29**(8): p. 2294-309.

136. Kang, T., et al., *Modular Engineering of Targeted Dual-Drug Nanoassemblies for Cancer Chemoimmunotherapy.* ACS Appl Mater Interfaces, 2019. **11**(40): p. 36371-36382.
137. Wang, T., et al., *Selective targeting of tumor cells and tumor associated macrophages separately by twin-like core-shell nanoparticles for enhanced tumor-localized chemoimmunotherapy.* Nanoscale, 2019. **11**(29): p. 13934-13946.
138. Tang, J., et al., *Gd-metallofullerenol drug delivery system mediated macrophage polarization enhances the efficiency of chemotherapy.* J Control Release, 2020. **320**: p. 293-303.
139. Wei, B., et al., *Polarization of Tumor-Associated Macrophages by Nanoparticle-Loaded Escherichia coli Combined with Immunogenic Cell Death for Cancer Immunotherapy.* Nano Lett, 2021. **21**(10): p. 4231-4240.
140. Shi, Y., et al., *The EPR effect and beyond: Strategies to improve tumor targeting and cancer nanomedicine treatment efficacy.* Theranostics, 2020. **10**(17): p. 7921-7924.
141. Storm, G., et al., *Surface modification of nanoparticles to oppose uptake by the mononuclear phagocyte system.* Advanced drug delivery reviews, 1995. **17**(1): p. 31-48.
142. Sun, T., et al., *Engineered nanoparticles for drug delivery in cancer therapy.* Angew Chem Int Ed Engl, 2014. **53**(46): p. 12320-64.
143. Soeny, K., et al., *Optimizing dose regimens and fixed dose combination ratios in clinical trials.* J Biopharm Stat, 2016. **26**(3): p. 432-51.
144. Wang, L., et al., *Nanoparticle enhanced combination therapy for stem-like progenitors defined by single-cell transcriptomics in chemotherapy-resistant osteosarcoma.* Signal Transduct Target Ther, 2020. **5**(1): p. 196.
145. Li, X., et al., *Sulfatide-containing lipid perfluorooctylbromide nanoparticles as paclitaxel vehicles targeting breast carcinoma.* Int J Nanomedicine, 2014. **9**: p. 3971-85.
146. Chitkara, D., et al., *Micellar delivery of cyclopamine and gefitinib for treating pancreatic cancer.* Mol Pharm, 2012. **9**(8): p. 2350-7.
147. Shin, H.C., et al., *A 3-in-1 polymeric micelle nanocontainer for poorly water-soluble drugs.* Mol Pharm, 2011. **8**(4): p. 1257-65.
148. Alfayez, M., et al., *CPX-351 (vyxeos) in AML.* Leuk Lymphoma, 2020. **61**(2): p. 288-297.
149. Batist, G., et al., *Safety, pharmacokinetics, and efficacy of CPX-1 liposome injection in patients with advanced solid tumors.* Clin Cancer Res, 2009. **15**(2): p. 692-700.
150. Park, J., et al., *Combination delivery of TGF-beta inhibitor and IL-2 by nanoscale liposomal polymeric gels enhances tumour immunotherapy.* Nat Mater, 2012. **11**(10): p. 895-905.
151. Tang, W.L., et al., *Systemic study of solvent-assisted active loading of gambogic acid into liposomes and its formulation optimization for improved delivery.* Biomaterials, 2018. **166**: p. 13-26.
152. Tang, W.L., et al., *Development of a Rapidly Dissolvable Oral Pediatric Formulation for Mefloquine Using Liposomes.* Mol Pharm, 2017. **14**(6): p. 1969-1979.
153. Tang, W.L., et al., *A Simple and Improved Active Loading Method to Efficiently Encapsulate Staurosporine into Lipid-Based Nanoparticles for Enhanced Therapy of Multidrug Resistant Cancer.* Pharm Res, 2016. **33**(5): p. 1104-14.
154. Kolishetti, N., et al., *Engineering of self-assembled nanoparticle platform for precisely controlled combination drug therapy.* Proc Natl Acad Sci U S A, 2010. **107**(42): p. 17939-44.
155. Donahue, N.D., H. Acar, and S. Wilhelm, *Concepts of nanoparticle cellular uptake, intracellular trafficking, and kinetics in nanomedicine.* Adv Drug Deliv Rev, 2019. **143**: p. 68-96.
156. Danhier, F., *To exploit the tumor microenvironment: Since the EPR effect fails in the clinic, what is the future of nanomedicine?* Journal of Controlled Release, 2016. **244**: p. 108-121.
157. Guo, X., et al., *Advances in redox-responsive drug delivery systems of tumor microenvironment.* J Nanobiotechnology, 2018. **16**(1): p. 74.
158. Lu, B., et al., *Redox-Sensitive Hyaluronic Acid Polymer Prodrug Nanoparticles for Enhancing Intracellular Drug Self-Delivery and Targeted Cancer Therapy.* ACS Biomater Sci Eng, 2020. **6**(7): p. 4106-4115.

159. Bai, S., et al., *Smart Unimolecular Micelle-Based Polyprodrug with Dual-Redox Stimuli Response for Tumor Microenvironment: Enhanced in Vivo Delivery Efficiency and Tumor Penetration.* ACS Appl Mater Interfaces, 2019. **11**(39): p. 36130-36140.
160. Wang, X., et al., *Amphiphilic redox-sensitive NIR BODIPY nanoparticles for dual-mode imaging and photothermal therapy.* J Colloid Interface Sci, 2019. **536**: p. 208-214.
161. Petrelli, A., et al., *Redox tunable delivery systems: sweet block copolymer micelles via thiol-(bromo)maleimide conjugation.* Chem Commun (Camb), 2016. **52**(82): p. 12202-12205.
162. Nguyen, C.T., et al., *Redox-sensitive nanoparticles from amphiphilic cholesterol-based block copolymers for enhanced tumor intracellular release of doxorubicin.* Nanomedicine, 2015. **11**(8): p. 2071-82.
163. Zhang, L., et al., *Degradable disulfide core-cross-linked micelles as a drug delivery system prepared from vinyl functionalized nucleosides via the RAFT process.* Biomacromolecules, 2008. **9**(11): p. 3321-31.
164. Fang, Y., et al., *Design and Fabrication of Dual Redox Responsive Nanoparticles with Diselenide Linkage Combined Photodynamically to Effectively Enhance Gene Expression.* Int J Nanomedicine, 2020. **15**: p. 7297-7314.
165. Baldwin, A.D. and K.L. Kiick, *Reversible maleimide-thiol adducts yield glutathione-sensitive poly(ethylene glycol)-heparin hydrogels.* Polym Chem, 2013. **4**(1): p. 133-143.
166. Wu, D., et al., *Oxidation-sensitive polymeric nanocarrier-mediated cascade PDT chemotherapy for synergistic cancer therapy and potentiated checkpoint blockade immunotherapy.* Chemical Engineering Journal, 2021. **404**.
167. Rajendrakumar, S.K., et al., *Hyaluronan-Stabilized Redox-Sensitive Nanoassembly for Chemo-Gene Therapy and Dual T1/T2 MR Imaging in Drug-Resistant Breast Cancer Cells.* Mol Pharm, 2019. **16**(5): p. 2226-2234.
168. Xu, F., et al., *Targeting death receptors for drug-resistant cancer therapy: Codelivery of pTRAIL and monensin using dual-targeting and stimuli-responsive self-assembling nanocomposites.* Biomaterials, 2018. **158**: p. 56-73.
169. Yuan, C.S., et al., *Hypoxia-modulatory nanomaterials to relieve tumor hypoxic microenvironment and enhance immunotherapy: Where do we stand?* Acta Biomater, 2021. **125**: p. 1-28.
170. Kumari, R., D. Sunil, and R.S. Ningthoujam, *Hypoxia-responsive nanoparticle based drug delivery systems in cancer therapy: An up-to-date review.* J Control Release, 2020. **319**: p. 135-156.
171. Thambi, T., et al., *Hypoxia-responsive polymeric nanoparticles for tumor-targeted drug delivery.* Biomaterials, 2014. **35**(5): p. 1735-43.
172. Li, M., et al., *Enzyme-Responsive Nanoparticles for Anti-tumor Drug Delivery.* Front Chem, 2020. **8**: p. 647.
173. Xu, C.F., et al., *Transformable Nanoparticle-Enabled Synergistic Elicitation and Promotion of Immunogenic Cell Death for Triple-Negative Breast Cancer Immunotherapy.* Advanced Functional Materials, 2019. **29**(45).
174. Gonzalez, H., C. Hagerling, and Z. Werb, *Roles of the immune system in cancer: from tumor initiation to metastatic progression.* Genes & development, 2018. **32**(19-20): p. 1267-1284.
175. Gun, S.Y., et al., *Targeting immune cells for cancer therapy.* Redox biology, 2019. **25**: p. 101174.
176. Ko, H.-J., et al., *A combination of chemoimmunotherapies can efficiently break self-tolerance and induce antitumor immunity in a tolerogenic murine tumor model.* Cancer research, 2007. **67**(15): p. 7477-7486.
177. Bourquin, C., et al., *Immunotherapy with dendritic cells and CpG oligonucleotides can be combined with chemotherapy without loss of efficacy in a mouse model of colon cancer.* International journal of cancer, 2006. **118**(11): p. 2790-2795.

178. Nowak, A.K., et al., *Induction of tumor cell apoptosis in vivo increases tumor antigen cross-presentation, cross-priming rather than cross-tolerizing host tumor-specific CD8 T cells.* The Journal of Immunology, 2003. **170**(10): p. 4905-4913.
179. Wan, S., et al., *Chemotherapeutics and radiation stimulate MHC class I expression through elevated interferon-beta signaling in breast cancer cells.* PloS one, 2012. **7**(3): p. e32542.
180. Zhu, L. and L. Chen, *Progress in research on paclitaxel and tumor immunotherapy.* Cellular & molecular biology letters, 2019. **24**(1): p. 40.
181. Toschi, L., et al., *Role of gemcitabine in cancer therapy.* 2005.
182. Chen, Y., et al., *Tumor-associated macrophages: an accomplice in solid tumor progression.* Journal of biomedical science, 2019. **26**(1): p. 1-13.
183. Zheng, X., et al., *Redirecting tumor-associated macrophages to become tumoricidal effectors as a novel strategy for cancer therapy.* Oncotarget, 2017. **8**(29): p. 48436.
184. Pusztai, L., et al., *New strategies in breast cancer: immunotherapy.* Clinical Cancer Research, 2016. **22**(9): p. 2105-2110.
185. Heidarli, E., S. Dadashzadeh, and A. Haeri, *State of the art of stimuli-responsive liposomes for cancer therapy.* Iranian journal of pharmaceutical research: IJPR, 2017. **16**(4): p. 1273.
186. Zhou, Y. and J. Kopeček, *Biological rationale for the design of polymeric anti-cancer nanomedicines.* Journal of drug targeting, 2013. **21**(1): p. 1-26.
187. Darvin, P., et al., *Immune checkpoint inhibitors: recent progress and potential biomarkers.* Experimental & molecular medicine, 2018. **50**(12): p. 1-11.
188. Nakamura, K. and M.J. Smyth, *Myeloid immunosuppression and immune checkpoints in the tumor microenvironment.* Cellular & molecular immunology, 2020. **17**(1): p. 1-12.
189. Xu, M., et al., *Intratumoral delivery of IL-21 overcomes anti-Her2/Neu resistance through shifting tumor-associated macrophages from M2 to M1 phenotype.* The Journal of Immunology, 2015. **194**(10): p. 4997-5006.
190. Genard, G., S. Lucas, and C. Michiels, *Reprogramming of tumor-associated macrophages with anticancer therapies: radiotherapy versus chemo-and immunotherapies.* Frontiers in immunology, 2017. **8**: p. 828.
191. Urban-Wojciuk, Z., et al., *The role of TLRs in anti-cancer immunity and tumor rejection.* Frontiers in immunology, 2019. **10**: p. 2388.
192. Lee, H., et al., *In vivo distribution of polymeric nanoparticles at the whole-body, tumor, and cellular levels.* Pharmaceutical research, 2010. **27**(11): p. 2343-2355.
193. Li, L., J. Sun, and Z. He, *Deep penetration of nanoparticulate drug delivery systems into tumors: challenges and solutions.* Current medicinal chemistry, 2013. **20**(23): p. 2881-2891.

Chapter 2:

Drug screening and combined chemo-immunotherapeutic activity

Introduction:

Even after decades of research for the development of advanced therapeutics, breast cancer remained the leading cause of cancer-associated death among women worldwide [1]. While mortality from other cancers has shown a gradual decline over the years, breast cancer mortality significantly increased from 1990 to 2017 [2]. The development of different subtypes, including triple-negative breast cancer (TNBC), makes therapeutic prognosis even poorer [3]. It has been observed that almost all types of breast cancers exhibit a significant increase in the infiltration of macrophages in the tumor [4]. These macrophages facilitate malignancy and promote therapy evasion and metastatic progression.

Cancer was considered a disease of the neoplastic cells for a long time. Due to this, cancer cells are the lone target against which almost all the anti-cancer drugs were developed, and chemotherapy has become the first-line therapy in most cancers, including breast cancer. However, the prognosis remained poor due to high toxicity and the development of drug resistance [5]. Many advanced studies have now established that cancer is supported by a complex interaction of neoplastic and non-neoplastic cells in a strong symbiotic relationship that helps the growth and progression of the malignant cells [6]. Conversely, most of the current therapeutic strategies against cancer are one-dimensional, i.e., it is directed against only one component (cancer cells) of the complex, multi-integrant tumor ecosystem. With most of these single-pronged therapeutic strategies, tumor regression was initially seen due to the death of bulk neoplastic cells; however, these tumors can relapse with aggressive resistant phenotypes developed due to modulation by the dynamic tumor microenvironment (TME) [7-9]. For a more successful treatment, multidimensional treatment modalities targeting different components of the tumor ecosystem need to be developed.

Among different non-neoplastic cells in the TME, tumor-associated immune cells play one of the most critical tumor-promoting roles by increasing angiogenesis, modifying other stromal cells, and maintaining an immune inhibitory milieu [10]. However, if adequately activated, these immune cells can become tumoricidal, as shown by multiple studies [11]. Activating the immune cells in the TME against the cancer cells is a multistep process. Antigen-presenting cells (APC) like macrophages and dendritic cells play one of the most critical roles in this process, as, without effective antigen presentation and co-stimulatory signals, no T-cell activation would occur. The primary APCs present in the tumor are tumor-associated macrophages (TAMs) [12]. However, TAMs maintain an immunosuppressive TME by

producing a host of immune inhibitory cytokines, including CCL2, TGF-β, and IL-10, and convert effector T-cells to regulatory T-cells [13]. Re-educating these TAMs from their immunosuppressive state to the immune-stimulatory phenotype can be a potential strategy for a successful anti-tumor response [14]. Toll-like receptor (TLR) agonists are one of the most potent ligands for activating macrophages. It has been proven that TLR7/8 agonists have enhanced immune response in mouse models of breast cancer [15]. Poly-IC, a synthetic double-stranded RNA targeting TLR3, has shown promising efficacy in a Phase II clinical trial against breast cancer [16]. In the current study, different TLR agonists were initially screened to evaluate their immune stimulatory activity. Among all the TLR-agonists screened, resiquimod (RSQ) was the most effective. In multiple studies, RSQ is a TLR7 and 8 agonist, showing significant TAM activation capability [17-19]. However, though highly effective for cancer immunotherapy, no systemic formulation of RSQ is available due to its solubility and toxicity problem, limiting its use. Also, as cancer cells are responsible for nurturing the immunosuppressive TME, activating the anti-tumor immune response is challenging without tumor depletion. Chemotherapeutic drugs can be used for this purpose. Unfortunately, most chemotherapeutic drugs are immunosuppressive, hence not helpful. One significant exception is paclitaxel (PTX), a potent anti-cancer agent that has been approved for the treatment of breast, ovarian, and other cancers [20]. PTX has shown immune stimulatory activity, including increased accumulation and activation of effector T cells, dendritic cells (DCs), natural killer (NK) cells, and macrophages [21]. Henceforth, co-delivery of PTX and RSQ can be highly effective for combined chemo-immunotherapy of breast cancer. This study aimed to evaluate the *in*-vitro efficacy of PTX and RSQ combination against breast cancer in a cancer cell–macrophage co-culture system using a 2D and 3D multi-cellular breast cancer spheroid model.

Materials and Methods

Chemicals and reagents:

PTX was received as a gift sample from INTAS Pharmaceuticals Ltd, and RSQ was purchased from TCI, India. Dimethyl sulfoxide (DMSO) and methanol were procured from Merck, India. 3-(4,5-dimethylthiazol-2yl)-2,5-diphenyltetrazolium bromide (MTT) were purchased from Sigma-Aldrich. cDNA synthesis kit and SYBR green qPCR kit were purchased from Bio-Rad. All other chemical reagents used were of A.R. grade.

Cell culture:

4T1 (a breast cancer cell line derived from the mammary gland tissue of a mouse BALB/c strain) and RAW 264.7 (mouse monocyte-macrophage cell line) were separately cultured in Dulbecco's Modified Eagle Medium (DMEM), supplemented with 10% fetal bovine serum and 50 units/mL penicillin, and 50 mg/mL streptomycin at 37 ◦C, 5%CO_2 in a humidified atmosphere. Cells were sub cultured at 90% confluency using Trypsin–EDTA solution (0.05%) for cell detachment.

Cancer-macrophage co-culture and complex spheroid model:

To better mimic the *in-vivo* tumor conditions, 4T1+RAW 264.7 spheroids were prepared. Briefly, cells (7,500 4T1 cells and 2,500 RAW 264.7) at 10,000 cells / 10µl (in 0.2% methyl cellulose-containing cell culture medium) were placed as hanging drops on the lid of the cell culture Petri dish. The hanging drops were humidified by putting PBS in the Petri dish's base to prevent the spheroid's drying. After that, the hanging drops were transferred to 1% agarose-coated round bottom 96 well plates with 200 µl cell culture medium and incubated for 24 h, yielding the 4T1+RAW 264.7 spheroids.

For RNA isolation from RAW 246.7 cells after co-culture with 4T1, only 4T1 spheroids were made and co-cultured with RAW 246.7. Briefly, 4T1 cells at 10,000 cells / 10µl (0.2% methyl cellulose-containing cell culture medium) were placed as hanging drops on the lid of the cell culture Petri dish. Spheroids were humidified by putting PBS in a Petri dish. After 24 h of incubation, spheroids were transferred into 1% agarose-coated wells (in 24 well plates) with 1 mL cell culture medium. Then RAW 246.7 cells at a density of 10,000 cells were plated on a transwell (0.4 µm, polycarbonate membrane) inserted in 4T1 spheroids (5 spheroids per well) containing well.

Cytotoxicity assay (2D and 3D):

For cell viability assay of 2D culture, 4T1/RAW cells were seeded at 5000 cells/ well density in a 96-well plate. After 24 h of incubation, cells were treated with drug solutions (0.5-500 nM PTX, 0.1-1µM RSQ in the initial screening, and 5nM PTX and 1µM RSQ in further studies) and incubated for 72 h at 37 °C with 5% CO_2. No drug treatment was given in the control cells, and the same amount of complete medium was added. After 72h of incubation, cells were treated with 200µl of 1 mg/mL MTT solution dissolved in a complete medium. After 4 h of incubation with MTT, the medium was replaced with 200 µl of DMSO to dissolve the formazan

crystal formed by the viable cells. Optical density at 570 nm was measured by removing background absorbance at 630 nm. Cell viability was calculated using the following formula:

Cell Viability (%) = (mean absorbance value of drug-treated cells)/ (mean absorbance value of control) × 100

For cell viability assay of 3D culture, treatment was given for 72 h with free drug and encapsulated drugs equivalent to 10nM PTX and 2μM RSQ. Further, the spheroids were collected into 1.5 mL centrifuge tubes with medium and centrifuged for 10 min at 200×g. The supernatant was removed and replaced with a medium containing MTT (1mg/mL). After 4 h of incubation, MTT was replaced with DMSO (500 μl) to dissolve the formazan crystals formed by the viable cells. Then, cell viability was calculated, as mentioned earlier.

Screening of TLR agonists:

Initially, different TLR-7/8 agonists, i.e., Imiquimod, Resiquimod, and Pidotimod, were screened for their toxicity effects against macrophage cell lines (Raw 264.7 cells) at different doses by using MTT assay and the effective M1 macrophage polarization was also evaluated with all the drugs selected by checking M1 macrophage marker- TNF-alpha expression using qRT-PCR.

Apoptosis assay:

PI/Annexin-FITC staining by flow cytometry was performed to measure apoptosis. This was achieved by using 2D co-culture conditioned media, where PTX(5nM), RSQ (1 μM), PTX (5nM) + RSQ (1 μM) were treated with RAW 264.7 cells, then the supernatant was collected and added to a plate seeded with 4T1 tumor cells for 24h. After 72h treatment, cells were trypsinized and washed twice with phosphate-buffered saline. Then, cells were suspended in 500 μl of 1× binding buffer (Annexin Binding Bufer (5X) for flow cytometry, Thermo Fisher Scientific). After that, the cells were stained with four μl Annexin V-FITC (Annexin V-FITC, Invitrogen™) and ten μl of PI (propidium iodide solution, FluoroPure™ Grade, Invitrogen™). The samples were incubated for 15 minutes at room temperature (25 °C) in dark conditions. The cytometric analysis was performed in a flow cytometer (CytoFLEX, Beckman Coulter), and the data were analyzed by CytExpert software. % Apoptosis was calculated over all viable cells and after subtracting the autofluorescence of cells. The results were represented as mean±SEM values.

Tumor-specific cell death

a) Live-Dead Staining:

We have used Transwell (Quasi 3D system) to identify the tumor-specific cell death. Here, we have made 4T1 spheroids and added them in the lower chamber of the Transwell and Raw macrophages (2D) on the transwell membrane in the top chamber. After 72h of treatment periods, we stained both the 4T1 spheroids and 2D macrophages using Annexin (10 µg/mL) and Propidium Iodide (PI- 1µg/mL) diluted with PBS. Annexin labels all the nuclei in blue of all the viable cells, and PI labels the nuclei of dead cells in red. The staining was attained after incubating it for 15 minutes in the dark at 37°C, followed by microscopy analysis.

b) Luciferin tagged 4T1 cells (LUC2-4T1):

We have used luciferin-tagged 4T1 cells to confirm further tumor-specific cell death to check the fluorescence intensity after treating the LUC2-4T1 cells with luciferin-D. The experiment was done in 2D conditioned media and 3D complex spheroid (4T1+RAW 264.7 cells). In 2D conditioned media, RAW 264.7 cells were initially treated for 24h. The treated media was added to luc-2-4T1 cells and incubated for 24h, followed by luciferase treatment (4µg/ml) for 1h. The cells were washed with PBS, then microscopic images were captured using a fluorescent microscope. The same procedure was followed for the 3D complex spheroid after 24 hours of treatment.

Intracellular reactive oxygen species (ROS) generation by DCFDA assay

Cellular ROS in 2D cells and 3D spheroids were analyzed by DCFDA assay. The ROS present in the cells can convert DCFDA into a highly fluorescent compound 2′, 7′–dichlorofluorescein (DCF). The amount of ROS can be quantified by measuring the fluorescence intensity of DCF. 2D cells and 3D tumor spheroids were treated with free drugs and combination for 24 h. Then, the drug-containing media was removed, followed by DCFDA incubation (20 µM) for 15 min. After that, fluorescent images were captured through an inverted fluorescence microscope (ZEISS, Axio Vert.A1) at 10X magnification.

Spheroid invasion assay:

3D invasion assay was performed using 24-well plates with Transwell inserts (Corning, New York, USA). Briefly, 24 well inserts were pre-coated with Matrigel (BD Biosciences, New

Jersey, USA), and 4T1+RAW 264.7 cell complex tumor spheroids were made and allowed to grow in the top chambers of the transwell. After that, the spheroids were treated with drugs (PTX, RSQ, PTX+RSQ). Parallely, 900 µL DMEM complete media was added to the transwell's lower chamber and kept for incubation for 24h at 37°C. After treatment, the cells on the transwell membrane were removed using a cotton swab. After that, the cells penetrated the membrane and were fixed using 4% ice-cold methanol and staining with 0.1% crystal violet. Microscopic images of the migrated cells were captured using an inverted microscope, and the number of migrated cells was counted using ImageJ software.

Macrophage marker expression analysis:

Total RNA was isolated using a TRI reagent to synthesize cDNA using a cDNA synthesis kit. Gene-specific primers were used for the amplification of templates. The qRT-PCR reactions were performed using the SYBR Green supermix, and the data was normalized against GAPDH as a housekeeping gene. The primers used for qRT-PCR are GAPDH F(5'-3') ACCCAGAAGACTGTGGATGG, R (3'-5') TCTAGACGGCAGGTCAGGTC, TNF-α F(5'-3') GCCTCTTCTCATTCCTGCTTG, R (3'-5') CTGATGAGAGGGAGGCCATT, CD86 F(5'-3') ACGATGGACCCCAGATGCACCA, R (3'-5') GCGTCTCCACGGAAACAGCA, TGF-β F(5'-3') CCTGTCCAAACTAAGGC, R (3'-5') GGTTTTCTCATAGATGGCG,IL-10 F(5'-3')CCCTGGGTGAGAAGCTGAAG,R (3'-5') CACTGCCTTGCTCTTATTTTCACA. qRT-PCR studies were performed on CFX Thermal Cycler (Bio-Rad). The 2(-Delta-Delta C(T)) method analyzed the relative RNA expression.

Statistical analysis

The graphs and data were analyzed using Graph Pad Prism software version 7.0. The significance level was indicated by **, where < 0.05 in all the figures. One-way ANOVA was used when ≥ 2 groups were compared to the same control, and post hoc Tukey's test was performed to compare the means of each group with every other group. Two-way ANOVA was used for the studies, where two or more groups were compared with the control group with more than two variables. Post-hoc Bonferroni, multiple comparison tests were used to compare the means of each group. Data were represented as mean ± SD.

Results and Discussion:

Screening of TLR-agonists for macrophage stimulating efficacy:

Initial screening was carried out using imiquimod (IMQ), resiquimod (RSQ), and pidotimod (PTM)to find out their macrophage polarization efficacy against RAW 264.7 cell line (5,000 cells/ well). They all exhibited more than 100% macrophage viability, indicating no cellular toxicity at the dose range tested (0.1µM to 10 µM) (**Figure 2.1A**). Next, macrophage stimulatory potency was evaluated by analyzing TNF-α expression, a major anti-cancer macrophage activation marker. After treating RAW 264.7 cells (50,000 cells/well in a 6-well plate) with the drugs for 12 h, TNF-α expression was studied using qRT-PCR. Among all the TLR-agonists tested, RSQ exhibited the highest potency. Figure 2.1B shows a highly significant (p<0.05), 16±3.4-fold increased TNF-α expression was observed with RSQ treatment at 1 µM concentration. In contrast, IMQ exhibited a moderated increase (3±0.32-fold), and with PTX, only a basal level of expression was observed (0.3±-0.2 fold). Even at a lower concentration of 500 nM, RSQ exhibited an 8±1.8-fold increase in TNF-α expression, signifying greater potency of RSQ. Based on these observations, RSQ was selected as the candidate TLR-agonist to be used with PTX for combined chemo-immunotherapy.

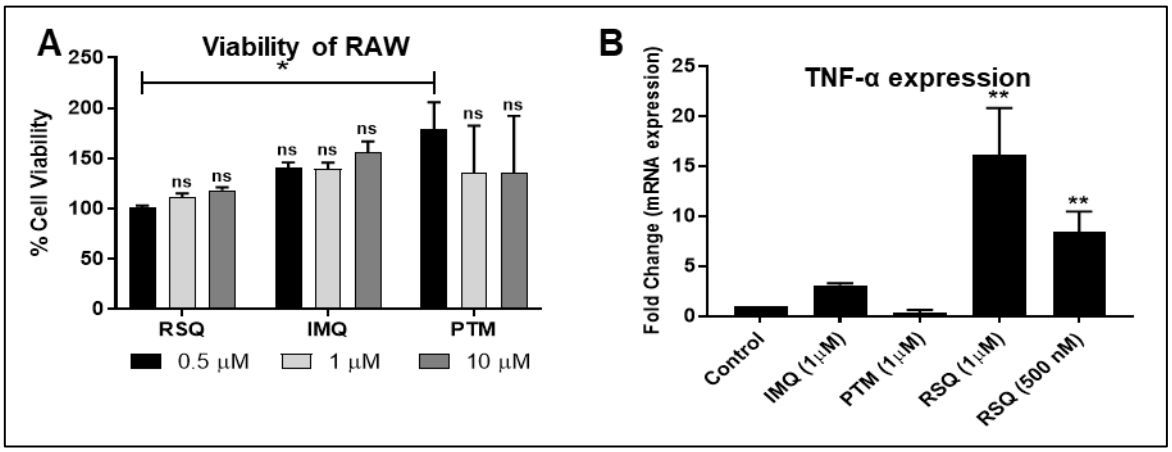

Figure 2.1: A: Evaluation of the cytotoxicity of different TLR agonists on RAW 264.7 cells. B: Evaluation of the macrophage stimulatory activity of different TLR agonists. ** indicates p< 0.05.

Evaluation of combined chemo-immunotherapeutic efficacy:

Immunotherapy can be combined with chemotherapy to improve its efficacy. PTX was selected as a model drug for combined chemo-immunotherapy and RSQ as the immune modulator. To determine whether RSQ treatment can directly influence the activity of PTX, 4T1 cancer cell viability was evaluated when treated with PTX alone and PTX+RSQ combination. As shown

in **Figure 2.2A**, dose-dependent cytotoxicity was observed for PTX treatment (in 0.5 to 500 nM range); however, the inclusion of RSQ at 1 μM dose did not significantly influence the cytotoxic potential of PTX, indicating no synergistic or additive effect of this drug combination against cancer cell alone. Next, to find out the chemo-immunotherapeutic efficacy of the PTX+RSQ combination, initially, RAW 264.7cells were treated with PTX alone (5 nM) or RSQ alone (1 μM) or PTX+RSQ combination for 24h. After 24h, the conditioned medium was added to 4T1 cells and incubated for 48h. 4T1 cells directly treated with PTX alone (5 nM), RSQ alone (1 μM), or PTX+RSQ combination for 48h were taken as controls to compare the efficacy of RAW 264.7 cells conditioned medium with drug treatments. Direct treatment on the 4T1 cells was found to have low cytotoxicity, with RSQ exhibiting no cytotoxicity, and PTX and PTX+RSQ showed 90±2.3% and 72±3.4% cell viability, respectively (**Figure 2.2A**). Treatment of the 4T1 cells with the RAW 264.7 conditioned medium with PTX or RSQ alone exhibited similar cytotoxicity (85±1.6% and 77±1.4%viability, respectively). Interestingly, treatment of the 4T1 cells with RAW 267.4 conditioned medium with PTX+RSQ combination exhibited significantly increased cancer cell death (49±1.2% viability, **Figure 2.2B**). This data signifies the improved chemo-immunotherapeutic efficacy of the PTX+RSQ combination.

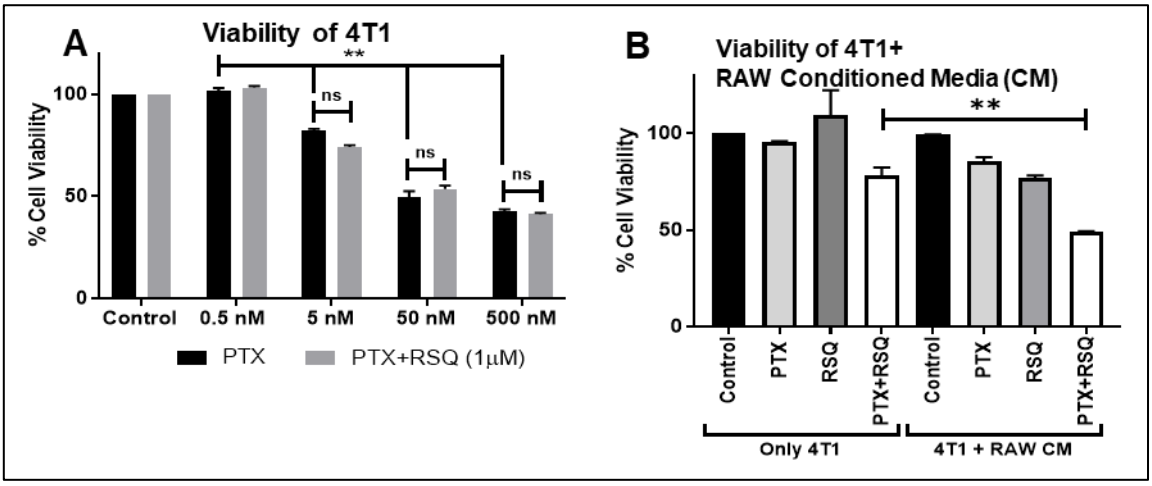

Figure 2.2: A: Evaluation of the effect of RSQ (1μM dose) treatment on the cytotoxic activity of PTX on 4T1 tumor cells. B: Analysis of the combined efficacy of PTX+RSQ treatment in a quasi-coculture experiment using 4T1 tumor cells and conditioned media of RAW 264.7 macrophages. ** indicates $p< 0.05$.

Next, the immunomodulatory potential of this drug combination was evaluated. 4T1 cells (50,000 cells/ well in a 6 well plate) were treated with PTX alone (5 nM), RSQ alone (1 μM), or PTX+RSQ combination for 24h, and the conditioned medium was transferred to RAW 264.7 cells. After 24h incubation with the conditioned medium, the expression of M1 (TNF-α, CD86) and M2 (IL10, CD206) markers were analyzed using qRT-PCR. Treatment of RAW264.7 with the native 4T1 conditioned medium was found to polarize the RAW 264.7 cells to an M2

phenotype with a significant increase in TGF-β(13±2.4-fold) and IL10 (8±1.3-fold) expression. In contrast, expression of M1 markers TNF-α and CD86 was at a basal level. However, treatment of the 4T1 cells with both PTX and RSQ alone abolished the M2 polarizing activity of the conditioned medium and restored the macrophages. Remarkably, treatment with PTX+RSQ combination to the 4T1 cancer cells normalized the M2 marker expression to the basal level and significantly increased the M1 marker TNF-α (9±0.5-fold) and CD86 (3±0.4-fold), indicating polarization of the macrophages to the immune stimulatory M1 phenotype.

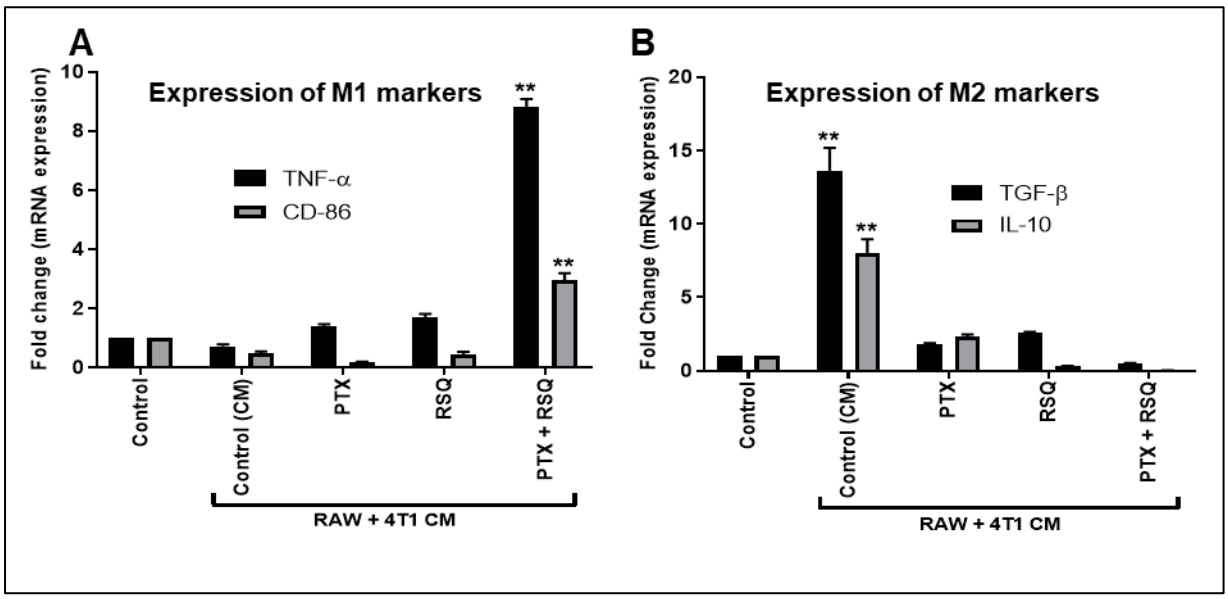

Figure 2.3: A: Analysis of the expression of M1 markers by RAW 264.7 macrophages exposed to conditioned media of 4T1 tumor cells treated with different drugs. B: Analysis of the expression of M2 markers by RAW 264.7 macrophages exposed to conditioned media of 4T1 tumor cells treated with different drugs. ** indicates $p < 0.05$.

Quasi-3D and 3D complex spheroid model:

Next, the cytotoxic potency of the drug combination against the co-culture of the 4T1 cancer cells and RAW 264.7 macrophage cells was evaluated. Initially, a complex cancer spheroid model, prepared with 4T1 and RAW 264.7 cells, was developed to mimic the TME in an *in-vitro* system (**Figure 2.4A**). These spheroids were treated with free drugs and combination at the dose of 10nM PTX and 2μM RSQ for 72 h. The dose of drugs was doubled for cancer spheroid treatment compared to monolayer culture because the cancer spheroids exhibit more resistance [22]. Cell viability was measured by MTT assay. As depicted in **Figure 2.4B**, treatment with PTX and RSQ alone resulted in marginal cell death, with 76±2.3% and 81±3.8% cell viability with PTX and RSQ, respectively. However, the drug combination group observed a significantly increased cell death. Cell viability was found to be 51±2.6% with PTX+RSQ

combination treatment. This data indicated that treatment with the drug combination could have synergistic efficacy.

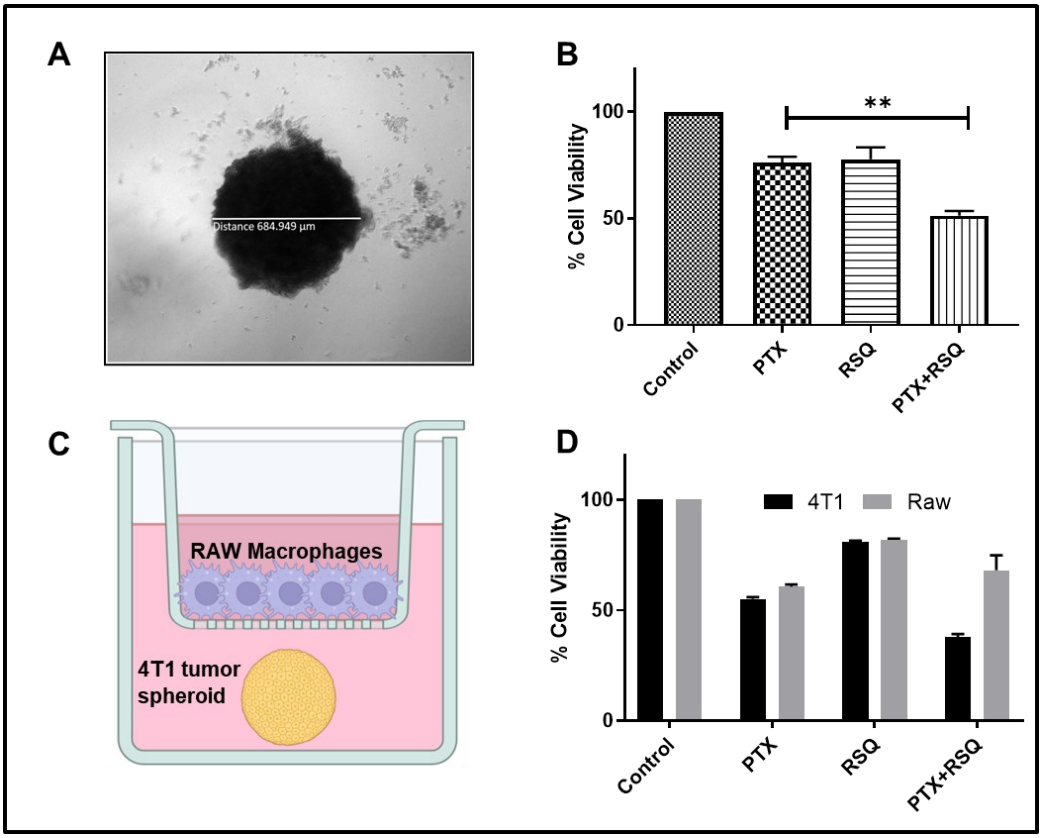

Figure 2.4: A. Microscopic image of a complex spheroid made with 4T1 tumor and RAW264.7 macrophage cells. B. Cytotoxic activity of the free drugs and combination against the complex spheroid model. C. Designing a quasi-3D-coculture system to analyze differential death of tumor cells and macrophages. D. Analysis of cell viability of 4T1 tumor and RAW 264.7 macrophages in the quasi-3D co-culture experiment. ** indicates $p<0.05$.

The mixed cancer spheroid model can mimic the actual in-vivo cancer more consistently. However, analyzing the death of individual cell types is challenging in that model. A transwell-based co-culture experiment was performed to understand the impact of the combination treatment on both 4T1 cancer cells and the RAW macrophages individually. In this experiment, cancer spheroids were made using 4T1 cancer cells, which were kept in the lower chamber of the trans-well, whereas RAW 264.7 cells were plated in the upper chamber (**Figure 2.4C**). Drug treatment was given in the lower chamber; however, as the RAW 264.7 cells are exposed in the same medium, they are equally exposed to the drug. Corroborating the observation in the experiment using the mixed cancer spheroid model, increased cancer cell death was observed with the PTX+RSQ combination treatment (38±1.5% viability). The death of the macrophages was relatively low (68±5.3% viability) (**Figure 2.4D**), supporting the observation in the previous experiment with a mixed cancer spheroid model.

Apoptosis assay:

After understanding the improved cytotoxic behavior of the combination, we wanted to check the contribution of apoptotic cell death with the PTX +RSQ combination. Here, we analyzed apoptosis using flow cytometry with Annexin V-FITC/PI staining. The treatment groups were PTX, RSQ, and PTX +RSQ combination. In 2D, quasi 3D (Transwell), and 3D, we have observed a slight increase in apoptotic cell death with the combination PTX (4T1-9folds, RAW-0.1folds, 3D Complex-15folds) and RSQ (4T1-2 folds, RAW-0.2 folds, 3D Complex-8folds). However, there is a significant increase in the percentage of the apoptotic cells (Annexin V+PI-positive cells) with PTX +RSQ (4T1-12 folds, RAW-8 folds, 3D Complex-24folds). Based on the results, we can say that PTX +RSQ combination cytotoxicity is mediated by apoptosis death concerning cancer cells. However, there is almost similar cell death (<10%) with macrophages even with the PTX+RSQ combination, and there is a drastic increase in tumor cell death in 3D compared to the 2D system. The improved cytotoxic behavior of the PTX +RSQ combination in the MTT assay complemented this data.

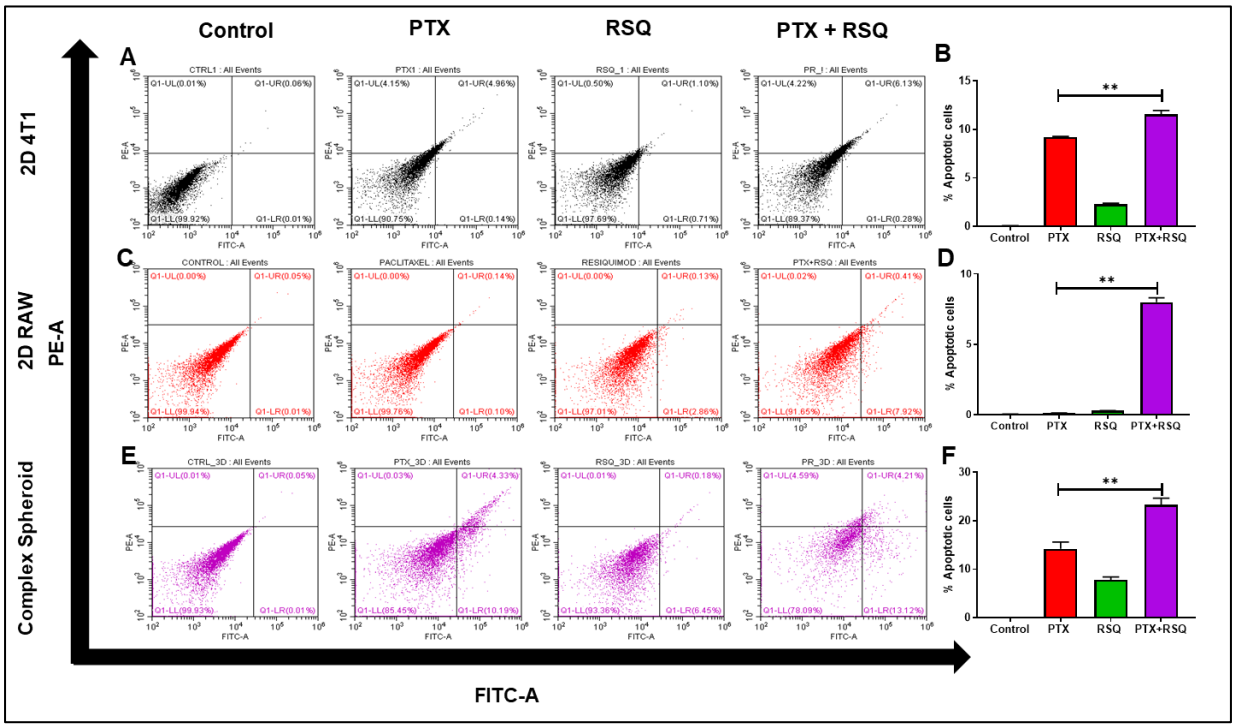

Figure 2.5: Apoptosis assay in A) 4T1 cells, B) Quantification of % apoptotic cells in 4T1 cells, C) RAW 264.7 cells, D) Quantification of % apoptotic cells in RAW 264.7 cells, E) 4T1+ RAW complex spheroid treated with different groups, F) Quantification of % apoptotic cells in 3D Complex spheroid (Control, PTX, RSQ, and PTX +RSQ)

Live/dead staining:

We conducted live-dead staining experiments to validate the tumor-specific cell death observed in our cytotoxicity data. In this study, we formed spheroids composed of 4T1 tumor cells and allowed them to grow in the lower chamber of a Transwell system. At the same time, 2D macrophages were cultured on the polycarbonate membrane in the upper chamber. We exposed all experimental groups, including those treated with PTX, RSQ, a combination of PTX and RSQ, for 72 hours, followed by the fluorescent images to assess changes in the morphology of both 4T1 spheroids and 2D macrophages.

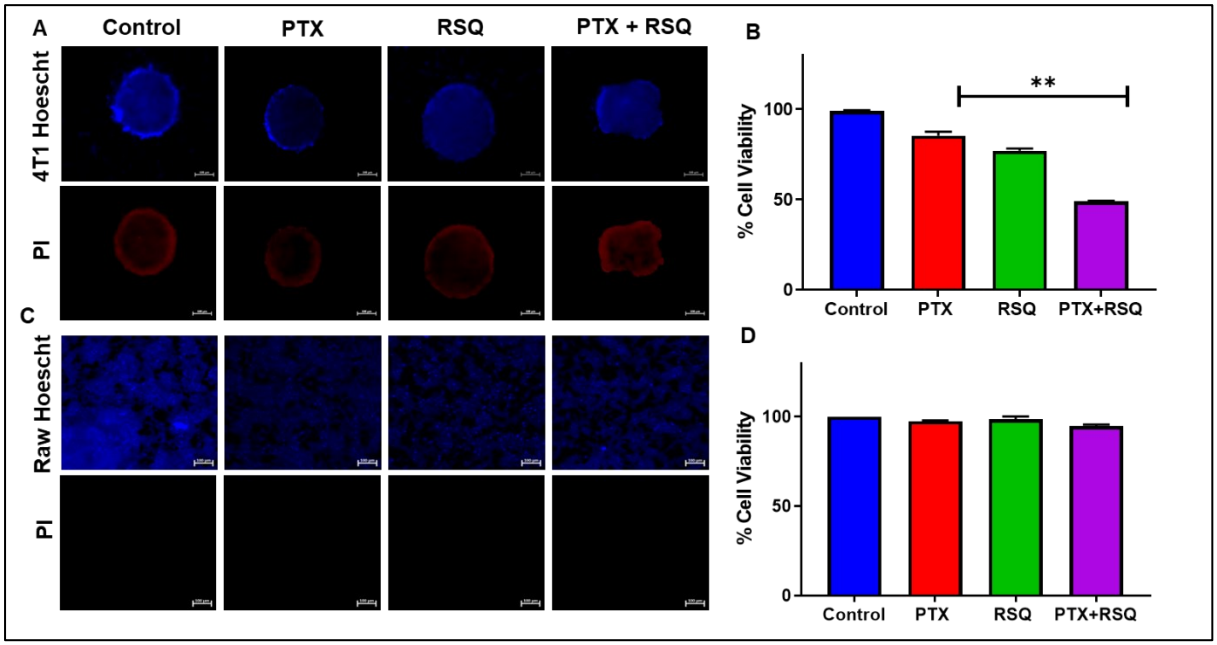

Figure 2.6: Live/dead staining in transwell system of 4T1 tumor and 2D raw 264.7 cells. A) Representative fluorescent images of 4T1 tumor spheroids used to analyze cell death stained with Propidium iodide (PI) and Hoechst 33342 as outlined. B) %Cell Viability with 4T1 spheroids. C) As outlined, Representative fluorescent images of RAW 264.7 cells were used to analyze cell death stained with Propidium iodide (PI) and Hoechst 33342. D) %Cell Viability with RAW 264.7 cells. Scale bars indicate100 µm

In **Figure 2.6A&B**, our observations reveal distinctive alterations after the 72-hour treatment period. Notably, the spheroids in the control and free drug groups, when given alone, maintained their shape and stability throughout the experiment. In contrast to the combination PTX+RSQ treatment, we observed significant spheroid shape deformity. This deformation is likely attributed to the cytotoxic effects induced by the treatment group on the spheroids. The free drugs alone displayed lower PI staining than the PTX+RSQ combination, indicating higher cytotoxicity and efficacy within tumor spheroids. Regarding macrophages, no cell death is observed with null PI staining in all the treatment groups, showing that the treatment groups are non-cytotoxic to macrophages (**Figure 2.6C&D**).

After observing the cancer cell death using live-dead staining, we have further used luc-2 tagged 4T1 tumor cells to confirm the tumor-specific cell death using luciferin expression. Here, we have performed this experiment in both 2D conditioned media and 3D complex spheroid, where in 2D conditioned media, we have observed that there is an increase in cell death of tumor cells when RAW 264.7 conditioned media was added along with decreased luciferase expression when treated with PTX+RSQ when compared to free drug treatment groups alone. Regarding 3D complex spheroid, luciferase expression was diminished to almost 50% in the PTX+RSQ group compared to control group signifying improved tumor-specific cell death. (**Figure 2.7**)

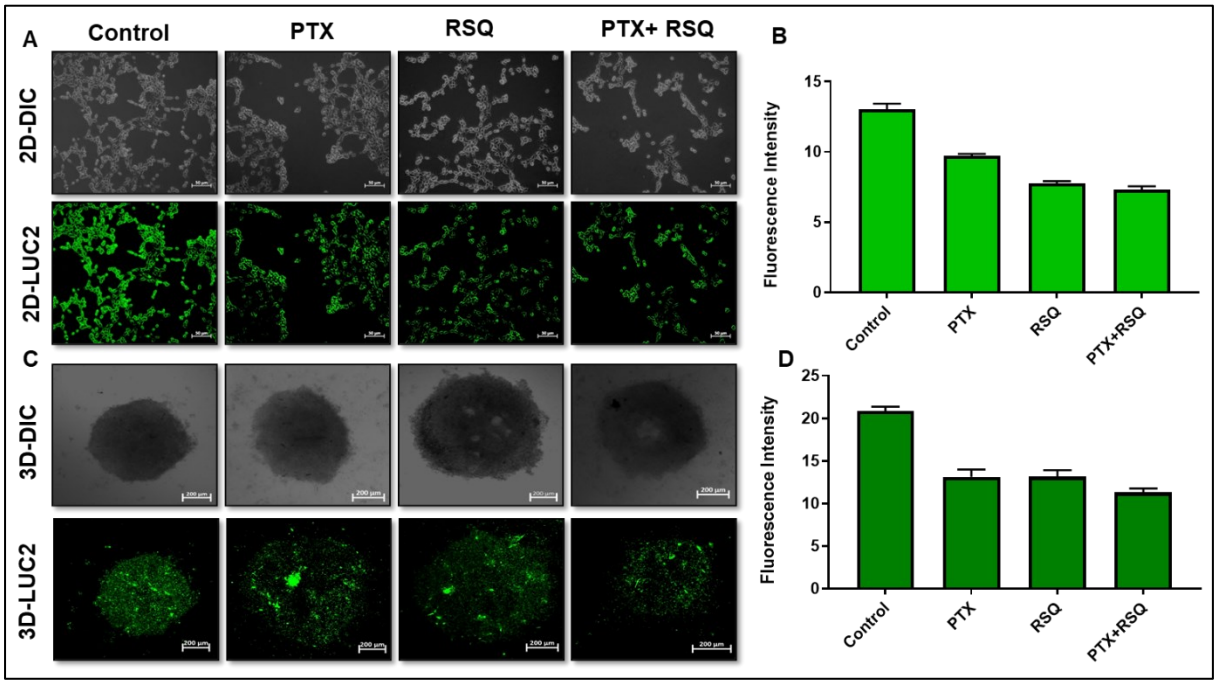

Figure 2.7: A) 2D Luciferin tagged 4T1 cell microscopy images when treated with conditioned media of RAW 264.7 cells and treatment groups, B) Quantification of fluorescence intensity in 2D CM. C) 3D LUC-2 4T1+RAW 264.7 complex spheroid expressing luciferin fluorescence after treatment for 72h. D) Quantification of fluorescence intensity in 3D complex spheroid.

Reactive oxygen species (ROS) generation:

After confirming the improved cytotoxic cell death of the drug combination, we studied ROS generation's role in tumor cell death. We have checked ROS generation capability in 4T1, RAW 264.7 cells alone, 2D conditioned media, and 3D complex spheroid system. Initially, with 2D RAW 264.7 cells, it is visible that there is not much ROS generation with PTX RSQ alone, but there is a bit of an increase in DCFDA fluorescence (1.5 folds) with the PTX+RSQ combination. When treated with 4T1 tumor cells alone, though there is similar fluorescence with the PTX group, there is an increased DCFDA fluorescence of 2folds with RSQ and 3folds

increase with PTX+RSQ treatment. For 2D conditioned media, Initially, we treated the macrophages for 24h and then transferred the media to previously seeded 4T1 cells for 24h. After that, DCFDA was added and incubated for 15min followed by imaging using fluorescent microscopy at 10X magnification in an inverted fluorescent microscope (ZEISS Axio Vert. A1). For complex spheroids, tumor-macrophage co-cultured 3D spheroids were treated with PTX (10nM) and RSQ (2µM) and with the same dose in PTX+RSQ combination for 24h, followed by DCFDA treatment for 15min and microscopy.

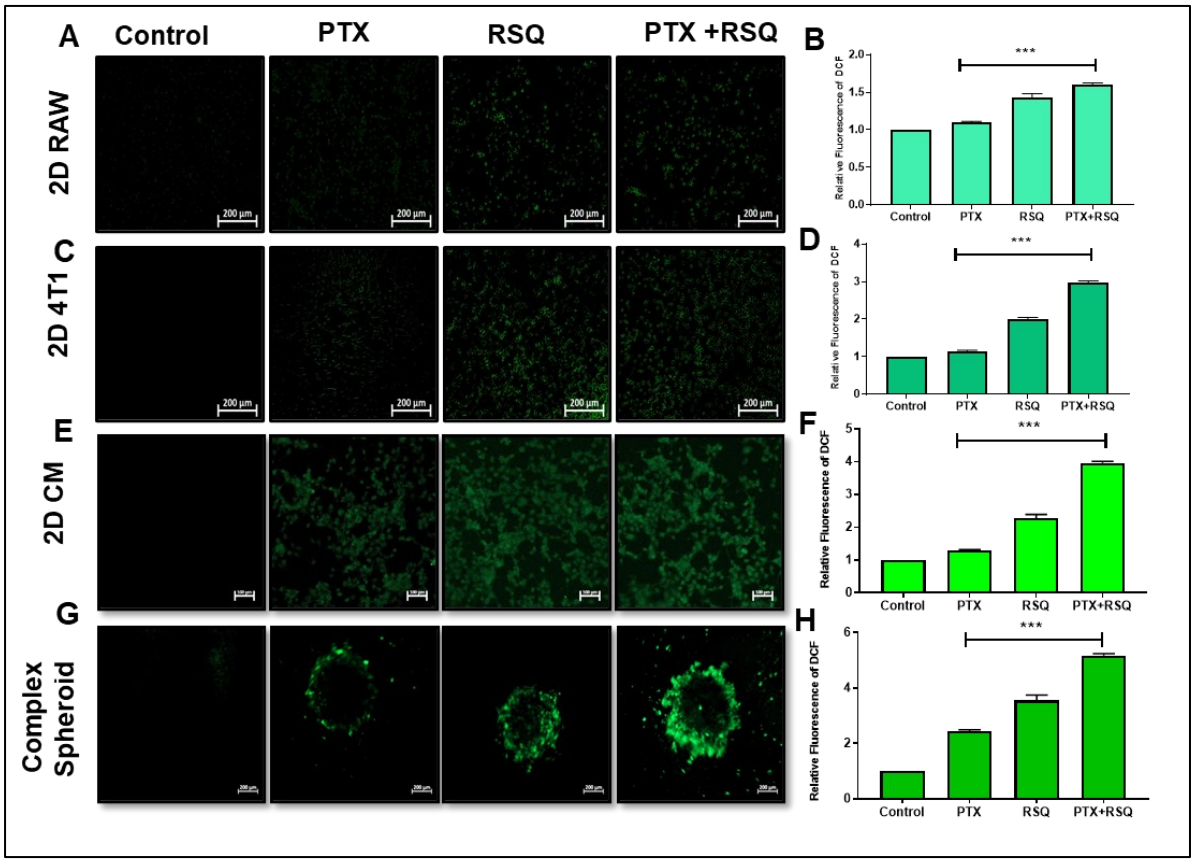

Figure 2.8: Induction of ROS in PTX+RSQ treatment. Fluorescent microscopic images of DCFDA stained A)Microscopic images of DCFDA treated RAW 264.7 Cells, B) Quantification of DCF fluorescence in RAW 264.7 cells, C) Microscopic images of DCFDA treated 4T1 Cells, D) Quantification of DCF fluorescence in 4T1 cells E) Microscopic images of DCFDA treated 2D conditioned media of RAW added to 4T1 cells, F) Quantification of DCF fluorescence in 4T1 CM cells and G) Microscopic images of DCFDA treated 4T1+RAW 3D complex spheroids. H) Quantification of DCF fluorescence in 3D complex spheroids (Treatment groups-Control, PTX, RSQ, PTX+RSQ). The scale bar in the image indicates 50 µm.

We have observed an increase in ROS generation with the PTX +RSQ combination (4folds) when compared to PTX (1.1 folds) and RSQ (2.5 folds) alone in 2D CM and in 3D complex spheroid systems as well we have also observed a similar pattern an increase in ROS generation with the PTX +RSQ combination (5.8folds) when compared to PTX (2.2 folds) and RSQ (3.5 folds) alone which proves that improved cytotoxicity of ROS might be because of ROS as well

(**Figure 2.8**). It was also evident that M1 macrophage activation leads to ROS activation, primarily because of the high production of TNF-α [23, 24] [25]. From this, it is evident that enhanced cytotoxicity and improved M1 macrophage stimulation (Immunostimulatory macrophage activation) of the PTX +RSQ combination might also be because of improved ROS generation.

Spheroid invasion assay:

To check the metastatic property of the tumor cells, we have performed a spheroid migration assay using a transwell system, using tumor-macrophage complex spheroid. We have observed that though there is a decrease in migration ability with PTX and RSQ alone, there is a significant decrease in the number of cells migrated to 50% with the PTX+RSQ combination when compared to control, proving the potential to inhibit the migration ability of the tumor cells effectively, indicating it can reduce metastasis as well (**Figure 2.9A&B**).

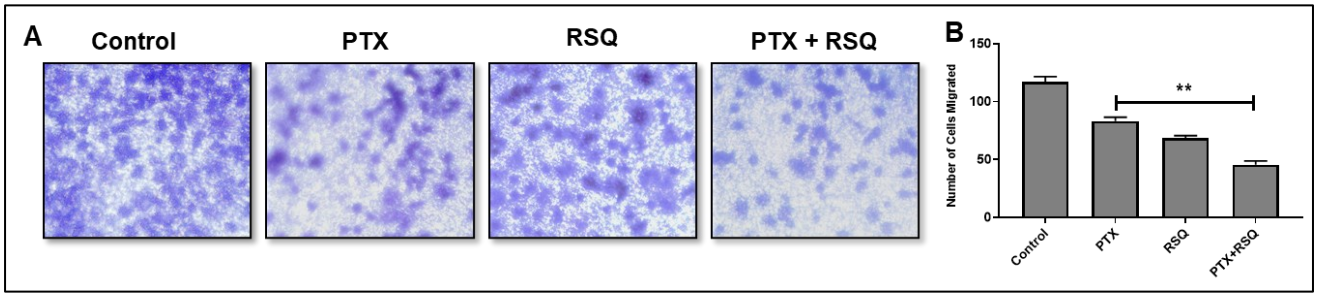

Figure 2.9: A) Microscopy images of cell migration assay of 4T1+RAW 264.7 complex 3D spheroids after 24 h treatment in 24-well transwell inserts with crystal violet staining. B) Quantification of the number of cells migrated in the migration assay.

Conclusion:

In the current study, initial screening of different TLR-agonists was performed. The most efficacious one, RSQ, was selected to be combined with PTX. The current study suggests that the PTX and RSQ combination has potent *in-vitro* chemo-immunotherapeutic activity through M1 macrophage polarization and tumor-specific cell death in 2D and 3D complex spheroid models. PTX and RSQ combination was also found to show improved efficacy by modulating ROS. Hence, this strategy can be developed as a therapeutic approach for chemo-immunotherapy of cancer in the future.

References:

1. Azamjah, N., Y. Soltan-Zadeh, and F. Zayeri, *Global Trend of Breast Cancer Mortality Rate: A 25-Year Study.* Asian Pac J Cancer Prev, 2019. **20**(7): p. 2015-2020.
2. Lima, S.M., R.D. Kehm, and M.B. Terry, *Global breast cancer incidence and mortality trends by region, age-groups, and fertility patterns.* EClinicalMedicine, 2021. **38**: p. 100985.
3. Hudis, C.A. and L. Gianni, *Triple-negative breast cancer: an unmet medical need.* Oncologist, 2011. **16 Suppl 1**: p. 1-11.
4. Williams, C.B., E.S. Yeh, and A.C. Soloff, *Tumor-associated macrophages: unwitting accomplices in breast cancer malignancy.* NPJ Breast Cancer, 2016. **2**.
5. Waks, A.G. and E.P. Winer, *Breast Cancer Treatment: A Review.* JAMA, 2019. **321**(3): p. 288-300.
6. Roy, A. and S.D. Li, *Modifying the tumor microenvironment using nanoparticle therapeutics.* Wiley Interdiscip Rev Nanomed Nanobiotechnol, 2016. **8**(6): p. 891-908.
7. Seebacher, N.A., et al., *Tumour Microenvironment Stress Promotes the Development of Drug Resistance.* Antioxidants (Basel), 2021. **10**(11).
8. Wu, P., et al., *Adaptive Mechanisms of Tumor Therapy Resistance Driven by Tumor Microenvironment.* Front Cell Dev Biol, 2021. **9**: p. 641469.
9. Kaemmerer, E., D. Loessner, and V.M. Avery, *Addressing the tumour microenvironment in early drug discovery: a strategy to overcome drug resistance and identify novel targets for cancer therapy.* Drug Discov Today, 2021. **26**(3): p. 663-676.
10. Gonzalez, H., C. Hagerling, and Z. Werb, *Roles of the immune system in cancer: from tumor initiation to metastatic progression.* Genes Dev, 2018. **32**(19-20): p. 1267-1284.
11. Gun, S.Y., et al., *Targeting immune cells for cancer therapy.* Redox Biol, 2019. **25**: p. 101174.
12. Petty, A.J. and Y. Yang, *Tumor-associated macrophages: implications in cancer immunotherapy.* Immunotherapy, 2017. **9**(3): p. 289-302.
13. Chen, Y., et al., *Tumor-associated macrophages: an accomplice in solid tumor progression.* J Biomed Sci, 2019. **26**(1): p. 78.
14. Zheng, X., et al., *Redirecting tumor-associated macrophages to become tumoricidal effectors as a novel strategy for cancer therapy.* Oncotarget, 2017. **8**(29): p. 48436-48452.
15. Yin, T., S. He, and Y. Wang, *Toll-like receptor 7/8 agonist, R848, exhibits antitumoral effects in a breast cancer model.* Mol Med Rep, 2015. **12**(3): p. 3515-3520.
16. Wang, S., et al., *Landscape and perspectives of macrophage -targeted cancer therapy in clinical trials.* Mol Ther Oncolytics, 2022. **24**: p. 799-813.
17. Zhang, H., et al., *Development of thermosensitive resiquimod-loaded liposomes for enhanced cancer immunotherapy.* J Control Release, 2021. **330**: p. 1080-1094.
18. Figueiredo, P., et al., *Peptide-guided resiquimod-loaded lignin nanoparticles convert tumor-associated macrophages from M2 to M1 phenotype for enhanced chemotherapy.* Acta Biomater, 2021. **133**: p. 231-243.
19. Chen, P.M., et al., *Modulation of tumor microenvironment using a TLR-7/8 agonist-loaded nanoparticle system that exerts low-temperature hyperthermia and immunotherapy for in situ cancer vaccination.* Biomaterials, 2020. **230**: p. 119629.
20. Long, H.J., *Paclitaxel (Taxol): a novel anticancer chemotherapeutic drug.* Mayo Clin Proc, 1994. **69**(4): p. 341-5.
21. Zhu, L. and L. Chen, *Progress in research on paclitaxel and tumor immunotherapy.* Cell Mol Biol Lett, 2019. **24**: p. 40.
22. Barrera-Rodriguez, R. and J.M. Fuentes, *Multidrug resistance characterization in multicellular tumour spheroids from two human lung cancer cell lines.* Cancer Cell Int, 2015. **15**: p. 47.
23. Mendoza-Coronel, E. and E. Ortega, *Macrophage Polarization Modulates FcγR- and CD13-Mediated Phagocytosis and Reactive Oxygen Species Production, Independently of Receptor Membrane Expression.* Front Immunol, 2017. **8**: p. 303.
24. Tan, H.Y., et al., *The Reactive Oxygen Species in Macrophage Polarization: Reflecting Its Dual Role in Progression and Treatment of Human Diseases.* Oxid Med Cell Longev, 2016. **2016**: p. 2795090.
25. Chen, X., et al., *Role of Reactive Oxygen Species in Tumor Necrosis Factor-alpha Induced Endothelial Dysfunction.* Curr Hypertens Rev, 2008. **4**(4): p. 245-255.
26. Delgado, M.A. and V. Deretic, *Toll-like receptors in control of immunological autophagy.* Cell Death Differ, 2009. **16**(7): p. 976-83.
27. Cho, J.H., et al., *The TLR7 agonist imiquimod induces anti-cancer effects via autophagic cell death and enhances anti-tumoral and systemic immunity during radiotherapy for melanoma.* Oncotarget, 2017. **8**(15): p. 24932-24948.

28. Dengjel, J., et al., *Autophagy promotes MHC class II presentation of peptides from intracellular source proteins.* Proc Natl Acad Sci U S A, 2005. **102**(22): p. 7922-7.
29. Shi, C.S. and J.H. Kehrl, *MyD88 and Trif target Beclin 1 to trigger autophagy in macrophages.* J Biol Chem, 2008. **283**(48): p. 33175-82.

Chapter 3:

Nanoparticle preparation, optimization, and synthesis of pH-sensitive NPs

3.1. Introduction:

After years of research in cancer treatment, chemotherapy remained one of the primary treatment modalities, used alone or in combination with surgery and/or radiation. The major problem associated with chemotherapy is its toxicity due to non-specific tissue distribution. Different strategies have been evaluated to reduce this off-target toxicity; tumor-targeted drug delivery is a major one among them. It has been demonstrated that delivering the drug encapsulated in a nano-carrier system can significantly improve its tumor bioavailability and reduce systemic toxicity due to the enhanced permeability and retention (EPR) effect in most solid tumors [1, 2]. Till now, several nanomedicines have been approved by the FDA for clinical therapy against cancer, including doxorubicin-loaded liposome, albumin-bound paclitaxel NPs, liposomal irinotecan, and many others [3]. Though these nanomedicines exhibited improved pharmacokinetics and reduced side effects, their extensive use is restricted due to their high cost. Developing new nanomedicine is challenging due to the complexities associated with scale-up and batch-to-batch uniformity, limiting clinical success. Most of the nanoparticle design strategy and fabrication process is highly complex, which is also a bottleneck for increasing the number of clinically approved nanomedicines [4]. The continuous-flow microfluidic-based system can be a viable alternative to improve the current state-of-the-art. Microfluidic-based method offers multiple advantages compared to other batch processes in terms of better manipulation of reagents, low sample consumption, synthesis with high reproducibility, and the possibility of streamlined continuous synthesis and precisely controlled size [5, 6]. This method makes manipulating the nanoformulation characteristics much easier, including size tuning, leading to enhanced clinical performance [7]. As reported earlier, the nanocarrier's ability to control its physical characteristics (size, shape, polydispersity, etc.) would be highly beneficial in enhancing its antitumor efficacy [8, 9].

Also, the use of easily available excipients would make them commercially viable. Paclitaxel (PTX) is a highly potent chemotherapeutic agent used for the treatment of various types of cancers, including ovarian, lung, gastro-esophageal, endometrial, and breast cancer, as well as lymphoma and leukemia [10]. PTX binds to cellular microtubules, promotes polymerization, and stabilizes the microtubule structure, thereby blocking the cell cycle in the late G2/M phase, resulting in cancer cell death [11, 12]. However, poor aqueous solubility and non-specific pharmacokinetics are some challenges associated with developing a successful PTX formulation. To address these problems, a few clinically approved nanoformulations of PTX have been developed, including albumin-bound PTX (Abraxane), poly-L-glutamic acid

conjugated PTX (Polyglumex/ Xyotax/ Opaxio), and mPEG-PLA micellar PTX (Genexol-PM) [13]. These formulations exhibited enhanced efficacy compared to native PTX; however, they are highly expensive and difficult to develop. Also, the size of the nano-carrier system plays a critical role in influencing their tumor bioavailability and penetration [14]. It has been proven that smaller particle size is better for tumor delivery and penetration [15]. However, it is highly challenging to prepare nano-carriers of a smaller size range due to their complex design strategy.

Polymeric NPs are getting significant attention among different nano-carrier systems due to their simplistic design, easy formation, and good drug-loading efficiency [16]. Amphiphilic block copolymers form these NPs via self-assembly into a core-shell structure. The hydrophobic segments of the polymer form the core, and the hydrophilic head forms the outside shell. The formation of such a structure aids in the solubilization of non-polar drugs by encapsulating them in the hydrophobic core. Many different block copolymers have been used for making drug-loaded NPs [16].

In the current study, we initially evaluated the effectiveness of a continuous-flow microfluidic-based nanoprecipitation method over conventional nanoprecipitation using Soluplus as a representative polymer. Further, the effect of NP size on the drug release kinetics, cytotoxicity against both 2D and 3D cancer cells, and cellular internalization was studied. A 3D spheroid penetration assay was carried out to understand tumor penetration. We have also evaluated the cellular uptake pathway by analyzing the cellular internalization of the NP with different uptake inhibitors.

Delivery of a multidimensional drug combination is more complicated than a single drug. Different drugs target different cells, so their bioavailability in the TME is critical. For delivery of a combination of drugs, an ideal delivery system should protect the drugs from metabolism during systemic circulation, minimize non-specific accumulation in normal tissues, and, upon reaching the TME, release the drugs to act on their specific targets. For this purpose, triggering the release of the drugs from the NPs at the TME can be an effective strategy by exploiting the acidic extracellular pH of the TME. After demonstrating the superiority of the continuous-flow microfluidic-based nanoprecipitation method for making NPs, we developed a pH-responsive NP to deliver the PTX and RSQ combination. The objective was to synthesize a pH-responsive polymer, formulate an NP system using that polymer co-encapsulating PTX and RSQ, and evaluate the pH-responsive behavior of the NPs.

3.2. Material and methods:

Materials:

Paclitaxel was a free gift from INTAS Pharmaceuticals Ltd, Ahmedabad, India. RSQ was purchased from TCI, India. Acetonitrile (HPLC grade), diethyl ether (DEE), chloroform ($CHCl_3$), dimethylformamide (DMF), dimethyl sulfoxide (DMSO), and methanol were procured from Merck, India. Hydroxyl-terminated linear PLGA, hydroxyl-terminated star-shaped PLGA, Boc-His(Dnp)-OH,N-(3-Dimethylaminopropyl)-N′-ethyl carbodiimide hydrochloride (EDC), 4-(dimethylamine)pyridine (DMAP), 3-(4,5-dimethylthiazol-2yl)-2,5-diphenyltetrazolium bromide (MTT) were purchased from Sigma-Aldrich. HPLC grade acetonitrile and methanol were purchased from SD Fine-Chem limited, Mumbai, India. All other chemicals, solvents, and reagents used for HPLC analysis were either of HPLC grade or analytical grade. HPLC analysis was performed on a Shimadzu liquid chromatography system (Kyoto, Japan) consisting of LC10AT binary pump, SPD-M20A Photo Diode Array detector, CTO-10ASP column oven, and SIL-HT autosampler. Phenomenex RP-18 column (#00G-0234-E0) was used for the HPLC. NP synthesis was done using a Mitos Duo XS-Pump and micromixer chip (part number 3200401) from Dolomite, Royston, UK. 3-(4,5-dimethylthiazol-2yl)-2,5-diphenyltetrazolium bromide (MTT) (#M2128), nystatin, chlorpromazine were procured from Sigma Aldrich, USA. Penicillin-Streptomycin (10,000 U/mL)(#15140122), DiI (#D3911), LysoTracker® Green DND-26 (LT, #L7526), ProLong™ Gold Antifade Mounted with DAPI (4′,6-diamidino-2-phenylindole) (#P36935), were purchased from Thermo Fisher Scientific, USA. MCF7 (human breast cancer) cell lines were purchased from the National Centre for Cell Science (NCCS), Pune.

Development of PTX-loaded polymeric NPs:

Variable sized PTX loaded NPs of Soluplus were prepared by using the continuous-flow microfluidic-based nanoprecipitation method. Briefly, PTX and polymer were solubilized at a specified ratio (0.5 mg/30 mg or 5 mg/30 mg of PTX to Soluplus) in the organic phase, methanol (1 ml). Distilled water was taken as an aqueous phase into pump "A" of the microfluidic syringe pump. Drug and polymer containing organic phase were delivered through pump "B". Pump "A" was divided into two channels using a "T" junction. Then, Pump A and B were connected to the micromixer chip as described in the schematic (**Figure 3.1**). The flow rate was controlled using syringe pumps, pump A at a flow rate of 250 µl/min and pump B at 50 µl/min. In the micromixer chip, due to the hydrodynamic flow focusing strategy, aqueous

flow squeezes and narrows the stream of the organic phase (Soluplus + PTX in methanol), which further enters into herringbone mixer in the micromixer chip, resulting in the formation of NPs due to rapid solvent exchange via diffusion. These NPs were collected and stirred overnight for solvent evaporation, then dialyzed for 6 h against distilled water to remove the unentrapped free drug; subsequently, nano-carriers were lyophilized and stored at 4°C. Blank NPs of soluplus were prepared by the same method as above, without PTX. DiI-loaded NPs were prepared by adding 1 mg/ml of DiI into methanol along with Soluplus and PTX; the rest of the processing was the same as drug-loaded SNP and LNP.

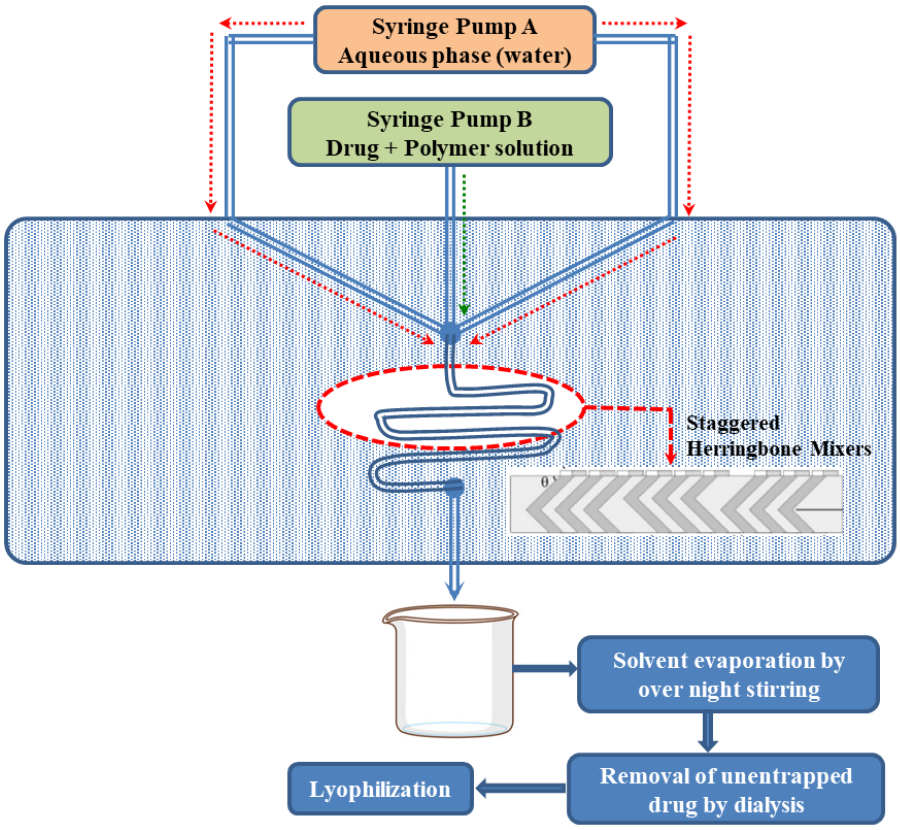

Figure 3.1: Schematic diagram of the Soluplus NP formation using the microfluidic system. PTX and polymer (Soluplus) were solubilized in methanol, which was delivered through pump B at a flow rate of 50 µl/min. Distilled water was delivered through pump "A" at a flow rate of 250 µl/min. The two miscible phases got mixed due to hydrodynamic flow focusing in the Herringbone mixer in the micromixer chip, resulting in rapid solvent exchange and NP formation. NPs were collected and stirred over night for solvent evaporation, then dialyzed for 6h against distilled water to remove the unentrapped free drug; subsequently the NPs were lyophilized and stored at 4°C.

Measurement of PTX concentration by HPLC method:

HPLC analytical method for PTX was developed to study drug entrapment efficiency and release profile of the prepared NPs. A reverse-phase isocratic analytical method was developed for the estimation of PTX. Briefly, Phenomenex RP C-18 analytical column was used as the stationary phase, and the mobile phase was 60:40 acetonitrile to water (v/v). A flow rate of 1 ml/min and an injection volume of 20 µl, with run time 10 min provided a sharp peak with

good intensity. PTX peak was detected at λ_{max} 227 nm. The retention time of the PTX was found to be 6.6 min. With this method, linearity was observed from 1 to 15 µg/ml and r^2 = 0.999.

Physicochemical characterization:

NP size (hydrodynamic diameter) and PDI were analyzed by dynamic light scattering (DLS), using Malvern Nano ZS (Malvern's instrument Ltd., UK) at 25ºC. A dilute suspension of NPs was used to determine the size (dilution was optimized to obtain consistent and reliable readings).

Morphology of the NP was analyzed by Scanning Electron Microscopy (SEM). NP suspension was placed on a glass coverslip and air-dried. The glass coverslips were dropped onto a double-sided carbon tape attached to the sample stub and coated under vacuum with gold in an argon atmosphere for about 45 seconds. Then morphology was examined by scanning at 20kv with SEM.

To calculate the percent encapsulation efficiency (%EE) and percentage drug loading (%DL), 1 mg of freeze-dried NPs were dissolved in 1 ml of methanol and vortexed for 5-10 minutes. Then the resulted solution was injected into HPLC, and the concentration of PTX was analyzed using a calibration curve prepared by using the developed PTX analytical method. %EE was calculated using the following formula:

%EE = weight of the drug in the NPs / initial weight of drug × 100

%DL was calculated by the formula:

%DL = weight of the drug in the NPs / total weight of the NP × 100

Solubility factor (f_s) of PTX in the NP formulations was calculated using the formula:

$$f_s = S_a/S_{water}$$

where S_a was the apparent solubility of PTX in the NP formulation and S_{water} was the intrinsic solubility of PTX in distilled water (0.19 µg/mL).

In-vitro drug release profile:

For the *in-vitro* release study, 1 mg of PTX loaded NPs were dispersed in 1 ml of phosphate buffer solution (PBS) (20 mM, 7.4 pH) and placed in a dialysis bag (MWCO-10,000, HiMedia, Mumbai). After hermetically sealing both the ends of the dialysis bag, it was dipped in 10 ml of release media (20 mM PBS with 1% tween 80) and was placed on a rotary flask shaker at

37ºC. 1% tween 80 in release media acts as a solubilizer to maintain sink conditions. 2 ml of sample was aliquoted at fixed time intervals i.e., 0.5, 1, 2, 4, 6, 8, 12, 24, 48, and 72 h, and the same amount was replaced with fresh buffer. Drug content was analyzed by using the developed HPLC method. From the obtained data, % cumulative drug release (CDR) was calculated. By using this data, the time vs. % CDR graph was plotted.

CDR (%) = (Amount of drug released from the NP at the time (t) / Amount of drug in the NP) × 100

2D cell culture:

MCF7 (human breast cancer) cells were cultured in Dulbecco's Modified Eagle's Media (DMEM) (Gibco) with 10% fetal bovine serum (HiMedia), 50 units/ml penicillin and 50 mg/ml streptomycin at 37ºC, 5% CO_2. Cells were sub-cultured at 80% confluency. Trypsin-EDTA solution (0.05%) was used for the detachment of cells.

3D (spheroid) cell culture model:

MCF7 cells were suspended in DMEM media containing 0.2% methylcellulose at density of 10,000 cells/ 10µl. Hanging drops (10 µl) of above cell suspension were incubated for 24 h at 37ºC, 5% CO_2. Then the spheroids from hanging drops were transferred into 96 well round bottom plate coated with 1% agarose, containing 200 µl media and cultured for three days, and experiments were performed.

In-vitro cytotoxicity study:

Cytotoxicity of SNP, LNP, and free PTX was examined against MCF-7 cell lines using MTT assay. In the case of 2D culture, the cells were seeded in a 96 well plate with a density of 2,000 cells per well and were cultured at 37ºC in the presence of 5% CO_2. After 24 h of incubation, cells were treated with either SNP or LNP or the free drug at different concentrations (0.64, 3.2, 16, 80, 400, 2000, 10000 nM) and incubated for 72 h. Blank NP was used as a control. The cells were then treated with MTT (1mg/ml) in cell culture media and incubated for 4 h. After this, the MTT solution was replaced with 200 µl of DMSO to dissolve the formazan crystals formed in viable cells. Finally, optical density (OD) was observed at 570 nm using a microplate reader with a reference wavelength of 630 nm. Percentage of viable cells was calculated using the following formula:

Cell viability (%) = (mean absorbance value of drug-treated cells) / (mean absorbance value of the control) x 100.

MTT assay for the 3D model was performed, as reported earlier, with some modifications [25]. Briefly, after 72 h of treatment to spheroids, MTT solution at a concentration of 1mg/ml was added to each well and then incubated for 4 h at 37° C. Then spheroids were carefully collected into 1.5 ml centrifuge tube, centrifuged at 500 × g for 10 min at 4°C. Then the intensity of formazan crystals was analyzed, and cytotoxicity was calculated the same way as before.

NP internalization study:

MCF7 cells were plated on a coverslip placed in a 6 well plate at a density of 50,000 cells/ well in 2 ml of DMEM media and then incubated for 24 h. The cells were then treated with DiI loaded NPs of variable size (1 µg/ml of DiI) and incubated for 4 h. After three times wash with PBS, the cells were fixed with 100% methanol at -20ºC for 15 min, and then the coverslips were mounted onto glass slides with antifade DAPI containing mounting media. Internalization was confirmed by examining these slides through the ZEISS Axio Scope A1 microscope at 63X magnification.

Colocalization analysis (Lysotracker assay):

MCF-7 cells (50000 cells/ well) were seeded on glass coverslips placed in a 6 well plate and were incubated in 2 mL of culture medium for 24 h. Subsequently, the DiI-loaded NPs (1 µg/ml of DiI) were added, and the cells were allowed to incubate for 4 h. Then the media was removed and 3 times PBS wash was done. Then the cells were incubated with lysotracker green (1 mM), for 20 min. After that, lysotracker green was removed and 3 times wash with PBS was done. After washing, cells were fixed with 100% methanol at -20º C for 15 min, and then the coverslips were mounted onto glass slides with antifade DAPI containing mounting media. Later the slides were examined by using the ZEISS Axio Scope A1 microscope with 63X magnification.

Spheroid penetration study:

Spheroids were treated with variable sized NPs loaded with DiI and were incubated at 37°C. To study the NPs' penetration into tumor spheroids, fluorescent images of spheroids were taken at 4 h and 24 h by using the ZEISS Axio Scope A1 microscope with 10X magnification.

Synthesis of pH-sensitive polymers: Linear PLGA-poly-histidine (l-PLGA-pH) and star PLGA-poly-histidine (s-PLGA-pH)

s-PLGA-OH (100mg) was reacted with succinic anhydride (20mg) in the presence of DMAP (20mg) in 1mL of anhydrous acetonitrile and was kept for continuous stirring for 24h in N_2

atmosphere at room temperature, which resulted in the formation of s-PLGA-COOH. It was then purified using 50 ml of ice-cold DEE and repeated 3 times to remove the unreacted polymer. Boc-His(DNP)-OH (1g) was suspended in 10mL of anhydrous acetonitrile, and 1mL of thionyl chloride was added dropwise under continuous stirring in an N2 atmosphere for 1hfor the formation of DNP-NCA-HCl. The product was precipitated using 100ml of ice-cold DEE with consecutive washing for 3 times (50ml each). Then obtained product DNP-NCA-HCl was dissolved in 10mL of anhydrous DMF, and then for ring-opening polymerization, isopropyl amine (1mL) was added, the product poly-(N-DNP-L-histidine) was purified by precipitation in an excess of ice-cold DEE in order to remove the unreacted reactants. Then, poly-(N-DNP-L-histidine)was reacted with s-PLGA-COOH in EDC and NHS to forms-PLGA-poly-histidine-(DNP).DNP deprotection was carried out by reacting s-PLGA-poly-histidine-(DNP) with 1mL of 50% 2-mercaptoethanol in DMF for 12h with continuous stirring and then precipitated by using 100ml of ice-cold DEE for 72 h, repeated for 3 times to obtain the final product s-PLGA-poly-histidine (s-PLGA-pH).The obtained precipitate was washed with Milli-Q, then lyophilized for 24h and stored at −20°C.

l-PLGA-pH was synthesized by conjugating l-PLGA-COOH with poly-histidine in EDC and NHS to obtain l-PLGA-poly-histidine-(DNP) followed by DNP deprotection and purification as that of s-PLGA-pH.

Structural identification of the synthesized pH-sensitive polymer:

^{1}H NMR and FTIR analyses were performed to confirm the formation of s-PLGA-pH and l-PLGA-pH. The chemical structures of s-PLGA, Boc-His (DNP)-OH, DNP-NCA-HCL, poly-histidine, s-PLGA-pH, and l-PLGA-pH were characterized by ^{1}H NMR spectroscopy at 300 MHz on a Bruker Avance spectrometer using tetramethyl silane as an internal standard. FTIR spectra in the range of 4000 to 400 cm^{-1} were also acquired using ATR-IR using a Bruker ATR-IR machine.

Preparation of drug-loaded NPs:

s-PLGA-pH and l-PLGA-pH NPs loaded with PTX and RSQ were prepared by the nanoprecipitation-based method, using microfluidic technology. Briefly, 0.5% Soluplus solution was used as the aqueous phase. PTX (100ug), RSQ (2mg), and s-PLGA-pH (20mg) were dissolved in 1mL ACN, which was used as the organic phase. Two separate pumps dispensed both the aqueous and organic phases at a flow rate of 100 µL/min for the aqueous

phase and 10µL/min for the organic phase. Outlets of both organic and aqueous pumps (A&B) were introduced into the micromixer chip, which combines the two solutions using a 'T' junction. Here, both the aqueous and organic phases were mixed by hydrodynamic flow focusing and staggered herringbone mixing, leading to the formation of the NPs due to nanoprecipitation of the polymer and drugs after mixing with the aqueous phase. These NPs were then collected and stirred overnight for the evaporation of ACN. Residual solvent and unentrapped (free) drugs were removed by dialyzing with an MWCO membrane of 10,000 Da (HiMedia) for 24h using 500ml of MQ water as an external medium with two changes of water at 6h and 12h. NPs were then concentrated by centrifugation at 2000 g for 15min. To obtain a 1:200 molar ratio of PTX: RSQ loading in NPs, variable drug concentrations were observed for entrapment and drug loading in the initial screening. DiI-loaded NPs were prepared in the same way, where 1mg of DiI and 20mg of polymer were dissolved in 1ml of ACN and used as the organic phase, and 10ml of 0.5% Soluplus solution was used as the aqueous phase. NPs were prepared by using microfluidics, as discussed earlier, followed by solvent evaporation and free drug removal by dialysis.

HPLC method for simultaneous estimation of PTX and RSQ:

An HPLC method was developed to simultaneously estimate both the drugs (PTX and RSQ). Briefly, HPLC analysis was done using a Zodiac C18 column as the stationary phase and ACN: pH 5 phosphate buffer (60:40) as the mobile phase, with a flow rate of 1mL/min, and 10minrun time. The column oven temperature was 40°C. HPLC analyses of all the samples were performed using a 20µL injection volume, where the samples were dissolved in 60% ACN. The linearity curve was plotted for both PTX and RSQ, R^2=0.99. The limit of detection (LOD) was found to be 0.04µg/mL, 0.075 µg/mL for PTX and RSQ, respectively, and the limit of quantification (LOQ) was found to be 0.14µg/mL and 0.2 µg/mL for PTX and RSQ respectively. Both LOD and LOQ were calculated according to ICH guidelines.

Drug loading and encapsulation in NPs:

5 mg of NP was taken and dissolved in 200µL of ACN, vortexed for 15 min and s-PLGA/s-PLGA-pH/l-PLGA/ l-PLGA-pH NPs were precipitated by adding1mL of methanol. The polymers were separated by centrifuging at 3000g for 30 min. The supernatant was collected, dried, and dissolved in 60% ACN before analyzing with HPLC.

The entrapment efficiency of the NPs was calculated by using the formula:

% Entrapment efficiency (%EE) = (Weight of actual drug loading /Total weight of drug added initially) × 100.

Loading capacity was calculated by using the formula:

% Loading capacity (%LC) = (Weight of total drug loading /Total NP weight) × 100.

Analysis of particle size, polydispersity index (PDI), and zeta potential:

The mean particle size, polydispersity index (PDI), and zeta potential of the NPs were measured using Zetasizer Nano ZS, Malvern Instruments, UK, at a backscattering angle of 173°.

Analysis of the pH-dependent size variation of the nanoparticles:

s-PLGA, l-PLGA, s-PLGA-pH, and l-PLGA-pH NPs 5mg/ml each were dispersed in phosphate buffers of pH 7.4 and 6.5. Particle sizes and PDI of NPs were analyzed using DLS at 6h time point. In addition to DLS, the pH-dependent change in the NP morphology was analyzed by field emission scanning electron microscopy (FESEM) after suspending the NPs for 3h in a buffer of pH 7.4 and 6.5. After that, the NP suspension was air-dried, placed on the sample stub by using double-sided carbon tape, and gold coated. These were then subjected to FESEM analysis.

***In-vitro* drug release study:**

The drug release studies in different pH buffers were performed by using the dialysis method. In brief, 5mg of the drugs-loaded NPs (s-PLGA (0.59µgPTX +53µg RSQ), l-PLGA (0.6µg PTX +58µg RSQ), s-PLGA-pH(0.64µg PTX +58µg RSQ), and l-PLGA-pH(0.7µgPTX +56µg RSQ) NPs) was diluted in 1mL of release medium in a dialysis bag and kept in a beaker containing 20mL of release medium (20 mM phosphate-buffered solution, pH 6.5 and 7.4).Sink condition was maintained using 0.2% tween 80 in the medium and kept on a magnetic stirrer (150 rpm) at 37°C. At 0, 0.25, 0.5, 1, 3, 6, 12, 24, 48, and 72h time intervals, 500 µL of the sample was collected and replaced with the same amount of buffer. The collected samples were then mixed with an equal volume of ACN and centrifuged at 3000×g for 30 min. The supernatant was taken and further analyzed using HPLC. Cumulative drug release (CDR) was calculated as follows:

% Cumulative release (% CDR) = (Drug released from the NPs at the time 't'/Amount of drug present in NPs) × 100

Statistical analysis:

The obtained data were analyzed, and graphs were made using Graph Pad Prism software version 5.0. In all the figures, the level of significance was indicated by * where $p < 0.01$. The student's t-test was performed when the comparison was made between 2 experimental groups. Two-way ANOVA was used when the comparison was made between 2 or more groups containing 2 independent variables; posthoc Bonferroni multiple comparison tests were performed to compare the means of each group. Data were represented as mean ± SD.

3.3. Results and Discussion:

A large number of studies have been done for the development of tumor-targeted nanoformulation of PTX [17]. Few formulations among them have been approved for clinical use. However, many of these formulations follow complex design parameters that make scale-up very difficult. Conventionally, nanoformulations are synthesized predominantly using batch processes, like ultrasonication, microemulsion, nanoprecipitation, thin film, etc. However, these processes often resulted in high batch-to-batch variation [18, 19]. For the successful translation of nano-carriers from bench to bedside, precise regulation of particle size distribution, uniformity, colloidal stability, batch-to-batch reproducibility, and scale-up facility are required [20].

In the current study, we initially evaluated the effectiveness of a continuous-flow microfluidic-based nanoprecipitation method over conventional nanoprecipitation using Soluplus as a representative polymer. Though Soluplus is mainly used as a solubility and bioavailability enhancing agent, being an amphiphilic copolymer, it can form micellar nanostructures, as it has been previously reported [21, 22]. We wanted to evaluate the feasibility of the microfluidic-based continuous flow technique for synthesizing simple Soluplus NPs for PTX loading and check the effect of NP size on *in-vitro* cellular internalization.

Synthesis and physicochemical characterization of the NPs:

Soluplus NPs were synthesized using a microfluidic-based continuous flow nano-precipitation technique, where variable-sized NPs were prepared by varying the drug/polymer ratio (**Figure 3.2A**). The critical NP concentration (CMC) of Soluplus is reported to be 0.8 mg/ml [23]. Keeping that in mind, we have taken a Soluplus concentration of 30 mg/ml, well above the CMC. Significant size variation of the NPs was observed between drug: polymer ratio of 0.5:30 and 5:30. Use of a lower drug: polymer ratio (0.5:30) resulted in significantly smaller NPs of the size ~90 nm, named hereafter as small-Soluplus NPs (SNP). Higher drug: polymer ratio

(5:30) made NPs of the size ~180 nm, named hereafter as large-Soluplus NPs (LNP) (**Figure 3.2 and Table 3.1**). This composition-dependent size variability was may be due to the highly lipophilic nature of PTX (logP 3.96). When a higher ratio of PTX was present, it aggregated into a larger core during the NP formation, whereas the presence of a lesser amount of PTX resulted in the opposite. This was also evident from the size of the blank Soluplus NPs (~60 nm), indicating the absence of the hydrophobic PTX might make smaller NP.

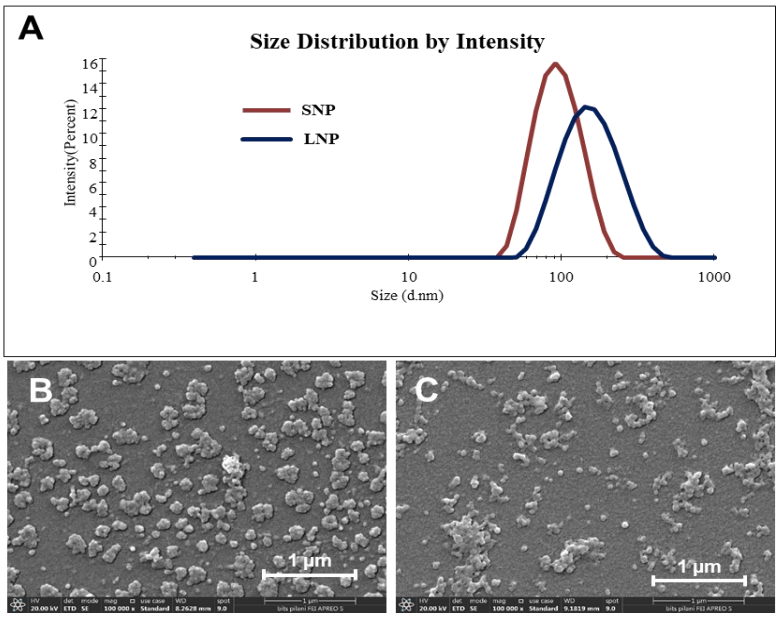

Figure-3.2: (A) Size distribution of SNP and LNP using DLS. Scanning Electron Microscopy (SEM) images of **(B)** LNP and **(C)** SNP.

Both SNP and LNP were relatively monodisperse with a PDI of 0.21 and 0.23, respectively (**Table 3.1**), establishing the usefulness of the microfluidic platform for NP synthesis. SEM analysis also indicated that the NPs were spherical without any aggregation (**Fig. 3.2B-C**). Encapsulation efficiency was calculated by HPLC, where significantly higher encapsulation efficiency was observed with the SNP (95.5±2.9%) compared to the LNP (51.8%±2.4%) (**Table 3.1**). Higher encapsulation efficiency in the SNP may be due to the higher ratio of the polymer relative to the drug. In the SNP, less PTX was present per unit of encapsulating polymer, improving the encapsulation efficiency. % drug loading was found out to be 7.4±2.7% for LNP and 1.6±2.9% for SNP (**Table 3.1**). Higher drug loading in the LNP was probably responsible for its larger size, as discussed previously. In terms of PTX solubility in these NPs, it was calculated to be 79 µg/mL for SNP and 433 µg/mL for LNP (**Table 3.1**). Almost 415- and 2280-fold increase in solubility of PTX was observed with SNP and LNP, respectively.

NPs	Organic: aqueous (v/v)	Drug: Polymer (w/w)	Size (nm)	PDI	Encapsulation Efficiency (%)	Drug loading (%)	Solubility (µg/ml)	Solubility factor (f_s)
Blank	1:5	0:30	62±0.8	0.05±0.03	-	-	-	-
SNP	1:5	0.5:30	95±3.6	0.21±0.02	95± 3.2	1±0.5	79±0.25	415±0.83
LNP	1:5	5:30	174±4.2	0.23±0.03	52±2.3	7±0.2	433±0.16	2280±0.51

Table-3.1: Physicochemical characterization of different PTX loaded and blank Soluplus NPs.

In-vitro drug release profile:

The in-vitro release of PTX from the NP was carried out by the dialysis method, where the drug release pattern of SNP was compared with that of the LNP formulation. In the initial stage till 6 h, a burst release was observed in both the formulations, and both the NPs showed similar drug release at this stage, with a cumulative release of 22.6±0.4% and 22.9±0.1% for SNP and LNP, respectively. However, after the initial burst release, a prolonged sustained release was observed, where the SNP exhibited a higher release rate than the LNP. At 72 h, PTX release from the SNP was found to be 96.9±0.05%, whereas the same with LNP was 51.3±0.04% (**Figure 3.3**).

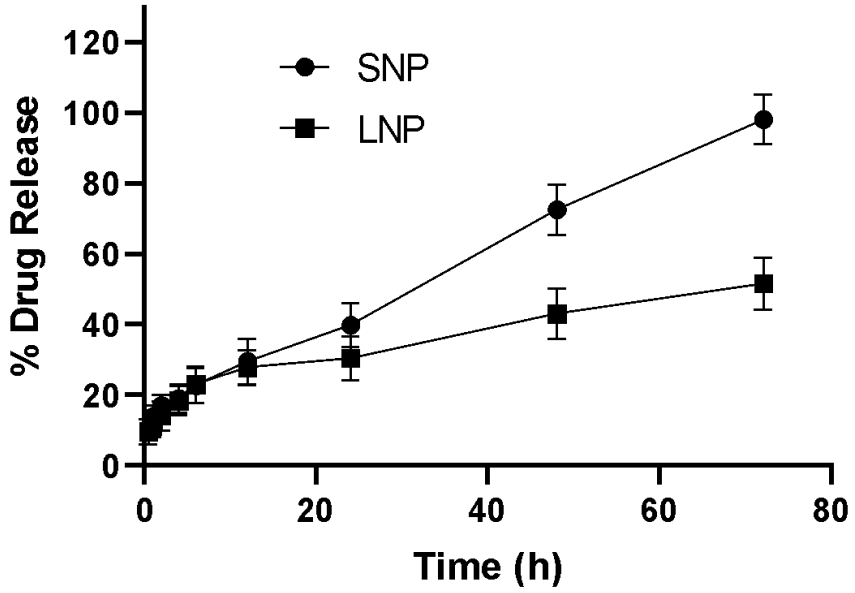

Figure 3.3: Cumulative PTX release profile of SNP and LNP. Data was expressed as mean ± SD of 3 independent experiments. * indicates $p < 0.01$, analyzed using 2-way ANOVA test followed by posthoc Bonferroni multiple comparison test.

From this data, it can be concluded that SNP showed faster drug release compared to LNP as smaller NPs have a larger surface area to volume ratio. In earlier studies, different PTX-loaded Soluplus NPs exhibited a low drug release rate. For example, Bernabeu *et al*. found ~30% PTX release at 72 h [24] from a Soluplus-TPGS NP with a size of ~120 nm. Surface modification

with glucose moiety of the same NP did not change the release pattern significantly [25]. Hou *et al*. reported a ~40% cumulative drug release at 48 h from the ~165 nm Soluplus-Solutol NPs {Hou, 2016 #231. These data support our observation that the drug release rate from larger-size NPs would be lower. In the current formulation, smaller NPs had a relatively higher amount of Soluplus, which could also enhance the hydration of the NPs, improving drug release.

In-vitro cytotoxicity studies using 2D and 3D culture systems:

Next, we compared the *in-vitro* cytotoxicity of SNP and LNP formulations using the MCF-7 cell line. MCF-7 is a human breast cancer cell line. As PTX is used as a first-line drug against breast cancer [40], we have selected MCF-7 as a model system for the *in-vitro* efficacy analysis of the PTX-loaded NPs. Both the traditional 2D culture system and the 3D spheroid model were used to evaluate the efficacy of the formulations. A concentration-dependent cytotoxic effect was observed with both LNP and SNP as well as the free drug in the 2D model. Interestingly, both the free drug and LNP showed similar efficacy, whereas a significant increase in cytotoxicity was observed with the SNP compared to both LNP and the free drug. As depicted in **Figure 3.4A**, the IC50 of both the free drug and LNP was found to be ~16 nM, whereas that of SNP was ~3.2 nM. The blank Soluplus NPs were found to be non-toxic at the dose tested.

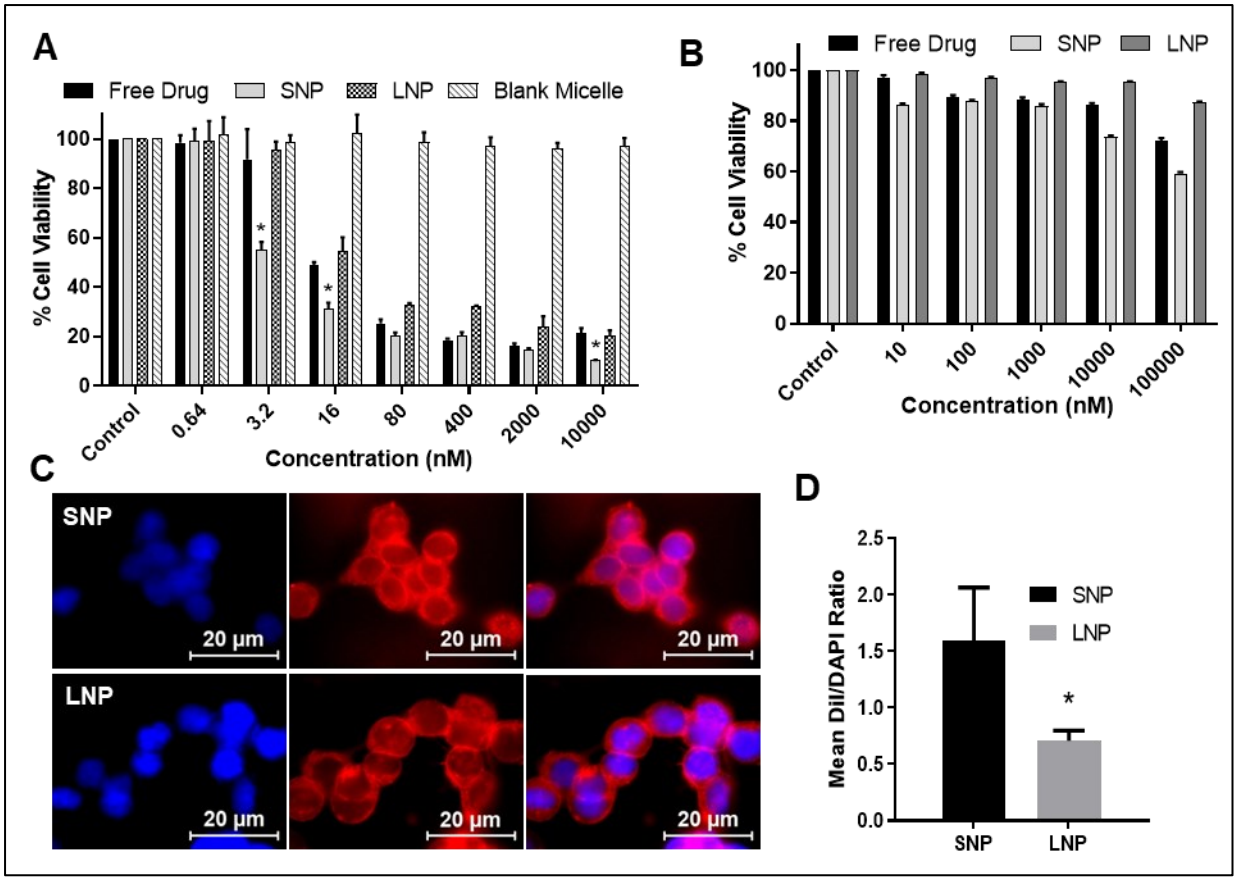

Figure 3.4: (A) Cell viability analysis by MTT assay after treatment with SNP and LNP in MCF-7 cells in 2D model. Blank NPs were used as a control. Data was expressed as mean ± SD of 3 independent experiments. * indicates a significant difference compared to LNP treatment, p <0.01, calculated using 2-way ANOVA followed by posthoc Bonferroni multiple comparison tests. **(B)** Cell viability assay in 3D model. Data was expressed as mean ± SD of 3 independent experiments. * indicate p <0.01, calculated using 2-way ANOVA followed by posthoc Bonferroni multiple comparison tests. **(C)** Fluorescent microscopy images of MCF-7 cells after treatment with DiI-tagged SNP and LNP. Cell nuclei were stained with DAPI. **(D)** Comparison of the relative DiI fluorescence intensity (DiI/DAPI ratio) of SNP and LNP. Data was expressed as mean ± SD of 3 independent experiments, * indicate p < 0.01 calculated using student's t-test.

Apart from the traditional monolayer cell culture system, we also evaluated the efficacy of the PTX-loaded NPs against the 3D spheroid model, as they better mimic the conditions and factors present in the *in-vivo* tumor [26]. Tumor cells are less sensitive to chemotherapeutics in 3D culture systems as they have a higher resistance than the monolayer culture system [27]; hence, an increased drug dose is needed for cytotoxic activity. Like the 2D culture study, both the free drug and LNP exhibited similar cytotoxic efficacy, whereas the SNP formulation exhibited higher potency (**Figure 3.4B**). The smaller size and enhanced hydrophilicity of the SNP may improve the spheroid penetration. In the case of free PTX, it may accumulate at the periphery of the spheroid due to its hydrophobic nature.

Effect of particle size on *in-vitro* cellular internalization and lysosomal colocalization study:

To confirm the improved efficacy seen with the SNP, we compared the cellular internalization of LNP and SNP. The therapeutic effects of nanoformulations would depend on the cells' internalization and retention of nano-carriers. To evaluate cellular internalization, we prepared DiI (red fluorescent probe) loaded NPs of the same composition and size as that of SNP and LNP. After treating MCF-7 cells with the fluorescent probed NPs for 4 h, the intracellular uptake was analyzed by fluorescent microscopy. Mean fluorescence intensities were calculated using ImageJ. As depicted in **Figures 3.4C** and **D**, SNP shows significantly higher fluorescence intensity than LNP. The ratio of red (DiI, representative of NPs) to blue (DAPI, representative of cell nucleus) fluorescent intensities for SNP and LNP were found to be 1.6±0.6 and 0.7±0.1, respectively (**Figure 3.4D**), which indicates greater cellular internalization of SNP compared to LNP. In multiple previous studies, it has been demonstrated that smaller nano-carriers exhibited better cellular internalization compared to larger ones [28]. Next, to understand the drug-loaded NPs intracellular fate, the lysosome colocalization study was performed using DiI-loaded LNP and SNP. As depicted in **Figure 3.5**, enhanced lysosomal localization was noted with the SNP compared to the LNP, corroborating the previous data. Increased lysosomal localization would improve the efficacy of the drug [29]. Paclitaxel is a lysosomal membrane permeabilizing agent, so delivering this drug to lysosomes provides an added advantage of lysosomal membrane permeabilization-induced cytotoxicity [30, 31]. This could be one of the reasons behind the higher cytotoxic efficacy of SNP over LNP as well as free PTX in the 2D *in-vitro* cytotoxicity study.

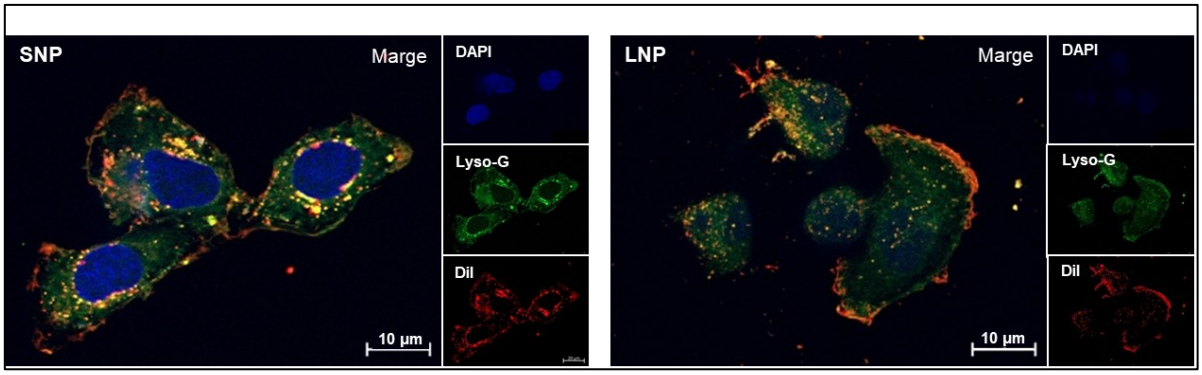

Figure 3.5: Comparative analysis of lysosomal localization of the DiI-loaded SNP and LNP NPs in the MCF-7 cells. Lysosomes were stained with lysotracker green, and the nuclei were stained with DAPI.

Tumor spheroid penetration:

Nano-carriers can accumulate at the tumor site, taking advantage of the EPR effect. However, after the accumulation of nano-carriers at the tumor periphery, its penetration into less perfused tumor core is impeded by high extracellular matrix, interstitial fluid pressure, and cell density [1]. As the tumor core is rich in highly resistant cancer cells, penetration of nano-carriers to the tumor core is a major limiting factor determining its efficacy [32]. To analyze the tumor penetration capacity of SNP and LNP, we have used a 3D *in-vitro* model. Unlike 2D cell cultures where cells grow in monolayers, in the 3D spheroids, tumor cells self-aggregate into a complex 3D structure that better mimics the intercellular and transcellular signaling present in the *in-vivo* solid tumors [33]. Due to that, 3D *in-vitro* tumor models are highly recommended for the screening and evaluation of anticancer drugs and formulations, and they are better models for evaluating the penetration capacity of nanocarriers [34]. We have analyzed the time-dependent penetration of SNP and LNP into the MCF-7 tumor spheroids. Penetration was assayed by a fluorescent microscopic study using DiI-loaded NPs of SNP and LNP with ~500 µm spheroids. Two time points were studied: 4 h and 24 h. After 4 h, a considerable amount of SNP was found to have penetrated and accumulated in the peripheral region of the tumor spheroid, whereas, with the LNP, only background signal was detected, signifying very low spheroid penetration. After 24h, SNP exhibited excellent spheroid core penetration with almost 100% coverage, while LNP showed a similar background signal as that of 4 h treatment (**Figure 3.6)**. SNP with NP size less than 100 nm shows effective penetration, whereas LNP with NP size greater than 100 nm shows restricted penetration. This may be because smaller nano-carriers have transportation access to the collagen fibrils as they are small enough to diffuse between them, as interfibrillar spacing will be almost 70-130 nm, as the size of LNP is larger than 130 nm they have restricted penetration capability [35].

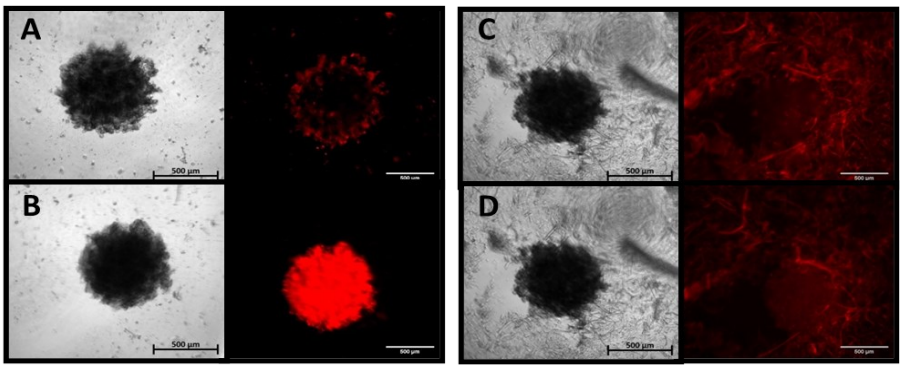

Figure-3.6: Spheroid penetration of DiI loaded SNP, after 4h incubation **(A)**, after 24h incubation **(B)** and DiI loaded LNP, after 4h incubation **(C)**, and 24h incubation **(D)**.

After successful optimization of the formulation process, a pH-sensitive nano-formulation was envisaged to evaluate their efficacy when co-encapsulated in an NP formulation. Designing nano-formulations for multi-drug delivery (in which different drugs target different cells) is significantly more challenging than designing single drug-loaded NPs. Nano-carriers, like liposomes, polymeric NPs, NPs, and drug-conjugates, can be taken up by cells [36], and the drug/s encapsulated in that nano-carrier would be effective against that cell only. Hence, a multi-drug-loaded nano-carrier targeting different types of cells should release the drugs efficiently upon reaching the TME so that the drug combination can act on their specific target cells. In this study, a pH-responsive polymer for TME-targeted drug release was synthesized. The extracellular pH in the TME is more acidic (pH 6.5 to 6.9) than the normal physiological pH (pH 7.2 to 7.5) due to the increased glycolysis and accumulation of lactic acid in the TME [37]. This lower pH in the TME was exploited for the NPs TME-specific release of PTX and RSQ. Due to the imidazole ring that contains s a lone pair of electrons on the unsaturated nitrogen atom, histidine can undergo pH-dependent protonation-deprotonation and polarity. Histidine remains in the non-protonated form at physiological pH, favoring interactions with other hydrophobic groups. At pH below its pKa, the imidazole ring becomes protonated and undergoes solubility transition, which can function as an efficient pH-sensitive moiety [38]. It has also been observed that histidine is responsible for the endosomal escape of the NPs because of its high pH buffering ability, commonly known as the proton sponge effect [39].

Synthesis and characterization of the pH-sensitive polymer:

We have developed a pH-sensitive NP delivery system for TME-targeted delivery of the drug combination. A five-armed star-shaped PLGA was modified by conjugating it with poly-(L-Histidine) as a pH-sensitive moiety at the end of each arm. This modified polymer should remain in the non-polar, unionized form in the systemic circulation at neutral pH, protecting the drug in encapsulated form. However, upon reaching the TME, it would get destabilized due to the protonation of histidine groups at the acidic pH and converted to ionic form, leading to a quick release of the entrapped drugs. The reaction scheme is depicted in **Scheme 1**. Initially, the terminal hydroxyl group of a commercially available star-shaped PLGA (s-PLGA-OH) was converted to the carboxyl (s-PLGA-COOH) by reacting with succinic anhydride. In a separate reaction, Boc-His (DNP)-OH was reacted with thionyl chloride in DMF to form DNP-NCA-HCl, then reacted with iso-propylamine for ring-opening polymerization and production of poly-(N-DNP-L-Histidine), which was then reacted with the previously formed s-PLGA-COOH to form s-PLGA-poly-Histidine-DNP in the presence of EDC and NHS.

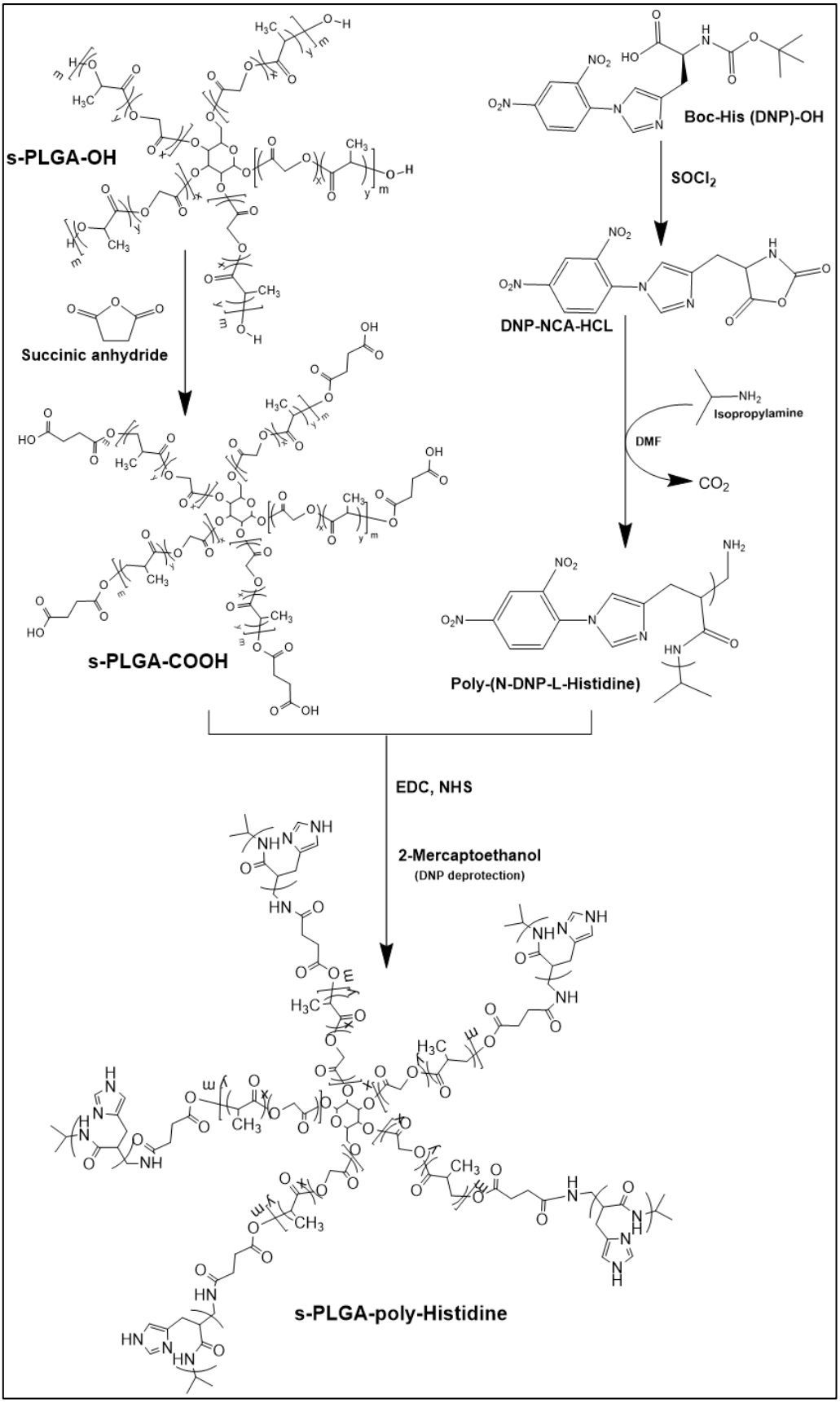

Scheme 1: Reaction scheme for the synthesis of s-PLGA-pH

After every step, the product was purified by precipitation in ice-cold DEE and dried under a vacuum. DNP deprotection was done by using 50% 2-mercaptoethanol. The final product was dialyzed against distilled water to remove byproducts if formed. It was then lyophilized, and the final yield was around 92%. It was then stored at -20 °C for further use. A linear PLGA (l-PLGA) was similarly modified to compare the polymer's shape to the pH-sensitive behavior. Poly-(N-DNP-L-Histidine) was reacted with l-PLGA-COOH in the presence of EDC and NHS and was purified with ice-cold DEE and dried under vacuum, followed by DNP deprotection. The final product obtained was characterized using 1H NMR (**Figure 3.7)**. Herein, Boc-His(DNP)OH has shown a peak at δ h12.6 ppm [which is of -COOH group of histidine, at δ 7.9, 8.63, and 8.68 ppm [which belonged to the DNP group (i1, i2, and i3)], and at δ j1.36 ppm [that corresponds to the Boc group] [40]. The 1H NMR spectrum (in DMSO- d_6) of NCA showed peaks at δ 8.2–9 ppm (the proton b, c, and d on phenyl group, DNP), δa 9.2 ppm (−N=CH−C), δe 7.9 ppm (−N=CH−N), δf 4.9 ppm (−CH−) and δg 3.20 ppm (−CH_2) (Figure-2). The 1H NMR spectrum (DMSO- d_6)) of poly-(Nim-L-histidine) has not shown peaks at δ 8.15–9.00 ppm (proton a, c, and d on phenyl group, DNP), which indicates the successful deprotection of DNP, δb 8.4 ppm (−N=CH−C), δe 7.4 ppm (−N=CH−N), δf 3.9 ppm (−CH−), δg 3.7 ppm (−CH2) and δh 1.4 ppm (−C(CH3)2) [40].

s-PLGA (sp) has shown peaks at δa 5.32, δb 4.81, and δc 1.7 ppm, which were also present in the final product, s-PLGA-pH.s-PLGA-pH (spH) showed peaks at δf1.2 ppm ((−$C(CH_3)_2$)), δ 7.3 ppm (−N=CH−N), δ 3.9 ppm (−CH−), and δd 3.6 ppm (−CH_2), which all are indicative of the histidine group. However, the peaks at δ 8.25–9.1 ppm (the proton on phenyl group, DNP) were absent, signifying the removal of the DNP moiety. Overall, the NMR spectrum established the successful formation of histidine-conjugated spH.

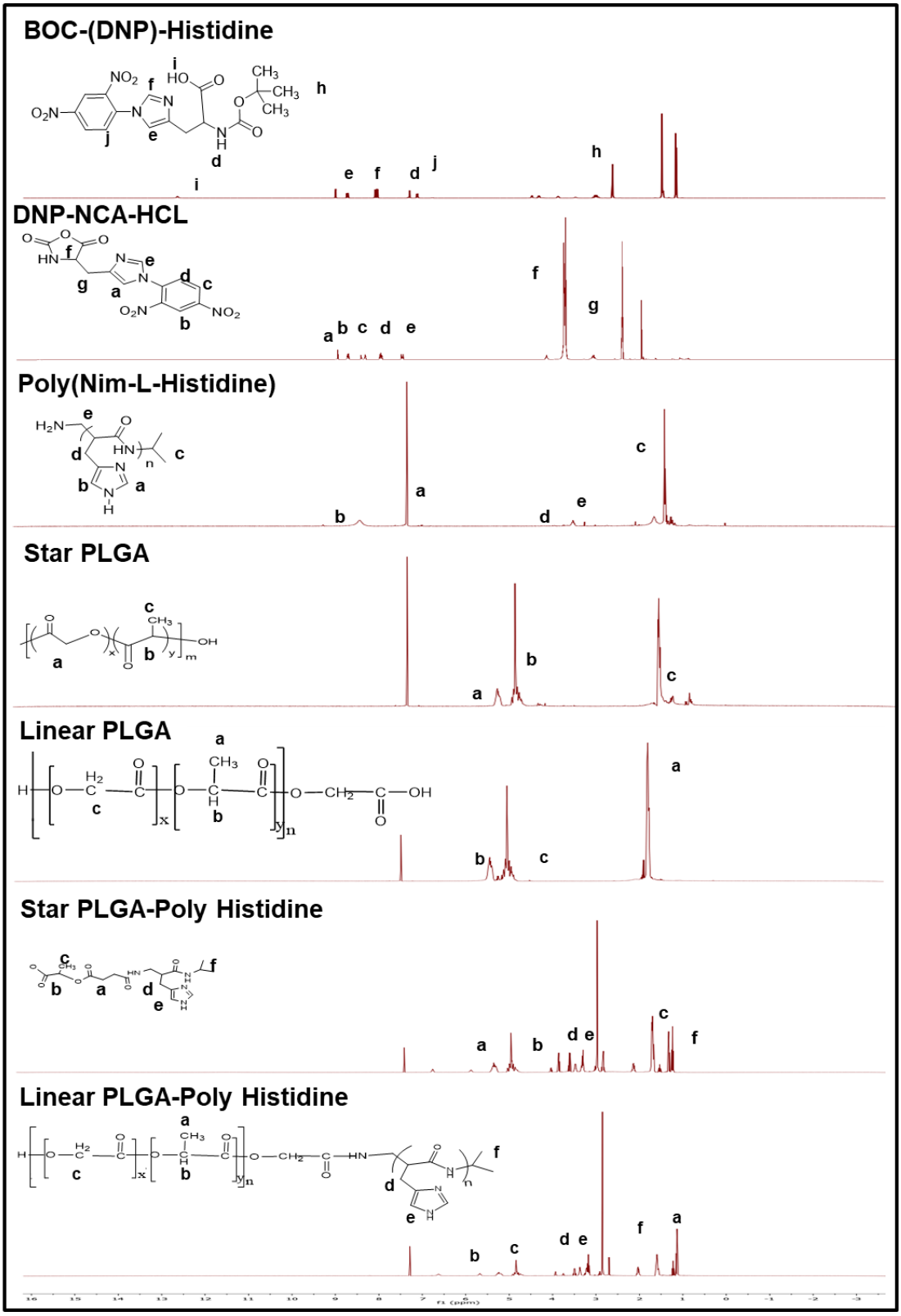

Figure 3.7: Structural characterization of the modified polymers using NMR spectroscopy.

Similarly, 1H NMR of l-PLGA (lp) revealed characteristic peaks at δa 1.6 ppm (−CH3), δc 4.97 ppm (−CH2 −), and δb 5.23 ppm (−CH−) [41]. l-PLGA-pH has shown the peaks similar to PLGA at δa 1.9 ppm (−CH_3), δc 4.99ppm (−CH_2−),andδb5.18 ppm (−CH−), along with δ d

1.5 ppm ((−C(CH$_3$)$_2$)), δ 7.24ppm (-N =CH -N), δ 3.9 ppm (−CH−), δe 3.6 ppm (−CH$_2$) of histidine group indicates the successful formation of histidine conjugated l-PLGA-pH (lpH).

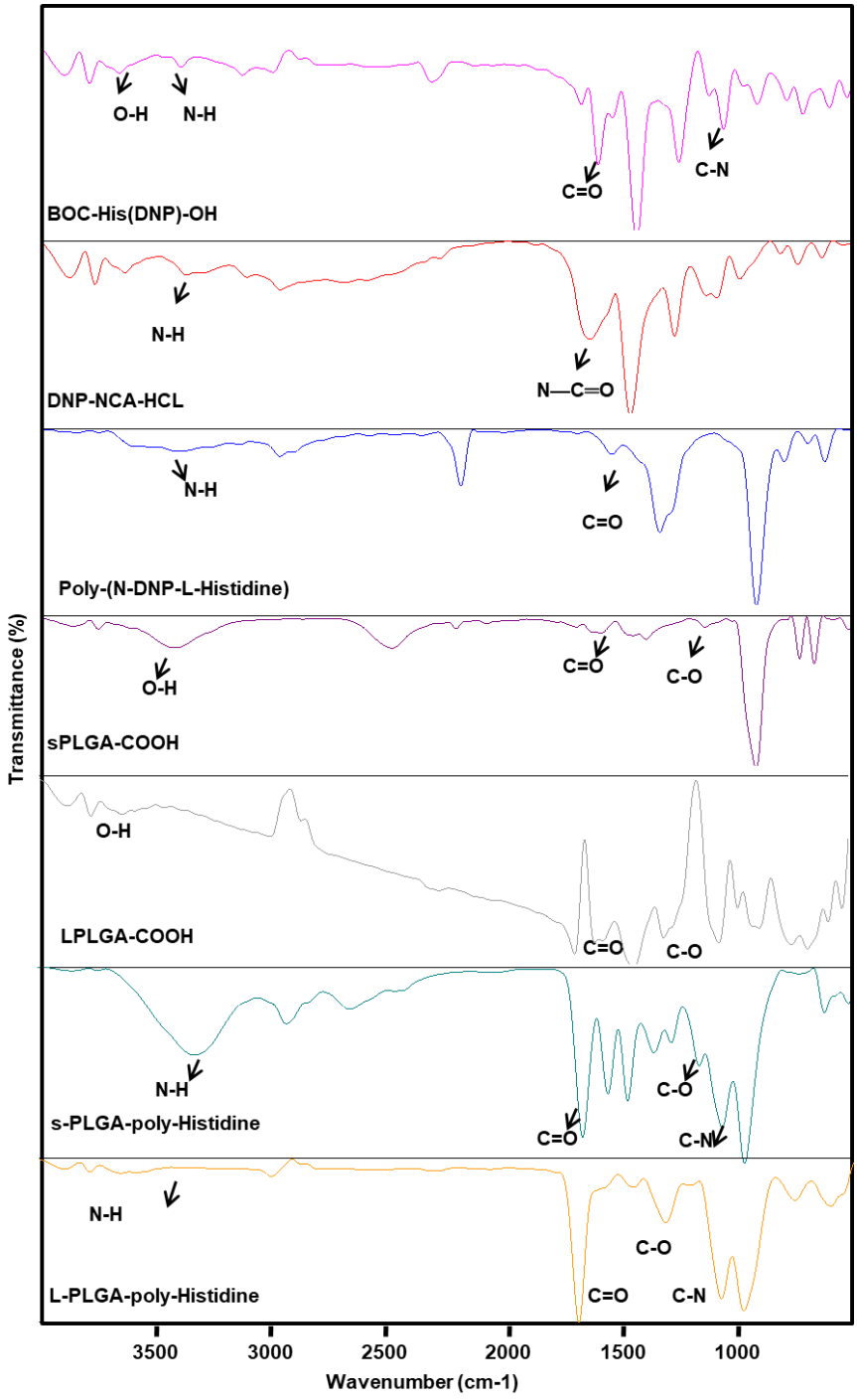

Figure 3.8: Structural characterization of the modified polymers using FT-IR spectroscopy.

Further FTIR analysis was carried out to confirm the successful conjugation of poly-histidine to sp (**Figure 3.8**). The absence of OH peak and presence of N-C=O peak has shown the DNP-NCA-HCl formation; after that, the presence of N-H and C=O has proved the formation of poly-(N-DNP-L-Histidine). In the FTIR spectra of spH, the absence of -OH stretch (at ~3200

cm^{-1}) indicated ester link formation between poly-histidine and sp. Along with the absence of the −OH group signal, spH also exhibited NH (3400cm^{-1}), stretching vibrations of histidine and C=O (1750 cm^{-1}), C-O (1100 cm^{-1}) stretching vibrations, and CN stretch (1089 cm^{-1}) of sp. Even with lp, the absence of O-H and the presence of C-N have shown the product formation of lpH. Altogether, 1H NMR and FTIR results confirmed the successful formation of spH and lpH.

Preparation and characterization of PTX and RSQ-loaded nanoparticles:

The microfluidic-based nanoprecipitation method was used to prepare the drug-loaded NPs using these pH-sensitive polymers. Both the drugs (PTX and RSQ [100µg and 2mg] were dissolved in ACN(1mL) containing 20 mg of the polymer. 0.5 % Soluplus (BASF Pharma) was used as a stabilizer in the aqueous phase (10mL). Both the phases (organic and aqueous) were injected into a micromixer chip with the help of a syringe pump. The aqueous-to-organic flow rate was optimized to a 1:10 ratio (organic 10 µL/min and aqueous 100 µL/min). Hydrodynamic flow focusing and turbulent mixing in the Herringbone mixture allowed for the rapid exchange of solvent, resulting in the drug-loaded NP formation. The resultant NP suspension was kept for overnight stirring at room temperature for solvent evaporation; then, it was dialyzed against distilled water to remove the organic solvent and un-entrapped drugs.

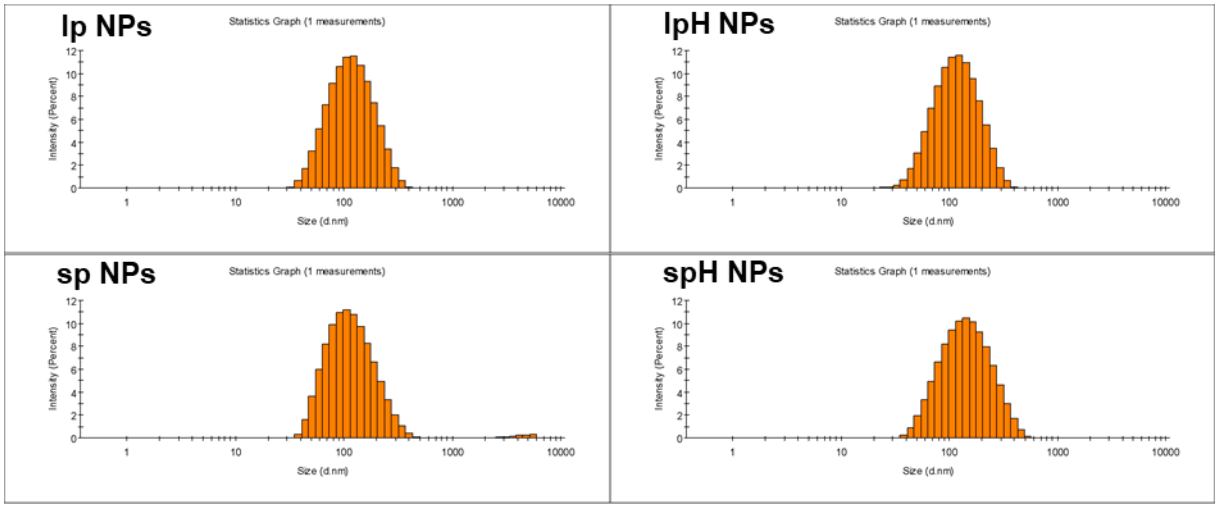

Figure 3.9: Particle size analysis of different NPs prepared with different polymers.

The same procedure was followed with all four polymers [linear PLGA (lp), star PLGA (sp), linear PLGA-polyhistidine (lpH), and star PLGA-polyhistidine (spH)] with similar amounts of drug, polymer, and stabilizer concentration to make NPs, and the particle size was analyzed. Uniform particle sizes and PDIs were observed with NPs prepared with all the polymers

(**Figure 3.9** and **Table 3.2).** The size was around 100-120nm, with a PDI of around 0.1-0.4. The Zeta potential of all four different NPs was found to be in the range of −6 to −8 **(Table 3.2**). Next, the entrapment efficiency and drug loading of PTX and RSQ were checked, as described in **Table 3.2**. All the NPs exhibited high entrapment efficiency and drug loading; however, moderately increased encapsulation was observed with the sp NPs over the lp NPs and after poly-histidine modification.

Table 3.2: Effect of polymer modification on physicochemical characteristics of NPs

Type	Size (nm)	PDI	EE (%)	LC (%)
sp NPs	120 ± 5.2	0.29 ± 0.03	74± 0.12% PTX, 69 ± 0.61% RSQ	10.5 ± 0.16%
spH NPs	128 ± 2.6	0.24 ± 0.12	80 ± 0.86% PTX, 85 ± 0.32% RSQ	9.83± 0.25%
lp NPs	121 ± 3.5	0.31 ± 0.02	69± 0.18% PTX, 64 ± 0.36% RSQ	9.61 ± 0.12%
lpH NPs	136 ± 3.2	0.28 ± 0.10	70 ± 0.21% PTX, 87 ± 0.32% RSQ	8.57 ± 0.27%

Next, the pH-dependent stability of all the formulations (sp, lp, spH, and lpH) was compared at two different pH: 7.4 and 6.5. First, pH-dependent change in the particle size was evaluated with the help of DLS. As depicted in **Figure 3.10A**, no significant change in size was observed in the lp and sp NPs at both pH levels even after 6h of incubation. Lp NPs had shown size of 212±1.7 nm in pH 7.4 and 191±2.3 in pH6.5. sp NPs exhibited a size of 174±2.5 nm in pH 7.4and 131±3.6 nm in pH 6.5.In both cases, PDI was between 0.1-0.3.On the other hand, both the pH-sensitive NPs exhibited pH-dependent size variation. lpH and spH NPs remained stable at pH 7.4 (169±5.3 nm and 195±6.2 nm, respectively) with a PDI of 0.1-0.3. However, at pH 6.5,a significant change in size happened. The size of lpH NPs was 2420±522.1 nm, and spH NPs were 8184±857.2 nm, with a PDI of 1, indicating high polydispersity (**Table 3.3**).

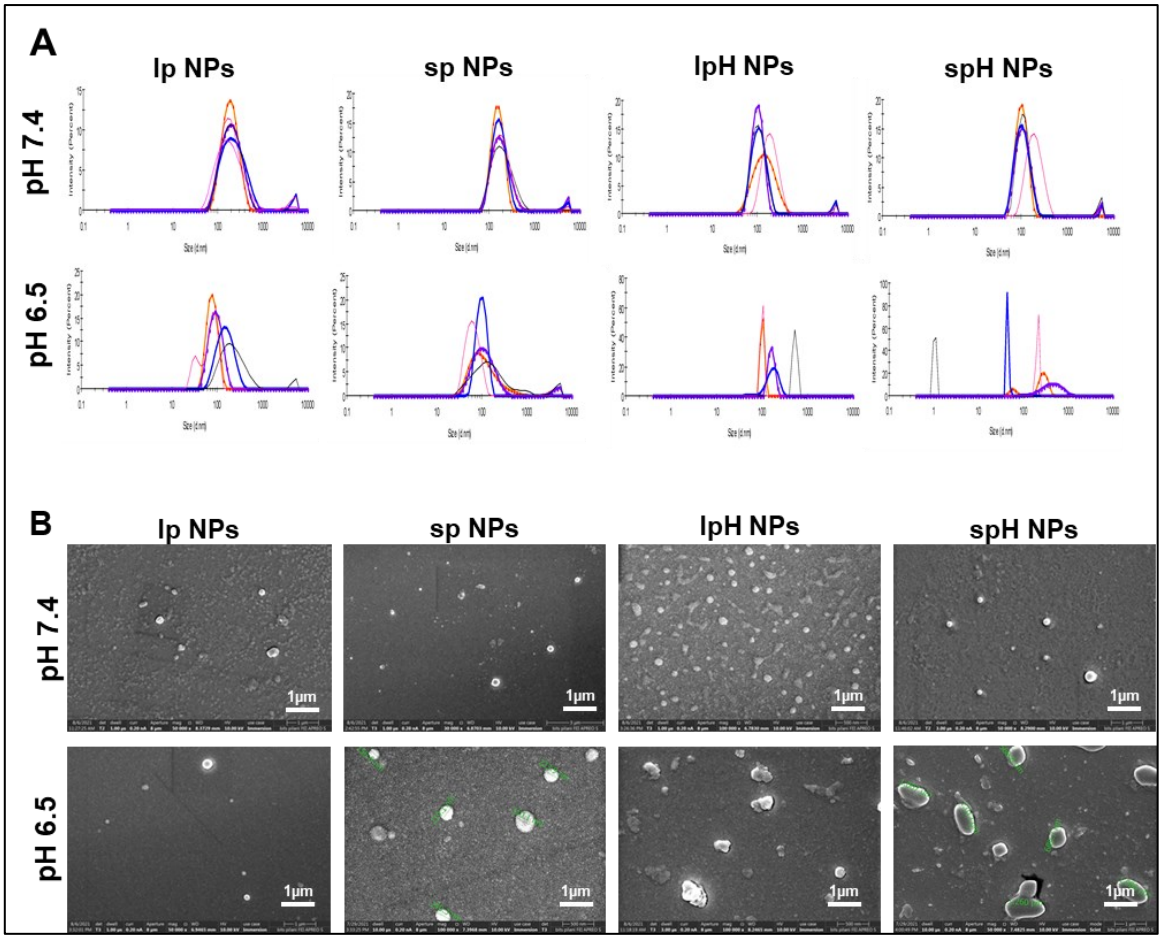

Figure 3.10:A: Particle size analysis through DLS of different NPs incubated at different pH (7.4 and 6.5) for 6h. **B:** SEM analysis of the size and shape of the NPs incubated at different pH (7.4 and 6.5).

Then, the pH-dependent change in particle size was evaluated by field emission scanning electron microscopy (FE-SEM) for further confirmation. Corroborating with the DLS data, lp and sp NPs were similar in size and morphology at pH 7.4 and 6.5 after 3h incubation (**Figure 3.10B**).

Table 3.3: Effect of pH on the size and PDI of the NPs measured using DLS (n = 3).

NP formulations	pH 7.4				pH 6.5			
	0h		6h		0h		6h	
	Size	PDI	Size	PDI	Size	PDI	Size	PDI
lp	176±3.1	0.2	212±1.7	0.3	109±2.4	0.2	191±2.3	0.2
lpH	98±2.4	0.2	169±5.3	0.2	280±2.3	0.3	2420±2.1	1
sp	164±4.1	0.2	174±2.5	0.1	101±3.7	0.3	131±3.6	0.1
spH	112±1.3	0.3	195±6.2	0.2	308±2.7	0.4	8184±8.2	1

In-vitro drug release:

To evaluate the effect of pH on the drug release pattern, an *in-vitro* cumulative drug release study of drug-loaded (PTX and RSQ) NPs prepared with different polymers incubated at different pH (7.4, 6.5, and 5.5) was performed. Compared to sp, lp was more sensitive to changes in the pH. The cumulative drug release after 72hfrom lp NPs was found to be 55±4.3%for PTX and 39±1.6% for RSQ in 5.5 pH buffer, while 26±3.5%PTX and 17±0.8% RSQ were released in 7.4 pH buffer (**Figure 3.11A**), an increase of more than20% in both of the drug released at pH 5.5 compared to pH 7.4. Contrarily, sp NPs were found to be more stable, with 52±3.3% PTX and 49±4.8% RSQ released in 5.5 pH buffer, whereas 42±2.4% PTX and 39±3.6% RSQ was released in pH7.4 buffer (**Figure 3.11B**), a difference of about 10%. However, with poly-His modification, both the polymers exhibited significantly increased drug release at acidic pH. lpH NPs exhibited 79±3.8% PTX release and 88±4.6% RSQ release at pH 5.5, compared to 64±4.5% PTX and 43±5.17% RSQ release at pH 7.4 (**Figure 3.11C**). spH NPs had shown even higher drug release at pH 5.5, which was 91±2.3% for PTX and 92±5.6% for RSQ, compared to 54±3.2% PTX and 51±3.4% RSQ release at pH 7.4 (**Figure 3.11D**).

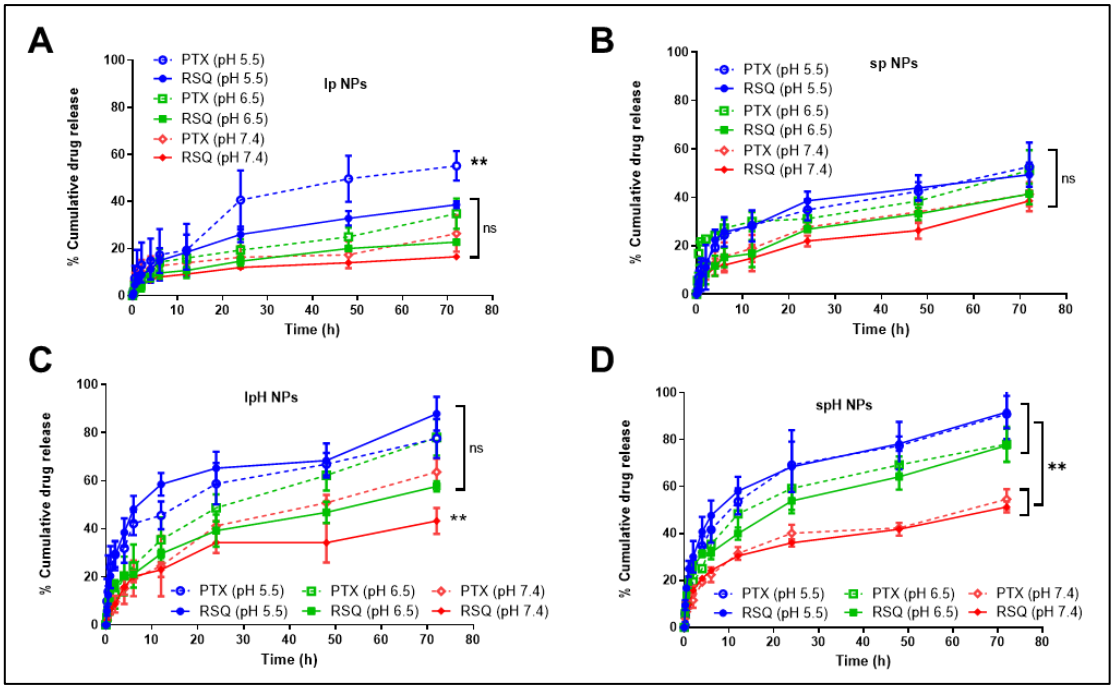

Figure 3.11: Cumulative drug release study from NPs prepared with different polymers.

Interestingly, for spH NPs, the drug release pattern showed almost 1:1 % release of PTX and RSQ. As our initial data indicated, maintaining this drug ratio might be necessary for improved synergistic efficacy. Earlier studies have demonstrated the impact of the polymer shape on drug loading and drug release [42]. It has been proven that multi-armed polymers have more drug loading than linear polymers [43]. In the drug release study, both lpH and spH NPs exhibited increased drug release at lower pH than neutral pH; however, with the spH NPs, the drug release ratio between PTX and RSQ was almost 1:1, which was not observed in lpH NPs (**Figure 3.11**). Maintaining the specific dose ratio could be beneficial for synergistic activity. The hypothesis was that in the case of the lpH NPs, only one end of the polymer was ionizing. However, the body of the polymer remained stable, which could lead to differential drug release. In the case of spH NPs, due to histidine modification at the end of each arm of its multi-arm structure, ionization would lead to the same charge repulsion among all the arms, leading to complete opening of the NPs, releasing the encapsulated drug entirely. This hypothesis was supported by the NP size variation at different pHs (**Figure 3.10** and **Table 3.3**).

3.4. Conclusion:

Clinical translation of nanomedicine is hindered due to the complexities associated with the formulation and scale-up process. The development of a simple, continuous flow process for the synthesis of nano-carriers with readily available and economical excipients can enhance the possibility of clinical success. The current study established that drug-encapsulated NPs

can be easily prepared with a continuous-flow microfluidics system. NPs smaller than 100 nm showed enhanced cytotoxic activity against both 2D and 3D in-vitro models, better tumor cell internalization, and 3D spheroid penetration. For tumor-targeted delivery of PTX+RSQ combination, a comparative study was done between two different pH-sensitive nano-delivery systems, one made with a linear polymer and the other with a multi-armed, star-shaped polymer, to evaluate the impact of polymer structure on the pH-sensitive property. The multi-arm polymer exhibited improved efficacy in terms of pH-dependent size variation and drug release; a smart carrier system for the TME-specific release of the drug combination further improved its *in-vitro* efficacy.

References:

1. Swetha, K.L. and A. Roy, *Tumor heterogeneity and nanoparticle-mediated tumor targeting: the importance of delivery system personalization.* Drug Deliv Transl Res, 2018. **8**(5): p. 1508-1526.
2. Ernsting, M.J., et al., *Factors controlling the pharmacokinetics, biodistribution and intratumoral penetration of nanoparticles.* J Control Release, 2013. **172**(3): p. 782-94.
3. Choi, Y.H. and H.K. Han, *Nanomedicines: current status and future perspectives in aspect of drug delivery and pharmacokinetics.* J Pharm Investig, 2018. **48**(1): p. 43-60.
4. Hua, S., et al., *Current Trends and Challenges in the Clinical Translation of Nanoparticulate Nanomedicines: Pathways for Translational Development and Commercialization.* Front Pharmacol, 2018. **9**: p. 790.
5. Abou-Hassan, A., O. Sandre, and V. Cabuil, *Microfluidics in inorganic chemistry.* Angew Chem Int Ed Engl, 2010. **49**(36): p. 6268-86.
6. Song, Y., J. Hormes, and C.S. Kumar, *Microfluidic synthesis of nanomaterials.* Small, 2008. **4**(6): p. 698-711.
7. Yang, Y., S. Liu, and J. Geng, *Microfluidic-Based Platform for the Evaluation of Nanomaterial-Mediated Drug Delivery: From High-Throughput Screening to Dynamic Monitoring.* Curr Pharm Des, 2019. **25**(27): p. 2953-2968.
8. Roy, A., et al., *Selective targeting and therapy of metastatic and multidrug resistant tumors using a long circulating podophyllotoxin nanoparticle.* Biomaterials, 2017. **137**: p. 11-22.
9. Yang, Y., et al., *Comparison of Tumor Penetration of Podophyllotoxin-Carboxymethylcellulose Conjugates with Various Chemical Compositions in Tumor Spheroid Culture and In Vivo Solid Tumor.* Bioconjug Chem, 2017. **28**(5): p. 1505-1518.
10. Barbuti, A.M. and Z.S. Chen, *Paclitaxel Through the Ages of Anticancer Therapy: Exploring Its Role in Chemoresistance and Radiation Therapy.* Cancers (Basel), 2015. **7**(4): p. 2360-71.
11. Mukhtar, E., V.M. Adhami, and H. Mukhtar, *Targeting microtubules by natural agents for cancer therapy.* Mol Cancer Ther, 2014. **13**(2): p. 275-84.
12. Orr, G.A., et al., *Mechanisms of Taxol resistance related to microtubules.* Oncogene, 2003. **22**(47): p. 7280-95.
13. Barkat, M.A., et al., *Nanopaclitaxel therapy: an evidence based review on the battle for next-generation formulation challenges.* Nanomedicine (Lond), 2019. **14**(10): p. 1323-1341.
14. Barua, S. and S. Mitragotri, *Challenges associated with Penetration of Nanoparticles across Cell and Tissue Barriers: A Review of Current Status and Future Prospects.* Nano Today, 2014. **9**(2): p. 223-243.
15. Tang, L., et al., *Investigating the optimal size of anticancer nanomedicine.* Proc Natl Acad Sci U S A, 2014. **111**(43): p. 15344-9.
16. Ahmad, Z., et al., *Polymeric micelles as drug delivery vehicles.* Rsc Advances, 2014. **4**(33): p. 17028-17038.
17. Ma, P. and R.J. Mumper, *Paclitaxel Nano-Delivery Systems: A Comprehensive Review.* J Nanomed Nanotechnol, 2013. **4**(2): p. 1000164.
18. Baer, D.R., *The Chameleon Effect: Characterization Challenges Due to the Variability of Nanoparticles and Their Surfaces.* Front Chem, 2018. **6**: p. 145.
19. Mülhopt, S., et al., *Characterization of Nanoparticle Batch-To-Batch Variability.* Nanomaterials (Basel), 2018. **8**(5).
20. Salvioni, L., et al., *Thirty Years of Cancer Nanomedicine: Success, Frustration, and Hope.* Cancers (Basel), 2019. **11**(12).
21. Zhang, S., et al., *Bile acid transporter mediated STC/Soluplus self-assembled hybrid nanoparticles for enhancing the oral drug bioavailability.* Int J Pharm, 2020. **579**: p. 119120.
22. Homayouni, A., et al., *Curcumin nanoparticles containing poloxamer or soluplus tailored by high pressure homogenization using antisolvent crystallization.* Int J Pharm, 2019. **562**: p. 124-134.

23. Tanida, S., et al., *Evaluation of the Micellization Mechanism of an Amphipathic Graft Copolymer with Enhanced Solubility of Ipriflavone.* Chem Pharm Bull (Tokyo), 2016. **64**(1): p. 68-72.
24. Bernabeu, E., et al., *Novel Soluplus(®)-TPGS mixed micelles for encapsulation of paclitaxel with enhanced in vitro cytotoxicity on breast and ovarian cancer cell lines.* Colloids Surf B Biointerfaces, 2016. **140**: p. 403-411.
25. Moretton, M.A., et al., *A glucose-targeted mixed micellar formulation outperforms Genexol in breast cancer cells.* Eur J Pharm Biopharm, 2017. **114**: p. 305-316.
26. Breslin, S. and L. O'Driscoll, *The relevance of using 3D cell cultures, in addition to 2D monolayer cultures, when evaluating breast cancer drug sensitivity and resistance.* Oncotarget, 2016. **7**(29): p. 45745-45756.
27. Perche, F. and V.P. Torchilin, *Cancer cell spheroids as a model to evaluate chemotherapy protocols.* Cancer Biol Ther, 2012. **13**(12): p. 1205-13.
28. Operti, M.C., et al., *Microfluidics-Assisted Size Tuning and Biological Evaluation of PLGA Particles.* Pharmaceutics, 2019. **11**(11).
29. Torchilin, V.P., *Recent approaches to intracellular delivery of drugs and DNA and organelle targeting.* Annu Rev Biomed Eng, 2006. **8**: p. 343-75.
30. Rathore, B., et al., *Nanomaterial designing strategies related to cell lysosome and their biomedical applications: A review.* Biomaterials, 2019. **211**: p. 25-47.
31. Serrano-Puebla, A. and P. Boya, *Lysosomal membrane permeabilization as a cell death mechanism in cancer cells.* Biochem Soc Trans, 2018. **46**(2): p. 207-215.
32. Zhang, Y.R., et al., *Strategies to improve tumor penetration of nanomedicines through nanoparticle design.* Wiley Interdiscip Rev Nanomed Nanobiotechnol, 2019. **11**(1): p. e1519.
33. Nunes, A.S., et al., *3D tumor spheroids as in vitro models to mimic in vivo human solid tumors resistance to therapeutic drugs.* Biotechnol Bioeng, 2019. **116**(1): p. 206-226.
34. Xu, X., M.C. Farach-Carson, and X. Jia, *Three-dimensional in vitro tumor models for cancer research and drug evaluation.* Biotechnol Adv, 2014. **32**(7): p. 1256-1268.
35. Pluen, A., et al., *Role of tumor-host interactions in interstitial diffusion of macromolecules: cranial vs. subcutaneous tumors.* Proc Natl Acad Sci U S A, 2001. **98**(8): p. 4628-33.
36. Donahue, N.D., H. Acar, and S. Wilhelm, *Concepts of nanoparticle cellular uptake, intracellular trafficking, and kinetics in nanomedicine.* Adv Drug Deliv Rev, 2019. **143**: p. 68-96.
37. Feng, L., et al., *The acidic tumor microenvironment: a target for smart cancer nano-theranostics.* National Science Review, 2018. **5**(2): p. 269-286.
38. Li, S. and M. Hong, *Protonation, tautomerization, and rotameric structure of histidine: a comprehensive study by magic-angle-spinning solid-state NMR.* J Am Chem Soc, 2011. **133**(5): p. 1534-44.
39. Swetha, K.L., et al., *Development of a tumor extracellular pH-responsive nanocarrier by terminal histidine conjugation in a star shaped poly (lactic-co-glycolic acid).* European Polymer Journal, 2021. **147**: p. 110337.
40. Hong, W., et al., *Thermo- and pH-responsive copolymers based on PLGA-PEG-PLGA and poly(L-histidine): synthesis and in vitro characterization of copolymer micelles.* Acta Biomater, 2014. **10**(3): p. 1259-71.
41. Dao, T.P.T., et al., *A new formulation of curcumin using poly (lactic-co-glycolic acid)—polyethylene glycol diblock copolymer as carrier material.* Advances in Natural Sciences: Nanoscience and Nanotechnology, 2014. **5**(3): p. 035013.
42. Chen, Y., et al., *Synthesis, characterization, and evaluation of paclitaxel loaded in six-arm star-shaped poly(lactic-co-glycolic acid).* Int J Nanomedicine, 2013. **8**: p. 4315-26.
43. Tao, W., et al., *Docetaxel-loaded nanoparticles based on star-shaped mannitol-core PLGA-TPGS diblock copolymer for breast cancer therapy.* Acta Biomater, 2013. **9**(11): p. 8910-20.

Chapter 4:

In-vitro efficacy of NPs

4.1 Introduction:

In the previous chapter, we screened different TLR agonists for their immunostimulatory activity and found that resiquimod (RSQ; TLR 7/8 agonist) was the most effective for TAM activation [1]. The only problem associated with RSQ is its solubility and toxicity, because of which there is no systemic formulation available, which also limits its use. Most of the chemotherapeutics available to date are immunosuppressive in nature, making it challenging for tumor depletion [2]. One significant exception is paclitaxel (PTX), which was found to show immune stimulatory activity against different cancers like breast and ovarian cancer [3, 4]. We have shown in the previous chapter that the PTX and RSQ combination has shown effective anticancer activity against cancer and macrophage cell lines when given in free drug form [1]. To deliver this drug combination targeted to the tumor, we need a drug delivery system that can deliver multiple drugs and should be able to protect the drugs from metabolism during systemic circulation and can release the payload upon reaching the TME and act on their target cells [5]. To attain this, triggered release NPs will be highly useful [6]. We have also explored the acidic pH of the TME to prepare pH-sensitive NPs that would remain stable in the vascular pH and get triggered with the acidic pH of the TME for the release of its cargo and its characterization in the previous experiments [7].

After successfully developing and optimizing the NPs, we aim to explore the efficacy of the prepared triggered release NPs encapsulating PTX and RSQ against tumor-macrophage co-culture systems in 2D and 3D. The activity of the pH-responsive NPs was evaluated in 2D, quasi-3D (Transwell system), and 3D multicellular spheroid (tumor + macrophage). We have evaluated macrophage uptake of the NPs, cancer cell uptake, spheroid penetration, macrophage polarization (M2 to M1), and mechanisms involved, like ROS induction.

4.2. Materials and Methods:

PTX was received as a gift sample from INTAS Pharmaceuticals Ltd, and RSQ was purchased from TCI, India. Soluplus was procured as a free gift sample from BASF. cDNA synthesis kit and SYBR green qPCR kit were purchased from Bio-RadThe solvents used for HPLC analysis and polymer synthesis: methanol (HPLC grade), Acetonitrile (HPLC grade), dimethylformamide (DMF), diethyl ether (DEE), dimethyl sulfoxide (DMSO), and chloroform (CHCl3), were procured from Merck, India. HPLC analysis was done using a Shimadzu LC instrument (Kyoto, Japan). Zodiac C-18 column (5 mm particle size, L £ ID 15 cm £ 4.6 mm) was used as the stationary phase. All other chemical reagents used were of AR grade.

Cell Culture:

4T1 (a mouse breast cancer cell line derived from the mammary gland tissue of BALB/c strain) and RAW 264.7 (mouse monocyte-macrophage cell line) were separately cultured in Dulbecco's Modified Eagle Medium (DMEM), with 10% fetal bovine serum and 50 units/ml penicillin, and 50 mg/ml streptomycin at 37 °C, 5% CO_2 in a humidified atmosphere. Cells were sub-cultured at 85% confluency using Trypsin−EDTA solution (0.05%) for cell detachment.

Cancer-Macrophage Co-Culture and Complex Spheroid Model

Quasi-3D RAW 246.7 cells after co-culture with 4T1, only 4T1 spheroids were made and co-cultured with RAW246.7. Briefly, 4T1 cells at 10,000 cells / 10ml (0.2% methyl cellulose-containing cell culture medium) were placed as hanging drops on the lid of the cell culture Petri dish. Spheroids were humidified by putting PBS in a Petri dish. After 24h of incubation, spheroids were transferred into 1% agarose-coated wells (in 24well plates) with 1ml cell culture medium. Then RAW246.7 cells at a density of 10,000 cells were plated on a Transwell (0.4mm, polycarbonate membrane) inserted in 4T1 spheroids (10 spheroids per well) containing well.

4T1+RAW264.7 spheroids were prepared. Briefly, cells (7,500 4T1 cells and 2,500 RAW 264.7) at 10,000 cells / 10ml (in 0.2% methyl cellulose-containing cell culture medium) were placed as hanging drops on the lid of the cell culture Petri dish. The hanging drops were humidified by putting PBS in the Petri dish's base to prevent the spheroid's drying. After that, the hanging drops were transferred to 1% agarose-coated round bottom 96 well plates with 200 µl cell culture medium and incubated for 24 h, yielding the 4T1+RAW 264.7 spheroids.

***In-vitro* tumor cell Internalization**

4T1 cells were seeded at a density of 50,000 cells on coverslips placed in a six-well plate with 2 mL DMEM media in each well and incubated for 24 h. Followed by four h treatment with DiI-loaded NPs. After treatment, the media was removed and washed thrice with PBS. After that, the cells were fixed with 100% methanol for 20 min at −20 °C, followed by washing with phosphate buffer saline (PBS) two times, and then the coverslips were placed on the glass slides using DAPI containing mounting media. The prepared slides were then examined using a Confocal microscope at 10X magnification.

Macrophage uptake study:

Macrophage uptake of the NPs was studied using fluorescently labeled NPs prepared by loading DiI in the NPs by substituting drugs. RAW 264.7 macrophage cells (50,000 cells/well) were seeded on coverslips placed in 6 well plates. After 24 h, macrophages were treated with lp NPs, lpH NPs, sp NPs, and spH NPs (1 µg/mL DiI). After 6 h incubation with DiI-loaded NPs, the media was removed, and the cells were washed thrice with PBS. Then, cells were fixed with 100% ice-cold methanol for 10 min. Then, they were washed three times with PBS. Next, the nucleus of the cells was stained by incubating the cells with DAPI (1 µg/ mL) solution for 10 min and then washed with PBS thrice. Afterward, the coverslips were drained and mounted on glass slides using glycerol. Microscopy was done using confocal laser scanning microscopy (CLSM) at 20× magnification.

Endosomal escape

4T1 cells were seeded on coverslips at 50,000 cells / well density in a six-well plate with 2 mL DMEM media and incubated for 24 h. After treatment with DiI-loaded NPs for 1h, NP-containing media was removed and washed with PBS three times. Then, the cells were incubated in DMEM media for 3 h. After that, media was removed, and cells were washed with PBS twice, followed by incubation with lysotracker green for 20 min; then, cells were fixed with 100% ice-cold methanol for 20 min at −20 °C. After that, cells were washed with PBS 2 times; the coverslips were then mounted on the glass slides using DAPI containing mounting media. The prepared slides were then examined using a confocal microscope at 20X magnification. The images were processed with ZEN 2.3 software, and colocalization was analyzed using ImageJ software (version: Fiji) with the Coloc 2 plugin.

Spheroid penetration of NPs:

Spheroid penetration of the NPs was studied using DiIl-loaded NPs. 5-day old spheroids were treated with NPs containing 10 µM of DiI and were incubated for 24 h. Imaging of spheroids was done through fluorescent microscopy (ZEISS, Axio Vert. A1) at 4X magnification. For optical sectioning, spheroids were treated for 48h, and image acquisition was performed using a Confocal microscope at 10X objective magnification. Ten z-stack images with 10% surface overlap were acquired for each spheroid with a 20 µm-z step. The image represented is the stacked image of 10 z-stack images captured. Images were then processed with Zen 2.3 software.

Evaluation of payload release of NPs using DiI/DiO colocalization in 3D spheroids:

Drug release from the NPs in the spheroid microenvironment was studied using DiI + DiO loaded NPs by evaluating DiI/DiO colocalization in the tumor spheroids. 5-day old spheroids were treated with 100 µg/ml of DiI + DiO loaded. They were incubated for 24h; after that, spheroids were taken for imaging through a confocal microscope (ZEISS LSM 880, AxioObserver) at 10X magnification. The green fluorescence of DiO was measured at an excitation wavelength of 488 nm and an emission wavelength of 532 nm. Red fluorescence of DiO was measured at excitation wavelength 514 nm and emission wavelength 560 nm. 10 z-stack images with 10% surface overlap were acquired with a 15 µm-z step. The image represented is the stacked image of 10 z-stack images captured. Images were then processed with Zen 2.3 software.

Analysis of drug release using FRET:

FRET analysis confirmed the payload release from the DiI + DiO NPs in the tumor spheroid microenvironment. After treating the tumor spheroids with DiI + DiO co-loaded NPs for 24h, microscopic analysis was done using ZEISS LSM 880, Axio Observer at 10X magnification. Images were captured using the DiO channel (488 nm excitation, 535 ± 20 nm emission) and FRET channel (488 nm excitation, 560 ± 20 nm emission). Z-stack images were captured with a 15 µm z-step. The FRET ratio was calculated using the following formula.

FRET ratio = $I_{FRET} / (I_{FRET} + I_{DiO})$

I_{FRET} is the intensity of the FRET signal, and I_{DiO} is the intensity of the DiO signal.

Cytotoxicity assay (2D and 3D):

For cell viability assay of 2D culture, 4T1/RAW cells were seeded at 5000 cells/ well density in a 96-well plate. After 24 h of incubation, cells were treated with drug solutions (0.5-500 nM PTX, 0.1-1µM RSQ in the initial screening, and 5nM PTX and 1µM RSQ in further studies) and incubated for 72 h at 37 °C with 5% CO_2. No drug treatment was given in the control cells, and the same amount of complete medium was added. After 72h of incubation, cells were treated with 200µl of 1 mg/ml MTT solution dissolved in the complete medium. After 4 h of incubation with MTT, the medium was replaced with 200 µl of DMSO to dissolve the formazan crystal formed by the viable cells. Optical density at 570 nm was measured by removing background absorbance at 630 nm. Cell viability was calculated using the following formula:

Cell Viability (%) = (mean absorbance value of drug-treated cells)/ (mean absorbance value of control) × 100

For cell viability assay of 3D culture, treatment was given for 72 h with free drug and encapsulated drugs equivalent to 10nM PTX and 2μM RSQ. Further, the spheroids were collected into 1.5 ml centrifuge tubes with medium and centrifuged for 10 min at 200×g. The supernatant was removed and replaced with a medium containing MTT (1mg/mL). After 4 h of incubation, MTT was replaced with DMSO (500 μl) to dissolve the formazan crystals formed by the viable cells. Then, cell viability was calculated, as mentioned earlier.

Apoptosis assay:

PI/Annexin-FITC staining by flow cytometry was performed to measure apoptosis. This was achieved by using only tumor cells (4T1), only macrophages (RAW 264.7), and 3D complex spheroid, where PTX(5nM), RSQ (1 μM), PTX (5nM) + RSQ (1 μM) sp NPs, and spH NPs were used as treatment groups. After 72h treatment, cells were trypsinized and washed twice with phosphate-buffered saline. Then, cells were suspended in 500 μl of 1× binding buffer (Annexin Binding Bufer (5X) for flow cytometry, Thermo Fisher Scientific). After that, the cells were stained with four μl Annexin V-FITC (Annexin V-FITC, Invitrogen™) and 10 μl of PI (propidium iodide solution, FluoroPure™ Grade, Invitrogen™). The samples were incubated for 15 minutes at room temperature (25 °C) in dark conditions. The cytometric analysis was performed in a flow cytometer (CytoFLEX, Beckman Coulter), and the data were analyzed by CytExpert software. % Apoptosis was calculated over all viable cells and after subtracting the autofluorescence of cells. The results were represented as mean±SEM values.

Tumor-specific cell death

a) Live-Dead Staining:

We have used Transwell (Quasi 3D system) to identify the tumor-specific cell death. Here, we have made 4T1 spheroids and added them in the lower chamber of the Transwell and Raw 264.7 macrophage cells (2D) on the Transwell membrane in the top chamber. After 72h of treatment, we stained the 4T1 spheroids and 2D macrophages using Annexin (10 μg/mL) and Propidium Iodide (PI- 1μg/mL) diluted with PBS. Annexin labels all the nuclei in blue of all the viable cells, and PI labels the nuclei of dead cells in red. The staining was attained after incubating it for 15 min in the dark at 37°C, followed by microscopic analysis.

b) Luciferin tagged 4T1 cells (LUC2-4T1):

We have used luciferin-tagged 4T1 cells to confirm further tumor-specific cell death to check the fluorescence intensity after treating the LUC2-4T1 cells with luciferin-D. The experiment was done in 2D conditioned media and 3D complex spheroid (4T1+RAW 264.7 cells). In 2D conditioned media, RAW 264.7 cells were initially treated for 24h. The treated media was added to luc-2-4T1 cells and incubated for 24h, followed by luciferin-D treatment (4µg/ml) for 1h. Afterward, the cells were washed with PBS, and microscopic images were captured using a fluorescent microscope. The same procedure was followed for 3D complex spheroid after 24h of treatment.

Spheroid invasion assay:

3D invasion assay was performed using 24-well plates with transwell inserts (Corning, New York, USA). Briefly, 24 well inserts were pre-coated with Matrigel (BD Biosciences, New Jersey, USA), and 4T1+RAW 264.7 cell complex tumor spheroids were made and allowed to grow in the top chambers of the transwell. After that, the spheroids were treated with PTX, RSQ, PTX+RSQ, sp NPs, and spH NPs. Parallely, 900 µL DMEM complete media was added to the transwell lower chamber and kept for incubation for 24h at 37°C. After the treatment, the cells on the transwell membrane were removed using a cotton swab. After that, the cells penetrated through the membrane and were fixed using 4% ice-cold methanol and staining with 0.1% crystal violet. Microscopic images of the migrated cells were captured using an inverted microscope, and the number of migrated cells was counted using ImageJ software.

Intracellular reactive oxygen species (ROS) generation by DCFDA assay

Cellular ROS in 2D cells and 3D spheroids were analyzed by DCFDA assay. The ROS present in the cells can convert DCFDA into a highly fluorescent compound 2′, 7′–dichlorofluorescein (DCF). The amount of ROS can be quantified by measuring the fluorescence intensity of DCF. 2D cells and 3D tumor spheroids were treated with free drugs and N.P.s, for 24 h. Then, the treatment containing media was removed, followed by DCFDA incubation (20 µM) for 15 min. After that, fluorescent images were captured through an inverted fluorescence microscope (ZEISS, Axio Vert.A1) at 10X magnification.

Gene expression Analysis:

Total RNA from the cells was isolated from TRI reagent, which was then used to synthesize cDNA using a cDNA synthesis kit. qRT-PCR reactions were carried out using SYBR green

super mix. GAPDH was used as a housekeeping gene, which normalized specific primer interest data. Primers used in the present study are given below:

GAPDH : F: ACCCAGAAGACTGTGGATGG, R : TCTAGACGGCAGGTCAGGTC,
TNF-α : F: GCCTCTTCTCATTCCTGCTTG, R: CTGATGAGAGGGAGGCCATT,
IL-10 : F: CCCTGGGTGAGAAGCTGAAG, R : CACTGCCTTGCTCTTATTTTCACA.
IL-12 : F: ACGAGAGTTGCCTGGCTACTAG, R: CCTCATAGATGCTACCAAGGCAC
CD-86 : F: ACGATGGACCCCAGATGCACCA, R: GCGTCTCCACGGAAACAGCA,
CD-206 : F: GTTCACCTGGAGTGATGGTTCTC, R: AGGACATGCCAGGGTCACCTTT
TGF-β : F: CCTGTCCAAACTAAGGC, R : GGTTTTCTCATA GATGGCG,
VEGF: F: ACAAACCGATCGGAGCTGG, R: CTTGGCATGGTGGAGGTACA,
iNOS : F: AACTTGTTTGCAGGCGTCAG, R: CACATTGCTCAGGGGATGGA
SOS2: F: CACCAGTGGAATGGCACATCAG, R : CTTTGGTCCAGACACTCCCTAC

Enzyme-linked immunosorbent assay (ELISA):

After confirming the macrophage polarization using PCR, we confirmed by using ELISA. After the treatment of cells 2D conditioned media, quasi 3D and 3D spheroids, the cell culture supernatant media were collected and analyzed for TNF-α and IL-10 secretion using an ELISA kit following the manufacturer's instructions (Ray biotech). All the samples were analyzed in triplicates. The data was analyzed by measuring the absorbance using a microplate reader (Epoch) at 450nm. TNF-alpha and IL-10 standard curves were plotted with the concentrations suggested according to the kit.

Ex-vivo stimulation studies of PD-MIP NP/CWNP on splenocytes

For evaluating the biological activity of the drug combination and the prepared NPs, Splenocytes were stimulated with these NPs ex-vivo. Briefly, Splenocytes were isolated from the spleen of BALB/C mice and co-cultured with 4T1 cells; then, the complex spheroids were made using splenocytes + 4T1 cells and transferred into a 6-well plate, 30 spheroids/well. The cells were then stimulated with treatment groups (PTX, RSQ, PTX+RSQ, sp NPs, spH NPs). After 72h of treatment, RNA was isolated and analyzed for M1 and M2 marker expression and antigen presentation ability using MHC-I and MHC-II expression.

Statistical analysis :

All the data were analyzed using GraphPad Prism software version 8. One-way ANOVA was used when there were≥ 2 groups compared to the control; post hoc Tukey's test was performed when the means of every group was compared with every other group. All the data was represented in mean ± SD. In all the graphs, ns indicates a nonsignificant difference, and * indicates $p < 0.001$.

4.3.Results and Discussion:

Cellular uptake analysis:

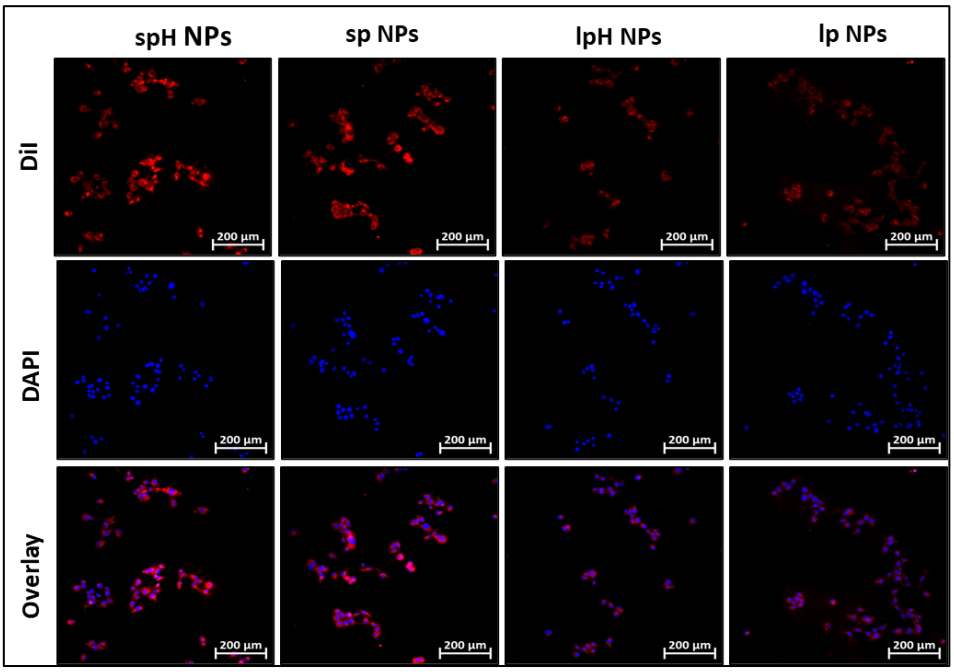

Figure 4.1 Tumor cell internalization of DiI loaded NPs in 4T1 tumor cells studied by confocal fluorescent microscope at 20X magnification (scale bar = 200 µm)

To evaluate the cellular uptake in tumor cells, macrophages, and colocalization studies, DiI-loaded NPs and DiO +DiI co-loaded NPs were prepared. Herein, we have screened all the 4 different NPs preparations, i.e, both pH-sensitive NPs [linear PLGA-polyhistine NPs (lpH NPs), star-PLGA-polyhistidine NPs (spH NPs)] and non-pH-sensitive NPs [(linear PLGA NPs (lp NPs), star PLGA NPs (sp NPs)], to confirm whether the pH-sensitive behavior and shape of the polymer affect the intracellular delivery of the NPs (**Figure 4.1**).

For tumor cell uptake, 4T1 cells were treated with DiI-loaded NPs for 4h, and then fluorescent microscopy was done using a ZEISS Axio Observer Z1/7 fluorescent microscope. Both lp and sp had a low accumulation of DiI, with most of the DiI in the periphery of the cell, representing a localized accumulation of NPs in the tumor cells. Both lpH and spH exhibited increased

intracellular distribution of the DiI. More uniform distribution was observed with spH NPs, which might be because of the uniform release of the payload from spH NPs, which also resembles the increased tumor cell death of spH NPs.

Macrophage Uptake:

As the NPs were prepared with a surface coating of Soluplus, to study the effect of this coating on lp NPs, sp NPs, lpH NPs, and spH NPs on macrophage uptake, we have treated DiI loaded NPs to macrophage cell RAW 264.7 for 24h and then observed under confocal microscopy. A moderate amount of macrophage uptake was observed with the lp, sp, and lpH NPs, whereas uptake of the spH NPs was found to be slightly lower. PLGA NPs have a high affinity towards serum proteins, which helps in macrophage uptake [8]. A uniform coating of Soluplus on spH NPs might reduce protein binding, leading to decreased macrophage uptake (**Figure 4.2**).

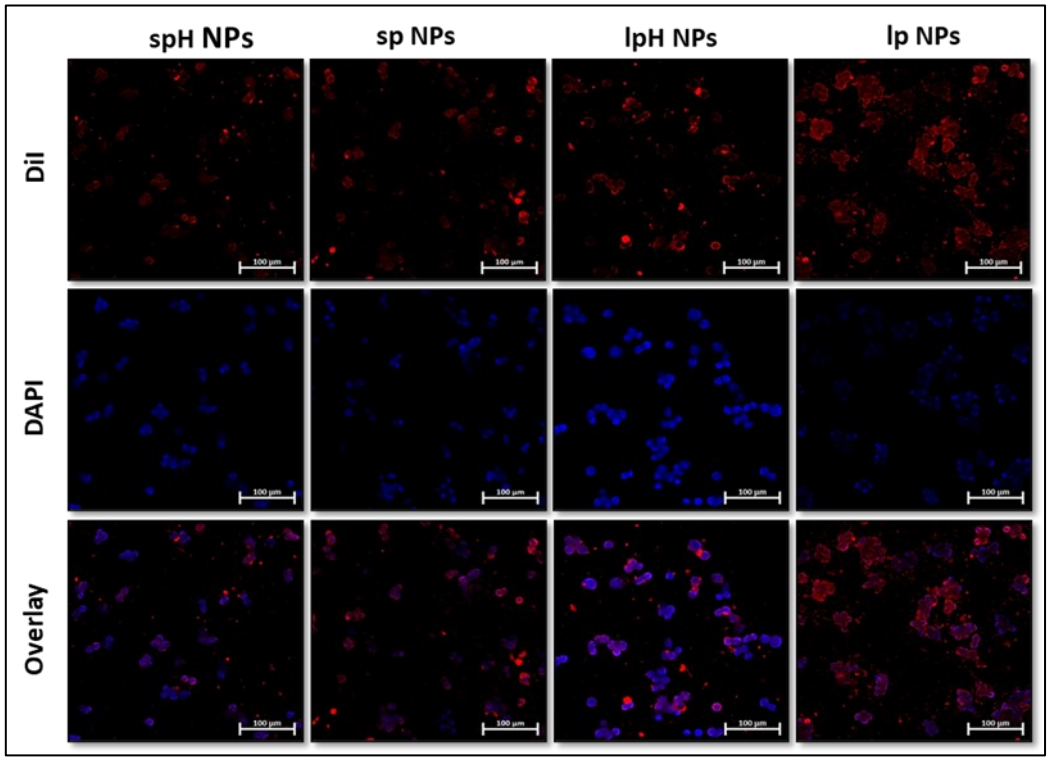

Figure 4.2: Macrophage uptake of DiI loaded NPs using confocal microscopy (scale bar= 100 µm)

Endosomal Escape:

Endosomal escape of the NPs keeps them stable by preventing their degradation in the lysosomal compartments, for which cytosolic delivery of the NPs is essential for maintaining their efficacy. This is because of the uniform distribution of the drug targets in the cytosol [9]. It can be achieved using pH-sensitive NPs, which help endosomal escape [10]. In multiple previous studies, uniform distribution of drugs in the cytosol from pH-sensitive NPs was

observed [11]. Here, we treated the 4T1 tumor cells with DiI-loaded lp, sp, lpH, and spH NPs for 4h, and then the cells were stained with lysotracker followed by DAPI as nucleus stain. Images were captured using the ZEISS Axio Observer fluorescent microscope, and colocalization analysis was done by using Zen software. **Figure 4.3** shows a higher colocalization index of lp and sp when compared to lpH and spH NPs.

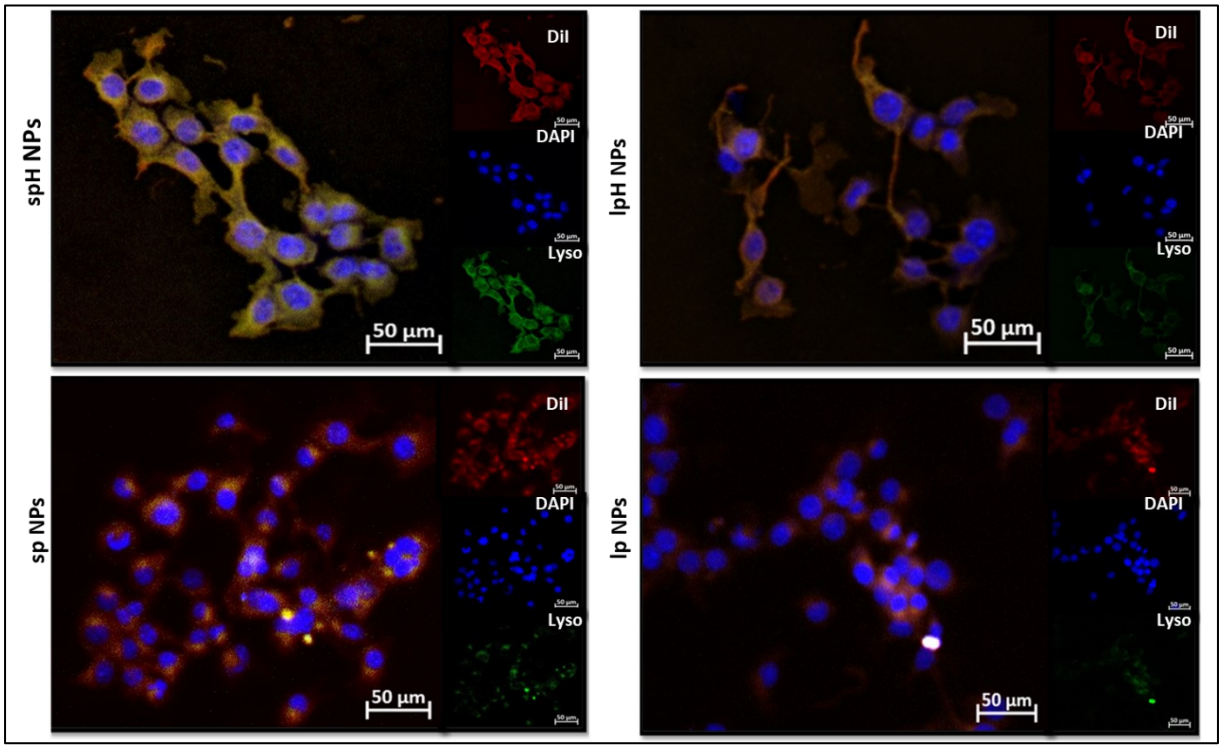

Figure 4.3: Endosomal escape of DiI-loaded NPs studied using lysotracker colocalization assay; images were captured using fluorescent microscopy at 40X magnification (scale bar = 50 µm).

3D Tumor Spheroid Penetration:

Next, drug penetration using these two pH-sensitive NPs (lpH and spH NPs) was analyzed in the cancer spheroids using DiI-loaded NPs. Non-pH-sensitive NPs were used as a control. Here, spheroids were treated with DiI-loaded lp, sp, lpH, and spH NPs and were observed under the microscope after 24h. **Figure 4.4A** shows a significant difference in the distribution and penetration of DiI fluorescence between the pH-sensitive and non-pH-sensitive NPs. With both lp and sp NPs, DiI fluorescence was mainly localized in the periphery of the cancer spheroid. However, with lpH and spH NPs, significantly increased spheroid core penetration was observed (**Figure 4.4B)**. Among all the groups, spH NPs exhibited the highest spheroid core penetration, significantly more than lpH NPs.

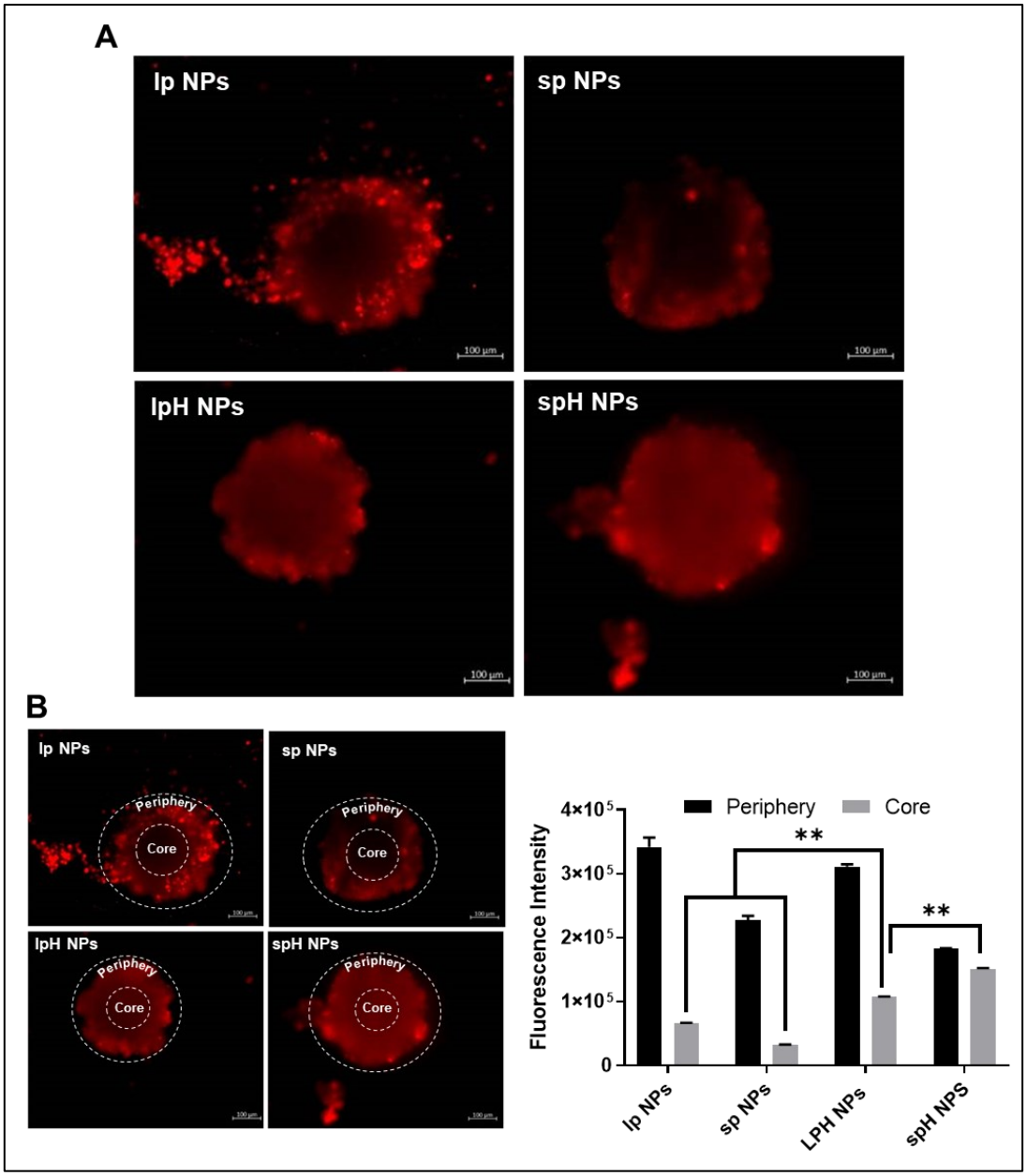

Figure 4.4: A. Tumor spheroid penetration of DiI loaded NPs was evaluated after 24 h treatment using fluorescence microscopy at 10X magnification (scale bar = 100 µm) B. Quantifying fluorescence intensity in tumor spheroid core and periphery using ImageJ software. ** indicates $p<0.01$.

DiI/DiO colocalization study in the tumor-macrophage complex spheroid:

pH-sensitive NPs help in deeper penetration of the NPs to the core of the spheroids when compared to non-pH-sensitive NPs. To confirm the pH-sensitive release of the NPs at the TME is the reason for the enhanced penetration, we have analyzed the colocalization of the NPs loaded with DiI and DiO in tumor complex spheroids. The images were captured using a confocal microscope, and Zen software calculated the colocalization index accordingly. After 24h of treatment of the DiO+DiI loaded NPs, we have found increased colocalization of non-pH-sensitive NPs, i.e., 0.84 with lp NPs and 0.75 with sp NPs, compared to 0.6 with lpH NPs

and 0.5 with spH NPs. The lowest colocalization index of spH NPs (**Figure 4.5**) indicated the release of payload, i.e., DiI +DiO at the acidic pH of the TME, when other groups were found to be stable with the dyes encapsulated inside showing increased colocalization.

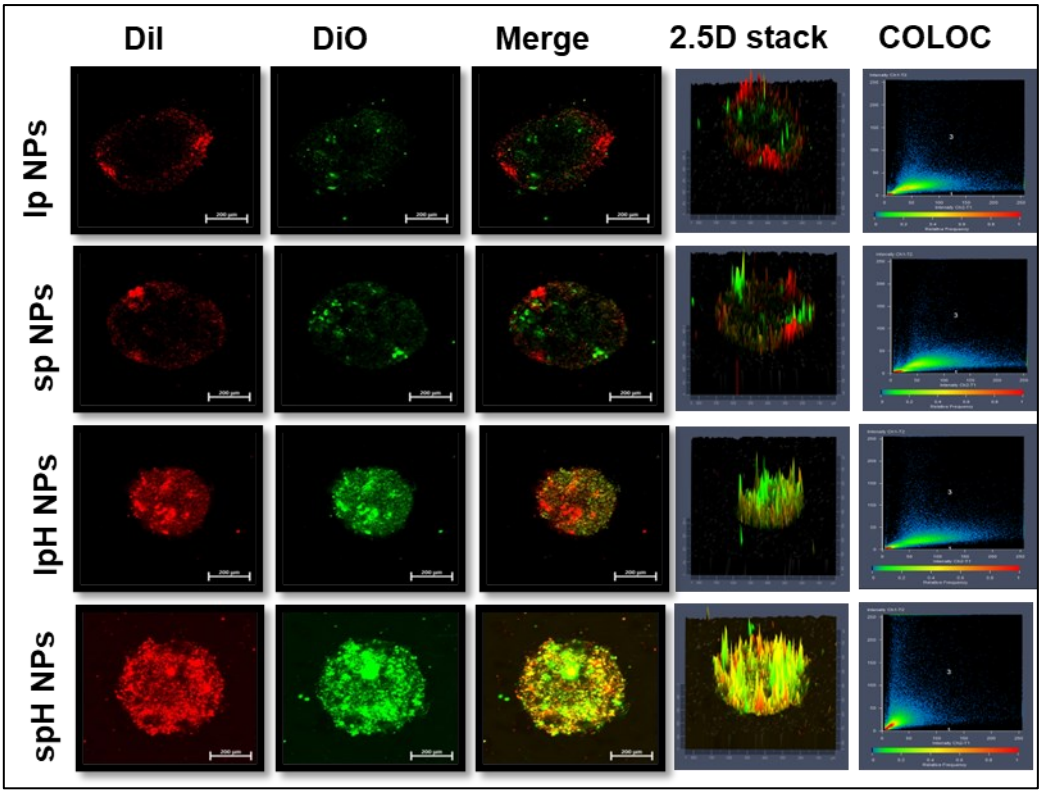

Figure 4.5: Analysis of the release of the payload by the dye-loaded NPs in the tumor spheroid model: A) Colocalization study of DiI and DiO, delivered using DiI + DiO loaded lp, lpH, sp, and spH NPs to the tumor spheroids (scale bar = 200 µm).

FRET analysis:

After confirming the pH-sensitive release of the payload from NPs, we cross-verified it using FRET signaling from DiO and DiI co-loaded NPs. FRET efficiency is calculated based on the closeness of the dyes present, and the excitation wavelength of one dye will be used as the emission wavelength of the other dye. When DiI and DiO are encapsulated in the NP, they will be very close to each other with higher FRET efficiency, whereas when they are released, their FRET efficiency decreases. After treating the spheroids with DiI +DiO loaded NPS, FRET images were captured using excitation 488nm and 535 nm emission for DiO, which is also used as excitation for DiI. Interestingly, we have observed a significant decrease in FRET signaling with spH NPs 0.39 when compared to others, i.e., lpH NPs- 0.41, sp NPs- 0.59, lp NPs -0.78, indicating effective release of payload with spH NPs when compared to others (**Figure 4.6A&B).**

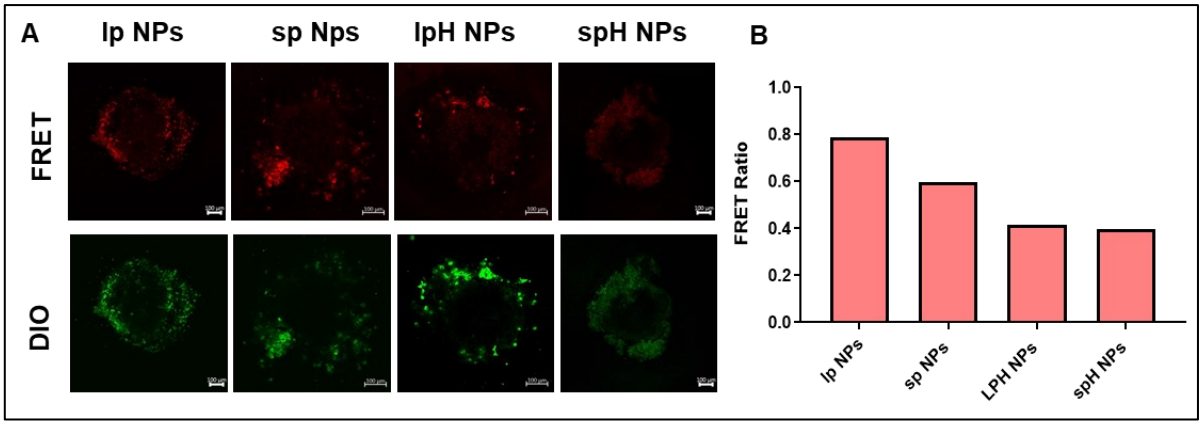

Figure 4.6: A) Microscopic evaluation of FRET analysis between DiO and DiI to evaluate the release of the dyes from the lp,lpH, sp, and spH NPs (scale bar = 200 µm). D) FRET ratio with all the NPs

Cytotoxicity analysis:

In the drug penetration analysis, spH NPs exhibited the highest penetration. Based on that observation, spH NPs were selected for further in-vitro efficacy analysis, and sp NPs were used as the control. Next, the effect of NP encapsulation of the drugs on the direct cytotoxic activity was evaluated with both spH and sp NPs. Both 4T1 cancer and RAW 264.7 macrophage cells were separately treated with the native drugs, their combination, and the drug combination encapsulated in the poly-His modified NPs at the dose of 5 nM PTX and 1 µM RSQ. Against only 4T1 cells, treatment with the drugs alone or in combination (both native and NP encapsulated) exhibited moderate cytotoxicity. Cell viability was found to be 75±2.3% with PTX alone, 86±1.1%with RSQ alone, and 74±2.3% with PTX+RSQ. With sp N.P.s, cell viability was 74±1.6%, and with spH N.P.s, it was 71±3.1% (**Figure 4.7A**). Against only RAW 264.7 cells, all drug treatments showed very low cytotoxicity, with more than 95% cell viability observed with all the treatments (**Figure 4.7B**).

Next, the cytotoxic potency of the drug combination against the co-culture of the 4T1 cancer cells and RAW 264.7 macrophage cells was evaluated. Initially, a complex cancer spheroid model, prepared with 4T1 and RAW 264.7 cells, was developed to mimic the TME in an *in-vitro* system (**Figure 4.7C**). These spheroids were treated with free drugs, and NP encapsulated drugs at the dose of 10nM PTX and 2µM RSQ for 72 h. The dose of drugs was doubled for cancer spheroid treatment compared to monolayer culture because the cancer spheroids exhibit resistance.[12] Cell viability was measured by MTT assay. As depicted in **Figure 4.7D**, treatment with PTX and RSQ alone resulted in marginal cell death, with 76±2.3% and 81±3.8% cell viability with PTX and RSQ, respectively. However, the drug combination group observed a significantly increased cell death. Cell viability was found to be 51±2.6% with PTX+RSQ

combination treatment. This data indicated that treatment with the drug combination could have synergistic efficacy. Interestingly, encapsulation of PTX+RSQ in the pH-sensitive NPs exhibited a differential effect. With the sp NPs, the cell viability was 58±5.5%, whereas, with spH NPs, the cell viability was 29±3.6%. The significantly higher (p<0.05) cell death with the spH NPs could be due to the more uniform (maintaining 1:1 ratio of PTX and RSQ, as shown in release data **Figure 3.12**) drug release observed in the spH NPs.

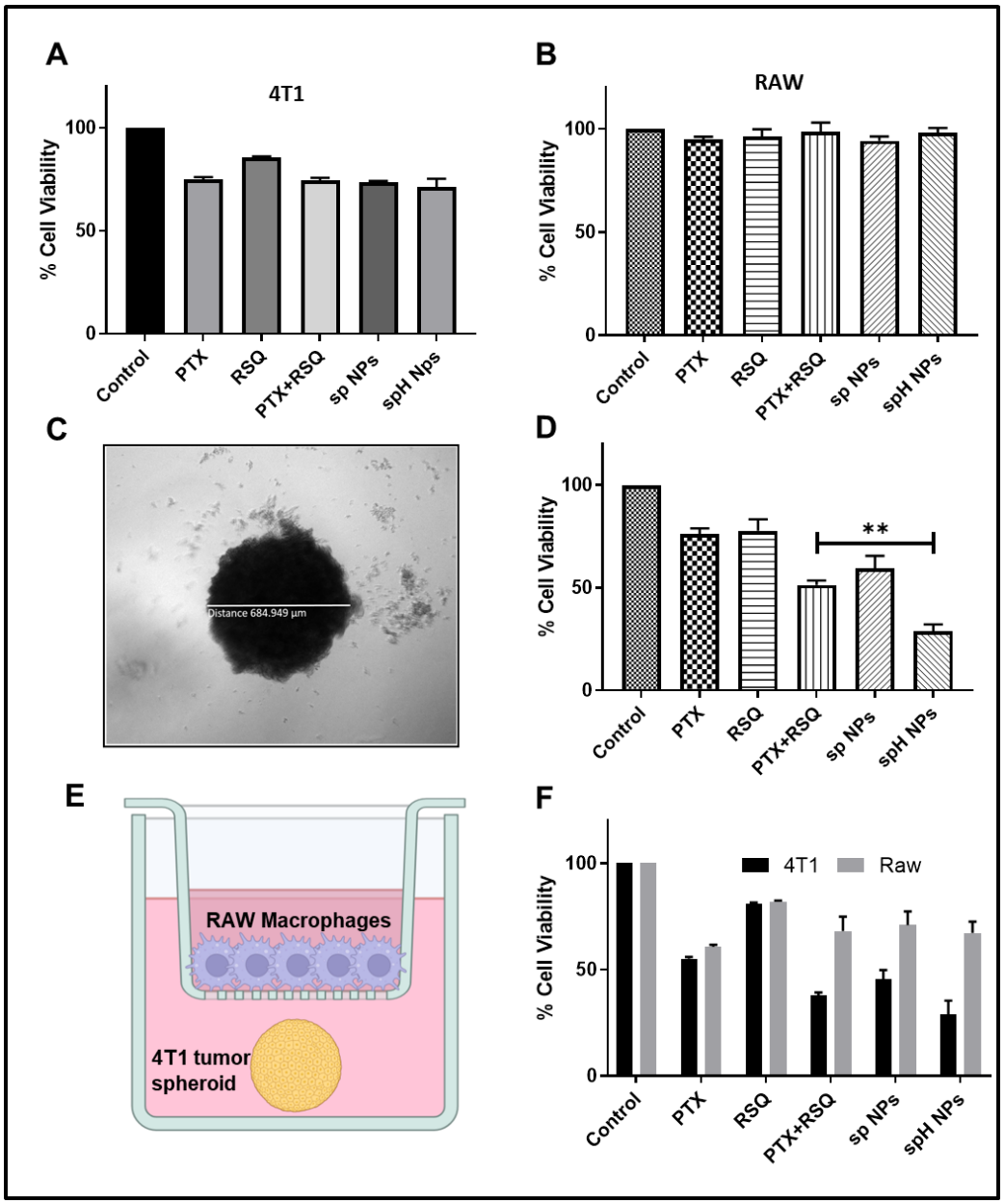

Figure 4.7:A. Direct cytotoxic activity of the drug-loaded NPs against 4T1 tumor cells. B. Direct cytotoxic activity of the drug-loaded NPs against RAW 264.7 macrophage cells. C. Microscopic image of a complex spheroid made with 4T1 tumor and RAW264.7 macrophage cells. D. Cytoxic activity of the drug-loaded NPs against the complex spheroid model. E. Designing a quasi-3D-coculture system to analyze differential death of tumor cells and macrophages. F. Analysis of cell viability of 4T1 tumor and RAW 264.7 macrophages in the quasi-3D co-culture experiment. ** indicates p<0.05.

The mixed cancer spheroid model can mimic the actual in-vivo cancer more consistently. However, analyzing the death of individual cell types is challenging in that model. A transwell-based co-culture experiment was performed to understand the impact of the combination treatment on both 4T1 cancer cells and the RAW macrophages individually. In this experiment, cancer spheroids were made using 4T1 cancer cells, which were kept in the lower chamber of the trans-well, whereas RAW 264.7 cells were plated in the upper chamber (**Figure 4.7E**). Drug treatment was given in the lower chamber; however, as the RAW 264.7 cells are exposed in the same medium, they are equally exposed to the drug. Corroborating the observation in the experiment using the mixed cancer spheroid model, increased cancer cell death was observed with the PTX+RSQ combination treatment (38±2.5% viability). The death of the macrophages was relatively low (68±5.3% viability). Among the NP encapsulated drug treatment, treatment with spH NPs exhibited increased cancer cell death (29±8.6% viability) compared to sp NPs (46±6.5% viability) (**Figure 4.7F**), supporting the observation in the previous experiment with mixed cancer spheroid model.

Apoptosis assay:

Following our observation of the enhanced cytotoxic effects associated with the PTX+RSQ combination and NPs, our interest turned to investigating the specific contribution of apoptotic cell death in the context of PTX+RSQ treatment. To address this, we conducted an apoptosis analysis utilizing flow cytometry with Annexin V-FITC/PI staining. The treatment groups encompassed the PTX+RSQ combination, sp NPs, and spH NPs. In both 2D and quasi-3D (Transwell) as well as 3D experimental setups, we observed a slight increase in apoptotic cells with the PTX+RSQ combination administered as free drugs (10%-4T1, 7%-RAW 264.7, 21%-3D complex spheroid). However, a substantial increase in the percentage of apoptotic cells (Annexin V+PI-positive cells) was observed in the spH NPs group (35%-4T1, 8%-RAW 264.7, 27%-3D complex spheroid), as depicted in **Figure 4.8**.

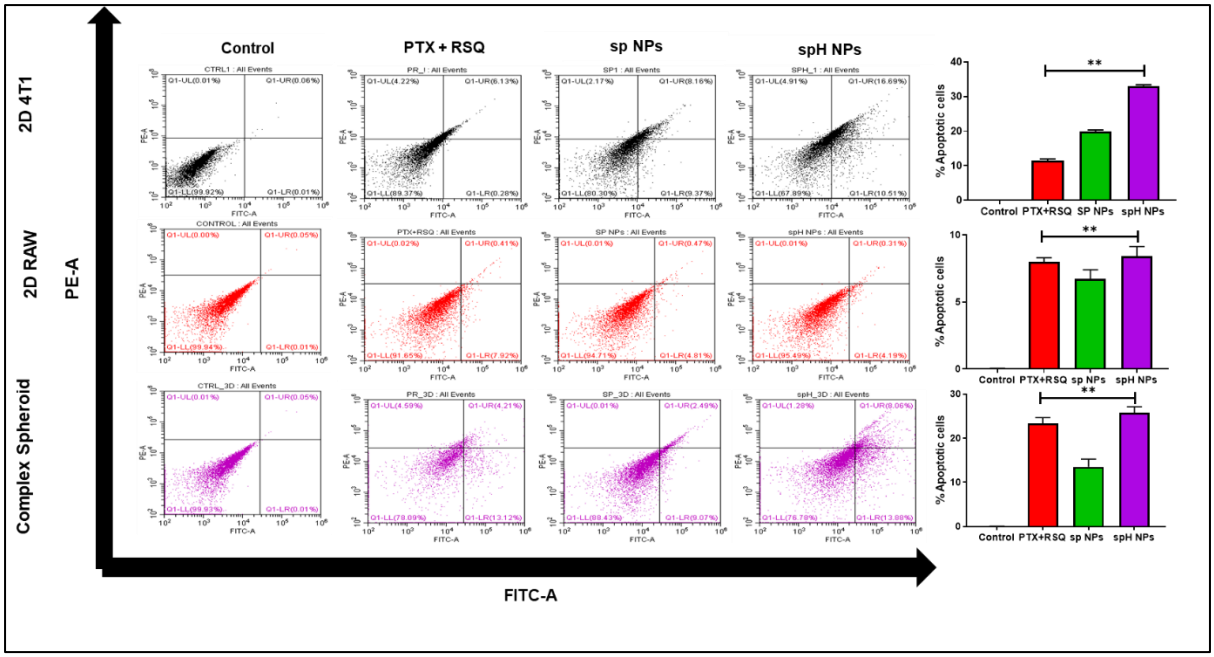

Figure 4.8: Apoptosis assay in A) 4T1 cells, B) RAW cells, C) 4T1+ RAW complex spheroid treated with different groups (control, PTX, RSQ, PTX +RSQ, sp NPs, and spH NPs)

This data strongly suggests that the cytotoxicity associated with the PTX+RSQ combination primarily operates through the mechanism of apoptosis. Importantly, these results are consistent with our previous findings of improved cytotoxic behavior exhibited by the PTX+RSQ combination in the MTT assay (**Figure 4.7**), and more improvement in the %apoptosis rate with spH NPs might be because of the triggered release of the payload at the acidic pH; thus the drug combination and NPs gave us complementary evidence of the efficacy of this treatment approach.

Live/dead staining:

We conducted live-dead staining experiments to validate the tumor-specific cell death observed in our cytotoxicity data. In this study, we formed spheroids composed of 4T1 tumor cells and allowed them to grow in the lower chamber of a Transwell system. At the same time, 2D macrophages were cultured on the polycarbonate membrane in the upper chamber. We exposed all experimental groups, including those treated with PTX, RSQ, a combination of PTX and RSQ, sp NPs, and spH NPs, for 72 hours, followed by the fluorescent images to assess changes in the morphology of both 4T1 spheroids and 2D macrophages.

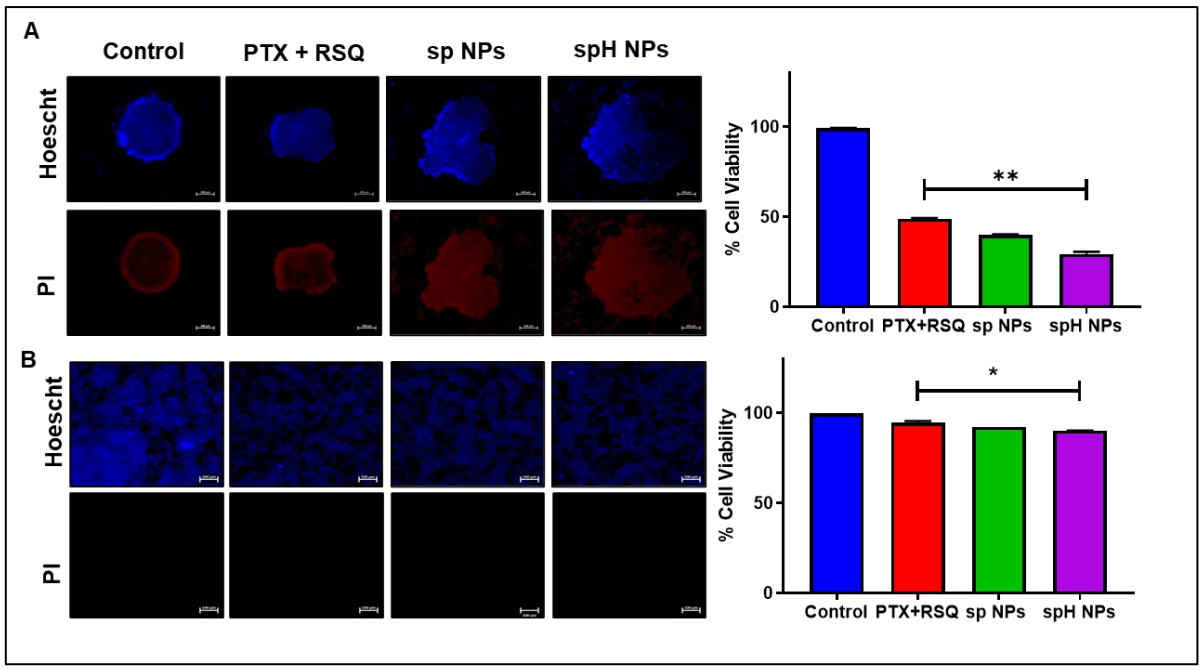

Figure 4.9: Live/dead staining in transwell system of 4T1 tumor and 2D raw 264.7 cells. **A)** Representative fluorescent images of 4T1 tumor spheroids used to analyze cell death stained with Propidium iodide (PI) and Hoechst 33342 as outlined. **B)** Representative fluorescent images of 2D RAW 264.7 cells to analyze cell death stained with Propidium iodide (PI) and Hoechst 33342. Scale bars indicate 100 µm.

In **Figures 4.9A** and **B**, our observations reveal distinctive alterations after the 72-hour treatment period. Notably, the spheroids in the control and PTX+RSQ group maintained their shape and stability throughout the experiment, unlike the combination treatment and NP groups, where we observed significant deformities. This deformation is likely attributed to the cytotoxic effects of the treatment groups on the spheroids. This discrepancy can be attributed to the distinct permeability characteristics of the treatment modalities. The NPs, owing to their pH-sensitive property, were destabilized within the spheroids' acidic environment. Consequently, the released drugs penetrated deeper into the spheroids, leading to enhanced tumor cell death. Unlike the NPs, the free drugs did not exhibit the same pH-sensitive release behavior, resulting in less effective penetration into the spheroids and lower levels of PI staining. These findings underscore the importance of triggered-release NPs, which can enhance drug permeability and efficacy within tumor spheroids.

Tumor-specific cell death using LUC2-tagged 4T1 cells:

After observing the cancer cell death using live-dead staining, for further verification, we have used luc-2 tagged 4T1 tumor cells to confirm the tumor-specific cell death using luciferin expression. The experiment was performed in both 2D conditioned media and 3D complex spheroid. In the 2D conditioned media experiment, where RAW 264.7 conditioned media (treated with free drugs or NP) was added to the tumor cells, significantly increased tumor cell

death was observed with the spH NP treatment, compared to others, including PTX+RSQ combination and spNP. In the 3D complex spheroid, luciferin fluorescence was found to be decreased significantly with the spH NP treatment, compared to others, which could be because of the pH-sensitive destabilization of the spH NPs at the tumor's acidic core pH. (**Figure 4.10A and B**)

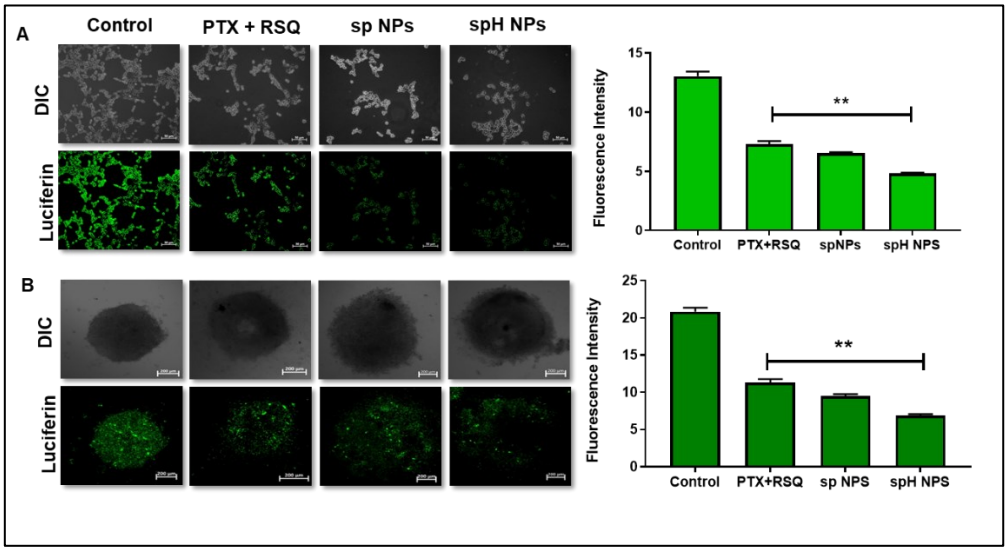

Figure- 4.10A) 2D Luciferin tagged 4T1 cell microscopy images when treated with conditioned media of RAW 264.7 cells and treatment groups, **B)** 3D LUC-2 4T1+RAW 264.7 complex spheroid expressing luciferin fluorescence after treatment for 72h.

Reactive oxygen species (ROS) generation:

After confirming the improved cytotoxic cell death of the drug combination and NPs, we studied the role of ROS generation in tumor cell death. We checked ROS generation capability in 2D conditioned media and 3D complex spheroid systems. For 2D conditioned media, we initially treated the macrophages for 24h and then transferred the media to previously seeded 4T1 cells for 24h. After that, DCFDA was added and incubated for 15 min followed by imaging using fluorescent microscopy at 10X magnification in an inverted fluorescent microscope (ZEISS Axio Vert. A1). For complex spheroids, tumor-macrophage co-cultured 3D spheroids were treated with PTX (10 nM) and RSQ (2 µM) and with the same dose in NPs for 24h, followed by DCFDA treatment for 15min and microscopy. We have observed an increase in ROS generation with the PTX +RSQ combination compared to PTX and RSQ alone in both 2D and 3D. It is also observed that a significant increase in ROS and DCFDA fluorescent intensity in spH NPs might be because the pH-sensitive nature of the NPs allowed them to penetrate more into the core of the spheroid, and more cellular localization in 3D helped improve ROS generation. It was also evident that M1 macrophage activation leads to ROS

activation, primarily because of the high production of TNF-α [13, 14]. From this, it is evident that enhanced cytotoxicity and M1 macrophage stimulation of the PTX +RSQ combination, when given as spH NPs, might also be because of improved ROS generation.

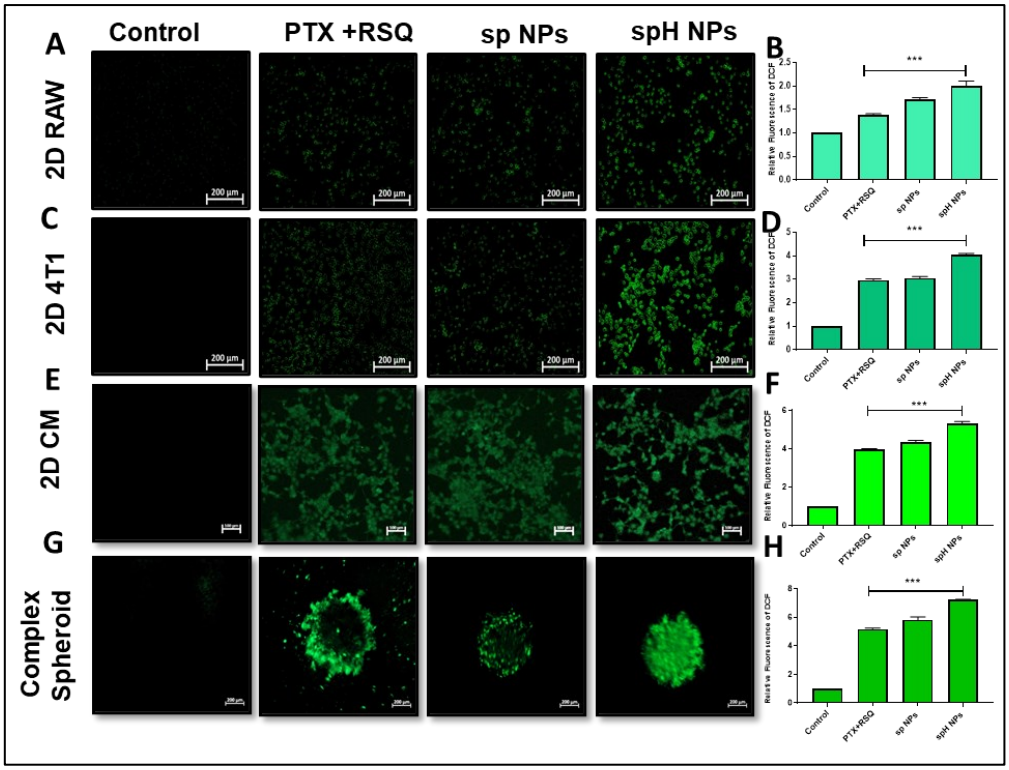

Figure-4.11: Induction of ROS in PTX+RSQ treatment. Fluorescent microscopic images of DCFDA stained 4T1 cells, RAW Cells, 2D conditioned media of RAW added to 4T1 cells and 4T1+RAW 3D complex spheroid after treatment with Control, PTX, RSQ, PTX+RSQ, sp NPs, and spH NPs, showing increased DCF fluorescence in spH NPs compared to control, and other treatment groups. The scale bar in the image indicates 50 µm.

In-vitro anti-metastatic property:

To check the metastatic property of the tumor cells, we have performed a spheroid migration assay using a transwell system, using tumor-macrophage complex spheroid. We have observed that though there is a decrease in migration ability with RSQ alone, there is a significant decrease in the number of cells migrated to 50% compared to the control. Interestingly, the % of cells that migrated decreased drastically to 20% with spH NPs treatment, which indicates that spH NPs have the potential to inhibit the migration ability of the tumor cells effectively, indicating it can reduce metastasis as well (**Figure 4.12A and B**).

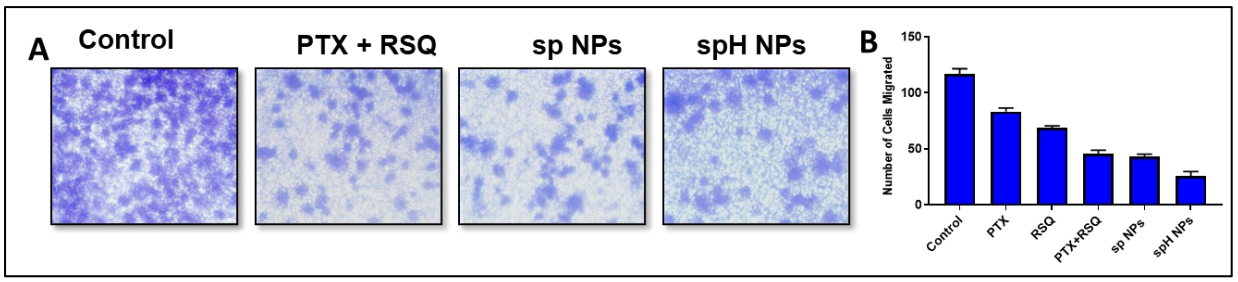

Figure-4.12: A) Microscopy images of cell migration assay of 4T1+RAW 264.7 complex 3D spheroids after 24 h treatment in 24-well transwell inserts with crystal violet staining. B) Quantification of the number of cells migrated in the migration assay.

Analysis of gene expression pattern:

After observing increased cancer cell death in the cancer spheroid model, we analyzed the macrophage polarization pattern following NP treatment in 2D conditioned media, a transwell-based mixed cancer spheroid model (Quasi 3D), and 3D. Initially, the treatment with spH NPs led to when we checked the M1 macrophage polarization marker, i.e., NF- kB, IFN-γ there was an increased expression with spH NPs (**Figure 4.13A and B**) when compared to PTX+RSQ and other treatment groups as well. NF-kB is also majorly known for its immune activation, playing a role in macrophage polarization towards the M1 state and also regulates the production of multiple cytokines like TF-alpha, IL-6, and many others, which helps in reducing the immune suppressive activity of macrophages in turn, enhancing the anti-tumor immune response of combined chemoimmunotherapy [15, 16].

Conversely, a diminished expression of M2-marker TGF-β was observed (**Figure 4.13C**) with the PTX+RSQ treatment, both free and NP-encapsulated drugs. In a similar pattern, we have observed decreased expression of Pgp, a major MDR protein capable of effluxing chemotherapeutics out of cancer cells, which can reduce the effectiveness of treatment. In TME, TAMs were also found to express high p-gp, leading to the maintenance of an immunosuppressive microenvironment and even leading to drug resistance, which can, in turn, decrease the effectiveness of therapy. Thus, decreased Pgp expression with the spH NPs (**Figure-4.13D**) suggests that it can also help diminish drug resistance [17]. After that, VEGFA expression was also found to decrease when compared to the control group and free drug combination. It is well known that VEGFA helps in angiogenesis, which helps form the blood vessels in the tumor. To avoid tumor growth and spread along with improved immune cell delivery, VEGFA should be inhibited [18]. Reduced VEGFA can also promote immune cell infiltration in macrophages, leading to enhanced immunotherapy by increased anti-tumor M1 macrophage polarization [19]. Thus, decreased VEGFA expression improved anti-tumor

activity (**Figure 4.13E**). Altogether, the data signifies the enhanced in-vitro immunotherapeutic ability of the PTX+RSQ drug combination encapsulated in a pH-sensitive NP.

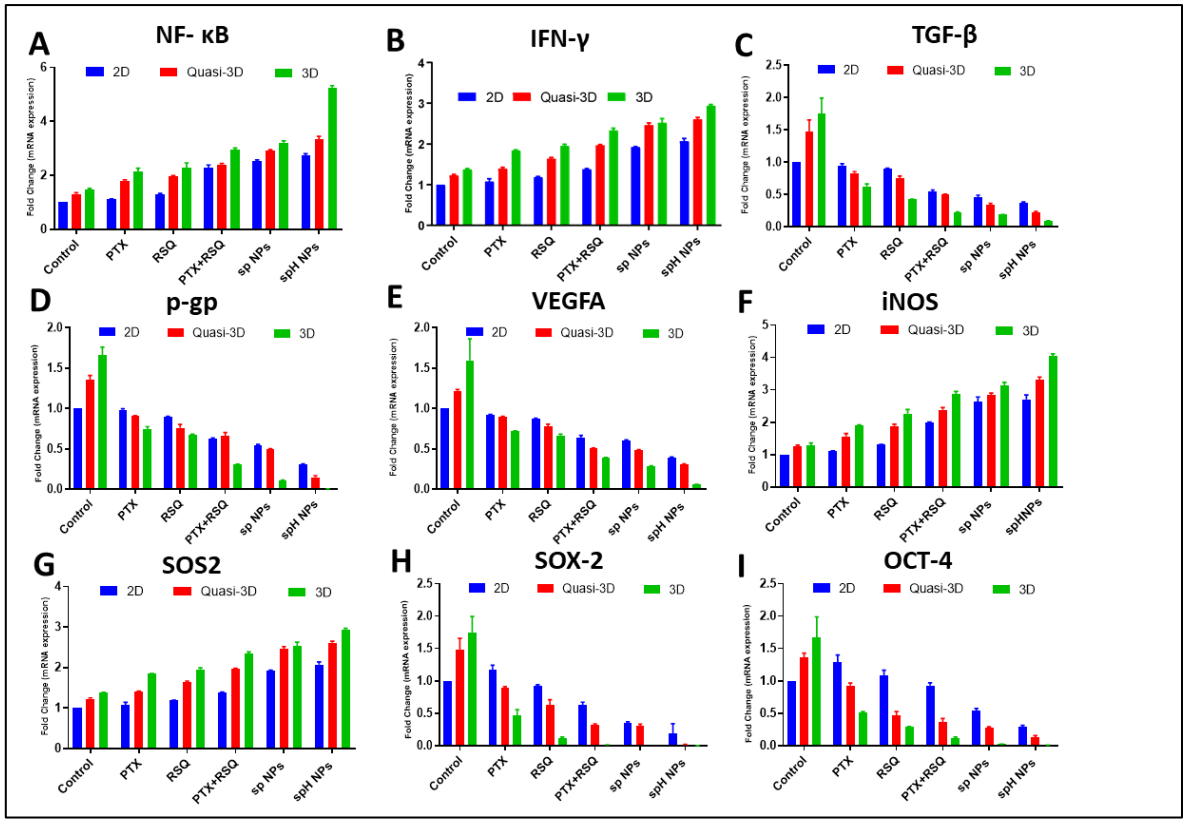

Figure-4.13: Quantification of gene expression after treatment to 2D conditioned media, Quasi-3D (Transwell system) 3D complex spheroid model A) NF-Kβ, B)IFN-γ, C) TGF-β, D) P-gp, E)VEGFA, F) iNOS, G) SOS2, H) SOX-2, I) OCT-4

The treatment with spH NPs has also led to increased iNOS and SOS2 expression when compared to the PTX+RSQ combination and free drugs alone. iNOS (Inducible Nitric Oxide Synthase) is majorly responsible for producing NO, which has both anti-tumor and pro-tumor effects; elevated Inos (**Figure 4.13F)**, in turn, increased NO leads to anti-tumor effects by becoming cytotoxic to cancer cells, through induction of DNA damage and programmed cancer cell death, Increased NO can also lead to enhanced antigen by increased MHC molecules on macrophages that in turn helps in activating Tcell activation as well [20-22]. Increased SOS2 could be because of the activation of Ras proteins that play a vital role in cell proliferation, survival, and differentiation (**Figure 4.13G**) [23, 24]

We have also observed almost basal level of stem cell marker expression, i.e., Sox-2 and Oct-4 with spH NPs treatment, compared to free drug combination and other groups. Thus, it was established that spH NPs encapsulated with PTX and RSQ can reduce therapeutic resistance

and tumor recurrence along with improved chemo-immunotherapeutic activity (**Figure 4.13H** and **I**) [25].

ELISA:

After successfully analyzing M1 and M2 polarization of macrophage markers using PCR, we analyzed protein level analysis of macrophage polarization using TNF-α and IL-10 using ELISA kits. In the supernatant of the cells treated with drugs and NPs in only RAW 264.7 cells, 2D conditioned media of 4T1 cells was added to RAW along 3D tumor-macrophage complex spheroid conditions. We have observed that there is an increase of TNF- α expression with almost 100-fold in 2D, 390-fold increase in conditioned media, and 410-fold increase in 3D complex spheroids when compared to control, indicating M1 macrophage polarization. With spH NPs, there was a drastic increase of TNF- α expression, i.e., 200-folds in 2D, 420-fold increase in conditioned media, and 820-fold increase in 3D complex spheroids as shown in **Figure 4.14**, which has a more effective macrophage activation with immune activation when compared to the free drug combination.

Similarly, with IL-10 expression, there is a decreased expression with PTX+RSQ combination, i.e., 50-fold in 2D, 100-fold increase in conditioned media, and 120-fold increase in 3D complex spheroids. When it comes to spH NPs, there is a 20-fold in 2D, 60-fold increase in conditioned media, and 70-fold increase in 3D complex spheroids, proving that M2 macrophage expression was about to basal level leading to decreased immunosuppressive nature of the TME (**Figure 4.14)**.

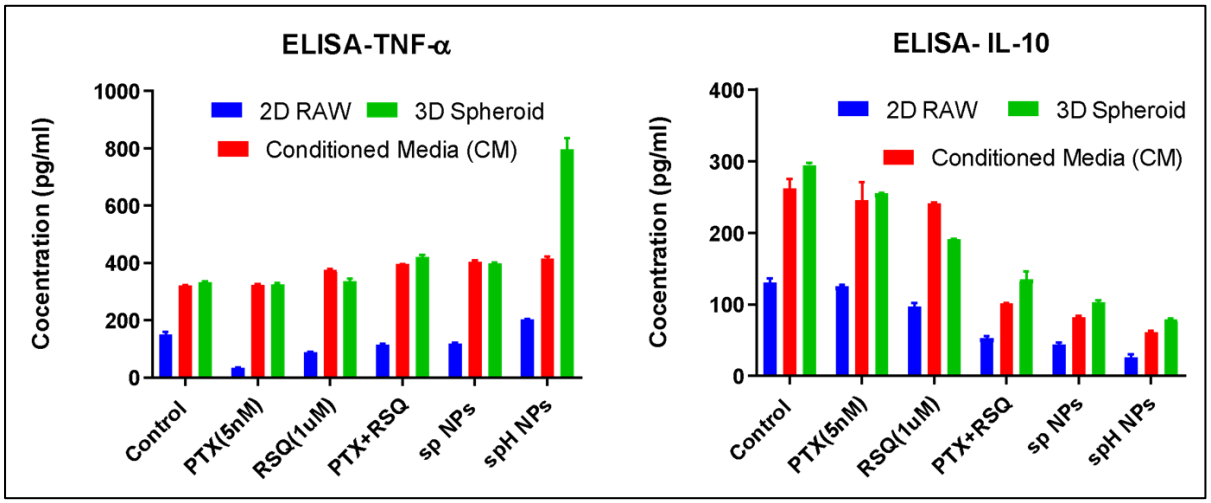

Figure-4.14: Quantitative estimation of M1 and M2 macrophage marker expression at protein level using ELISA TNF-α and IL-10.

Ex vivo immunostimulatory activity of NPs:

The immunogenic potential of the TLR agonist by macrophage polarization has become the key to immune-mediated tumor growth reduction in almost all types of cancers. To evaluate the macrophage polarization ability of the drug combination along with NPs, they were co-incubated with the primary splenocytes for 72 h. Interestingly, PTX+RSQ and spH NPs exhibited a Th1 type response stimulated splenocytes by secreting higher amounts of pro-inflammatory cytokines, TNFα, IL-12, IFNγ and CD86 as compared to the free drugs individually, which could be attributed to the M1 macrophage polarization of RSQ drug combination and the pH sensitivity of the NPs as evident from the immunostimulatory activity of sp NPs (non-pH sensitive NPs) (**Figure 4.15**). After 72h, CD206, IL-10, and TGF-β levels were also estimated from the culture supernatant, which mainly indicated the pro-tumorogenic cytokines, leading to the immune suppression of the TME. Interestingly, both PTX+RSQ and spH NPs have reduced secretion of all the M2 marker expression compared to the free drugs, suggesting T cell activation [26, 27].

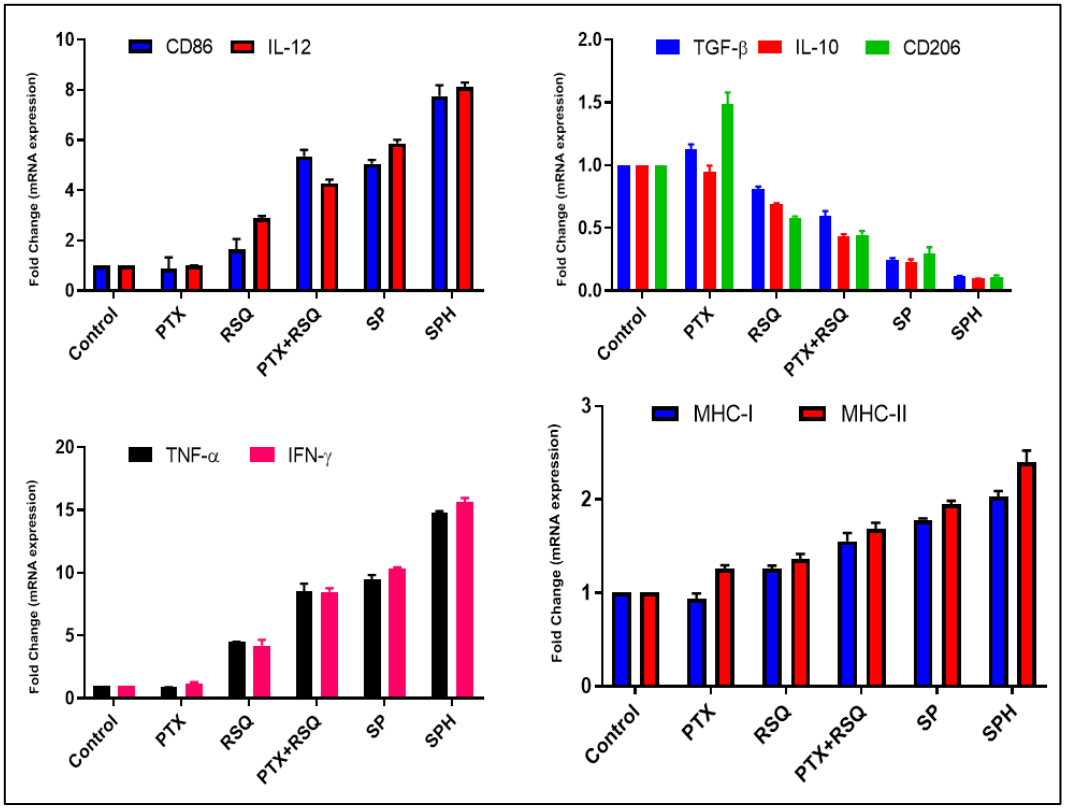

Figure 4.15: EX-vivo analysis: Protein level expression of M1 marker expression –CD86, IL-12, TNF-α, IFN-γ expression using splenocyte + tumor cell complex spheroid. M2 marker expression, i.e., TGF-β, IL-10, and CD206. Antigen presentation capability by MHC-I and MHC-II expression.

Hereafter, as we know, MHC plays a crucial role in the immune system by presenting antigens to T cells, a crucial component of the adaptive immune response. So, after confirming the

macrophage polarization, we have checked the immunogenic potential of cancer cells as we are targeting macrophages, one of the significant antigen-presenting cells in the TME. The primary role of MHC-I is to present antigens to CD8+ cytotoxic T cells (CTL) by encountering antigens presented by MHC-I, activating by killing antigen-presenting cells along with cancer cells. Interestingly, when we checked the MHC-I expression in splenocytes after 72h of treatment, we observed increased MHC-I expression in spH NPs when compared to free drug combination and alone, proving that improved immunogenic potential as it is allowing CTLs to recognize macrophage, in turn leading to M1 polarization[23]. Surprisingly, we have also observed improved MHC-II expression (**Figure 4.15**), which might be because of the antigen-presenting capability of macrophage, which can help in activating CD4+T cells, that, in turn, helps in the immunogenic potential of other immune cells, which is mere because MHC-II can typically be expressed by immune cells but not cancer cells for helping ineffective immune response to cancer cells [28-30].

4.4. Conclusion:

The current study compared the tumor-targeted delivery of PTX+RSQ drug combination with *in-vitro* cell culture techniques. Initially, we have observed improved tumor-specific cell death and macrophage polarization. In continuation, the final formulation was found to have improved cancer cell uptake, decreased macrophage uptake along with improved endosomal escape and cytosolic distribution, proving the uniform distribution of payload and pH-dependent destabilization of NPs have been found using 3D spheroid penetration, where improved tumor core penetration of spH NPs when compared to lpH and non-pH sensitive NPs (lp and sp NPs) proving the pH-sensitive release of the payload. The spH NPs showed potent in-vitro chemo-immunotherapeutic activity through M1 macrophage polarization and tumor-specific cell death in both 2D and 3D complex spheroid models. PTX and RSQ combination was also found to show improved efficacy by modulating ROS.

Overall, the efficacy of finally optimized spH NPs was also predominantly higher in comparison with free drug combination and non-pH sensitive NPs in terms of tumor cell cytotoxicity and macrophage immune stimulatory marker expression, showing that spH NPs have improved *in-vitro* chemo-immunotherapeutic activity. A further *in-vivo* study is warranted to evaluate its potential for clinical translation.

References:

1. Maravajjala, K.S., K.L. Swetha, and A. Roy, *pH-Responsive Nanoparticles for Multidimensional Combined Chemo-Immunotherapy of Cancer.* J Pharm Sci, 2022. **111**(8): p. 2353-2368.
2. Zitvogel, L., et al., *Immunological aspects of cancer chemotherapy.* Nat Rev Immunol, 2008. **8**(1): p. 59-73.
3. Kim, S.H., et al., *Breast cancer cell debris diminishes therapeutic efficacy through heme oxygenase-1-mediated inactivation of M1-like tumor-associated macrophages.* Neoplasia, 2020. **22**(11): p. 606-616.
4. Kampan, N.C., et al., *Paclitaxel and Its Evolving Role in the Management of Ovarian Cancer.* Biomed Res Int, 2015. **2015**: p. 413076.
5. Ma, Z., et al., *Dual drug-loaded nano-platform for targeted cancer therapy: toward clinical therapeutic efficacy of multifunctionality.* J Nanobiotechnology, 2020. **18**(1): p. 123.
6. AlSawaftah, N., W.G. Pitt, and G.A. Husseini, *Dual-Targeting and Stimuli-Triggered Liposomal Drug Delivery in Cancer Treatment.* ACS Pharmacol Transl Sci, 2021. **4**(3): p. 1028-1049.
7. AlSawaftah, N.M., et al., *pH-Responsive Nanocarriers in Cancer Therapy.* Polymers (Basel), 2022. **14**(5).
8. El-Hammadi, M.M. and J.L. Arias, *Recent Advances in the Surface Functionalization of PLGA-Based Nanomedicines.* Nanomaterials (Basel), 2022. **12**(3).
9. Swetha, K.L., et al., *Development of a tumor extracellular pH-responsive nanocarrier by terminal histidine conjugation in a star shaped poly (lactic-co-glycolic acid).* European Polymer Journal, 2021. **147**: p. 110337.
10. Yang, Y., et al., *A Smart pH-Sensitive Delivery System for Enhanced Anticancer Efficacy via Paclitaxel Endosomal Escape.* Front Pharmacol, 2019. **10**: p. 10.
11. Karimi, M., et al., *pH-Sensitive stimulus-responsive nanocarriers for targeted delivery of therapeutic agents.* Wiley Interdiscip Rev Nanomed Nanobiotechnol, 2016. **8**(5): p. 696-716.
12. Barrera-Rodriguez, R. and J.M. Fuentes, *Multidrug resistance characterization in multicellular tumour spheroids from two human lung cancer cell lines.* Cancer Cell Int, 2015. **15**: p. 47.
13. Mendoza-Coronel, E. and E. Ortega, *Macrophage Polarization Modulates FcγR- and CD13-Mediated Phagocytosis and Reactive Oxygen Species Production, Independently of Receptor Membrane Expression.* Front Immunol, 2017. **8**: p. 303.
14. Tan, H.Y., et al., *The Reactive Oxygen Species in Macrophage Polarization: Reflecting Its Dual Role in Progression and Treatment of Human Diseases.* Oxid Med Cell Longev, 2016. **2016**: p. 2795090.
15. Liu, C.P., et al., *NF-κB pathways are involved in M1 polarization of RAW 264.7 macrophage by polyporus polysaccharide in the tumor microenvironment.* PLoS One, 2017. **12**(11): p. e0188317.
16. Mancino, A. and T. Lawrence, *Nuclear factor-kappaB and tumor-associated macrophages.* Clin Cancer Res, 2010. **16**(3): p. 784-9.
17. Cory, T.J., et al., *Alterations in P-Glycoprotein Expression and Function Between Macrophage Subsets.* Pharm Res, 2016. **33**(11): p. 2713-21.
18. Mu, G., et al., *Calmodulin 2 Facilitates Angiogenesis and Metastasis of Gastric Cancer via STAT3/HIF-1A/VEGF-A Mediated Macrophage Polarization.* Front Oncol, 2021. **11**: p. 727306.
19. Hwang, I., et al., *Tumor-associated macrophage, angiogenesis and lymphangiogenesis markers predict prognosis of non-small cell lung cancer patients.* J Transl Med, 2020. **18**(1): p. 443.
20. Mas-Rosario, J.A., et al., *Murine macrophage-based iNos reporter reveals polarization and reprogramming in the context of breast cancer.* Front Oncol, 2023. **13**: p. 1151384.
21. Vannini, F., K. Kashfi, and N. Nath, *The dual role of iNOS in cancer.* Redox Biol, 2015. **6**: p. 334-343.
22. Rahat, M.A. and B. Hemmerlein, *Macrophage-tumor cell interactions regulate the function of nitric oxide.* Front Physiol, 2013. **4**: p. 144.

23. Kerneur, C., C.E. Cano, and D. Olive, *Major pathways involved in macrophage polarization in cancer.* Front Immunol, 2022. **13**: p. 1026954.
24. Punekar, S.R., et al., *The current state of the art and future trends in RAS-targeted cancer therapies.* Nat Rev Clin Oncol, 2022. **19**(10): p. 637-655.
25. Müller, L., et al., *Bidirectional Crosstalk Between Cancer Stem Cells and Immune Cell Subsets.* Front Immunol, 2020. **11**: p. 140.
26. Mantovani, A., et al., *Macrophages as tools and targets in cancer therapy.* Nat Rev Drug Discov, 2022. **21**(11): p. 799-820.
27. Chakraborty, A., et al., *Tumor targeted delivery of mycobacterial adjuvant encapsulated chitosan nanoparticles showed potential anti-cancer activity and immune cell activation in tumor microenvironment.* Int Immunopharmacol, 2023. **114**: p. 109463.
28. Ahmed, I. and N. Ismail, *M1 and M2 Macrophages Polarization via mTORC1 Influences Innate Immunity and Outcome of Ehrlichia Infection.* J Cell Immunol, 2020. **2**(3): p. 108-115.
29. Helleberg Madsen, N., et al., *In vitro 2D and 3D cancer models to evaluate compounds that modulate macrophage polarization.* Cell Immunol, 2022. **378**: p. 104574.
30. Chen, X., et al., *Effective chemoimmunotherapy with anti-TGFβ antibody and cyclophosphamide in a mouse model of breast cancer.* PLoS One, 2014. **9**(1): p. e85398.

Chapter 5:

In-vivo studies

5.1. Introduction:

It is well established that mouse physiology and anatomy are similar to humans. To take advantage of this and avoid the harm associated with human studies, animal models can be used for cancer research and new drug discovery processes [1-3]. Most commonly used animal models for cancer research consist of immune-competent or immunocompromised mice where the tumor can be transplanted orthotopically or subcutaneously with either xenograft or syngenic tumors, which are straightforward and cost-effective in tumor model development when compared to other models [4, 5].

Hence, after the successful demonstration of the improved efficacy of the PTX+RSQ combination for chemo-immunotherapeutic potential against tumor cells and macrophage co-culture in both 2D and 3D *in-vitro* systems, next, we analyzed the *in-vivo* pharmacokinetic, bio-distribution, and efficacy in tumor-induced mice models. As we have developed pH-triggered NPs, the pharmacokinetic profile of PTX and RSQ must be checked for its absorption, distribution, metabolism, and elimination rate to confirm the safety profile after a successful treatment period. As we have observed *in-vitro* pH-dependent stability and destabilization, an *in-vivo* tumor model would give us a clear picture of these NPs to confirm their payload in TME at acidic pH and tumor bio-distribution.

We here initially checked the safety profile of free drugs and both NPs [sp NPs (non-pH sensitive) and spH NPs (pH-sensitive)], followed by tumor biodistribution and pharmacokinetics. Then, after this initial screening, the better formulation was taken forward for efficacy and other confirmational *in-vivo* studies.

5.2. Materials and Methods:

PTX was received as a gift sample from INTAS Pharmaceuticals Ltd, and RSQ was purchased from TCI, India. Soluplus was procured as a free gift sample from BASF. The solvents used for HPLC analysis and polymer synthesis: methanol (HPLC grade), Acetonitrile (HPLC grade), dimethylformamide (DMF), diethyl ether (DEE), dimethyl sulfoxide (DMSO), and chloroform (CHCl3), were procured from Merck, India. HPLC analysis used a Shimadzu LC instrument (Kyoto, Japan). Zodiac C-18 column (5 mm particle size, L £ I.D. 15 cm £ 4.6 mm) was used as the stationary phase. All other chemical reagents used were of A.R. grade.

Animals:

Female Balb/C mice aged 5-7 weeks, with a weight range of 18-20 g, were procured from the National Centre for Laboratory Animal Sciences, National Institute of Nutrition in Hyderabad, India, with approved protocol no IAEC/RES/31/08. The mice were housed in standard cages with five individuals per cage within a temperature-controlled environment (23-24 ºC) with a relative humidity of 50-60 %. They followed a 12-hour light/dark cycle and were provided with appropriate quantities of food and water.

Preparation of stock solutions calibration standards and quality control (QC) samples:

10 mg/ml of PTX and RSQ stock solutions were prepared with ACN. Diazepam, 100 µg/ml solution working stock, was prepared in ACN and used as an internal standard at 1 µg/mL in all the samples. 100 µg/ml of working solution was prepared for PTX and RSQ. Then, the dilutions were made accordingly with 100 µl of mice plasma to obtain 500, 750, 1500, 4500, and 6000 ng/ml calibration standards of PTX and RSQ. Similarly, 5500 ng/ml (HQC), 4000 ng/ml (MQC), 200 ng/ml (LQC), and 100 ng/ml (LLOQC) QC samples were made for PTX and 5500 ng/ml (HQC), 4000 ng/ml (MQC), 200 ng/ml (LQC) and 100 ng/ml (LLOQC) for RSQ. All QC samples were prepared in six replicates independent of calibration standards.

Liquid chromatographic conditions:

Chromatographic separation of PTX and RSQ from mice plasma interferences was achieved by using C18 (5 µm particle size, L × I.D. 15 cm × 4.6 mm) column as stationary phase and gradient method was used where, A: acetate buffer (pH-3.5), adjusted with 0.1% formic acid, B: ACN as mobile phase. The flow rate was set at 1 ml/min, with a run time of 20 min. The elution method was as follows: 0-6.5 min, A was maintained at 35%, then A was changed to 80% in 6.5-6.7 min, and it was hold at 80% till 13 min, after which A was changed to 35% at 13-13.2 min, then it was hold at 35% till 20 min for column equilibration. Samples were injected at 40 µl injection volume, PTX absorbance was measured at 230 nm, and RSQ absorbance at 249 nm wavelength. Hardware control and data interpretation of the obtained data were performed by using LC solution software version 1.22 SP1.

Extraction of drugs from plasma:

The protein precipitation method was used to extract PTX and RSQ from mice plasma, where 100 µl of mice plasma was spiked with PTX and RSQ concentrations ranging from 500 ng/ml to 6000 ng/ml. Diazepam was taken as an internal standard, and 0.5 µg/ml concentration of

diazepam was added to the plasma with all the samples analyzed. Then, the plasma with drugs was precipitated with ACN, followed by vertexing for 60 seconds, then centrifuged for 20 minutes at 10,000rpm and 4°C. After that, the obtained supernatant was kept for drying at 60°C, then the dried samples were reconstituted with ACN, and the supernatant was analyzed using HPLC.

Calibration curve and linearity range:

All calibration standards ranging from 500 ng/ml to 6000ng/ml for PTX and RSQ were prepared and analyzed using the HPLC method. The graph was plotted between concentration (on the X-axis) Vs peak area (on the Y-axis). The relation between the x and y-axis was expressed through the equation y = mx + c, where m is the slope and c is the intercept of the line. The obtained data was calibrated by using linear regression analysis.

Validation of the developed method:

The developed bioanalytical method was validated per the US Food and Drug Administration (US-FDA, 2018) guidelines [6]. The following parameters were analyzed accordingly.

a) Selectivity:

The selectivity of the above-developed method was enacted to examine the significant chromatographic interferences that can be because of the plasma matrix. To perform the selectivity, plasma was collected from six different mice and analyzed using the abovementioned procedure [7].

b) Linearity and calibration curve:

Calibration standards of PTX and RSQ were prepared, which ranging from 500 ng/ml to 6000 µg/ml, and analyzed using HPLC; the obtained data was used to plot a graph with peak area ratios of both the drugs and IS (Diazepam). The relationship between the x-axis (concentration) and the y-axis peak area ratio) was expressed using the y = mx + c, where m and c are the slope and intercept, respectively. The linear regression analysis was performed using calibration data.

c) The lower limit of quantitation (LLOQ) and limit of detection (LOD):

Signal-to-noise ratios (S/N) of the response of the drug in the samples were considered to analyze the sensitivity of the developed bioanalytical method. According to the USFDA guidelines, the S/N ratio should be >3 for the LOD and >10 for the LLOQC. LLOQC was determined as the concentration of the PTX and RSQ that showed acceptable accuracy and

precision (± 20%). The LOD was analyzed by spiking PTX and RSQ at concentrations less than the LLOQC at which the drug could be detected [8].

d) Accuracy and precision:

The developed method's intra-day and inter-day accuracy and precision were ensured by analyzing LLOQC, LQC, MQC, and HQC in six replicates (n = 6). The accuracy was expressed as % Bias and precision as % RSD or % Coefficient of Variation. According to the guidelines for accuracy, the acceptance limit is ± 15% SD from the nominal concentration. For precision, it is ±15% SD from nominal concentration, whereas for LLOQC, it should not be greater than ± 20% for both accuracy and precision.

e) Recovery (%):

The percentage recoveries of PTX, RSQ, and IS were analyzed by comparing the area of six replicate samples of LQC, MQC, and HQC (n=6), along with the corresponding standard concentrations. The percentage recovery of IS was also calculated at a single concentration of 1 µg/mL in six replicates (n = 6).

f) Carry-over effect:

The carry-over effect of the blank plasma samples was analyzed by injecting immediately after injecting the HQC samples. The acceptable limit for blank plasma samples is less than 20% compared to LLOQC, according to the USFDA guidelines.

Toxicity study

Female BALB/c mice weighing 20 ± 5 g were divided into six groups (Control, PTX, RSQ, PTX+RSQ, PNPs, and spH NPs) containing three mice in each group. After overnight fasting, animals were treated with PTX (5 mg/kg), which was administered intravenously (i.v.) via tail vein, where 0.5 mg PTX in 100 µl of ethanol+ 100 µl of Tween 80 (1:1) and 800 µl of normal saline (N.S.). RSQ, Dissolve 19 mg RSQ in 100 µl of ethanol+ 100 µl of Tween 80 (1:1) and add 800 µl of normal saline (N.S.). From this, inject 200 µl through the tail vein (I.V.) into 20 g mice; for PTX+RSQ and NPs, equivalent doses were given through i.v. Route. The treatment was carried out with repeated doses at intervals of 0, 4, and 8. Animals were monitored regularly for skin color, eye color, fur levels, locomotion activity, water intake, tears production, abnormal stereotypy, and death recorded. After eight-day treatments, animals were sacrificed on the 8th day, and all the major organs (Lungs, Liver, Kidneys, Heart, and Spleen)

were collected, followed by slicing and H & E staining. The tissue sections were then captured using light microscopic imaging at 40× magnification.

H & E staining:

Tissues were isolated, washed with saline, and fixed with 4% paraformaldehyde. Then, tissues were sliced at five μm thickness using a microtome. After mounting the slices on a glass slide, the manufacturer's protocol was followed with H & E staining. Histological modifications of tissue sections were performed using the light microscope.

Pharmacokinetic studies:

Pharmacokinetic studies were performed on female BALB/c mice, 4-6 weeks old 20 ± 5 g; animals were divided into six groups (Control, PTX, RSQ, PTX+RSQ, sp NPs, and spH NPs) with three animals in each group. Treatment for all the groups was administered by i.v. Route with the following doses: PTX (5mg/kg) and RSQ (150mg/kg). Equivalent amounts of PTX RSQ in PTX+RSQ, sp NPs, and spH NPs were also administered through i.v. Route. By retro-orbital plexus, blood was collected at pre-determined time points from each animal (0.25, 1,2,4,6,12,24, 48, and 72h). Blood was collected into a tube containing 10% disodium EDTA as an anti-coagulant; plasma was isolated by centrifuging these tubes at 6,000 rpm for 15 minutes at 4 ◦C and then analyzed using HPLC. Plasma concentration Vs area profiles of PTX and RSQ were plotted. Different pharmacokinetic parameters, including area under the curve (AUC), apparent volume of distribution (Vd), drug concentration at t = 0 (C0), elimination half-life ($t_{1/2}$), and systemic plasma clearance were obtained by applying a non-compartmental model in Phoenix 8.0 WinNonlin (Pharsight Corporation, USA).

Establishment of the 4T1-Luc orthotopic tumor-bearing mice model:

To study the tumor biodistribution and in-vivo efficacy of prepared NPs, the 4T1-Luc orthotopic tumor- model was developed in Balb/c mice. Briefly, 100 μL of 4T1-Luc cell suspension (50,000 cells in 100 μL) was injected into the lower-left mammary fat pad of the female BALB/c mice to develop 4T1-Luc orthotopic breast cancer model

Biodistribution study:

The *in-vivo* biodistribution analysis of Dil-labeled nanoparticles (sp NPs and spH NPs) was conducted using an *in-vivo* imaging system (IVIS® Lumina III, PerkinElmer, USA). A dose of 100 μg/kg DiI equivalent of [DiI] loaded sp NPs and [DiI] loaded spH NPs was intravenously

administered to BALB/c mice bearing 4T1-Luc tumors via the tail vein. Following injection, the biodistribution patterns were assessed at different time points (0.5, 1, 3, 6, 12, and 24 hours). Images were captured using the in-vivo imaging system with an excitation filter set at 550 nm and an emission filter set at 567 nm. Furthermore, 24 hours post-injection, the treated mice were euthanized. The main organs were collected, and ex-vivo images were acquired using the same *in-vivo* imaging system.

Tumor growth inhibition studies:

4T1-Luc ($1.5x10^6$) cells were suspended in 100 µL of cold PBS and injected into the mammary fat pad of female Balb/c mice to induce tumor growth. Once the tumor volume reached 50-60 mm^3, the mice were divided randomly into five groups (n = 5 each): control, PTX, RSQ, PTX+RSQ, and spH NPs. Formulations were administered intravenously through the tail vein every other day for 0, 4, and 8 days. The mice were regularly weighed during this period, and the tumor volume was recorded. On days 0, 5, 10, 15, and 21, the mice received intraperitoneal injections of D-luciferin (150 mg/kg), and imaging was conducted using IVIS Lumina (PerkinElmer Inc, USA; Ex/Em. 620/780 nm) to monitor tumor progression. After the completion of the treatment regimen, the mice were anesthetized using ketamine/xylazine; the tumors were surgically excised and weighed.

TUNEL assay:

The assessment of apoptosis within the tumor tissues was conducted through the TUNEL assay. Tumor sections underwent treatment with the TUNEL reagent (TACS®TdT-Fluor). In Situ Apoptosis Detection Kit, R&D Systems, USA) following the guidelines provided by the manufacturer. Subsequently, the sections were examined using a fluorescence microscope. DAPI staining was observed using a blue filter (Ex/Em. 359/457 nm), while TUNEL-positive cells were visualized using a green filter (Ex/Em 488/520 nm).

KI67 assay:

Initially, tumor sections were incubated with a blocking buffer (1% BSA) for 1 hour. Following this, the sections were exposed to the Ki-67 primary antibody (Rabbit mAb #9129) for 12 hours at a temperature of 4°C. After being washed three times with PBS, the sections underwent an additional 2-hour incubation with a secondary antibody (Alexa Fluor® Plus 488) at room temperature in a dark environment. Following three additional washes with PBS, the sections were observed in a fluorescent microscope.

ROS detection assay:

Reactive oxygen species (ROS) production within the tumor tissue was evaluated using the fluorescent probe DCFH-DA. Following a 21-day treatment regimen involving different drugs and formulations, an intratumoral injection of DCFH-DA (50 µL, 25 µM) was administered to BALB/c mice bearing 4T1-Luc tumors. After a 30-minute incubation period, the mice were anesthetized and observed using an in-vivo imaging system (IVIS® Lumina III, PerkinElmer, USA). Subsequently, the tumors were isolated and cut into 5 µm-thick sections using a cryostat (Leica Biosystems, Germany). These tissue sections were subjected to staining with DAPI, mounted onto glass slides, and examined using a fluorescence microscope (Leica, Germany).

***In-vivo* lung metastasis analysis:**

After the surgical excision of tumors, the animals were allowed to recover. On the 9^{th} day following the surgery, metastasis of the 4T1-Luc tumors was assessed through bioluminescence imaging using luciferin-D. Subsequently, the animals were euthanized, and their lungs were extracted. Changes in total lung weight resulting from tumor metastasis were determined by weighing the lungs. The lungs were then photographed, and the count of tumor nodules was recorded.

BrdU (Bromodeoxyuridine / 5-bromo-2′-deoxyuridine) is an analog of the thymidine nucleoside, commonly employed in the BrdU assay for identifying proliferating cells within cancer. To prepare a sterile solution of 10 mg/mL, BrdU was diluted in PBS. This solution, measuring 150 µL, was intraperitoneally injected into distinct tumor-bearing mice on the 30th day post-tumor inoculation after each treatment. After a 2-hour interval, the lungs were surgically resected and then embedded in OCT media. The following day, the frozen lung exhibiting metastasis was sectioned via cryo-sectioning, producing slices with a thickness of 5 µm. These sections underwent DNA denaturation using 1 N HCl for 10 minutes, followed by an additional 10-minute exposure to 2 N HCl, all performed at room temperature. Subsequently, the sections were immersed in 0.1 M borate buffer for 15 minutes, facilitating the removal of HCl, and then subjected to three 5-minute washes using 1% Triton X-100 in PBS with a pH of 7.4. To enhance permeability, the sections were exposed to 1.5% Triton X-100 in PBS for 1 hour, followed by an overnight incubation at 4°C with anti-BrdU rabbit IgG. On a subsequent day, the sections were subjected to a PBST wash, followed by a 1-hour incubation with a secondary anti-Rabbit IgG antibody. After a final PBS wash, the sections were examined under a fluorescence microscope.

To perform collagen I staining in metastatic lung tissue, 1% BSA-blocked tumor sections were incubated with Anti-Collagen I primary antibody (Abcam #ab138492) at a dilution of 1/1000, left overnight at 4°C. On the following day, the tissue sections underwent PBS washing and were subsequently incubated with Alexa Fluor® 488 secondary antibody for 2 hours in the dark at room temperature. After the 2 hours, the tissues were PBS-washed, treated with DAPI for 5 minutes, and then observed under a fluorescence microscope.

For hematoxylin and eosin (H&E) staining, lung tissue sections measuring 4 µm in thickness were utilized. The sections were sequentially exposed to xylene, varying alcohol concentrations (30 % to 100 %), and water. Hematoxylin was employed to stain the nuclei, followed by thorough washing with tap water. Subsequently, eosin staining was applied to highlight the cytoplasm, followed by washing with dehydrated alcohol and xylene. The slides were then affixed using mounting media and inspected under a microscope with 10× magnification.

Statistical analysis:

All the data were analyzed using GraphPad Prism software version 8. One-way ANOVA was used when there were≥ 2 groups compared to the control; post hoc Tukey's test was performed when the means of every group was compared with every other group. All the data was represented in mean ± SD. In all the graphs, ns indicates a nonsignificant difference, and * indicates $p < 0.001$.

5.3. Results and Discussion:

Bioanalytical method development and validation:

Drug recovery from the plasma samples was done using the protein precipitation method, where we found zero matrix effect and better extraction of PTX and RSQ from the plasma matrix. Wherein the recovery of both the drugs was found to be more than 85%.

a) Selectivity and Specificity:

Different concentrations of PTX and RSQ spiked into the plasma along with IS were used to analyze the selectivity of the developed method using the protein precipitation method. To check the specificity of the method, blank plasma samples without any drugs were used using the same method to check for any interferences from the plasma matrix. Where the retention time of PTX was 14.75 min, RSQ was 6.72 min, and IS was 17.5 min, and it was found that no interferences were observed from the plasma matrix near this Rt (**Figure 5.1**).

b) Calibration Curve, Linearity, LLOQ and LOD:

The bioanalytical method developed for both drugs was characterized by analyzing plasma samples spiked with different concentrations of PTX and RSQ along with IS. The calibration curves obtained lay in the range of 500 ng/ml to 6000 µg/ml for both PTX and RSQ, showing an R^2 of 0.998 and 0.998, respectively (**Figure 5.1 B and C**). Five calibration curves consisted of six different concentrations of PTX and 5 different concentrations of RSQ along with IS (500ng/ml), zero sample (IS only), and blank sample. The percentage RSD for LLOQ 0.05 µg/ml and 0.1 µg/ml for PTX and RSQ, respectively, was < 20%. From the acquired calibration curve, precision (%RSD) and accuracy (%Bias) were calculated and were found to be within limits for PTX and RSQ.

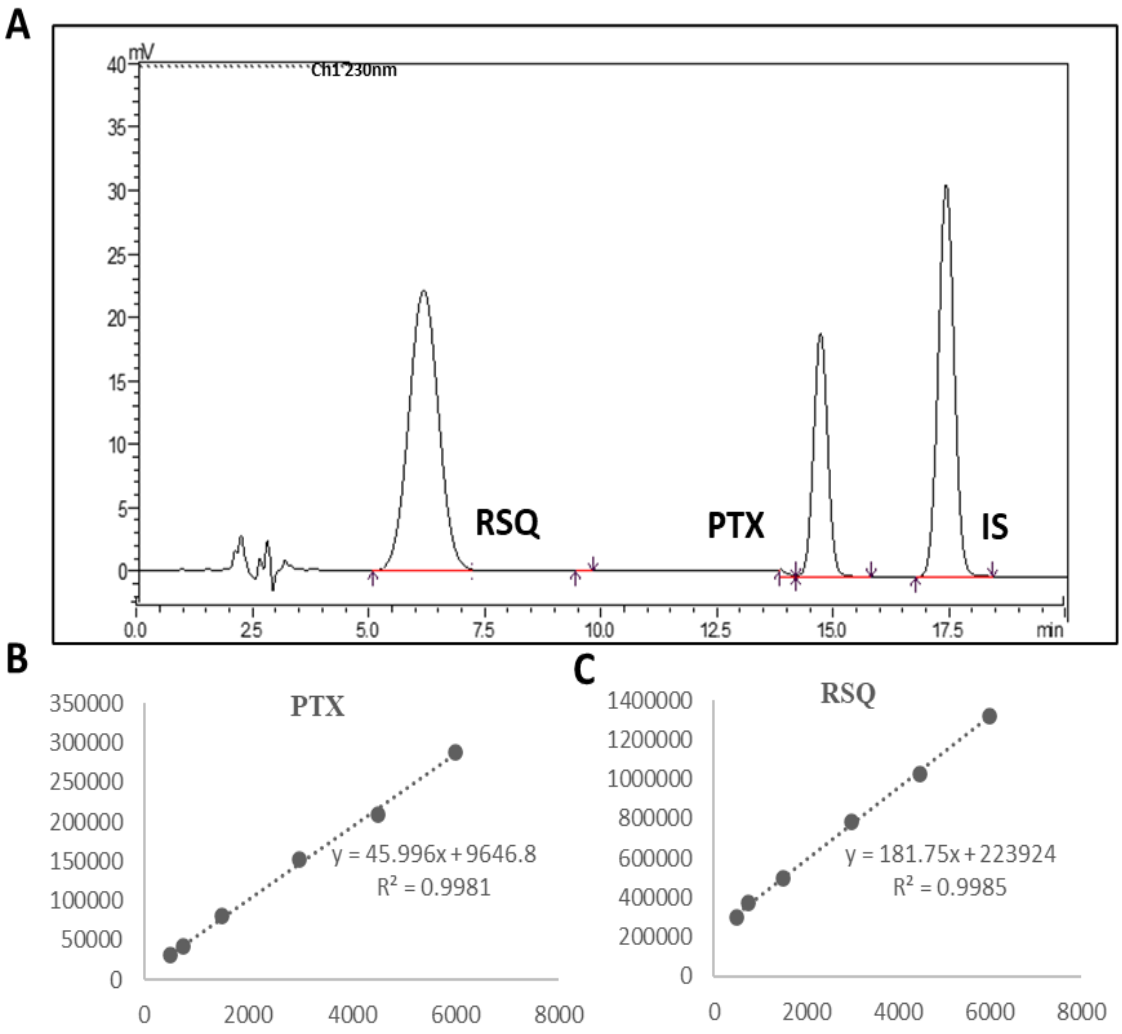

Figure 5.1: A) Chromatogram of PTX, RSQ and IS (Diazepam) at LQC. **B)** Calibration curve of PTX and **C)** Calibration curve of RSQ.

c) Accuracy and Precision:

Table 5.1: Intra-day and inter-day precision and accuracy of PTX in mice plasma.

Intra-day					**Inter-day**		
Level	**Nominal Conc (ng/ml)**	**Observed Conc (ng/ml) Mean ± SD**	**%RSD**	**%Bias**	**Observed Conc (ng/ml) Mean ± SD**	**%RSD**	**%Bias**
LLOQC	100	98.05 ± 1.46	1.497777	-1.95	94.21±1.11	1.186122	-5.78117
LQC	200	183.96±5.14	2.797389	-8.01667	178.3±1.75	0.984225	-10.8215
MQC	4000	3970.87±37.80	0.952087	-0.72817	3919.0±56.17	1.432832	-2.02258
HQC	5500	5406.03±50.01	0.925117	-1.70842	5386.3±10.8	0.200619	-2.0657

Intraday and inter-day precision (%RSD) and accuracy (%Bias) of PTX and RSQ were determined in mice plasma samples at 4 QC levels, i.e., HQC, MQC, LQC, and LLOQC. Both % RSD and %Bias data of PTX and RSQ indicate that the developed method was accurate. The %bias range was within the acceptable limits with LQC, MQC, and HQC, i.e., ±15%, and for LLOQC, is ±20%. According to the ICH-Q-2-R1 guidelines as well, the LLOQC limits were ≤ 20% and ≤ 15% for QC samples (LQC, MQC, and HQC); this proves that the developed method for PTX and RSQ in mice plasma is suitable and acceptable for analyzing any plasma samples within the detectable range.

Table 5.2: Intra-day and Inter day precision and accuracy of RSQ in mice plasma

Intra-day					**Inter-day**		
Level	**Nominal Conc (ng/ml)**	**Observed Conc (ng/ml) Mean ± SD**	**%RSD**	**%Bias**	**Observed Conc (ng/ml) Mean ± SD**	**%RSD**	**%Bias**
LLOQC	100	97.1±0.286	0.295448	-2.9	94.7±1.8	1.973439	-5.27
LQC	200	178.5±5.55	3.113482	-10.72	180.0±4.3	2.422039	-9.99667
MQC	4000	3814.3±1180	3.093848	-4.64242	3790.6±76.8	2.027543	-5.23475
HQC	5500	5456.6±49.5	0.904468	-0.78782	5427.4±85.5	1.575504	-1.31855

In-vivo toxicity studies:

After observing the improved *in-vitro* efficacy of this drug combination, we tested the established therapeutic doses (PTX- 5mg/kg and RSQ-150mg/kg) for their *in-vivo* toxicity studies. During and after the treatment period, the animals exhibited no significant weight

variation (**Figure 5.2)** and no behavioral changes. Tissues were isolated and sectioned, followed by H&E staining on the 9th day. Microscopic images of all the tissues exhibited typical structures without any signs of toxicity, like inflammation and fibrosis (**Figure 5.3**). These results show that PTX, RSQ, PTX +RSQ, and NPs are non-toxic at these doses (PTX- 5mg/kg and RSQ-150mg/kg) within this period.

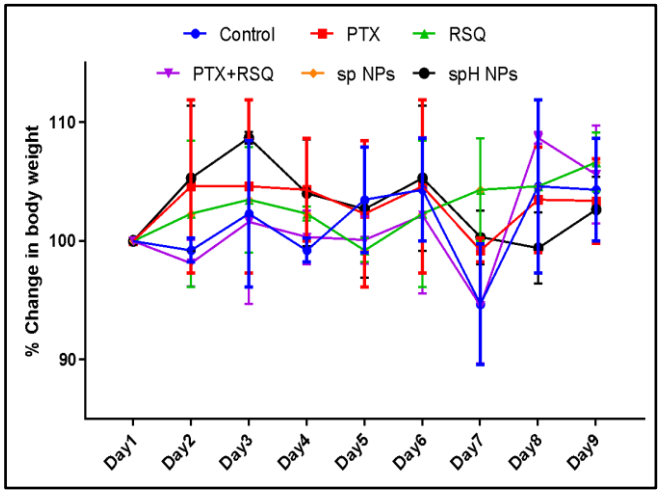

Figure 5.2. % Change in the body weight of the animal concerning the number of days after treatment with different groups

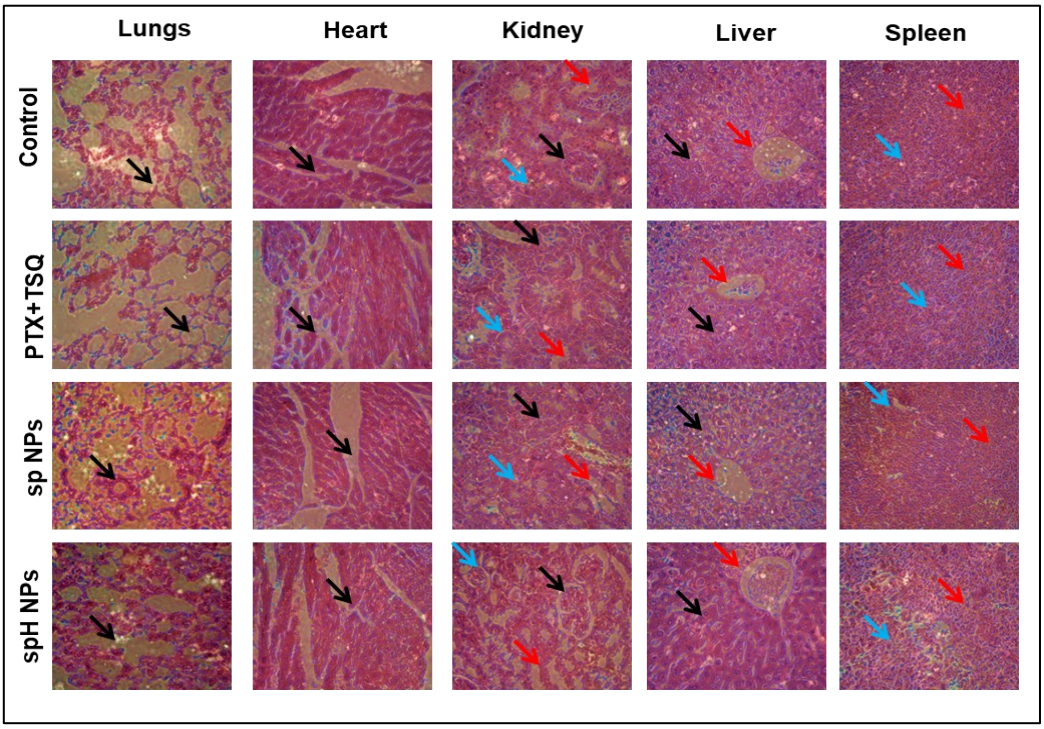

Figure 5.3: Histopathological evaluation (H&E staining, 40X) of highly perfused organs (Lung, Heart, Kidney, Liver, and Spleen) for toxicity study. **Lungs:** Black arrow: normal architecture of alveolar spaces with thin alveolar septa. **Heart:** Black arrow: normal architecture of cardiac myocytes with centrally placed nuclei. **Kidney:** Black arrow: glomerulus; Blue arrow: Proximal convoluted tubules PCT; red arrow: distal convoluted tubules (DCT). **Liver:** Black arrow: hepatocytes, red arrow: central vein. **Spleen:** Blue arrow: white pulp; red arrow: red pulp.

***In-vivo* pharmacokinetic studies**:

After determining the safe dose of the drugs, pharmacokinetic study was performed. Female Balb/c mice were divided into different groups; they were treated with equal doses of PTX, RSQ, PTX +RSQ, sp NPs, and spH NPs using the i.v. route. Plasma was isolated from the blood collected at different intervals and analyzed using the HPLC method. A significant difference was observed in the PK profiles of free drugs and NPs (**Figure 5.4**). Concerning the PK parameters, the plasma half-life ($t_{1/2}$) of PTX and RSQ demonstrated approximately ~2-fold improvement when administered in combination with PTX+RSQ. Similarly, improved PK parameters were observed when delivered in spH NPs, where PTX exhibited a ~7-fold increase in the AUC, ~11-fold reduction in clearance (cl), and ~150-fold increase in $t_{1/2}$. Similarly, RSQ showed a ~68-fold increase in the AUC (0-∞), ~16-fold reduction in clearance, and ~130-fold increase in $t_{1/2}$. Multiple studies have also reported that RSQ [9] and PTX [10, 11] have improved pharmacokinetic profiles with NP drug delivery systems.

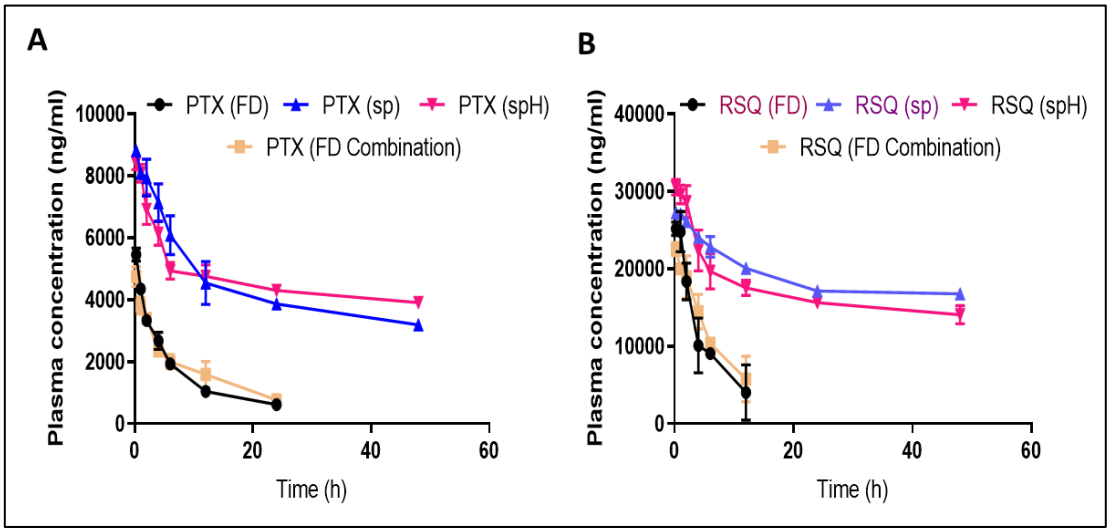

Figure 5.4: A) Plasma drug concentration-time profile of PTX and B) Plasma drug concentration-time profile of RSQ.

Table 5.3: Pharmacokinetic parameters of PTX alone, PTX in combination with RSQ, sp NPs, and spH NPs after administration of free PTX, NPs at a dose of 5 mg/kg.

Pharmacokinetic parameters	**PTX (FD)**	**PTX (FD-Combination)**	**PTX (sp NPs)**	**PTX (spH NPs)**
Cmax (ng /mL)	5889.25±212	5114.3711±319	8517.75±17.5	9080.18±212
AUC0- ∞(µg*h/L)	38521.28±908	43132.42±397	222090.8±498	212151.14±718
MRT(0-∞) (h)	14.3±2.27	16.80±3.65	101.50±36.2	187.11±19.8
Cl (mL/h/kg)	0.18±0.10	0.1572±0.07	0.0164±0.007	0.0094±0.001
Kel	0.060±0.01	0.054±0.012	0.009±0.001	0.005±0.002
$t_{1/2}$kel (h)	11.42±2.78	12.74±2.09	72.79±11.65	130.92±19.76

Table 5.4: Pharmacokinetic parameters of RSQ alone, RSQ in combination with PTX, sp NPs, and spH NPs after administration of free RSQ, NPs at a dose of 150 mg/kg.

Pharmacokinetic parameters	**RSQ (FD)**	**RSQ (FD-combination)**	**RSQ (sp NPs)**	**RSQ (spH NPs)**
Cmax (ng /mL)	25301.55± 855	23444.84±860	27354.01±277	30848.62±1024
AUC0- ∞(µg*h/L)	133788.31±895	147991.7±675	820555.45±760	9107528.87±654
MRT(0-∞) (h)	7.26±1.2	8.72±2.7	169.53±21.9	226.09±27.9
Cl (mL/h/kg)	0.184±0.12	0.155±0.03	0.0096±0.0012	0.0066±0.002
Kel	0.119±0.06	0.110±0.09	0.005±0.002	0.004±0.002
$t_{1/2}$kel (h)	5.82±1.26	6.24±1.83	119.04±12.80	157.26±22.37

In-vivo biodistribution study:

The tumor biodistribution of Dil-loaded NPs (sp NPs and spH NPs) was assessed following intravenous administration in the 4T1-Luc tumor-bearing mice. Near-infrared fluorescence (NIFR) images were captured using the IVIS Lumina system for the mice's entire bodies at various time points (30, 60, 180, 360, 720, and 1440 min). Mice treated with spH NPs displayed consistently superior fluorescence intensity at all time points compared to those treated with sp NPs. Notably, spH-treated mice showed higher fluorescence in the tumor tissue and other organs than sp NPs-treated mice (**Figure 5.5**). Both sp and spH NPs demonstrated increased accumulation in the tumor compared to other organs, possibly attributed to the prolonged plasma half-life observed in the pharmacokinetic study (**Figure 5.3**).

In the case of spH NPs, the DiI fluorescence was significantly higher in the tumor tissue than in sp NPs (**Figure 5.5 C** and **D**). Building upon our earlier findings that demonstrated enhanced payload delivery with spH NPs in a tumor spheroid model (**Chapter 4**, **Figure 4.4-4.6**), this suggests that the pH-sensitive nature of spH NPs enables payload release at the tumor extracellular pH. This phenomenon leads to an enhanced accumulation of DiI in the tumor tissue, distinguishing it from the non-pH-sensitive sp NPs. The observed improvement in payload delivery to the tumor tissue holds promise for enhancing the efficacy of anti-cancer agents.

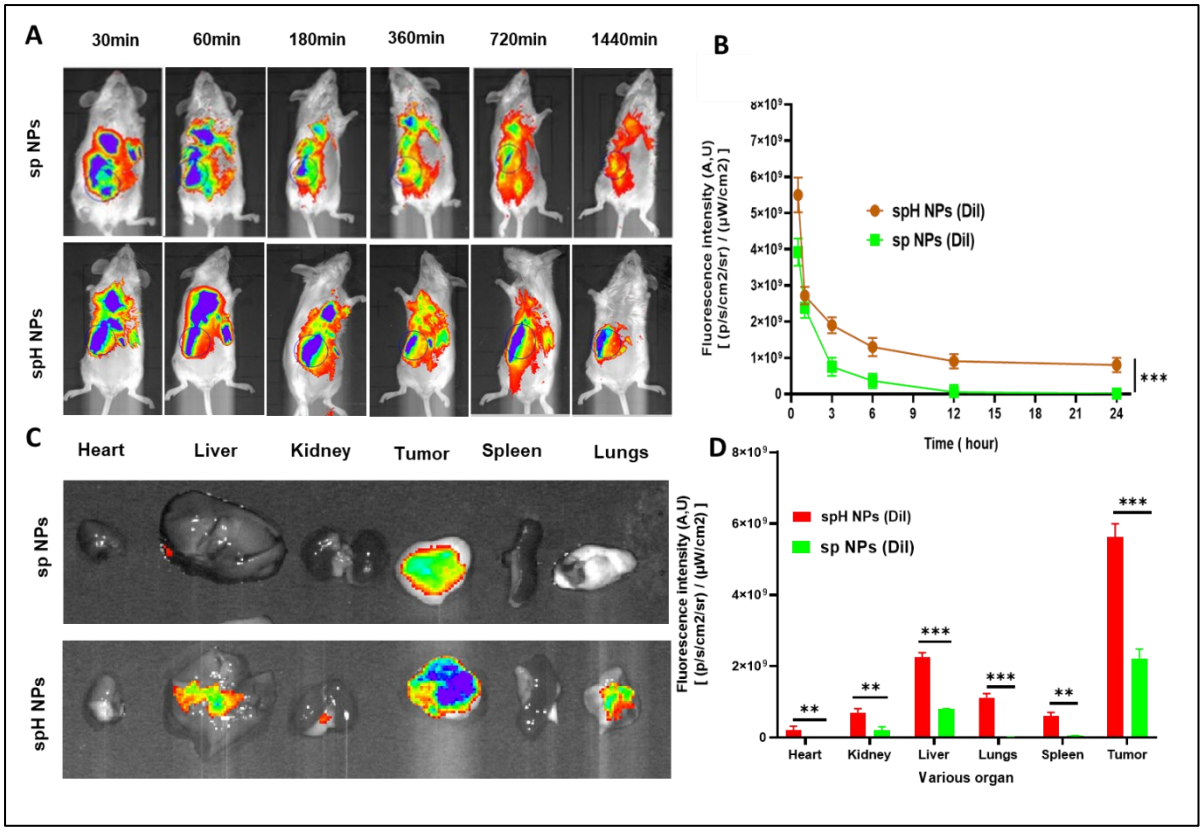

Figure 5.5: A) Representative fluorescent images of the whole body of the mice captured by the IVIS Lumina system at various time points (0.5, 1, 3, 6, 12, and 24 h) after DiI-encapsulated NP administration **B)** Total body fluorescent intensity and time plot. **C)** Representative fluorescent images of the tumor, liver, lungs, kidney, spleen, and heart. **D)** Fluorescent intensity of different organs after isolation indicating increased tumor distribution of spH NPs(DiI) and sp NPs.

In-vivo anti-tumor efficacy study:

Subsequently, the NP's efficacy in inhibiting tumor growth was evaluated *in vivo* in the orthotopic breast tumor (4T1-Luc) bearing female BALB/c mice. The NPs were administered at the exact dosage employed in the toxicity study on days 0, 4, and 8. Tumor growth was quantified using bioluminescence through luciferin-mediated detection (**Figure 5.6**). The control group consistently exhibited a significant increase in luminescence signal, indicating rapid tumor growth (**Figure 5.6C**). Conversely, the treatment groups displayed markedly reduced luminescence signals. Notably, the spH NPs group exhibited the lowest luminescence, significantly lower than all other groups. In addition to bioluminescence measurements, tumor volume was determined by assessing tumor dimensions using the formula [(length × width^2)/2]. After 21 days of treatment, the mean tumor volumes were as follows: 624 ± 23 mm^3 for the PTX group, 510 ± 28 mm^3 for the RSQ group, 310 ± 87 mm^3 for the PTX+RSQ group, and 167 ± 23 mm^3 for the spH NPs group **(Figure 5.6E**). After the 21-day treatment period, tumors were extracted from the mice to assess their weight and histology.

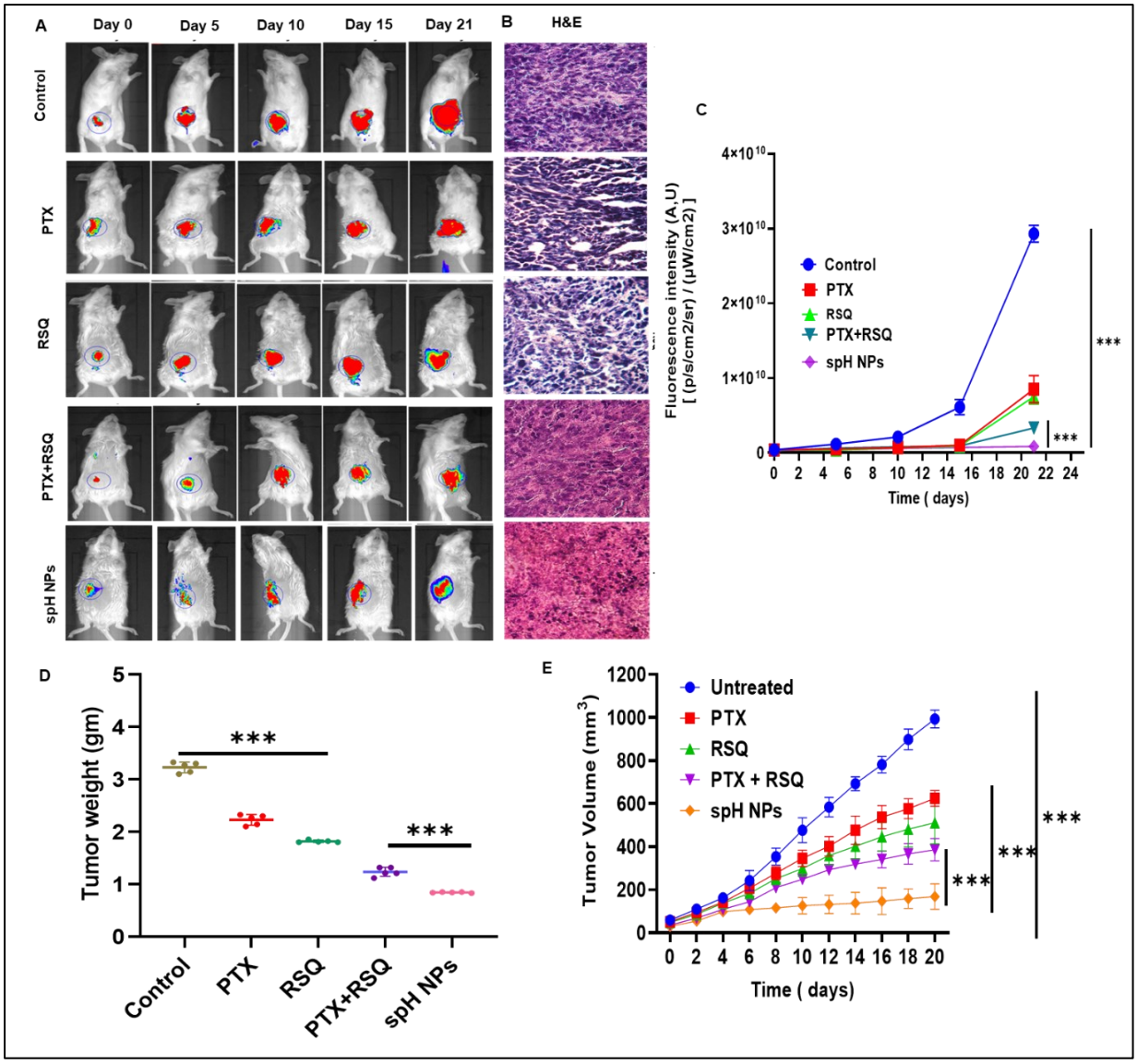

Figure 5.6:A) Quantification of bioluminescence of the whole animal. Representative IVIS images of whole animals at different time intervals and H and E stained tumor tissue images. **C)** Quantification of bioluminescence of the whole animal. **D)**average weight of tumors isolated from various treatment groups**. E)** average volume of tumors isolated from various treatment groups. *, ** and *** indicate $p < 0.05$, $p < 0.01$ and $p < 0.001$ respectively. Data are represented as mean ± SD, where n = 5.

Tumor weight displayed a consistent trend, with average tumor weights of 3.82 ± 0.20 g for the control group, 2.62 ± 0.12 g for the PTX group, 1.67 ± 0.70 g for the RSQ group, 1.20 ± 0.45 g for the PTX+RSQ group, and 0.32 ± 0.12 g for the spH NPs group (**Figure 5.6D**). Histological examination of tumor sections stained with hematoxylin and eosin (H&E) revealed the fewest viable cancer cells in the spH NPs group, followed by the PTX+RSQ group. The notable enhancement in the efficacy of the combined drug treatment could be attributed to synergistic effects between PTX and RSQ [9, 12, 13].

Effect on apoptosis

At the culmination of the 21 days, tumor sections were obtained and subjected to the TUNEL assay to evaluate the initiation of apoptosis. The results revealed the highest level of apoptosis within the spH NPs-treated group, followed by PTX, RSQ, and PTX+RSQ groups (as depicted in **Figure 5.7A** and **B**). This data is in corroboration with the in-vitro apoptosis analysis, where we have found an increased apoptosis rate with PTX+RSQ combination when compared to free drugs alone, and spH has shown a striking increase in apoptosis induction when compared to PTX+RSQ combination, thus we can conclude that improved plasma half-life and pH-sensitive release of payload at the TME might be the reason behind the enhancement of apoptosis rates observed in in-vitro studies.

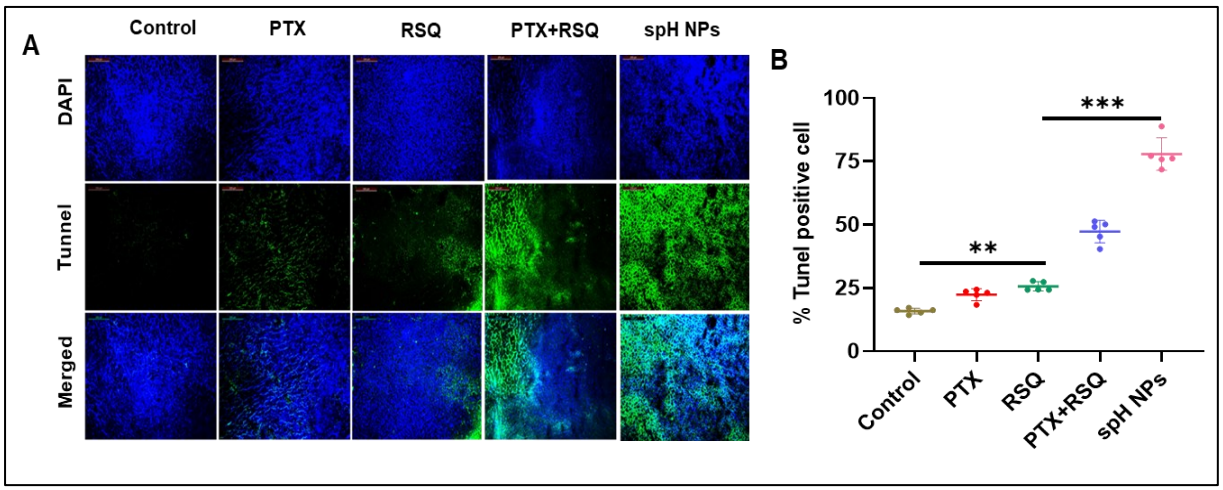

Figure 5.7: Effect of PTX+ RSQ loaded NPs treatment on tumor **A)** Evaluation of apoptosis in tumor tissues by TUNEL assay. **B)** Quantification of fluorescence from TUNEL assay. (In all the panels, * represents $p < 0.05$, ** represents $p < 0.01$, *** represents $p < 0.001$, **** represents $p < 0.0001$, and ns represents no significant difference).

Ki67 analysis:

Uncontrolled proliferation stands as a hallmark of cancer. Ki67 is a widely accepted marker for proliferation and is frequently employed in standard pathological cancer assessments due to its clinical relevance to metastasis and cancer stages.

In the context of this research, we examined Ki67 expression in tumors collected after 21 days of treatment through immune-histofluorescence analysis. Remarkably, the expression of Ki67 in animals treated with spH NPs was notably lower when contrasted with animals treated with PTX+RSQ and the individual drug treatments corroborating with *in-vitro* data as well as previous reports (**Figure 5.8A** and **B**) [10].

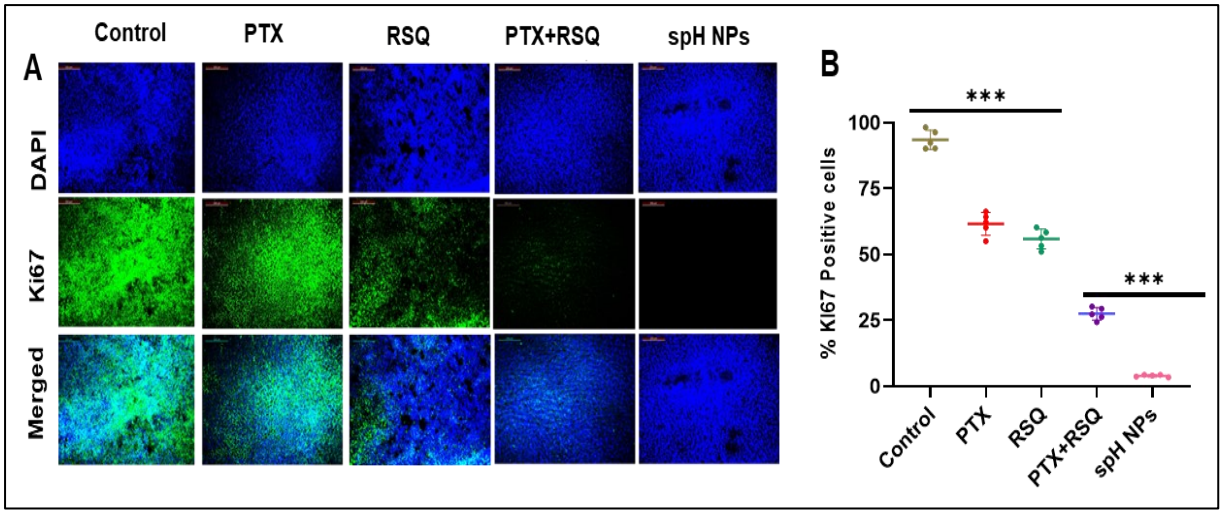

Figure 5.8: A) Evaluation of cell proliferation in tumor tissues by Ki67 immunohistofluorescence assay. B) Quantification of fluorescence from Ki-67 assay. (In all the panels, * represents $p < 0.05$, ** represents $p < 0.01$, *** represents $p < 0.001$, **** represents $p < 0.0001$, and ns represents no significant difference).

Effect on ROS

We noted a synergistic promotion of cancer cell apoptosis by generating reactive oxygen species (ROS) upon combining PTX with RSQ through *in-vitro* analysis. Thus, our objective was to investigate the production of ROS within tumor tissue in response to NP formulations in an *in-vivo* setting. On the 21st day, the levels of ROS were quantified by measuring DCFH-DA fluorescence using the IVIS-Lumina in-vivo imaging system from PerkinElmer, Inc., USA, which has shown a drastically increased production of ROS with spH NPs treatment even in comparison with PTX+RSQ combination showing its pH triggered destabilization even in *in-vivo* tumor developed animals which is corroborating with *in-vitro* studies as well as previous literature (as depicted in **Figure 5.9**) [14].

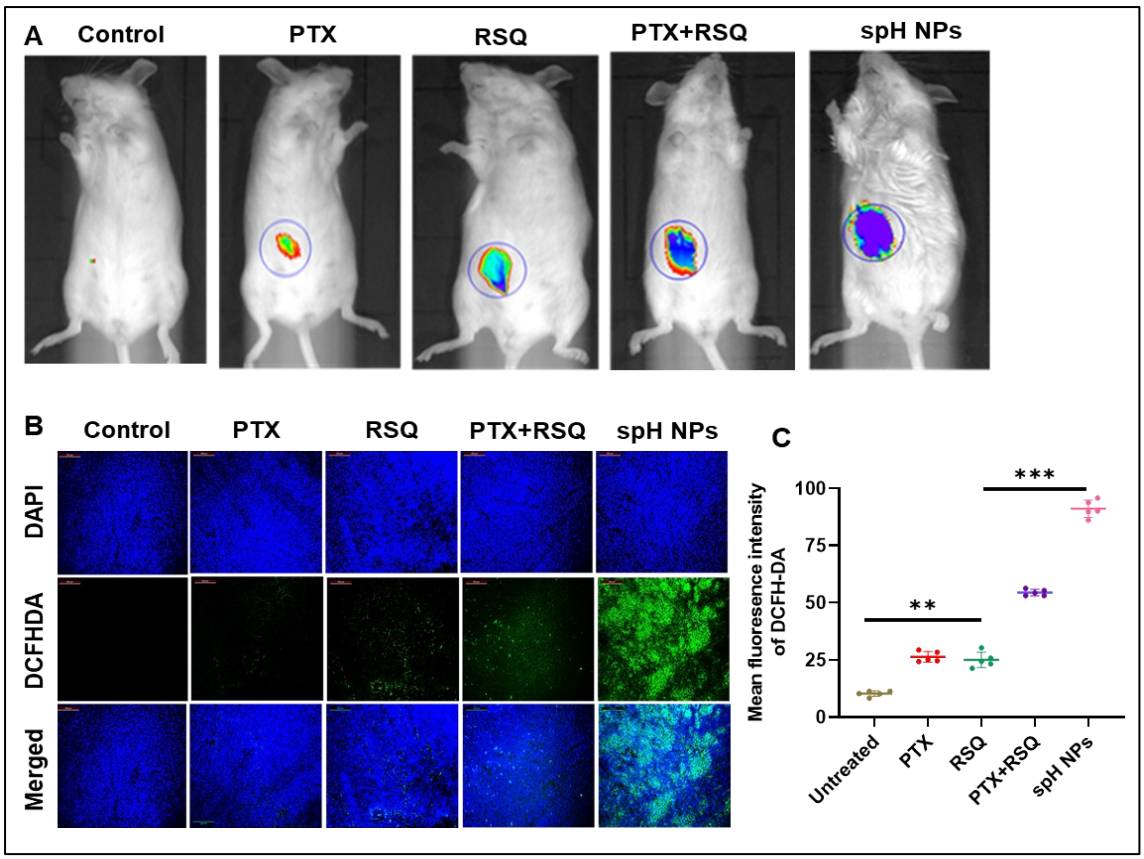

Figure 5.9: *In-vivo* ROS analysis. A) DCFH-DA fluorescent images of the whole mice body with different treatments. B) DAPI (blue) and DCFH-DA (green) fluorescence images of the sectioned tumor tissues. C) fluorescent intensity analysis. (** represents $p < 0.01$, **** represents $p < 0.0001$).

Effect on metastasis

From a clinical perspective, more than 90% of breast cancer-related fatalities can be traced back to metastasis, with the lungs standing out as the primary destination for breast cancer metastatic spread. Given this context, we focused on examining the developed NP potential to influence breast tumors' metastatic behavior.

After removing tumors on the 21st day, a 9-day monitoring period was initiated to observe metastatic events. The metastasis was evaluated by measuring luciferin-induced bioluminescence emanating from the 4T1-Luc cells. The control group exhibited prominent lung metastasis, and substantial bioluminescent signals were similarly detected in the PTX, RSQ, and PTX+RSQ groups. In stark contrast, the spH NPs group exhibited no noticeable signal (as depicted in **Figure 5.10A**). More precisely, the control and drug-treated groups (PTX, RSQ, PTX+RSQ) displayed significantly elevated luminescence compared to those treated with NPs. The control group had the highest cumulative lung bioluminescence, followed by the PTX, RSQ, and PTX+RSQ groups. Moreover, the spH NPs demonstrated the lowest overall lung weight (**Figure 5.10D**).

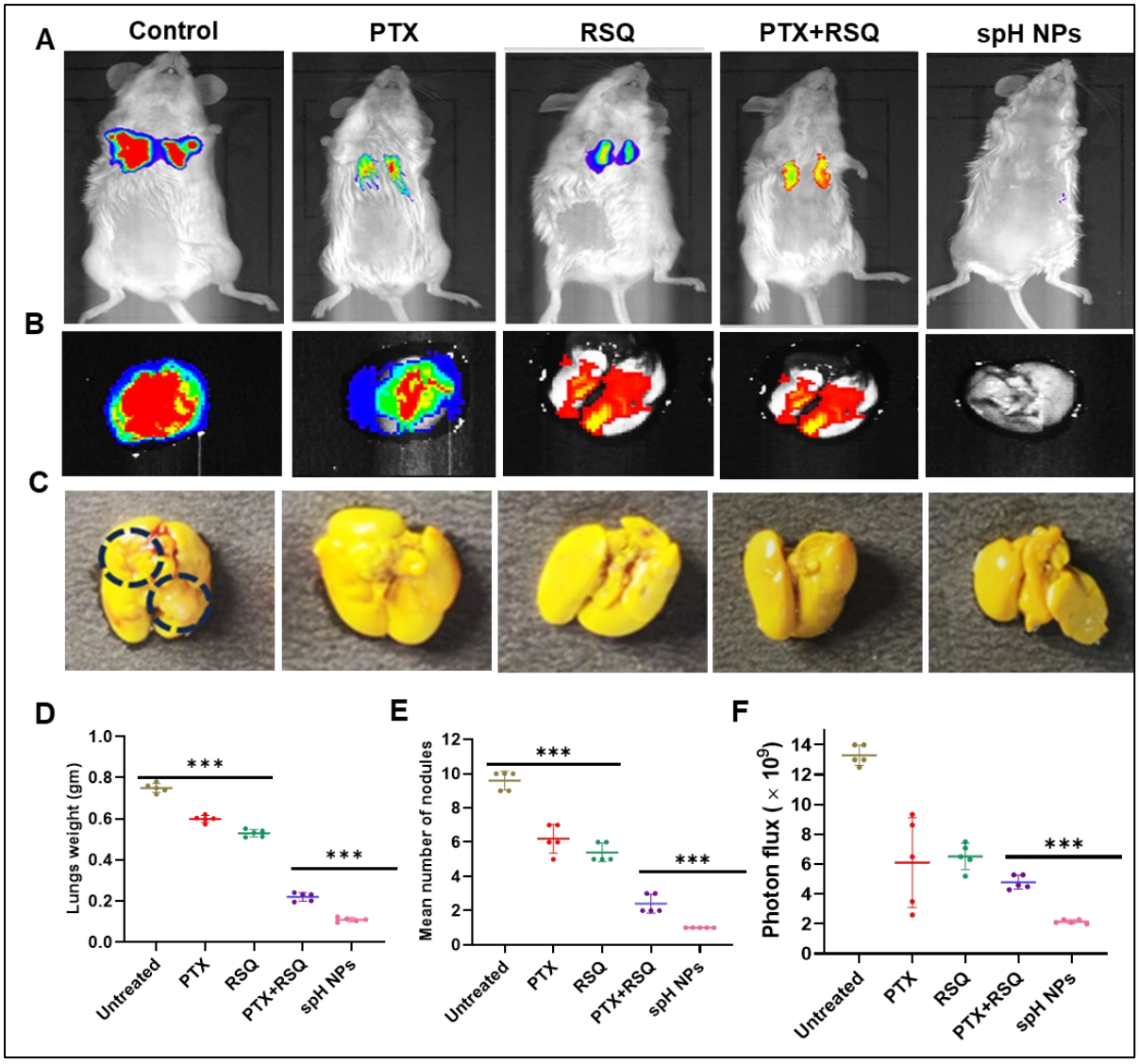

Figure 5.10: Analysis of *in-vivo* tumor metastasis. A) Tumor metastasis was assessed by whole animal bioluminescence imaging of 4T1-Luc tumors. B) Isolated lung image of 4T1 Luc tumor. C) Bioluminescence imaging of lung metastatic 4T1-Luc tumors. D) Analysis of lung weight, E) Number of metastatic nodules in lungs, F) Analysis of bioluminescence of 4T1-Luc tumor metastasis to lungs. Suppression of lung metastasis. G) Proliferation of the metastatic cells in lung tissue was detected by injecting BrdU into the tail vein, followed by lung resection 2 h and stained with anti-BrdU antibody. The section was stained with collagen1A1 antibody to see the collagen level in the lung. H&E staining of the lung section showed more proliferation of cells compared to treatment groups. (In all the panels, * represents $p < 0.05$, ** represents $p < 0.01$, *** represents $p < 0.001$, and **** represents $p < 0.0001$).

BrdU, an analog of the nucleoside thymidine, is employed in the BrdU assay to identify actively proliferating cells. Consequently, it stands as a crucial marker in discerning cellular proliferation. The lung sections stained with BrdU were subjected to microscopic examination, revealing that the count of proliferating endothelial cells in lungs affected by metastasis was significantly higher in the untreated group and quite the opposite with spH NPs group even in comparison to the other treatment groups (as depicted in **Figure 5.11**). This observation might be attributed to the potential entrapment of cancer cells within vessels, subsequently leading to

metastatic foci within the lungs. Furthermore, the spH NPs treated group exhibited a reduction in collagen levels compared to the untreated group, corroborating earlier literature reports of PTX and RSQ [15-17].

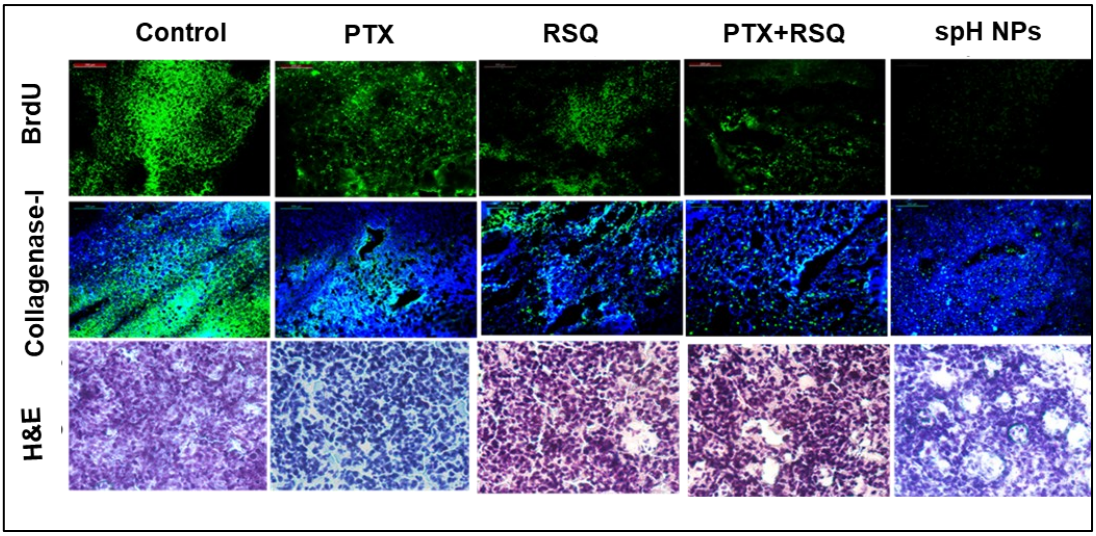

Figure 5.11: Proliferation of the metastatic cells in lung tissue was detected by injecting BrdU into the tail vein, followed by lung resection 2 h and stained with anti-BrdU antibody. The section was stained with collagen1A1 antibody to see the collagen level in the lung. H&E staining of the lung section showed more proliferation of cells compared to treatment groups.

5.4. Conclusion:

In conclusion, we have found that PTX and RSQ, when administered in free drug form alone, in combination, and with NPs at the particular dose, didn't exhibit any toxicity signs. In continuation with pharmacokinetic studies, both PTX and RSQ pharmacokinetic profile has shown prolonged circulation of time, targeted drug delivery at the tumor site with enhanced EPR effect, reduced systemic toxicity, and enhanced therapeutic efficacy. Improved PK parameters such as half-life, clearance, Vd, Cmax, and Tmax were observed when the drug combination was given in spH Nps form when compared to free drugs alone and in combination. After that, tumor core penetration of spH NPs was visualized when compared to sp NPs, without any other tissue distribution, which might be because of the triggered release of the payload of spH Nps at the acidic pH of the TME in the tumor-bearing mice, which corroborates with our *in-vitro* 3D penetration study.

Further in-vivo efficacy studies have demonstrated decreased tumor volume, tumor growth, and improved apoptosis rate and ROS induction with negligible proliferation and metastasis rate with least lung nodules with spH NPs compared to PTX+RSQ combination and free drugs alone. Altogether, we can conclude that spH NPs loaded with PTX and RSQ has shown improved *in-vivo* efficacy in a breast cancer model.

References:

1. Li, Z., et al., *Application of Animal Models in Cancer Research: Recent Progress and Future Prospects.* Cancer Manag Res, 2021. **13**: p. 2455-2475.
2. Onaciu, A., et al., *Spontaneous and Induced Animal Models for Cancer Research.* Diagnostics (Basel), 2020. **10**(9).
3. Curt, G.A., *The use of animal models in cancer drug discovery and development.* Stem Cells, 1994. **12**(1): p. 23-9.
4. Singhal, S.S., et al., *Recent Advancement in Breast Cancer Research: Insights from Model Organisms-Mouse Models to Zebrafish.* Cancers (Basel), 2023. **15**(11).
5. Long, J.E., M. Jankovic, and D. Maddalo, *Drug discovery oncology in a mouse: concepts, models and limitations.* Future Sci OA, 2021. **7**(8): p. Fso737.
6. Kadian, N., et al., *Comparative assessment of bioanalytical method validation guidelines for pharmaceutical industry.* J Pharm Biomed Anal, 2016. **126**: p. 83-97.
7. Tiwari, G. and R. Tiwari, *Bioanalytical method validation: An updated review.* Pharm Methods, 2010. **1**(1): p. 25-38.
8. Pourvasei, R., et al., *Specific method validation and sample analysis approaches for biocomparability studies of denosumab addressing method and manufacture site changes.* Aaps j, 2013. **15**(1): p. 70-7.
9. Kakwere, H., et al., *Systemic Immunotherapy with Micellar Resiquimod-Polymer Conjugates Triggers a Robust Antitumor Response in a Breast Cancer Model.* Adv Healthc Mater, 2021. **10**(10): p. e2100008.
10. Symmans, F.W., *Breast cancer response to paclitaxel in vivo.* Drug Resist Updat, 2001. **4**(5): p. 297-302.
11. Luo, K., et al., *Co-delivery of paclitaxel and STAT3 siRNA by a multifunctional nanocomplex for targeted treatment of metastatic breast cancer.* Acta Biomater, 2021. **134**: p. 649-663.
12. Song, J., et al., *Efficient tumor synergistic chemoimmunotherapy by self-augmented ROS-responsive immunomodulatory polymeric nanodrug.* J Nanobiotechnology, 2023. **21**(1): p. 93.
13. Zhang, H., et al., *Development of thermosensitive resiquimod-loaded liposomes for enhanced cancer immunotherapy.* J Control Release, 2021. **330**: p. 1080-1094.
14. Mantovani, A., et al., *Macrophages as tools and targets in cancer therapy.* Nat Rev Drug Discov, 2022. **21**(11): p. 799-820.
15. Chakraborty, A., et al., *Tumor targeted delivery of mycobacterial adjuvant encapsulated chitosan nanoparticles showed potential anti-cancer activity and immune cell activation in tumor microenvironment.* Int Immunopharmacol, 2023. **114**: p. 109463.
16. Ahmed, I. and N. Ismail, *M1 and M2 Macrophages Polarization via mTORC1 Influences Innate Immunity and Outcome of Ehrlichia Infection.* J Cell Immunol, 2020. **2**(3): p. 108-115.
17. Helleberg Madsen, N., et al., *In vitro 2D and 3D cancer models to evaluate compounds that modulate macrophage polarization.* Cell Immunol, 2022. **378**: p. 104574.

Chapter 6:

Conclusion and Future Prospective

Conclusion

Breast cancer is a devastating global health issue that continues to claim the lives of women each year. Recent cutting-edge research has shown that the multifaceted nature of the tumor microenvironment (TME) is a significant contributor to treatment failures. However, many conventional therapies available in the market are one-dimensional, focusing solely on cancer cells, resulting in resistance to treatment and early tumor recurrence. These single-faceted approaches often encourage the tumor microenvironment to become more aggressive, thus promoting resistance. To improve treatment outcomes, adopting a multidimensional approach is crucial. One promising emerging strategy is the concept of combined chemo-immunotherapy. However, it's worth noting that some chemotherapeutic agents possess inherent immunosuppressive properties, making them unsuitable for this approach. Exceptions such as paclitaxel (PTX) are noteworthy for stimulating the immune system at therapeutic levels, leading to improved activation of anti-tumor CD8+ T cells and enhanced infiltration of immune cells. However, the effective activation of T cells depends on the presentation of antigens. Within the TME, macrophages, the primary antigen-presenting cells, often exist in an immunosuppressed state. Toll-like receptor (TLR) agonists possess potent immunogenic properties by triggering the activation of these macrophages. As a result, targeted delivery of chemotherapeutic agents and TLR agonists to tumors offers substantial potential for synergistic chemo-immunotherapy. Due to their distinct cellular targets, it is crucial to maintain these agents in their free form within the TME. A stimuli-responsive NP delivery system can protect these agents during their circulation in the bloodstream and facilitate their controlled release within the TME, effectively engaging the specific cells they target.

During the initial phase, we screened different TLR agonists to evaluate their potential for chemoimmunotherapy and their impact on macrophage polarization. Among the TLR agonists evaluated, resiquimod (RSQ) showed the most promising results, even at the lowest dose, by enhancing TNF-α expression. Therefore, we selected RSQ to be combined with PTX. The combination of PTX+RSQ showed improved induction of tumor-specific cell death, which we confirmed through live-dead staining and luciferin-tagged cells. We also observed strong chemoimmunotherapeutic activity when the PTX and RSQ combination promoted M1 macrophage polarization in 2D and 3D complex spheroid models. Moreover, the combination of PTX and RSQ modulated ROS leading to enhanced efficacy.

Following the successful in-vitro demonstration of the chemoimmunotherapeutic activity of the PTX+RSQ combination, our next objective is to create a formulation that can safeguard the drug payload during circulation in the bloodstream and deliver it in a targeted manner to tumor sites. It's well-known that the clinical translation of nanomedicine faces challenges related to complex formulation and scale-up processes. To increase the likelihood of clinical success, we aim to develop a straightforward, continuous flow process for synthesizing uniform nanocarriers. We could prepare highly reproducible PTX-encapsulated NPs with a continuous flow microfluidics system. By varying the PTX: polymer ratio, we can modulate the NPs' size while ensuring their uniformity. Our research has shown that NPs smaller than 100 nm exhibit enhanced cytotoxic activity against both 2D and 3D in-vitro models, improved internalization by tumor cells, and better penetration of 3D spheroids. Altogether, this formulation technique using a microfluidic-based continuous flow process holds great promise for developing an economical and effective PTX delivery system.

With the successful optimization of the formulation preparation and procedure, our next goal is to load PTX and RSQ to target two different cell types: tumor cells and macrophages. To achieve this, we require a tumor-targeted drug delivery system. We have chosen pH as a trigger for this purpose, as it is well-established that pH-sensitive NPs remain stable in the neutral pH of the bloodstream and release their payload in the acidic pH of the tumor microenvironment (TME), typically around 6.5. We have synthesized a pH-sensitive polymer conjugated with poly-histidine using two different polymers, one linear PLGA and the other star-shaped PLGA with five arms. A comparative study was conducted between these two pH-sensitive nano-delivery systems to assess the influence of polymer structure on their pH-sensitive properties. The multi-armed polymer exhibited superior pH-dependent size variation and drug release performance. This smart carrier system for TME-specific drug release further improved the in-vitro efficacy of the drug combination.

Subsequently, we conducted in-vitro cell culture studies utilizing 2D, quasi-3D, and 3D complex spheroid models. Initially, we observed enhanced tumor-specific cell death and improved macrophage polarization, which resulted in superior chemo-immunotherapeutic activity. The final formulation exhibited several key advantages. It demonstrated increased cancer cell uptake, decreased macrophage uptake, improved endosomal escape, and efficient cytosolic distribution.

Additionally, our formulation displayed pH-dependent destabilization of NPs, as evidenced by improved penetration into the tumor core of 3D spheroids, particularly with spH NPs, compared to lpH and non-pH sensitive NPs (lp and sp NPs). This confirmed the pH-sensitive release of the drug payload. Furthermore, spH NPs exhibited robust in-vitro chemo-immunotherapeutic activity by promoting M1 macrophage polarization and inducing tumor-specific cell death in both 2D and 3D complex spheroid models. The PTX and RSQ combination also demonstrated improved efficacy by modulating ROS.

In ex-vivo studies involving splenocytes and cancer cell complex spheroids, we observed enhanced macrophage polarization and increased expression of MHC-I and MHC-II, indicating a potential improvement in antigen presentation capabilities. Overall, the efficacy of the optimized spH NPs surpassed that of the free drug combination and non-pH sensitive NPs in terms of tumor cell cytotoxicity and the expression of macrophage immune stimulatory markers, underscoring the enhanced in-vitro chemo-immunotherapeutic activity of spH NPs. To fully assess its potential for clinical translation, further *in-vivo* studies are warranted.

Thus, After successful understanding and observations of *in-vitro* chemo-immunotherapeutic activity of spH NPs when compared to PTX+RSQ and alone as well, we then thought to found that PTX and RSQ toxicity when administered in free drug form alone, in combination, and with NPs at the particular dose, wherein we have found none of the treatment groups didn't exhibit any toxicity signs. In continuation, we have checked the pharmacokinetic profile of both PTX and RSQ in comparison with PTX+RSQ combination and NPs, where we have observed spH NPs have shown prolonged circulation of time, targeted drug delivery at the tumor site with enhanced EPR effect, reduced systemic toxicity and enhanced therapeutic efficacy. Improved PK parameters such as half-life, clearance, Vd, Cmax, and Tmax were observed when the drug combination was given in spH Nps form when compared to free drugs alone and in combination. After that, tumor core penetration of spH NPs was visualized when compared to sp NPs, without any other tissue distribution, which might be because of the pH-triggered release of the payload of spH NPs at the acidic pH of the TME in the tumor-bearing mice, which corroborates with our in-vitro 3D penetration study. Further *in-vivo* efficacy studies have demonstrated the decreased tumor volume, tumor growth, and improved apoptosis rate and ROS induction with negligible proliferation and metastasis rate with the least lung nodules with spH NPs when compared to PTX+RSQ combination and free drugs alone. We can conclude that spH NPs loaded with PTX and RSQ have improved *in-vivo* efficacy in a breast cancer model.

Briefly, the PTX+RSQ combination co-loaded in the pH-sensitive polymer was found to have improved chemotherapeutic activity and enhanced macrophage polarization (Immunotherapeutic potential) against 2D, quasi-3D, and 3D *in-vitro* tumor models. spH NPs were found to show decreased macrophage uptake, increased intracellular tumor cell internalization by endosomal escape in a 2D system, and enhanced tumor spheroid core penetration and colocalization in the 3D system. spH NPs have also resulted in improved circulation half-life and decreased clearance rate of both PTX and RSQ, along with decreased toxicity, improved pharmacokinetic profile, enhanced tumor biodistribution, superior anti-tumor efficacy, and decreased metastasis rate.

Future scope

- The optimized NP preparation and pH-sensitive NPs can be used as a platform technology to deliver other combinations to tumors.
- The optimized combination of drugs and NPs can be studied in other immune cell modulation in detail.
- This combined chemo-immunotherapeutic strategy targeting macrophages (PTX+RSQ) can be studied in other tumor models.
- *In-vivo* macrophage polarization, immune cell activation, and antigen presentation can be performed for successful translation.

LIST OF PUBLICATIONS

Research articles

1. Maravajjala, K.S., Swetha, K.L. and Roy, A., 2022. pH-responsive nanoparticles for multidimensional combined chemo-immunotherapy of cancer. Journal of Pharmaceutical Sciences.
2. Maravajjala KS, Swetha KL, Sharma S, Roy A#. Development of a size-tunable paclitaxel micelle using a microfluidic-based system and evaluation of its in-vitro efficacy and intracellular delivery. Journal of Drug Delivery Science and Technology. 2020; 60:102041.
3. Sumit; Kavya M; Khanna, S; Kachwal V; Karnam S; Santosh M; Chowdhury R; Roy A and Laskar I. Rational molecular designing of aggregation enhanced emission (AEE) active red-emitting Iridium (III) complexes: effect of lipophilicity and nanoparticle encapsulation on photodynamic therapy efficacy. ACS Applied Biomaterials; 2023; March.
4. K Laxmi Swetha, Milan Paul, Kavya Sree Maravajjala, Soniya Kumbham, Swati Biswas, Aniruddha Roy. Overcoming drug resistance with a docetaxel and disulfiram-loaded pH-sensitive nanoparticle. Journal of Controlled Release. 2023;356: 93-114
5. Swetha, K.L., Maravajjala, K.S., Sharma, S., Chowdhury, R., Roy, A#. Development of a tumor extracellular pH-responsive nanocarrier by terminal histidine conjugation in a star shaped poly(lactic-co-glycolic acid). European Polymer Journal. 2021; 147:110337
6. Sharma S, Madhyastha H, Swetha KL, Maravajjala KS, Singh A, Madhyastha R, Nakajima Y, Roy A#. Development of an in-situ forming, self-healing scaffold for dermal wound healing: in-vitro and in-vivo studies. Materials Science and Engineering: C. 2021; 112263

Review articles

7. Padhye, T., Maravajjala, K.S., Swetha, K.L., Sharma, S., Roy, A#. A comprehensive review of the strategies to improve oral drug absorption with special emphasis on the cellular and molecular mechanisms. Journal of Drug Delivery Science and Technology. 2021; 61:102178.
8. Swetha, K.L., Maravajjala, K.S., Li, S.D., Singh, M.S. and Roy, A., 2022. Breaking the niche: multidimensional nanotherapeutics for tumor microenvironment modulation. Drug Delivery and Translational Research, pp.1-30.

Conference presentations

1. Kavya Sree Maravajjala, Aniruddha Roy. ‘Development of a tumor-responsive nanoparticle-based multi-dimensional therapeutics against cancer’ Oral presentation at the international conference “PHARMACON-2022” held at NIPER, Mohali, India.

Biography of Prof. Aniruddha Roy (Supervisor)

BIOGRAPHICAL SKETCH

Name	**Current Position**
Aniruddha Roy	Associate Professor Department of Pharmacy Birla Institute of Technology & Science, Pilani VidyaVihar, Pilani, Rajasthan 333031

Professional Experience

Associate Professor, Birla Institute of Technology & Science, Pilani Campus, Aug, 2021 – Present.
Assistant Professor, Birla Institute of Technology & Science, Pilani Campus, Nov, 2015 – July, 2021.

Education/Training

Institution and Location	Degree	Duration	Field Of Study
Jadavpur University, Kolkata, India	B. Pharm.	1999-2003	Pharmacy
Jadavpur University, Kolkata, India	M. Pharm.	2004-2006	Pharmacology
National Institute of Immunology, New Delhi, India	Ph.D.	2006-2012	Drug delivery
Indian Institute of Technology (IIT), New Dehi, India	Post-doc	2012-2013	Polymer Chemistry
Ontario Institute for Cancer Research, Toronto, Canada	Post-doc	2013-2014	Drug delivery
University of British Columbia, Vancouver, Canada	Post-doc	2014-2015	Drug delivery

Personal Statement

Dr. Aniruddha Roy holds a Bachelor's and Master's degree in Pharmacy from Jadavpur University in Kolkata, India, and a PhD from the National Institute of Immunology in New Delhi, India. He also completed post-doctoral training at the Ontario Institute of Cancer Research in Toronto, Canada, and the University of British Columbia in Vancouver, Canada. Currently, he serves as an Associate Professor at Birla Institute of Technology and Science - Pilani. Dr. Roy is a highly accomplished scientist who has made significant contributions in the areas of targeted drug delivery and pharmacokinetics-pharmacodynamics evaluation, with a focus on cancer therapy. His research expertise includes nanomedicine, combination therapeutics, and the treatment of resistant cancer. His research work resulted in the publication of 37 research articles in leading journals. Currently, he has more than 1900 citations from his publications, with an h-index of 20. As a lead researcher, he is the inventor of 4 patented platform technologies. One of these technologies has been taken up by FACIT (the commercialization agent for Ontario Institute for Cancer Research, Toronto, Canada) and another one by Alicorn Med. Pvt. Ltd., an Indian start-up company, for possible commercialization.

Biography of Prof. Gautam Singhvi (Co-supervisor)

Dr. Gautam Singhvi is working as an Associate Professor in the Department of Pharmacy, BITS, Pilani. He obtained his Ph.D. from BITS Pilani. He has 3 years of industrial research and 12 years of academic teaching and research experience. During his industrial tenure, he worked on solid oral, pellets, and complex pharmaceutical product development for regulated market. Currently, he is involved in industrially feasible nanocarriers-based formulation development and optimization for various therapeutic agents. His team is extensively working on topical and transdermal drug delivery systems for rheumatoid arthritis, psoriasis, pain management, skin cancer and fungal infections. He has published more than 100 publications in reputed international peer-reviewed journals and 20 book chapters in international publishers such as Elsevier, Springer, and Willy. He is actively involved in sponsored research projects sponsored by pharmaceutical industries and govt funding agencies. As an inventor, he has been granted 3 Indian patents and his 8 patents under examination. He is also a peer reviewer of several international journals. Recently, he was listed in "World Ranking of Top 2% Scientists" in 2023 database (Published: 5 October 2023) created by experts at Stanford University, USA. Published in the Journal of PLOS Biology.

Biography of Ms. Maravajjala Kavya Sree

BIOGRAPHICAL SKETCH

Name	**Current Position**
Maravajjala Kavya Sree	Research Scholar Department of Pharmacy Birla Institute of Technology & Science, Pilani VidyaVihar, Pilani, Rajasthan 333031

Professional Experience

Junior Research Fellow (JRF), Birla Institute of Technology and Science in collaboration with INTAS Pharmaceuticals – 2019

Education/Training

Institution and Location	Degree	Duration	Field Of Study
Vaagdevi College of Pharmacy, Warangal, Telangana, India	B. Pharm.	2012-2016	Pharmacy
St. Peters Institute of Pharmaceutical Sciences, Warangal, Telangana India	M. Pharm.	2016-2018	Pharmaceutics
Birla Institute of Technology and Science, Pilani, Pilani Campus, Rajasthan, India	PhD	2019-now	Pharmaceutics

Personal Statement

Maravajjala Kavya Sree joined BITS-Pilani, Pilani campus in 2019 as a Project JRF in a collaborative project with INTAS Pharmaceuticals. Thereafter, she continued pursuing her doctoral research under the guidance of Prof. Aniruddha Roy. Herein, she has started working on tumor-targeted drug delivery systems for combined chemo-immunotherapy of cancer. Over this period, she had a very good experience in targeted polymer synthesis and characterization, Size tunable and translatable nanoparticle preparation, and characterization. Apart from these, she has also worked on 2D and 3D multi-cellular tumor models to check the efficacy of different drug combinations targeting cancer. During this tenure, she has published 6 research articles and 2 review articles in peer-reviewed international journals. She has presented her work in several national and international conferences. Her main area of research expertise includes cancer biology, tumor-targeted drug delivery systems, nanomedicine, macrophage targeting and chemoimmunotherapy. She has extensive experience in molecular techniques, nanoparticle drug delivery system design and development, *in-vitro/ex-vivo/in-vivo* analysis of anticancer therapeutics.